Star formation and merger trees in dwarf galaxy simulations

Stervorming en versmeltingsbomen in simulaties van dwergsterrenstelsels
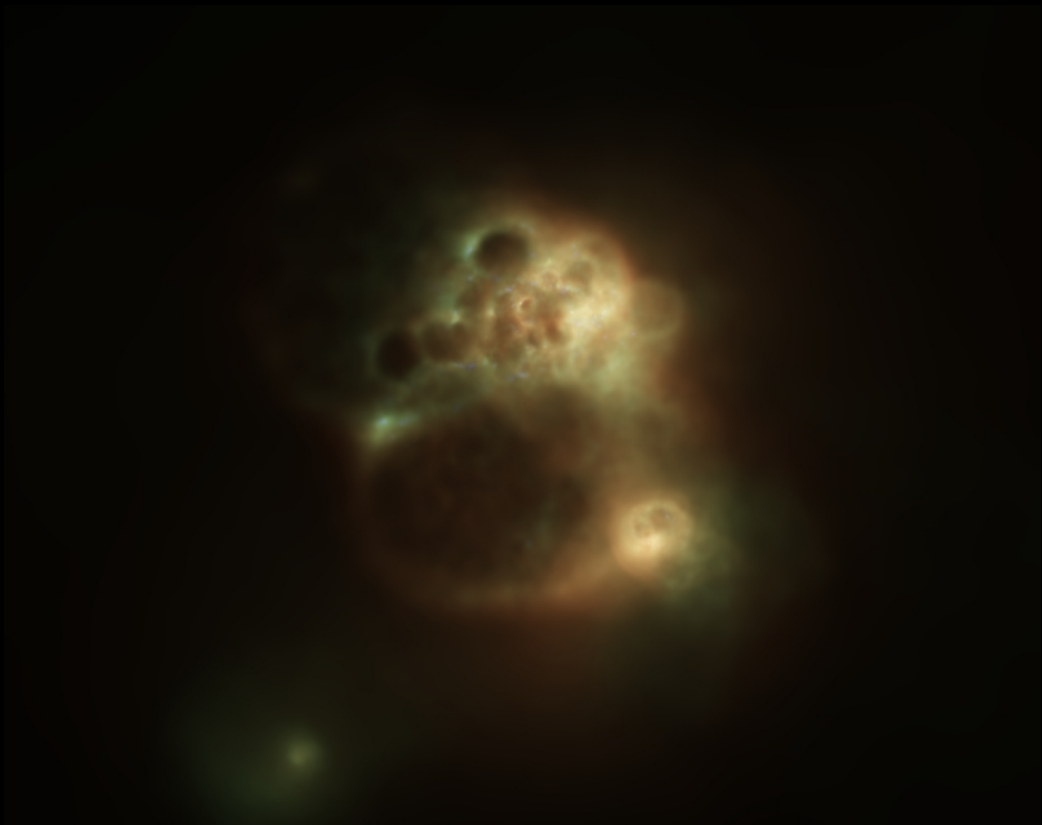
Annelies Cloet-Osselaer

Promotor: Prof. Dr. Sven De Rijcke

Figuur voorpagina: De gasverdeling in een simulatie met een versmeltingsboom. De feedback van de sterren blaast bellen in het gas van de modellen.

Dankwoord

Het is vele jaren geleden dat de sterrenkundemicrobe me te pakken kreeg: van de heldere nachten in de Provence en de koude practica op het dak van de S9 naar de warme bureaus op de Sterre, waar computers de vorming van het universum nabootsen. Mijn jeugdig enthousiasme om 's nachts in de kou naar de sterren te kijken is ondertussen toch al een beetje verwaterd, al heb ik mooie herinneringen aan de waarnemingspractica op het dak waar ik samen met Steven de studenten enthousiast begeleidde. Tijdens mijn studies leerde ik ook dat sterrenkunde meer was dan nachtelijke waarnemingen. Mijn doctoraat liet me dan ook een totaal andere, maar even boeiende zijde van de sterrenkunde zien: het modelleren van de vorming van dwergsterrenselsels en wat we daaruit kunnen leren over de vorming van ons heelal in het algemeen.

In de eerste plaats wil ik zeker mijn ouders bedanken om me te steunen in mijn niet zo alledaagse hobby, mijn streven naar onafhankelijkheid door vanaf mijn eerste jaar op kot te mogen gaan en zoveel meer. En hoewel ik volgens de Simon-test van de UGent helemaal niet sociaal ben wil ik ook graag mijn collega's bedanken voor de vele astronomische en niet-astronomische discussies tijdens de koffiepauzes om 9u30. Ik hoop dat jullie de traditie zullen blijven verderzetten zonder dat ik 'koffie' kom roepen in jullie kantoren of waar jullie nieuwe levens jullie ook naartoe leiden.

En dan nog het serieuze werk. Eerst wil ik mijn promotor Sven bedanken, in de eerste plaats om mij de kans te geven dit doctoraat te maken, maar ook om de problemen die ik onderweg tegenkwam te structureren en eenvoudige oplossingen voor te stellen en voor het nalezen van mijn artikels. Verder wil ik iedereen van onze Dwarf Galaxy Group bedanken: Bert, Joeri, Mina, Robbert, Sander en Sven, voor het gezelschap op conferenties, goede ideeën, toffe groupmeetings, mijn gevecht met computercodes, …

Tot slot wil ik Simon bedanken om er voor mij te zijn wanneer het nodig is, om alle dingen die we samen beleefd hebben, alle toekomstplannen die we gemaakt hebben en voor onze kleine Anna: haar enthousiaste glimlach en schaterlach brengen elke dag het zonnetje in huis.

Gent, maart 2015
Annelies

Table of Contents

1
Introduction

How the Universe has become as we observe it today has been a question that kept people wondering forever. Now, the most accepted theory describing the evolution of our Universe is the ΛCDM model, often referred to as 'the standard cosmological model'. According to this theory our Universe consists of matter, both luminous and dark, and dark energy. Different experiments have tried to observe the cosmic microwave background (CMB) from which the contribution of each component can be determined, for example WMAP (Bennett et al., 2013) and Planck (Planck Collaboration et al., 2014). They have determined that we are very likely living in a spatially infinite and geometrically flat universe, meaning that the mean energy density is equal to the critical density of the universe. After 9 years of observations by the WMAP satellite, Hinshaw et al. (2013) reported the following composition of our Universe:

4.6% baryons: be it in the form of gas, dust or stars, are the most accessible form of matter, emitting radiation over the whole electromagnetic spectrum.

24% cold dark matter: only interacts gravitationally and is much more difficult to 'observe'. The *'cold'* dark matter (CDM) has velocities which are non-relativistic.

71% dark energy: is responsible for the accelerating expansion of the universe. It is quantified in the Einstein field equations by the cosmological constant, Λ.

The ΛCDM model is consistent with the creation of space-time at the Big Bang and is able to explain most observed phenomena like the existence and fluctuations of the cosmic microwave background, the large scale structure of galaxy clusters, the distribution of the elements and the expansion of the Universe. Structure formation in the Universe started in the small adiabatic overdensities visible in the cosmic microwave background. They functioned as seeds for gravitational instabilities in which dark matter clumped together. After recombination, baryons fall into dark matter perturbations and these overdensities can then grow and when

they get dense enough they collapse to form the first proto-galaxies. Galaxies like we observe them today are created 'hierarchically' by subsequent merging of these smaller components and by smooth accretion of dark matter to larger structures that are able to support star formation.

Our interest in dwarf galaxies partially lies in the hierarchical bottom-up structure formation of the Universe since the large structures were constructed in the early Universe by the merging of similar haloes from which the present day dwarfs originated. In addition, large surveys have shown that dwarf galaxies are the most common type of galaxies in the Universe and they are well represented in our Local Group. Recently, the number of observations of dwarf galaxies has increased and improved dramatically by surveys like THINGS (Walter et al., 2008), FIGGS (Begum et al., 2008b), SHIELD (Cannon et al., 2011), LITTLE THINGS (Hunter et al., 2012), the ACS LCID project (Gallart and Lcid Team, 2007; Monelli et al., 2010b,a; Skillman et al., 2014), the dwarfs in the ANGST sample (Dalcanton et al., 2009; Weisz et al., 2011), VLA-ANGST (Ott et al., 2012), etc.

Dwarf galaxies can be simply defined as a small version of a galaxy like our own Milky Way. Tammann (1994) defined them to have absolute B-band magnitudes fainter than -16 mag, which separates them from the 'normal' galaxies, and they can be distinguished from globular clusters by their larger size. They are also dark matter dominated and have high M/L ratios compared to globular clusters (GCs) which generally contain little or no dark matter. Fig. 1.1 gives an overview of the general properties characterizing dwarfs and the different dwarf galaxies subclasses (Tolstoy et al., 2009). We give a short summary of these subclasses:

Early-type galaxies (dE/dSph): often referred to as 'red and dead' galaxies as they are deprived of gas and don't have ongoing star formation. They are generally found in the vicinity of clusters of galaxies or around massive companions and can be subdivided into into dwarf ellipticals (dE) and dwarf spheroidals (dSph). The distinction between dE and dSph is mainly based on a luminosity cut with: M_B = -18 mag < dEs < -14 mag < dSph < -8 mag, where the dSph are fainter, less massive and dark-matter dominated compared to dE. Both types have smooth elliptical isophotes.

Late-type galaxies (dIrr/BCD): are galaxies that contain gas and have ongoing star formation. They are usually located in isolated environments, they often rotate and have irregular isophotes. Therefore, they are classified as dwarf irregulars (dIrr) or blue compact dwarf (BCD). BCDs are distinguished from dIrr as they are generally bluer, more compact and they have a higher central surface brightness (Papaderos et al., 1996; Salzer and Norton, 1999).

Transition type galaxies (dTrans): these dwarfs have properties of both early- and late-type dwarf galaxies, for example smooth elliptical isophotes but with some residual star formation and/or gas. Possible scenarios of one type being converted to another are discussed in Da Costa et al. (2007); De Looze et al. (2013); Koleva et al. (2013).

Tidal dwarf galaxies (TDG): these dwarf galaxies are formed in self-gravitating clumps located in the tidal tails of interacting galaxies. As a consequence, they are expected to have a low dark matter content. As a result of them being formed out of pre-enriched material originating of their parent giant galaxy, they can have high metallicities (Duc et al., 2000; Weilbacher et al., 2003; Sweet et al., 2014).
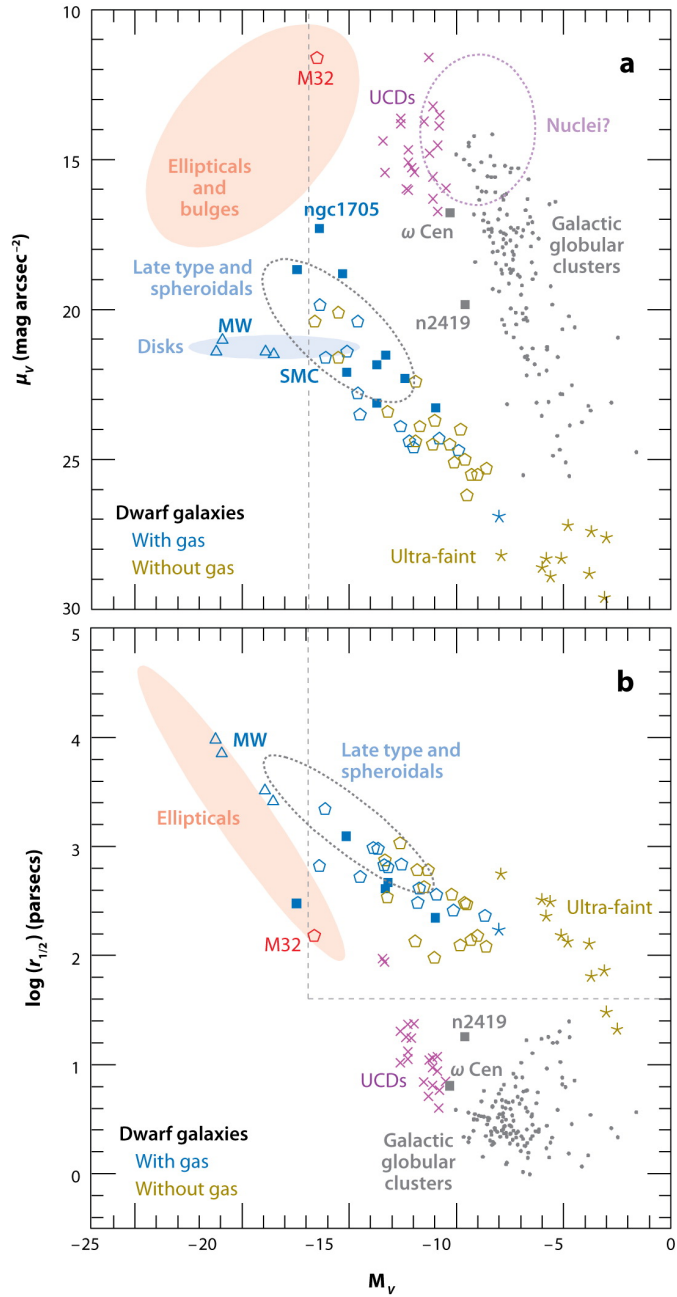
Tolstoy E, et al. 2009.
Annu. Rev. Astron. Astrophys. 47:371–425

Figure 1.1: An overview of the different dwarf galaxy classes from Tolstoy et al. (2009). In the top panel, the V-band central surface brightness, μ_V, is plotted as a function of the V-band magnitude, M_V. The lower panel shows the relation between the size and the V-band magnitudes of the different models.

Ultra-faint dwarfs (uFd):   As observations are improving, more extreme faint dwarfs are discovered. They are assumed to had only one star formation event, or only a few, after which they remained quiescent due to the presence of only ancient stellar populations. This makes them ideal probes to investigate the early stages of chemical enrichment. Fig. 1.1 shows that the properties of these galaxies indicate that they might be an extension of the dSph class down to lower luminosities. They can have very low mean metallicities, e.g. $\langle$[Fe/H]$\rangle$ < -2 (Kirby et al., 2008; Brown et al., 2014), lower then the most metal-poor GCs. Another difference with GC, of which the stars have almost identical abundances due to a homogeneous mixing, is that uFd show a metallicity spread which indicates mixing was very inefficient in these early systems (Frebel and Bromm, 2012). In addition, they are probably extremely dark matter dominated, with $M/L > 100$ $M_\odot/L_\odot$.(Bromm and Yoshida, 2011; Salvadori and Ferrara, 2009)

Ultra-compact dwarfs (UCD):   are dwarfs with half-light radii in the range of 10-100 parsec and with an absolute V-band magnitude fainter then -8 mag (Penny et al., 2014). There are different formation scenarios for UCDs: small UCDs might be simply an extension of the GCs towards fainter magnitudes and larger sizes. More massive UCDs might be the result of multiple mergers between massive GC or star-forming structures while the most massive ones might be tidally stripped dEs (Penny et al., 2014). Compared to uFd they are much more compact and less dark matter dominated.

The different classes of dwarfs are based on their different properties. The question might arise if these differences are based on their 'nature', e.g. internal galaxy properties, or based on their 'nurture', e.g. heavily determined by the environment (Annibali et al., 2011; Sawala et al., 2012; Gallart, 2012). The existence of the dTrans might be proof of a transition between the early- and late-type dwarfs (Grebel et al., 2003) or they might just be a late-type dwarf in a quiescent period (Skillman et al., 2003).

The observed morphology-density relation supports the 'nurture idea', as the different dwarf types can be linked to specific environments, for example, dIrr are generally found in quite isolated environments, where dE/dSph are more found in large groups or near large galaxies.

In essence, this means that dE/dSph were originally dIrr that lost their gas. As shown in simulations, gas removal can happen through external processes like ram pressure stripping and tidal interactions (Mayer et al., 2001b, 2006; Klimentowski et al., 2009). Figure 1.2 shows the normalized star formation rate of the LCID sample which contains six isolated Local Group dwarfs, of which two dIrr galaxies (IC1613 and Leo A), two dIrr/dSph (LGS3 and Phoenix) and two dSph (Cetus and Tucana). The early star formation of the different types is very different contradicting the hypothesis that they are originating from a similar dIrr-kind of galaxy (Gallart, 2012). These star formation histories (SFHs) are generated with very deep color-magnitude diagrams and hence have a very good resolution but their sample is very limited. Weisz et al. (2011) determined the general SFH of dI, dSph and dTrans of the ANGST program. They found the mean SFH of the different morphological types show similar properties up to approximately 1 Gyr ago. However, their resolution at large look-back times is poor. They conclude that the SFH of individual galaxies are quite diverse. This might indicate that there is a large variation on the SFH which depends little on the morphological type and this could explain the very different SFH of the limited sample of LCID dwarfs.
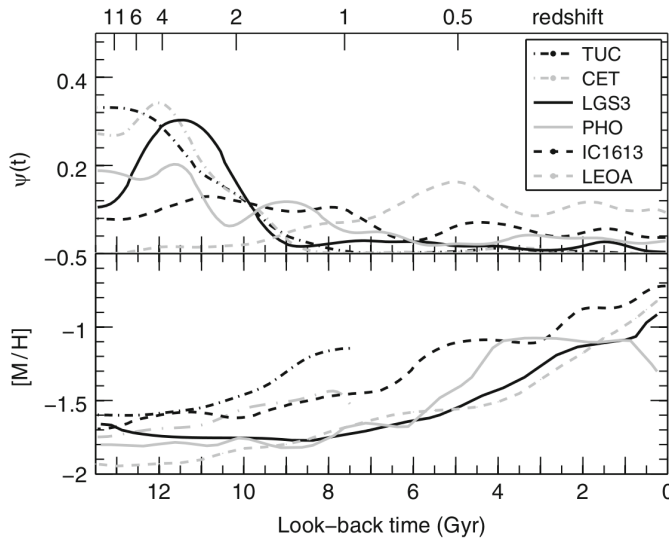
Figure 1.2: Upper panel: the normalized star formation rate as a function of the look-back time for the six LCID galaxies. Lower panel: the age-metallicity relation of the same galaxies. Figure taken from Gallart (2012).

In addition, isolated simulations of dwarf galaxies have shown that in simulations without the ultra-violet background (UVB), supernova feedback is responsible for a self-regulated 'breathing' star formation (Stinson et al., 2007b; Valcke et al., 2008; Schroyen et al., 2011). These simulations are able to produce realistic dwarf galaxies that align with the observed scaling relation but they have a larger gas content than observed dwarfs as they lack gas removing processes like an environment or the UVB. In section 3.3.4 we will look at the effects of supernova feedback, among others, in simulated dwarf galaxies and compare them with the observed scaling relations of dwarfs.

This UVB is expected to have a great influence on the evolution of dwarf galaxies as it heats and disperses their gas. Their gas content is less protected by self-shielding as they have lower gas densities. Cosmological hydrodynamic simulations show that re-ionization does shut down star formation in haloes with $M_h < 3 \times 10^9$ $M_\odot$ or $v_{max} \sim 25$ km/s (Sawala et al., 2014; Nickerson et al., 2011; Shen et al., 2014), for more massive haloes self-shielding prevents the gas from heating and allows stars to be formed. However, Gallart (2012) reported that they do not observe a truncation of the SFH in the dwarfs of the LCID sample due to re-ionization. However, Fig. 1.2 does show a more moderate star formation rate from $z \approx 2$ on, where the UVB peaks (Faucher-Giguère et al., 2009). Their limited sample of 6 galaxies in the LCID sample have dynamical masses (within the half-light radius) in the range $10^7 M_\odot$-$10^8 M_\odot$. These masses were determined by Kirby et al. (2014) based on stellar velocities. As the stellar body generally is less extended compared to the dark matter halo, comparing these observationally determined masses with cosmological simulations is rather difficult and the limited sample might be a poor representation of the general dwarf galaxy population.

It would be better to compare properties of galaxies and our models that are more easy to deduce from the observations and the simulations. Hence, in section 5.4 we will compare our

simulations with the observed "baryonic Tully-Fisher relation" (BTFR), where the baryonic mass, i.e. the sum of stellar and gas mass is compared to the maximum circular velocity of the gas. Observationally, the maximum rotation velocity of the gas can be determined from the width of the 21cm radio emission of neutral hydrogen. The HI gas content is also determined from the 21cm observations. For the stellar content, luminosity needs to be converted to stellar mass with the help of the M/L ratio. Fig. 1.3 shows the BTFR of observed galaxies from Bernstein-Cooper et al. (2014) which is mainly based on observational results of McGaugh (2012). The low mass end is determined by the gas-rich dwarf galaxies Leo P, indicated by the cyan square, and the recently discovered Pisces A. Both galaxies have $v_{max} \sim 15$ km/s. This result is in contradiction with the prediction of the simulations that show that models with $v_{max} < 25$ km/s can not survive reionization and are thus devoid of neutral gas (Sawala et al., 2014; Nickerson et al., 2011; Shen et al., 2014). In Section 5.4, we will look at the agreement between our models and the BTFR.

Finally, Sawala et al. (2012) looked at the combined effects of internal and external processes on dwarf galaxies in the Aquila simulation (Scannapieco et al., 2009) and reported that their properties only weakly depend on the environment and strongly depend on the mass of the dark matter halo they originate from.

We can conclude that it is still under debate if 'nurture' is at the basis of the different morphology classes. It is supported by the observed density-morphology relation but the wide range of SFH of the different dwarf-types and within each dwarf-type indicate the real mechanisms are more complex.

Observations take an image of the Universe at a certain time which is a combination of different physical processes. To gain insight into the role of each process, we can numerically simulate them and compare the resulting models with the observations. Because of their modest dimensions, dwarf galaxies are of interest to simulators because they allow very high spatial resolutions to be reached, which allows us to study in detail the different physical processes involved in their evolution.

Pelupessy et al. (2004), Stinson et al. (2007a), Valcke et al. (2008), Revaz et al. (2009), Sawala et al. (2010) and Schroyen et al. (2013) present dedicated dwarf galaxy simulation codes. These simulations have shown to be able to produce dwarf galaxies with kinematic and photometric properties that are largely in agreement with those of observed dwarf galaxies. Despite the high resolution achieved by these simulations, it is still necessary to implement sub-grid physics to describe the processes which take place on scales below the resolution, for example star formation, feedback, gas cooling and heating. Continued efforts are being made to improve the implementation of these sub-grid physics (Sawala et al., 2010; Pontzen and Governato, 2012; Cloet-Osselaer et al., 2012; De Rijcke et al., 2013; Vandenbroucke et al., 2013). For example, in chapter 3 we will explore a high-density (HD) threshold for star formation that is introduced to better sample the regions of star formation (Saitoh et al., 2008; Governato et al., 2010), but this revealed the need to increase the feedback efficiency (Governato et al., 2010; Cloet-Osselaer et al., 2012; Brook et al., 2012; Stinson et al., 2012). Also, in section 5.1 we discuss the influence of the improved cooling and heating curves of De Rijcke et al. (2013) that provide a better chemical evolution model for the gas and include a UVB.

In addition, the low masses of dwarf galaxies make them sensitive tracers of internal and external processes, such as star formation, supernova feedback, and interactions with the
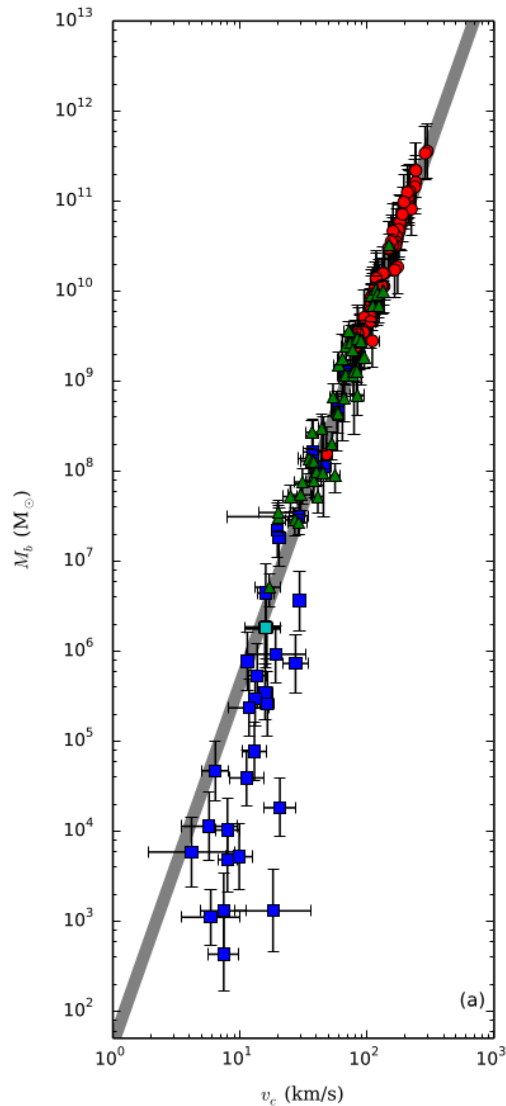
Figure 1.3: Observational baryonic Tully-Fisher (Bernstein-Cooper et al., 2014). The baryonic mass is plotted as a function of the circular velocity of the galaxy. The red circles represent star-dominated galaxies, the green triangles show gas-rich galaxies and the blue squares are dSph galaxies. The gray line shows the BTFR as fitted to the gas-rich galaxies by McGaugh (2012). The cyan square represents the observation of the lowest mass gas-rich dwarf galaxy: Leo P.

environment, for example tidal stripping. The internal processes can be easily investigated in isolated dwarf galaxy simulations, see chapter 3 where we performed a parameter survey of star formation parameters. For the external processes, where the interaction with the environment is important, a larger simulation volume at the cost of less resolution is needed.

Large cosmological simulations, for example Millennium-II (Boylan-Kolchin et al., 2009) and Bolshoi (Klypin et al., 2011) have played an important role in understanding how structure

formation in the Universe happened. These DM-only simulations supported the idea of a hi-
erarchical structure formation and were able to confirm the theoretically predicted conditional
mass function. But, the mass resolution of these simulations is unable to supply statistics
for dwarf galaxies. Zoom-in simulations like the Aquarius project (Springel et al., 2008) and
ELVIS (Garrison-Kimmel et al., 2014) are run to improve the resolution. Analysis of these
simulations showed a discrepancy with the observations often referred to as the *cusp-to-core*
problem: the dark matter haloes in cosmological simulations have a cusped density profile
(Navarro et al., 1996b), with $\rho \sim r^\alpha$ and $\alpha = -1$ in the inner region, while the ones deduced
from observations show a cored density profile (de Blok, 2010), with $\alpha > -1$. The left panel
in Figure 1.4, shows the inner cored density profiles of the seven THINGS dwarfs, which
are deduced from their DM rotation curves. These DM rotation curves are generated by a
thorough kinematic analysis (see Oh et al. (2011b) for more details). Also the cuspy density
profiles from dark matter only simulations are shown by gray lines corresponding to increasing
maximum rotation velocities. Finally, the density profiles of DG1 and DG2 (Governato et al.,
2010) are overplotted showing that these simulations, which include baryonic physics, are
able to produce 'cored' dark matter profiles.
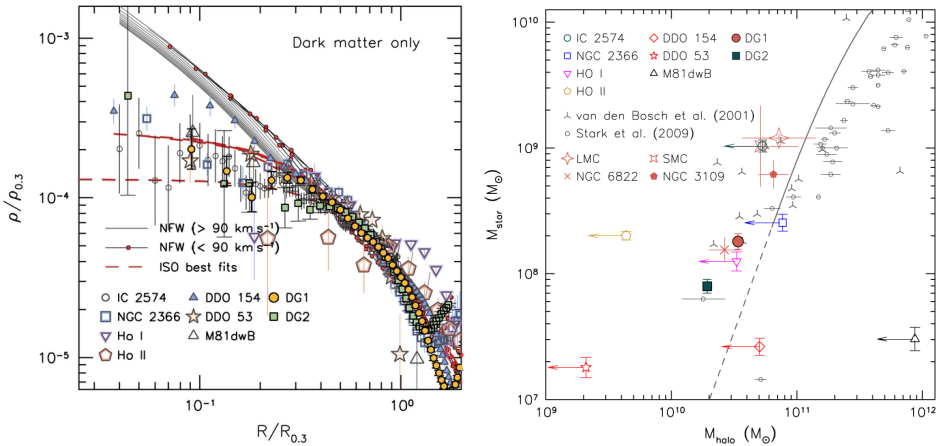
Figure 1.4: Left panel: The scaled DM density profile of the simulated dwarfs DG1 and DG2,
simulated by the N-body/SPH-code Gasoline, compared to the seven THINGS galaxies.
The density profiles are deduced from the rotation curves. The gray lines represent
the NFW profiles of dark matter haloes of dark matter only simulations with increasing
V_{max}. Right panel: the solid black line shows the stellar-to-halo mass relation based on
abundance matching techniques from Guo et al. (2010). The dashed line shows the
extrapolation to the lower mass regime. Again, the relation is shown for DG1, DG2, the
THINGS dwarfs, galaxies from the literature and Local Group galaxies (for references,
see Oh et al. (2011a)). Both figures are taken from Oh et al. (2011a).

Very often, baryonic processes are taken to be responsible for the conversion of the cusp to
core as they introduce fluctuations in the gravitational potential to which the dark matter halo
reacts non-adiabatically and reduces the central density. These fluctuations can be caused
by the fast removal of gas from the inner regions by SN and/or active galactic nuclei (AGN)
feedback as suggested by Navarro et al. (1996a) and confirmed by Read and Gilmore (2005);
Governato et al. (2010); Pontzen and Governato (2012); Teyssier et al. (2013). In chapter
3 (Cloet-Osselaer et al., 2012), we shall show that the initially cuspy density profiles of our
isolated models convert into a cored density profile when we simulate them with baryonic

physics included.

As baryonic physics are shown to be of great importance, dedicated cosmological simulations are run with hydrodynamics included (e.g. Illustris (Vogelsberger et al., 2014) and EAGLE (Schaye et al., 2015)), and zoom-simulations of previous cosmological simulations with hydrodynamics are run (e.g. Aquila (Scannapieco et al., 2009), DG1 and DG2 (Governato et al., 2010), the ERIS simulation (Guedes et al., 2011), ARGO simulation (Feldmann and Mayer, 2015) ,...). They benefit from a realistic formation history but generally still have quite limited mass resolutions. In chapter 4 we will present an alternative approach to cosmological simulations incorporating a hierarchical formation history and with the benefit of a better mass resolution.

The ease with which ΛCDM explains the large scale structure is not applicable to the small scale structure, where local processes like star formation and gas cooling complicate the situation. Initially, it was argued that structure formation was mainly determined by gravity and that baryonic physics would only have a minor influence on the process of structure formation. However, when comparing the results of cosmological simulations with observations of the local Universe some problems arise, suggesting a more important role for the baryonic physics.

The *missing satellite problem* addresses the fact that the number of low-mass subhaloes created in cosmological simulations is orders of magnitudes larger than the number of observed Milky Way satellites (Klypin et al., 1999; Moore et al., 1999). Nowadays, due to better observations and automated large sky surveys, still new ultra-faint dwarfs are discovered (for example Tollerud et al. (2015)). But there are still of the order ∼10 times more subhaloes in the cosmological simulations compared to the observed number of MW satellites. In addition, different mechanisms are investigated to align the simulations with the observations by limiting star formation in low mass haloes resulting in 'dark' haloes which cannot be observed. For example, Okamoto et al. (2008) determined from a cosmological hydrodynamical simulation how galaxies are able to lose their gas due to photo-heating from an UVB. They found that galaxies with circular velocities smaller than ∼25 km/s are influenced by the UVB and are unable to retain enough gas to form stars. Other environmental influences with the same net effect, meaning removing the gas from the dark matter haloes and hence making star formation less efficient, are tidal interactions and ram-pressure stripping (Zolotov et al., 2012; Collins et al., 2013).

The lowering of the SF efficiency with decreasing mass, e.g. a M_{star}-M_{halo} relation that falls off steeply with decreasing mass, would be able to partially solve the missing satellite problem naturally within the ΛCDM theory as a large set of satellites would remain 'dark'.

Abundance matching techniques link halo masses of cosmological simulations to observed galaxies with SDSS (Guo et al., 2010; Behroozi et al., 2010; Trujillo-Gomez et al., 2011). The right panel in Fig. 1.4 shows the stellar-to-halo mass relation from the THINGS sample, DG1 and DG2, together with galaxies from van den Bosch and Swaters (2001) and Stark et al. (2009). The solid black line shows the relation from Guo et al. (2010), with the dashed line extending this relation to the lower mass regime. In section 3.4.1 we will review this relation for the isolated simulations in the dwarf regime. Sawala et al. (2011) already discusses that individual simulations in the dwarf regime generally overpredict the corresponding stellar masses (Pelupessy et al., 2004; Stinson et al., 2007a, 2009; Valcke et al., 2008; Governato et al., 2010). Hence, mechanisms are needed to reduce the SF efficiency in the dwarf

regime. This M_{star}-M_{halo} relation was our initial motivation to start a parameter survey of star formation parameters and in section 3.4.1 we will show the results of our efforts.

Finally, there is also the more recent too-big-too-fail (TBTF) problem addressing the problem that most massive subhaloes from cosmological simulations are generally too dense to be dynamically consistent with the MW satellites, e.g. their v_{max} are larger than the observed ones (Garrison-Kimmel et al., 2013). As we expect the most massive observed dwarfs to correspond with the most massive subhaloes in the simulations this introduces a discrepancy between the observations and the simulations/theory. In addition, Papastergis et al. (2014) argued that the same problem exists for a large set of dwarf galaxies in the field. Tollerud et al. (2014) confirmed the TBTF problem to exist for the satellites of the Andromeda galaxy and is not just a statistical outlier. Possible scenarios to solve the TBTF problem boil down to the formation of cored dark matter profiles. The literature proposes two ways of generating these cored dark matter profiles: the same baryonic processes that are responsible for solving the cusp-to-core problem could be accounted for to solve the TBTF problem, but it is argued that for dwarfs with $M_{star} \sim 10^6 M_\odot$ the feedback may be insufficient to dynamically heat the central cusp and expand the orbits of the DM particles, necessary for a lowering of the center density (Peñarrubia et al., 2012; Garrison-Kimmel et al., 2013; Amorisco et al., 2014). Environmental effects are also expected to have little influence as the TBTF problem is also observed in the field and in the Andromeda galaxy. Elbert et al. (2014) found self-interacting dark matter (SIDM) to be able to produce constant density cores that are comparable to the half-light radii of dwarfs with stellar masses of the order of 10^{5-7} $M_\odot$. This enables them to have core formation below the mass regime where feedback is assumed to be responsible for producing a core. Bastidas Fry et al. (2015) compared the first cosmological hydrodynamic simulation including SIDM, implemented with a constant cross section of 2 cm^2/g, with similar simulations with CDM. The simulations include stellar feedback that generates fluctuations in the potential and these are responsible for the flattening of the dark matter core. However, they report that the SIDM seems to be unable to lower the central DM density of hales with peak velocities $v_{max} < 30$ km/s because these haloes have relatively small central velocity dispersions and densities, leading to time scales for SIDM collisions to be longer then the Hubble time.

2

Simulations

Astronomy of extragalactic objects has the drawback that we are unable to investigate our subjects in large details in a lab. As a consequence, we are generally limited to a projected view of the objects we want to investigate and we need to retain as much information as possible from what we observe. Another approach is to model these objects. In this chapter, we look at the different ingredients and recipes used in the simulation code to simulate dwarf galaxies.

2.1 Simulation code

We use a modified version of the publicly available N-body/SPH code Gadget-2 (Springel, 2005). The code is highly parallelized and all the simulations that are presented here were run on our clusters (ronny and gandalf) and on the Stevin Supercomputer Infrastructure[1]. The original Gadget-2 code, which includes gravity and hydrodynamics, was extended by Valcke et al. (2008) with the following subgrid physics (see section 2.3): star formation, feedback, and radiative cooling. Our simulations start with two types of particles: dark matter (DM) and gas particles. The DM only interacts gravitationally whereas the gas particles also obey the equations of hydrodynamics.

N-body Gravity is sampled by an N-body system. The gravitational force of one particle on another particle is given by:

$$F = -G\frac{m_1 m_2}{r_{12}^2},\tag{2.1}$$

with r_{12} the distance between the two particles and m_1 and m_2 the masses of the

---

[1]located in the Flemish Supercomputer Center, funded by Ghent University, the Hercules Foundation and the Flemish Government department EWI

particles. The particle representation introduces problems when determining the gravitational force of close encounters: as each particle represents a certain mass, it will have a certain extend in reality and determining the gravitational force between particles at distances shorter then their extend is unphysical. The effect of close encounters may be reduced by the introduction of a "softening length", ϵ, in the gravitational force by replacing the r^{-2} dependence by $(r^2 + \epsilon^2)^{-1}$ (Aarseth, 2003). Doing this for each particle would come at a computational cost of the order of N^2. The Gadget-2 code uses an oct-tree algorithm to group distant particles into increasingly larger cells when further away and to allow them to jointly exert gravity on a particle by means of a single multipole force (Barnes and Hut, 1986). This reduces the computational cost of the gravitational force to the order of $(N \log N)$. The code also has a treePM algorithm implemented that combines the tree algorithm to calculate contributions on short scales with a particle-mesh method for large scales which is ideal for large, fairly homogeneous mass distributions. Since our simulations have a relatively small simulation box compared to cosmological simulations, only the tree algorithm is used.

SPH   Smoothed particle hydrodynamics (SPH) is a Lagrangian method used to approximate the continuum dynamics of fluids through the use of particles. This approach was first developed in astrophysics by Lucy (1977) and Gingold and Monaghan (1977). The original Gadget-2 code uses an entropy based implementation. The gas is represented by SPH particles that are tracer particles following the movement of the gas and interacting thermodynamically with the particles that are located within their smoothing length. The interaction is described by the "smoothing kernel function", $W(r, h)$. We use a Cubic Spline Kernel which is a decreasing function of radius with compact support. For example, the density of the gas at the location of the i-th particle is given by the following summation over all neighboring particles:

$$\rho_i = \sum_{j=1}^{N} m_j W(r_{ij}, h_i), \tag{2.2}$$

with the distance $r_{ij} = |\vec{r}_i - \vec{r}_j|$, h_i the smoothing length of the *i*-th particle and W the SPH smoothing kernel. The smoothing length of each particle is adaptive and defined by a fixed number of gas particles, e.g. 50, that have to reside within this smoothing length. The oct-tree that is used for the gravitational force is also used for the search for SPH neighbors in a hierarchical manner: when there is a geometric overlap between the current tree node and the search region, defined as the region within the smoothing radius, the daughter nodes are considered and so on, when, on the other hand, there is no overlap, no further computational time is wasted (Springel, 2005). With this approach we can define for every quantity F a smoothed interpolated version through a convolution with the SPH kernel that can be represented by a discrete sum when the kernel is sampled by particles:

$$F(r) \approx \sum_{j} \frac{m_j}{\rho_j} F_j W(r - r_j, h). \tag{2.3}$$

(Eqn. 2.2 is an example of this formula with F(r)=ρ(r)).

While the initial conditions of the simulations are cosmologically motivated (see section 2.2), we do not perform full cosmological simulations. Still, previous work by Valcke et al. (2008),

Valcke et al. (2010) and Schroyen et al. (2011) has shown that with our code realistic dwarf galaxies, following the known photometric and kinematic scaling relations, can be produced. Our approach yields a high mass resolution at comparatively low computational cost.

2.2 Initial conditions

At the start of the simulations, the models only contain dark matter and gas. The dark matter only interacts gravitationally and the gas follows the laws of gravity and hydrodynamics (see section 2.1). Due to the gravitational potential of the dark matter, the gas collapses during the first few 10^8 years of the simulation. We use a flat Λ-dominated cold dark matter cosmology with the following cosmological parameters: $h = 0.71, \Omega_{\text{tot}} = 1, \Omega_{\text{m}} = 0.2383, \Omega_{\text{DM}} = 0.1967$ (Spergel et al., 2007). However these cosmological parameters are only used during the setup of the simulation, e.g. the density of the dark matter and the gas halo is determined by the characteristic density of the universe today (see respectively section 2.2.1 and section 2.2.2). In addition, the gas mass is scaled to the dark matter mass according to the cosmological fraction of baryonic to dark matter mass, which is 0.2115.

2.2.1 Dark matter halo

We use the spherical symmetric cusped NFW profile (Navarro et al., 1996a), with a radial profile of the form:

$$\rho_{\text{NFW}}(r) = \frac{\rho_{\text{s}}}{(r/r_{\text{s}})(1 + r/r_{\text{s}})^2}, \tag{2.4}$$

where ρ_{s} and r_{s} are, respectively, the characteristic density and the scale radius. We use the relations from Wechsler et al. (2002) who found a correlation between these two parameters reducing the NFW density distribution to a one-parameter family of the dark matter virial mass, M_{DM}. This mass can be linked to ρ_s, r_s and the concentration parameter, c, defined as the ratio of the virial radius, r_{vir} to the scale radius r_{s}: starting from the following equation defining that the mean density inside the virial radius is Δ_{vir} times the mean universal density ρ_u at that redshift,

$$M_{\text{vir}} = (4/3)\pi\Delta_{\text{vir}}\rho_{\text{crit}}r_{\text{vir}}^3, \tag{2.5}$$

and with Δ_{rvir} the virial overdensity which is often taken to be 200 which requires the mean density within the virial radius to be 200 times the critical density of the universe. If we replace M_{rvir} in this equation with the total halo mass M_{h}, defined by Eq. A.7 and assuming all the mass to reside within the virial radius, we find the following relation for ρ_{s}:

$$\rho_{\text{s}} = \frac{\Delta_{\text{vir}}}{3}\frac{c^3}{\ln(1 + c) - c/(1 + c)}\rho_{\text{crit}}. \tag{2.6}$$

We calculate ρ_{s} as a function of the critical density of the universe at $z = 0$ since we do not run a cosmological simulation during which the properties of DM haloes evolve. In section 3.3.1 the implementation of the dark matter halo is discussed and the stability of the halo is tested. In the Appendix A, the techniques to sample these DM haloes are discussed. When we further in this work refer to the halo mass, we refer to the total dark matter mass present in our model, this will only be equal to the virial mass at the start of the simulation.

In chapter 3 we use the correlation between the concentration parameter and the scale radius that was found by Wechsler et al. (2002) and Gentile et al. (2004), (NFW$_1$):

$$c \simeq 20 \left(\frac{M_h}{10^{11} M_\odot} \right)^{-0.13}$$

$$\rightarrow r_s \simeq 5.7 \left(\frac{M_h}{10^{11} M_\odot} \right)^{0.46} \text{kpc.} \qquad (2.7)$$

In chapter 4, we updated these relations to the Strigari et al. (2007) relations that are more appropriate for the dwarf regime (e.g. $M_h \leq 10^8 M_\odot$), (NFW$_2$):

$$c \approx 33 \left(\frac{M_h}{10^8 M_\odot} \right)^{-0.06}$$

$$\rightarrow r_s = \left(\frac{M_h}{4\pi \rho_s} \frac{1}{\ln(1+c) - c/(1+c)} \right)^{1/3}. \qquad (2.8)$$

In Figure 2.1 two haloes with a mass of 2.5 10^9 M$_\odot$ and constructed with these different sets of equations, e.g. NFW$_1$ and NFW$_2$ represented by respectively the blue and red line, are compared with each other. The halo constructed with NFW$_1$ (eqn. (2.7)) is more concentrated, $c = 32.3$, compared to the halo created with NFW$_2$ (eqn. (2.8)), $c = 27.2$.

Finally, since we know all the parameters necessary for the density distribution of the dark matter, the halo can be constructed with the 'quiet' start method where for every particle a symmetric partner is created and which is discussed in section 3.3.1.

2.2.2   Gas halo

The mass of the gas halo is determined from the dark matter mass according to the cosmological parameters that are used: the dark matter mass is multiplied by the ratio of the baryonic mass fraction, Ω_b, and the dark matter fraction, Ω_{DM} which amounts to 0.2115. There are two density profiles implemented in the code with which we can construct the gas halo and which are visualized in Fig. 2.1

Homogeneous density profile   The density of the gas cloud has a constant value over its entire volume and is set to 5.55 $\rho_{crit}(z)$, with ρ_{crit} the critical density of the universe at the halo's formation redshift (e.g. the starting redshift of the simulation) and the value of 5.55 which is used for the overdensity of matter is determined as the point where the local flow detaches itself from the Hubble flow, according to the Tolman model. In addition, from the total mass and the constant density, the radius, $R_{5.5}(z)$, out to which the gas halo has to extend can be determined. Then, the gas halo can be constructed by randomly sampling a sphere with radius $R_{5.5}(z)$.

Pseudo-isothermal density profile   The gas also can be sampled as a pseudo-isothermal density profile of the following form:

$$\rho_g(r) = \frac{\rho_{g,c}}{1 + (r/r_c)^2}, \qquad (2.9)$$
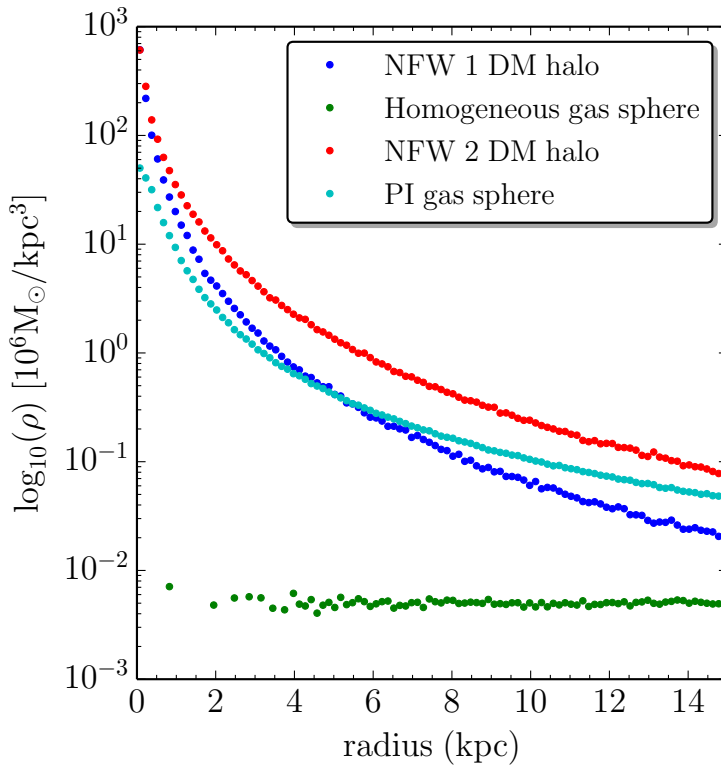
Figure 2.1: Comparison of the two sets of equation that were used to set up the dark matter haloes, respectively the blue line showing the DM density profile for NFW$_1$ (eqn. (2.7)) and the red line for NFW$_2$, (eqn. (2.8)) for a halo mass of 2.5 10^9 M$_\odot$). Also the two types of gas haloes are shown, the homogeneous gas sphere and the pseudo-isothermal gas sphere are plotted by respectively green and cyan dots.

which depends on the distance to the center, r, and the characteristic density and scale radius, respectively $\rho_{g,c}$ and r_c. The characteristic density is determined from the characteristic density of the dark matter, ρ_s, by multiplying it by the fraction of the baryonic to the dark matter mass. The outer radius is calculated similarly to the case of the homogeneous sphere. Finally, from the total mass, the outer radius and the density profile, the scale radius, r_c can be determined.

2.3   Subgrid physics

2.3.1   Criteria for Star formation

Star formation is assumed to take place in cold, dense, converging and gravitationally unstable molecular clouds (Katz et al., 1996). Gas particles that fulfill the star formation criteria (SFC)

are eligible to be turned into stars. These SFC are:

$$\rho_{\mathrm{g}} \quad \geq \quad \rho_{\mathrm{SF}} \tag{2.10}$$

$$T \quad \leq \quad T_{\mathrm{c}} = 15000\mathrm{K} \tag{2.11}$$

$$\vec{\nabla}.\vec{v} \quad \leq \quad 0, \tag{2.12}$$

with ρ_{g} the gas density, T its temperature and $\vec{v}$ its velocity field. ρ_{SF} is the density threshold for star formation. We employ a Schmidt law (Schmidt, 1959) to convert gas particles that fulfill the SFC into stars:

$$\frac{\mathrm{d}\rho_{\star}}{\mathrm{d}t} = -\frac{\mathrm{d}\rho_{\mathrm{g}}}{\mathrm{d}t} = c_{\star}\frac{\rho_{\mathrm{g}}}{t_{\mathrm{g}}}, \tag{2.13}$$

with $\rho_{\star}$ the stellar density and $c_{\star}$ the dimensionless star formation efficiency. The timescale t_{g} is taken to be the dynamical time for the gas, i.e. $1/\sqrt{4\pi G \rho_{\mathrm{g}}}$. Here, we choose $c_{\star} = 0.25$. Stinson et al. (2006) showed that the influence on the mean SFR of the value of $c_{\star}$ with values in the range of 0.05 to 1 is negligible. Lowering $c_{\star}$ reduces the star formation efficiency as well as the amount of supernova feedback, causing more particles to fulfill the density and temperature criteria. This compensates for the lower value of $c_{\star}$, producing a star formation rate (SFR) which is roughly independent of $c_{\star}$. In addition, a higher $c_{\star}$ will produce more feedback, a more disrupted ISM and less SF during the next timestep. Recently, Gatto et al. (2013) argued that the widely used Schmidt law, which is deduced from observations of bright galaxies, might not be validate in low density regimes. The results from Roychowdhury et al. (2009) suggest, based on the analysis of 23 faint dwarfs, that the star formation might be less efficient in dwarf galaxies. However, we expect that due to the self-regulated nature of star formation the effect of less efficient star formation will increase the amount of stars that can fulfill the SFC at a next timestep.

Revaz et al. (2009) also investigated the influence of $c_{\star}$ by varying it between the values of 0.01 and 0.3. They concluded that the star formation history is mainly determined by the initial total mass with a minor influence of $c_{\star}$. Self-regulating models, in which star formation occurs in recurrent bursts due to the interplay between cooling and supernova feedback, were achieved for $c_{\star} \sim 0.2$. Such models best resemble real dwarf galaxies.

2.3.2 Feedback

The code is implemented with feedback of Type Ia supernovae (SNIa), Type II supernovae (SNII) and stellar winds (SW) as described in Valcke et al. (2008). When stars die they deliver thermal energy and mass to the ISM and enrich the gas. Feedback is distributed over the gas particles in the neighborhood of the star particle according to the SPH smoothing kernel of the gas particle the star particle originates from. Massive stars, with lower mass limit $m_{\mathrm{SNII,l}}=8$ $M_{\odot}$ and upper mass limit $m_{\mathrm{SNII,u}}=60$ $M_{\odot}$, die as SNII supernovae, while less massive stars, with lower mass limit $m_{\mathrm{SNIa,l}}=3$ $M_{\odot}$ and upper mass limit $m_{\mathrm{SNIa,u}}=8$ $M_{\odot}$, will explode as SNIa supernovae. The total energy released by supernova explosions is set to 10^{51} ergs and for stellar winds to 10^{50} ergs (Thornton et al., 1998). As massive stars only live shortly, they release their feedback quite fast after a stellar particle is born, i.e. within $\sim 10^7$ yr. For the SNIa, we employ a delay of 1.5 Gyr as this is the mean lifetime of SNe Ia as deduced by (Yoshii et al., 1996). The main sequence lifetime is a function of the mass m

of the star and is given by (David et al., 1990):

$$\log t(m) = 10 - 3.42 \log(m) + 0.88(\log(m))^2. \tag{2.14}$$

Implementing the upper and lower mass limits of the SNe in eq. 2.14 define the time interval in which the energy is released after a stellar particle is created. We assume stellar winds to start instantaneous when the stellar particle is born and to end together with SNII. The energies are distributed to the environment at a constant rate during their corresponding main sequence lifetime.

Each star particle represents a single-age, single-metallicity stellar population (SSP). The stars within each SSP are distributed according to a Salpeter initial mass function (Salpeter, 1955):

$$\Phi(m)dm = Am^{-(1+x)}dm, \tag{2.15}$$

with $x = 1.35$ and $A = 0.06$. The limits for the stellar masses are $m_l = 0.1\ M_\odot$ and $m_u = 60\ M_\odot$. As our SSP particles actually represent a distribution of stars the total energy released by SNII:

$$E_{tot,SNII} = E_{SNII} \int_{m_{l,SN}}^{m_{u,SN}} \Phi(m)dm \times \frac{M_{SSP}}{\int_{0.1M_\odot}^{60M_\odot} m\ \Phi(m)dm}, \tag{2.16}$$

with $m_{l,SNII}$ and $m_{u,SNII}$ the corresponding lower and upper mass for SNII. An analoguous formula is used for the energy released by stellar winds. In the case of SNIa, a multiplication with a factor A_{SNIa} is needed because the masses of the stars can be so low that not all the stars in the SSP will end as supernova explosions. The number of SNIa relative to the number of SNII which is taken to be 0.15, in combination with the following equation from Tsujimoto et al. (1995) enables us to determine this factor A_{SNIa}:

$$\frac{N_{SNIa}}{N_{SNII}} = 0.15 = A_{SNIa} \frac{\int_{m_{SNIa,l}}^{m_{SNIa,u}} \Phi(m)dm}{\int_{m_{SNII,l}}^{m_{SNII,u}} \Phi(m)dm}. \tag{2.17}$$

When applying the previously mentioned upper and lower limits, A_{SNIa} has a value of 0.0507. The energy effectively absorbed by the ISM is obtained by multiplying these total energies with the feedback efficiency factor, ϵ_{FB}, which is one of the main subjects in chapter 3.

Not only energy is released when stars undergo a supernova explosion. Also part of their mass and metals is returned to the ISM. The returned mass fraction is calculated as the difference between the total stellar mass that underwent a supernova and the stellar mass of the supernove that is not returned to the ISM, divided by the total stellar mass. For example, we assume that a constant remnant mass of $M_{rem} \approx 1.4M_\odot$ remains in dark objects after a star undergoes a SNII. Hence, the returned mass fraction for SNII is:

$$F_{SNII} = \frac{\int_{m_{SNII,l}}^{m_{SNII,u}} m\ \Phi(m)dm - M_{rem} \int_{m_{SNII,l}}^{m_{SNII,u}} \Phi(m)dm}{\int_{m_l}^{m_u} m\ \Phi(m)dm} = 0.112. \tag{2.18}$$

A similar equation can be used to determine the returned mass fraction of SNIa's: when taking into account that only a fraction of the stars in the mass limit of the SNIa's will end by a supernova explosion by using the factor A_{SNIa} and that there is no remnant mass after a SNIa explosion, the reduced mass fraction is $F_{SNII} = 0.00502$.

The metal yield of the element i that is released in SNII is given by:

$$M_{\text{SNII,i}} = M_{\text{SSP}} \frac{\int_{m_{\text{SNII,l}}}^{m_{\text{SNII,u}}} M_i(m)\Phi(m)dm}{\int_{m_l}^{m_u} m\Phi(m)dm}, \qquad (2.19)$$

for which we use the tabulated metal yields $M_i(m)$ of Travaglio et al. (2004) for SNIa and of Tsujimoto et al. (1995) for SNII. In the case of SNIa this equation simplifies as the metal yields don't depend on the progenitors mass because SNIa take place when white dwarfs reach the Chandrasekhar limit (1.4 $M_\odot$) to:

$$M_{\text{SNIa,i}} = M_{\text{SSP}} F_{\text{SNIa,i}} \qquad (2.20)$$

with $F_{\text{SNIa,i}}$ the returned metal yield fraction given by:

$$F_{\text{SNIa,i}} = \frac{A_{\text{SNIa}} \int_{m_{\text{SNIa,l}}}^{m_{\text{SNIa,u}}} M_i\Phi(m)dm}{\int_{m_l}^{m_u} m\Phi(m)dm} \qquad (2.21)$$

$$= 0.0011 M_i M_\odot^{-1} \qquad (2.22)$$

2.3.3   Cooling

In order to realistically simulate the behavior of the interstellar gas in the models we need a good description of the cooling and heating rate of the gas. The SN explosions and stellar winds (see section 2.3.2) through the energy they inject into the ISM and the ultra-violet background (see section 5.1) are responsible for heating of the gas. In general, the cooling rate from radiative processes depends on the temperature, the density, the composition and irradiation of the gas by the UVB.

In our specific case, we assume collisions with free electrons to be the only ones responsible for keeping atoms ionized (e.g. collisional ionization equilibrium, CIE) then the recombination rate and the ionization rate are both directly proportional to the electron density. As a consequence, the ionization equilibrium is only a function of the temperature for a given element abundance mix. At low gas densities this ionization will be followed by a radiative de-excitation and the cooling rate will be proportional to the density squared times a temperature-dependent function.

In chapter 3 and 4 we use the widely used metallicity-dependent cooling curves from Sutherland and Dopita (1993), which describe the cooling of gas for different metallicities down to a temperature of 10^4 K. These cooling curves are extended to lower temperatures using the cooling curves of Maio et al. (2007) as described by Schroyen et al. (2013) because the spatial resolution of our simulations is sufficiently high to follow the star-formation clouds to temperatures below 10^4 K. The normalized cooling rate Λ_0' obtained from the cooling curves with the corresponding temperature and metallicity are multiplied with the hydrogen number density, n_H, and the electron number density, n_e, to provide the density squared dependence.

Still, we are unable to resolve the hot, low density cavities that are generated by the supernova explosions. To correct for this, a particle which is in one time-step heated by a supernova explosion will be unable to cool radiatively during the time-step where the SN explosion occurred. The size of the time-step that is used in the simulations is based on dynamical considerations: it is limited by the Courant-Friedrichs-Lewy condition.
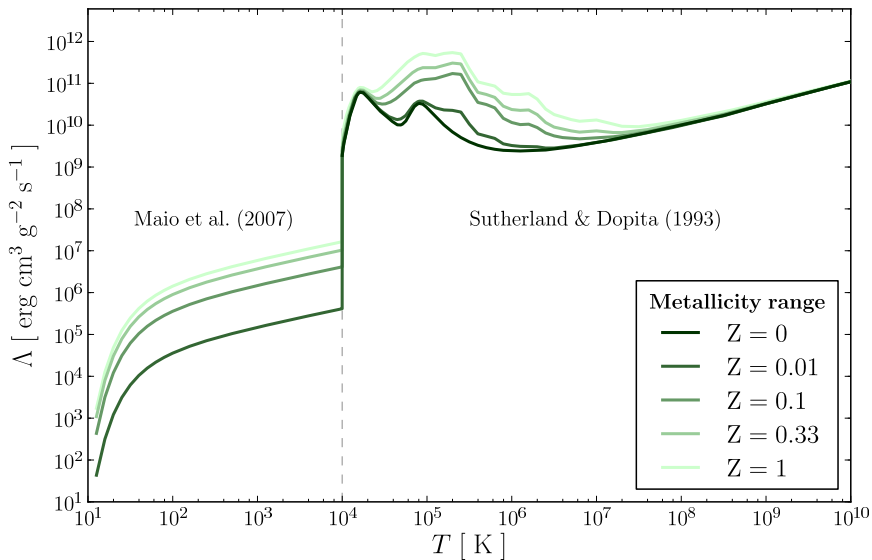
Figure 2.2: Visualization of the cooling curves that are used in Cooling recipe I. Figure from Schroyen et al. (2013).

These sets of cooling curves are easily implemented in simulations codes as only an interpolation between temperature and density is needed. However, in section 5.1, a new set of self-consistent heating and cooling curves including an UVB will be discussed and shown to be a better description of the behavior of the ISM (De Rijcke et al., 2013).

2.4   Visualization and analysis.

Our results are visualized with our own software package HYPLOT. This is freely available from SourceForge[2] and is used for all the figures in this work.
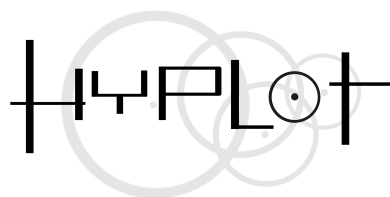
The simulation code supplies us with snapshots at certain time intervals. Each snapshot contains information about positions, velocities and masses of each particle. Additionally, for the gas that is sampled by SPH particles their temperature, density, pressure, specific energy and smoothing length are memorized. Every snapshot also contains the metallicity, the magnesium abundance [Mg/Fe], and the iron abundance [Fe/H], for the gas and star particles. For star particles their initial mass, birth time, luminosity, and magnitude are

---

[2]http://sourceforge.net/projects/hyplot/

stored. For the luminosities we interpolate over metallicity and age in the MILES population synthesis data (Vazdekis et al., 1996) which provides mass/luminosity values for our star particles.

With the HYPLOT package we can analyze this data and extract meaningful parameters that can be compared to real galaxy data, for example the half light radius, the velocity dispersion, etc. The HYPLOT software can be used directly in a GUI or can be implemented in Python scripts. The GUI is used to get a quick view of the simulations but most figures in this work are produced using Python scripts as this allows more freedom in the use of the data.

3

Star formation parameters and $M_\star$-M_{halo} relation

"The degeneracy beween star formation parameters in dwarf galaxy simulations and the $M_\star$-M_{halo} relation"

3.1   Introduction

Gravity is the main driver behind the structure formation of the Universe. Therefore, it is important to know how all the matter is distributed. Due to its light emitting character, the baryonic matter content is more easy to determine compared to the dark matter content which presence can only be inferred from observations. There have been many attempts to estimate dark halo masses and mass-to-light ratios for galaxies and clusters of galaxies from direct observations. These include methods that make use of gravitational lensing (Mandelbaum et al., 2006; Liesenborgs et al., 2009) and dynamical modeling of the observed properties of a kinematical tracer such as stars or planetary nebulae (Kronawitter et al., 2000; De Rijcke et al., 2006; Napolitano et al., 2011; Barnabè et al., 2009). One thing virtually all these works have in common is the relatively limited size of the data set they are based on. For dwarf galaxies in particular, Battaglia et al. (2013) gives a review of dynamical modeling for Local Group dwarf galaxies. They discuss the benefits and drawbacks of the different techniques used for modeling, which generally assume spherical symmetry. These observational results have been able to confirm that dSph are very dark matter dominated

although they were unable to restrict the cusp-to-core problem as observations of the inner regions are very hard.

Guo et al. (2010) determined the halo mass as a function of stellar mass for a large sample of galaxies using a statistical analysis of the Sloan Digital Sky Survey, which yields the observed stellar masses function, and the Millennium Simulation, which yield the halo mass function. Assuming the most massive galaxy lives in the most massive halo, galaxies are assigned to a halo by matching $n(> M_\star)$ to $n(> M_h)$ and from this, a general dependence of stellar-to-halo mass can be deduced. In the range of the most massive haloes and bright galaxies, the derived M_{star}-M_{halo} relation, which is of the form $M_{star} \propto M_{halo}^{0.36}$, is found to be in good agreement with gravitational lensing data (Mandelbaum et al., 2006). Below a halo mass of $M_{halo} \sim 10^{11.4}$ $M_\odot$, this relation becomes much steeper: $M_{star} \propto M_{halo}^{3.26}$. Guo et al. (2010) extrapolate the latter relation into the dwarf regime, where $M_{halo} < 10^{10}$ $M_\odot$. This leads then to the prediction that faint dwarf galaxies with stellar masses of the order of $M_{star} \sim 10^6$ $M_\odot$ should live in comparatively massive $M_{halo} \sim 10^{10}$ $M_\odot$ dark-matter haloes.

The Guo et al. (2010) M_{star}-M_{halo} relation was compared with that found in simulations of dwarf galaxies by Sawala et al. (2011) and Sawala et al. (2012). They found that simulated dwarf galaxies had stellar masses that were at least an order of magnitude higher at a given halo mass than predicted by Guo et al. (2010). There could be several causes for numerical dwarf galaxies to be overly prolific star formers:

- The star formation efficiency could be too high because of an underestimation of the feedback efficiency. Stinson et al. (2006) investigated the influence of the feedback efficiency on the mean star formation rate (SFR). The general trend they have observed was a decrease of the mean SFR when increasing the feedback efficiency.

- Stinson et al. (2006) also reported finding a decreasing mean SFR with increasing density threshold for star formation. Recently, high density thresholds for star formation have come in vogue because due to a higher mass and spatial resolution they are able to resolve the giant molecular clouds where star formation actually occurs (Governato et al., 2010; Oñorbe et al., 2015; Hopkins et al., 2013) whereas the previously common used value of 0.1 amu/cm$^-$3 for the density threshold (Katz et al., 1996) only selects the gas at the point where the thermal instability sets in.

- Dwarf galaxies, due to their low masses, are expected to be particularly sensitive to reionization. Not properly taking into account the effects of reionization may lead to an overestimation of the gas content of dwarfs and an underestimation of the gas cooling time.

- Dwarf galaxies are metal poor and hence also dust poor. This lowers the production of H_2 molecules and causes poor self-shielding of molecular clouds (Buyle et al., 2006) which could be expected to inhibit star formation. Not taking these effects into account will lead to an overestimation of the SFR (Gnedin et al., 2009).

Using the high values for the density threshold above which gas particles become eligible for star formation, denoted by ρ_{SF}, as promoted by Governato et al. (2010), in combination with radiative cooling curves that allow the gas to cool below 10^4 K (Maio et al., 2007), makes the gas collapse into small, very dense and cool clouds before star formation ignites. If the supernova feedback ϵ_{FB}, defined as the fraction of the average energy output of a supernova that is actually absorbed by the interstellar medium (ISM), is too weak to sufficiently heat

and/or disrupt such a star-forming cloud, one can consequently expect the mean SFR to be very high, leading to overly massive (in terms of M_{star}) dwarfs. Therefore, one could hope to remedy this situation by increasing ϵ_{FB} accordingly. In that case, a degeneracy between ϵ_{FB} and ρ_{SF} would be expected to exist.

In this chapter, we analyze a large suite of numerical simulations of isolated, spherically symmetric dwarf galaxies in which we varied both the feedback efficiency ϵ_{FB} and the density threshold ρ_{SF}. Our goal is to investigate *(i)* if such a degeneracy between ϵ_{FB} and ρ_{SF} exists and, if it exists, how to break it, *(ii)* which ϵ_{FB}/ρ_{SF}-combinations lead to viable dwarf galaxy models in terms of the observed photometric and kinematic scaling relations, and *(iii)* how well these models approximate the aforementioned M_{star} -M_{halo} relation.

3.2   Simulations

In this chapter, we simulate models with a spherically symmetric dark matter halo with an NFW density profile and a homogeneous gas cloud, as described in respectively subsection 2.2.1 and subsection 2.2.2. The simulations start at a redshift of $z = 4.3$ and run for 12.22 Gyr until $z = 0$. The gas particles are initially at rest at the start of the simulations, their initial metallicities are set to 10^{-4} $Z_{\odot}$, their initial temperature is 10^4 K and the constant number density of the gas will be 0.0011 hydrogen atoms per cubic centimeter. We start the simulations with 200,000 gas particles and 200,000 DM particles. Depending on the model's total mass, this results in gas particle masses in the range of $350 - 2,620$ $M_{\odot}$ and DM particle masses in the range of $1,650 - 12,380$ $M_{\odot}$. We use a gravitational softening length of 0.03 kpc based on the analysis of Valcke et al. (2008) who found little difference between simulations with softening lengths of 30 pc and 60 pc. They selected these two values based on the the criterion that in SPH simulations, the gravitational softening length should be equal or larger then the SPH smoothing length because the gravitational resolution is then larger compared to the hydrodynamical resolution and artificial fragmentation is suppressed (Bate and Burkert, 1997). In Table 3.1, we give an overview of the different mass models. A benefit of our code is that we can retain the same initial conditions and easily adapt our parameters to perform a detailed parameter survey.

Table 3.1: Details of the basic spherical dwarf galaxy models that were used in the simulations. Initial masses for the DM halo and gas are given in units of $10^6 M_{\odot}$, radii in kpc.

model	$M_{DM,i}$ $[10^6 M_{\odot}]$	$M_{g,i}$ $[10^6 M_{\odot}]$	r_s [kpc]	r_{max} [kpc]	c
N03	330	70	0.412	17.319	42.04
N05	660	140	0.566	21.742	38.41
N06	825	175	0.627	23.393	37.31
N07	1238	262	0.756	26.755	35.39
N08	1654	349	0.863	29.428	34.10
N09	2476	524	1.040	33.634	32.34

The simulations are run with subgrid physics as defined in section 2.3. In the following, we will investigate the influence of the density threshold by increasing its value from $n_{SF} = 0.1$ cm^{-3}, over $n_{SF} = 6$ cm^{-3} to $n_{SF} = 50$ cm^{-3}. In addition, the influence of the feedback efficiency is

checked by varying its value between $\epsilon_{FB} = 0.1$ and 0.9 and between $\epsilon_{FB} = 0.3$ and 0.9 for respectively the intermediate-density simulations and the high-density simulations.

3.3 Analysis

3.3.1 The NFW halo

The DM halo with NFW profile for the dark matter halo is constructed using a Monte Carlo sampling technique, the numerical details of this process are described in Appendix A.

They have "quiet" initial conditions, meaning that for each particle, a symmetric partner is constructed with position coordinates (r, $180° - \theta$, $-\phi$) and velocity coordinates ($-v_r, -v_\theta, -v_\phi$). This drastically improved the stability of the central parts of the haloes. The very inner part of the steep cusp of the NFW model is populated by relatively few particles, destroying its spherical symmetry and introducing unbalanced angular momenta. This initial deviation leads to the ejection of particles from the cusp and triggers a more widespread dynamical response of the DM halo, over time erasing the inner cusp. Introducing the partner particles, canceling out the angular momenta and increasing the symmetry of the particles' spatial distribution, greatly alleviates these problems. This technique has been applied before with great success, see e.g. Sellwood and Athanassoula (1986). The improvement of the stability of the DM halo in simulations with a "quiet" start over simulations without a "quiet" start is illustrated in the top panel of Fig. 3.1 where the density distribution of both haloes at $z = 0$ is plotted as red and green dots, respectively.

First, to test the stability of the NFW haloes, we ran several simulations for the N03 and N05 mass models:

Run 1: only DM

Run 2: DM and gas but no star formation

Run 3: DM and gas and star formation

For these test simulations an n_{SF} of 0.1 cm^{-3} (Katz et al., 1996) and ϵ_{FB} of 0.1 (Thornton et al., 1998) was used.

Fig. 3.1 shows the density profile of the test simulations for the N03 mass model. From the upper panel, it is evident that the DM density of the DM-only simulation remains stable and cusped until the end of the simulation. The simulations presented in the middle and bottom panels, show a clear conversion of the cusp into a core over time. Without the 'quiet' start method, the cusp is only stable outside 0.3 kpc or $\sim$10 times the softening length at the end of the simulation. In the case of the 'quiet' start method, the stability of the cusp is improved and it is stable starting from 0.1 kpc or $\sim$3 times the softening length. The simulations presented in the middle and bottom panels, show a clear conversion of the cusp into a core over time. In Fig. 3.2 the DM density profile is shown of the N03 model and the more massive N09 model at $z = 0$ by respectively blue and green dots. This figure shows the core of the more massive halo is larger $\sim$0.5 kpc compared to the $\sim$0.3 kpc core of the less massive model. We can conclude that the width of the core depends on the mass of the system, with more massive haloes having larger cores.
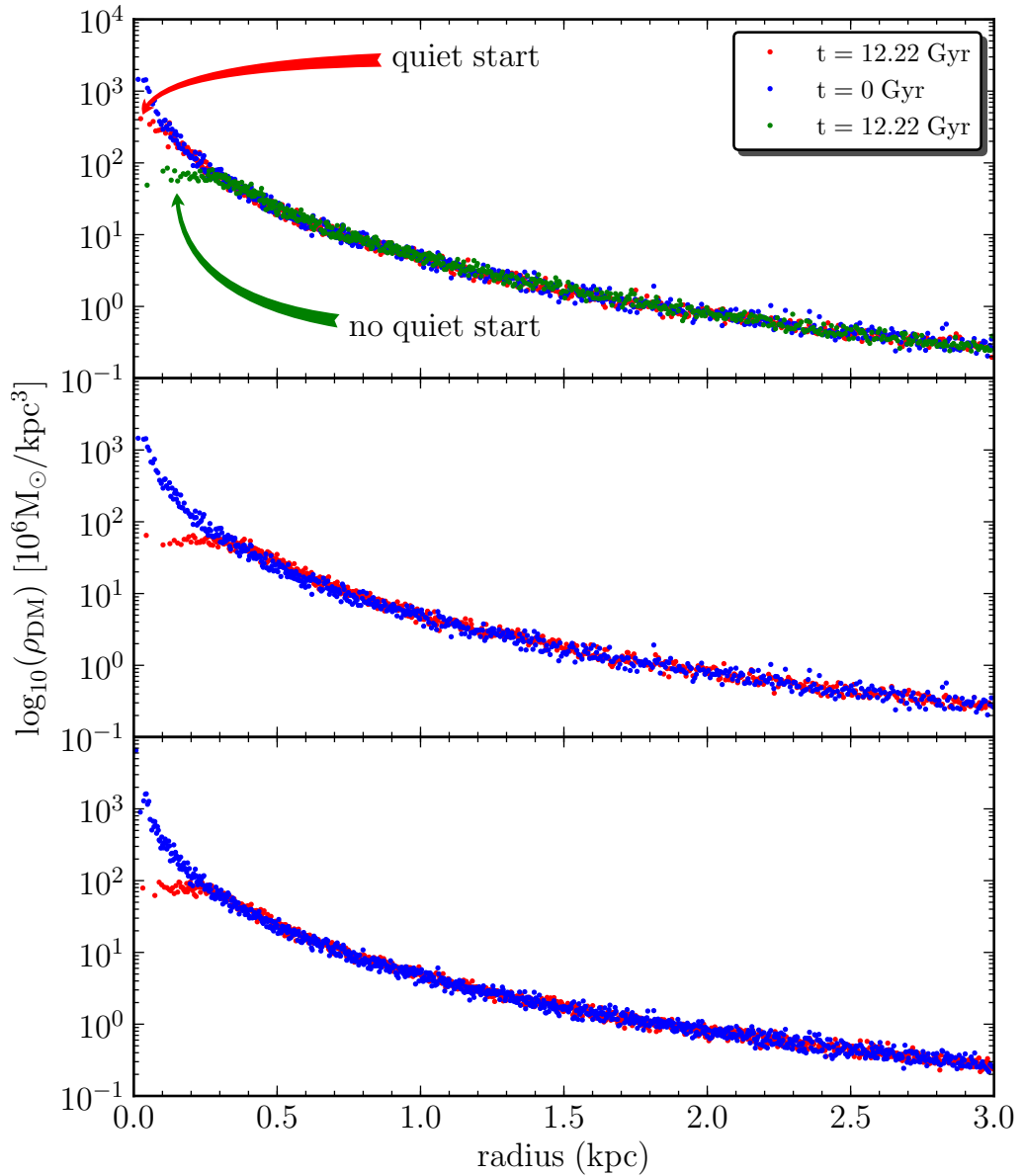
Figure 3.1: The density profile of the N03 NFW halo for different simulations: in the upper panel
only DM was included, in the central panel DM, gas is included but star formation was
turned off. The bottom panel shows the results of a simulation with DM, gas and star
formation.

Our simulations largely confirm the results from Read and Gilmore (2005), where a rapid
removal of gas results in a conversion from cusp to core as stated first by Navarro et al.
(1996a). As gas cools and flows into the halo, the center of the dark matter halo is adia-
batically compressed. Without star formation, the central gas pressure builds up, eventually
stops further inflow, and even makes the gas re-expand somewhat. This re-expansion hap-
pens rapidly enough for the DM halo to respond non-adiabatically: the central DM density
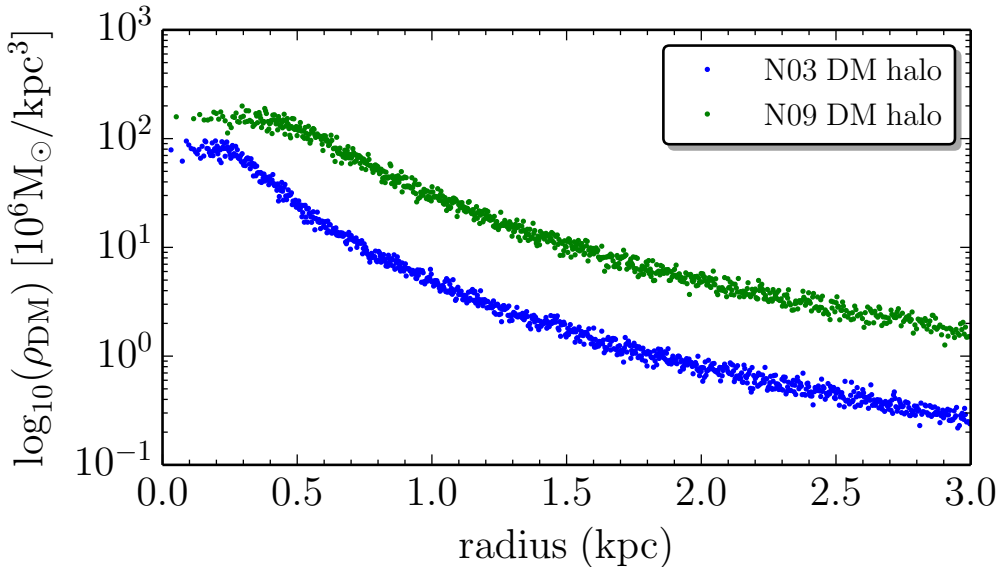
Figure 3.2: The density profile of lightest halo (N03) shown by blue dots and the most heavy halo
(N09) shown by green dots at the end of a simulation where star formation is included
and with $n_{SF} = 0.1$ cm^{-1} and $\epsilon_{FB} = 0.1$.

experiences a net lowering and the cusp is transformed into a core. With star formation
turned on, the gas also falls into the halo, however, never reaching such high central density
as in the case without star formation as the feedback smears out the gas. In this case,
feedback is responsible for a fast removal of gas from the central parts of the DM halo, with
the same effect: a conversion from a cusp to a core.

Unlike us, Governato et al. (2010) found that the density threshold for star formation needed
to be high enough for a cusp-to-core conversion to occur. Only for $n_{SF} \geq 10$ cm^{-3} does
supernova feedback lead to sufficient gas motions to flatten the cusp in their simulated
dwarfs, which are taken from a larger cosmological simulation. In contrast, in our more
idealized, initially spherically symmetric setup, even a low density threshold leads to sufficient
gas outflow for the cusp to flatten.

3.3.2 Star formation histories

In Fig. 3.3, we show the star-formation histories (SFHs) of different realizations of the N07
mass model. Also, in table 3.2, the starting time of star formation is tabulated along with
the final total stellar mass. Several conclusions can be drawn:

- The delay between the start of the simulation and the start of the first star-formation
  event is an increasing function of n_{SF}. This appears logical: it takes longer for the gas
  to collapse to higher densities and ignite star formation. Comparing different mass
  models, star formation starts earlier in more massive models for a given n_{SF}. This is
  most likely due to the more massive models having steeper gravitational potential wells,
  increasing their ability to compress the inflowing gas.

- If n_{SF} is increased while ϵ_{FB} is kept fixed, more stars are formed (e.g. going from the
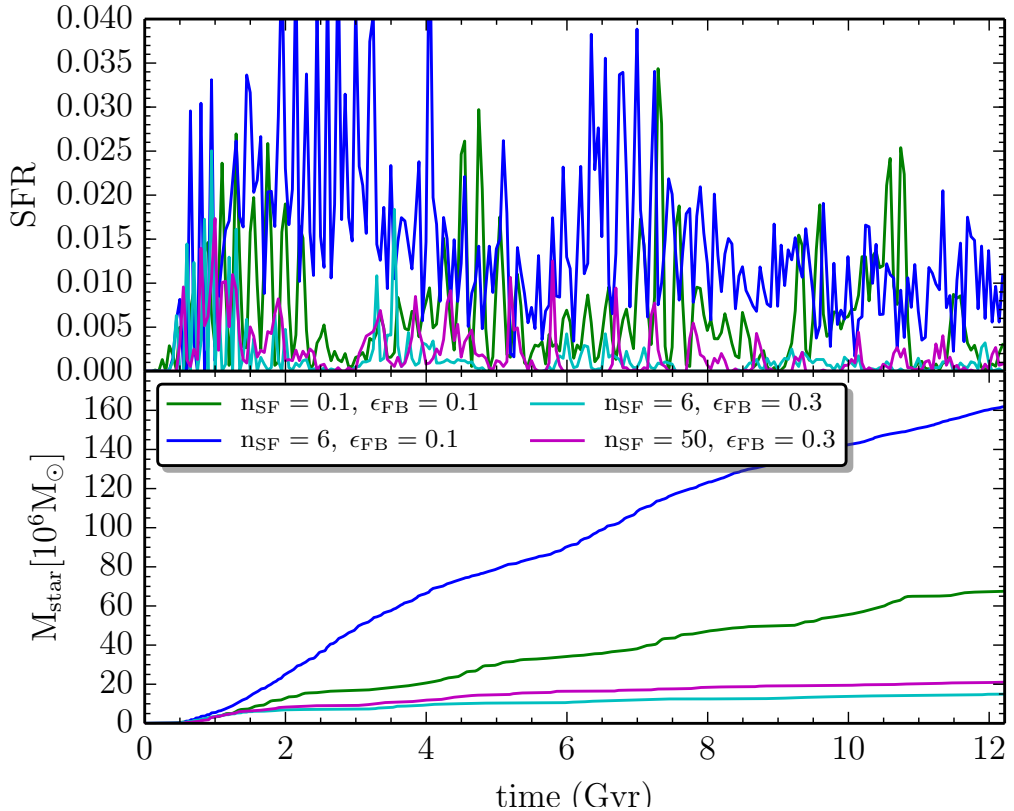
Figure 3.3: Top panel: the SFR of several N07 models as a function of time. Bottom panel: the stellar mass as a function of time.

green to the blue curve or similarly from the cyan to the magenta curve in Fig. 3.3). This is because gas collapses to higher densities and the feedback is no longer able to sufficiently heat and expel this gas and to interrupt star formation.

- Related to the previous point, the SFR also becomes more rapidly varying if n_{SF} is increased while ϵ_{FB} is kept fixed. The reason is that in the small high-density star-forming regions, feedback can only locally interrupt star formation during short timespans. At lower n_{SF}, star formation is more widespread, leading to more global behavior: as supernovae go off, star formation can be completely halted.

- Increasing ϵ_{FB} while n_{SF} is kept fixed leads to a decrease in star formation (e.g. going from the blue to the cyan curve in Fig. 3.3). This is because once feedback is strong enough, it is able to extinguish star formation, even at high gas densities.

- The most low-mass models fail to form stars for high n_{SF} values. E.g. no stars form in the N03 models for $n_{SF} > 0.1$ cm^{-3}. This is due to the masses of these models being too small for gas to collapse to densities where stars can be formed. This point is further elaborated in the next paragraph.

3.3.3 Density distribution of the ISM

In Fig. 3.4, the density of the ISM is plotted as a function of radius. For the N03 model in the left panel a density threshold of 0.1 cm^{-3} was used while for the model in the right panel, the density threshold was set to a value of 6 cm^{-3}. The red points show the gas distribution at the moment just before the start of star formation in the case of $n_{SF} = 0.1$ cm^{-3}. Since up to that moment, all models have experienced the same evolution, there is no difference between the red points in both panels. As can be seen in the left panel, the gas density in this N03 model reaches the star-formation threshold and star formation occurs. Moreover, the influence of supernova feedback can be seen in the green and blue points, where gas expands to larger radii and lower densities after having been heated. As is clear from the right panel, for $n_{SF} = 6$ cm^{-3} the gas simply keeps falling in. It will continue to do so during the first 4 Gyr until the built-up central pressure causes the gas to re-expand again. No stars are formed during the course of this simulation.
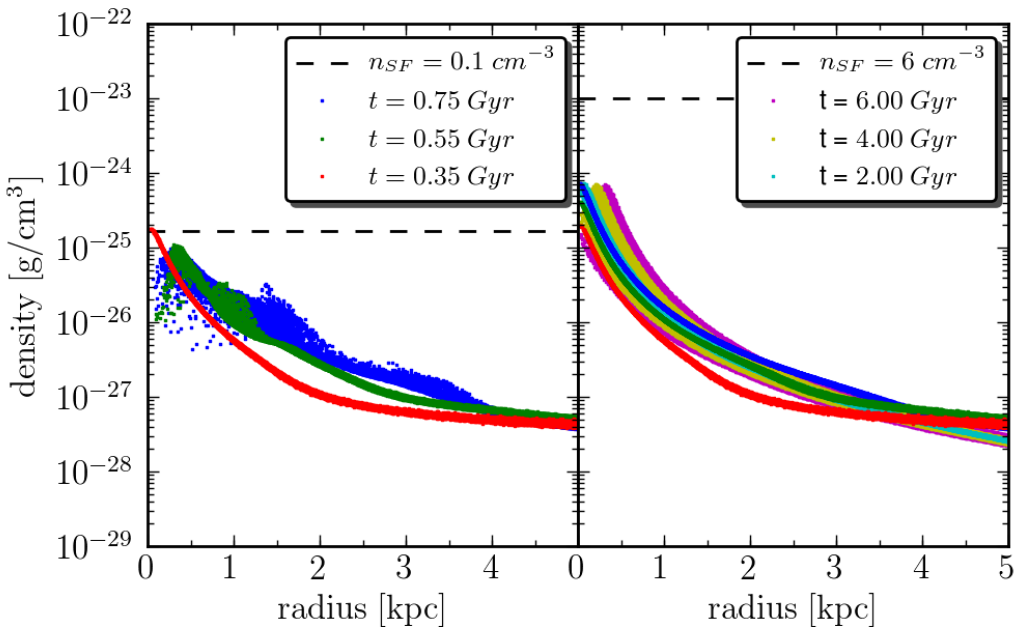
Figure 3.4: The density distribution of the ISM for the least massive galaxy, N03, with different density threshold and a fixed feedback efficiency of 0.1. In the left panel, the density distribution is shown at 0.35 Gyr (red dots), 0.55 Gyr (green dots) and at 0.75 Gyr (blue dots) for the simulation with $n_{SF} = 0.1$ cm^{-3}. The right panel shows the density distribution for the simulation with $n_{SF} = 6$ cm^{-3} at the identical times and color scales as in the left panel, additionally, the density distribution at 2, 4 and 6 Gyr is shown by respectively cyan, yellow and magenta dots.

As the density threshold is increased to higher values, star formation tends to occur more and more in small collapsed clumps. This becomes clear when comparing the panels from Figs. 3.4 and 3.5. The latter shows the gas density distributions of two N07 models with $n_{SF} = 6$ cm^{-3} and $n_{SF} = 50$ cm^{-3}. While the $n_{SF} = 50$ cm^{-3} model only exhibits star formation in a small number of discrete high-density clumps, the $n_{SF} = 6$ cm^{-3} model lacks such well-defined clumps and star formation occurs more widespread.
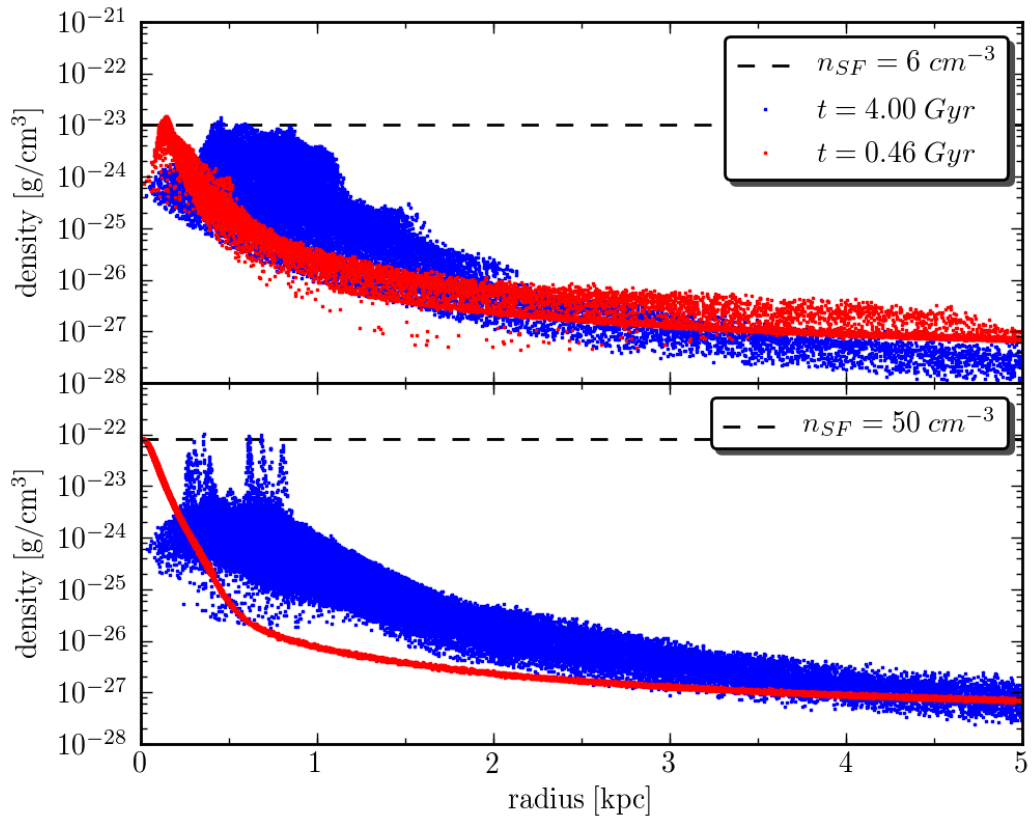
Figure 3.5: The density distribution of the ISM at different times for the N07 model, with different density thresholds and a fixed feedback efficiency of 0.7.

3.3.4 Scaling relations

In this section we discuss the properties of each of our models and draw some conclusions regarding the influence of the n_{SF} and ϵ_{FB} parameters on the models. An overview of some basic properties can be found in Table 3.2.

3.3.4.1 Half-light radius R_e

The half-light radius, or effective radius, denoted by R_e, encloses half of a galaxy's luminosity. In panel a.) of Fig. 3.6, R_e is plotted as a function of the V-band magnitude. The following trends can be observed in this figure:

- For a fixed n_{SF}, the effective radius varies only very slightly throughout the ϵ_{FB}-range and this without a clear trend between R_e and ϵ_{FB}. However, for a fixed n_{SF} and dark-matter mass the stellar mass and consequently the luminosity decrease with increasing ϵ_{FB}. This is due to star formation being shut down more rapidly when feedback is more effective. As a result, galaxies tend to have higher stellar densities for smaller ϵ_{FB}.

- For a fixed ϵ_{FB} of 0.1, an increase of n_{SF} from 0.1 to 6 cm^{-3} results in a decrease of

Table 3.2: Final properties of our large set of simulations. Columns: (1) model number (see Table 3.1), (2) density threshold for star formation, (3) feedback efficiency, (4) final stellar mass, (5) starting time of star formation, (6) half-light radius, (7) mean surface brightness within the half-light radius, (8) central one dimensional velocity dispersion, (9) mass-weighted metallicity, (10) central surface brightness, (11) Sérsic parameter, (12) circular velocity.

Model	n_{SF} [cm^{-3}]	ϵ_{FB}	$M_{\star,f}$ [$10^6\,M_\odot$]	ΔT_{SF} [Gyr]	R_e [kpc]	I_e	$\sigma_{1D,c}$ [km/s]	$V-I$	$[Fe/H]$	μ_0 [mag]	n	V_c [km/s]
N03	0.1	0.1	0.285	0.342	0.100	3.176	6.806	0.835	-1.183	23.603	1.496	16.176
N05	0.1	0.1	5.667	0.168	0.230	10.779	12.190	0.860	-1.236	23.170	0.959	20.396
N05	6	0.1	17.867	0.546	0.130	88.566	12.253	0.910	-0.659	20.920	1.025	22.574
N05	6	0.3	4.049	0.546	0.142	18.222	9.131	0.870	-1.130	23.005	0.877	20.483
N05	6	0.5	2.021	0.546	0.134	11.813	8.310	0.839	-1.302	22.586	1.137	20.590
N05	6	0.7	1.174	0.546	0.118	9.252	8.107	0.817	-1.542	22.694	1.231	20.555
N05	6	0.9	1.017	0.546	0.122	7.070	8.195	0.831	-1.552	24.139	0.785	20.096
N05	50	0.3	6.116	0.688	0.244	10.945	8.346	0.852	-1.016	23.154	1.104	21.158
N05	50	0.5	3.230	0.688	0.152	11.699	8.116	0.878	-1.242	22.952	1.117	20.342
N05	50	0.7	2.128	0.688	0.141	10.182	8.362	0.829	-1.426	23.141	1.112	20.038
N05	50	0.9	1.625	0.688	0.157	5.196	8.423	0.864	-1.461	24.313	0.928	19.563
N06	0.1	0.1	15.616	0.137	0.384	11.813	16.209	0.856	-1.108	23.730	0.718	23.290
N06	6	0.1	42.542	0.460	0.150	198.791	16.779	0.870	-0.540	20.383	0.892	27.277
N06	6	0.3	5.154	0.460	0.149	22.155	9.430	0.845	-1.289	22.362	1.005	21.828
N06	6	0.5	3.425	0.460	0.156	16.053	8.875	0.832	-1.329	22.981	0.872	21.335
N06	6	0.7	2.030	0.460	0.136	11.336	8.956	0.823	-1.459	23.181	0.993	21.764
N06	6	0.9	2.255	0.460	0.161	9.701	8.640	0.830	-1.437	23.493	0.935	21.668
N06	50	0.3	10.227	0.591	0.256	15.982	9.629	0.856	-1.054	23.001	0.905	23.250
N06	50	0.5	5.780	0.591	0.173	16.660	9.040	0.866	-1.228	22.497	1.142	21.697
N06	50	0.7	3.306	0.591	0.187	8.347	9.634	0.843	-1.392	23.103	1.228	21.332
N06	50	0.9	2.718	0.591	0.180	7.722	9.041	0.838	-1.408	23.093	1.228	21.089

Table 3.3: Table 3.2 continued.

Model	n_{SF} [cm^{-3}]	ϵ_{FB}	$M_{\star,f}$ [$10^6\ M_\odot$]	ΔT_{SF} [Gyr]	R_e [kpc]	I_e	$\sigma_{1D,c}$ [km/s]	$V-I$	$[Fe/H]$	μ_0 [mag]	n	V_c [km/s]
N07	0.1	0.1	67.575	0.135	0.693	14.994	23.992	0.887	-0.808	23.281	0.889	30.289
N07	6	0.1	161.970	0.336	0.206	326.861	28.621	0.900	-0.361	19.621	0.910	39.206
N07	6	0.3	14.933	0.336	0.220	31.447	10.274	0.843	-1.133	21.839	1.076	23.908
N07	6	0.5	8.008	0.336	0.190	20.299	10.485	0.825	-1.415	22.718	0.899	23.673
N07	6	0.7	5.046	0.336	0.192	13.261	9.642	0.816	-1.480	22.874	1.054	23.759
N07	6	0.9	4.246	0.336	0.193	9.060	10.028	0.853	-1.562	23.629	0.977	23.004
N07	50	0.3	21.037	0.460	0.322	18.593	9.452	0.870	-1.056	22.234	1.146	24.773
N07	50	0.5	14.128	0.460	0.340	11.805	10.721	0.864	-1.168	23.296	0.965	24.948
N07	50	0.7	9.027	0.460	0.477	3.644	10.586	0.862	-1.294	24.391	1.066	24.018
N07	50	0.9	4.908	0.460	0.396	3.605	8.229	0.819	-1.415	24.532	0.972	24.537
N08	0.1	0.1	155.430	0.131	0.812	25.902	29.448	0.871	-0.665	22.506	0.966	35.875
N08	6	0.1	271.070	0.278	0.163	839.934	-99.000	0.893	-0.261	17.300	1.467	43.269
N08	6	0.3	24.623	0.278	0.253	34.853	12.685	0.864	-1.019	21.662	1.111	27.178
N08	6	0.5	12.423	0.278	0.248	17.704	12.089	0.838	-1.404	22.986	0.846	25.561
N08	6	0.7	9.402	0.278	0.229	14.476	11.430	0.842	-1.534	22.917	1.003	24.198
N08	6	0.9	0.610	0.278	0.086	128.570	8.947	0.454	-4.277	20.621	1.077	27.395
N08	50	0.3	42.956	0.392	0.362	26.137	11.375	0.900	-0.931	21.234	1.542	27.570
N08	50	0.5	22.743	0.393	0.481	9.039	11.535	0.860	-1.147	23.855	0.768	27.479
N08	50	0.7	15.763	0.393	0.437	9.845	11.364	0.819	-1.186	23.771	0.737	28.530
N08	50	0.9	9.019	0.393	0.400	5.897	12.584	0.842	-1.331	24.193	0.836	27.050
N09	0.1	0.1	394.500	0.104	0.616	109.262	38.883	0.841	-0.382	20.759	0.943	48.060
N09	6	0.1	477.620	0.235	0.224	385.748	-99.000	1.051	-0.215	18.931	1.351	57.020
N09	6	0.3	86.095	0.235	0.278	82.718	18.482	0.898	-0.911	20.249	1.388	31.210
N09	6	0.5	30.470	0.235	0.324	21.627	13.867	0.874	-1.282	22.310	1.132	29.103
N09	6	0.7	19.274	0.235	0.500	6.815	11.576	0.843	-1.356	23.629	0.969	29.240
N09	6	0.9	12.881	0.235	0.318	9.233	12.614	0.853	-1.640	23.104	1.236	28.515
N09	50	0.3	94.102	0.324	0.382	45.638	14.780	0.901	-0.917	20.402	1.541	31.697
N09	50	0.5	40.965	0.324	0.409	17.192	14.266	0.883	-1.218	22.887	0.930	29.369
N09	50	0.7	23.972	0.324	0.559	5.967	13.400	0.867	-1.330	23.974	1.037	29.311
N09	50	0.9	15.385	0.324	0.503	6.225	12.743	0.830	-1.396	24.465	0.691	30.326

the effective radius. This is due to the size of the region where the SFC are fulfilled, which is much smaller for $n_{SF} = 6$ cm^{-3} than for $n_{SF} = 0.1$ cm^{-3}, and the feedback is too weak to overcome this. In the case of an increase of n_{SF} from 6 to 50 cm^{-3}, the effective radius increases which is caused by the higher star formation peaks resulting in more supernovae explosions which redistribute the gas more efficiently.

- The simulations with high density threshold, $n_{SF} > 0.1$ cm^{-3}, and high feedback efficiency, $\epsilon_{FB} > 0.1$, have effective radii which are in agreement with the observations.

From this scaling relation we can constrain the ϵ_{FB}-parameter to be higher then 0.1 to produce galaxies with effective radii in agreement with observations of dwarf galaxies.

3.3.4.2 The fundamental plane

The fundamental plane (FP) is an observed relation between the effective radius, R_e, the mean surface brightness within the effective radius, I_e, and the central velocity dispersion, σ_c of giant elliptical galaxies. It is a linear relation, given by

$$\log(R_e) = -0.629 - 0.845\log(I_e) + 1.38\log(\sigma_c), \tag{3.1}$$

between the logarithms of these quantities (Burstein et al., 1997). In panel b.) of Fig. 3.6, we plot the "vertical" deviation of the simulated galaxies from the giant galaxies' FP.

Dwarf galaxies generally lie above the FP in this projection. This is thought to be a consequence of their having shallower gravitational potential wells than giant galaxies. This, together with the feedback, results in more diffuse systems. Models with a high star-formation threshold in combination with a low supernova feedback turn out to be very compact. They actually populate the FP at low luminosities. However, this region of the three-dimensional space spanned by $\log(R_e)$, $\log(I_e)$, and $\log(\sigma_c)$ is observed to be devoid of galaxies. Hence, models with low stellar feedback, ϵ_{FB} up to 0.3, and high density thresholds, $n_{SF} > 0.1$ cm^{-3}, can be rejected.

3.3.4.3 Color $V - I$

Fig. 3.6, panel c.) shows the $V - I$ color in function of the V-band magnitude. The color scatter between the different models is rather small. The observed galaxies follow a mass-metallicity relation so the metallicity generally increases with the galaxy (stellar) mass, resulting in increasing $V - I$ values for increased galaxy mass. Within the relatively small mass range covered by the models, color is only a very weak function of stellar mass. For a fixed feedback efficiency, when increasing the density threshold the $V - I$ also increases slightly resulting in bluer galaxies for the models with low density threshold. This is due to the effect that stars are formed in more metal enriched regions in the models with high density threshold. When the density threshold is kept constant and only the feedback efficiency is increased the $V - I$ slightly decreases, so the models get slightly bluer due to a dilution of the gas when it is more spread out by supernovae explosions.
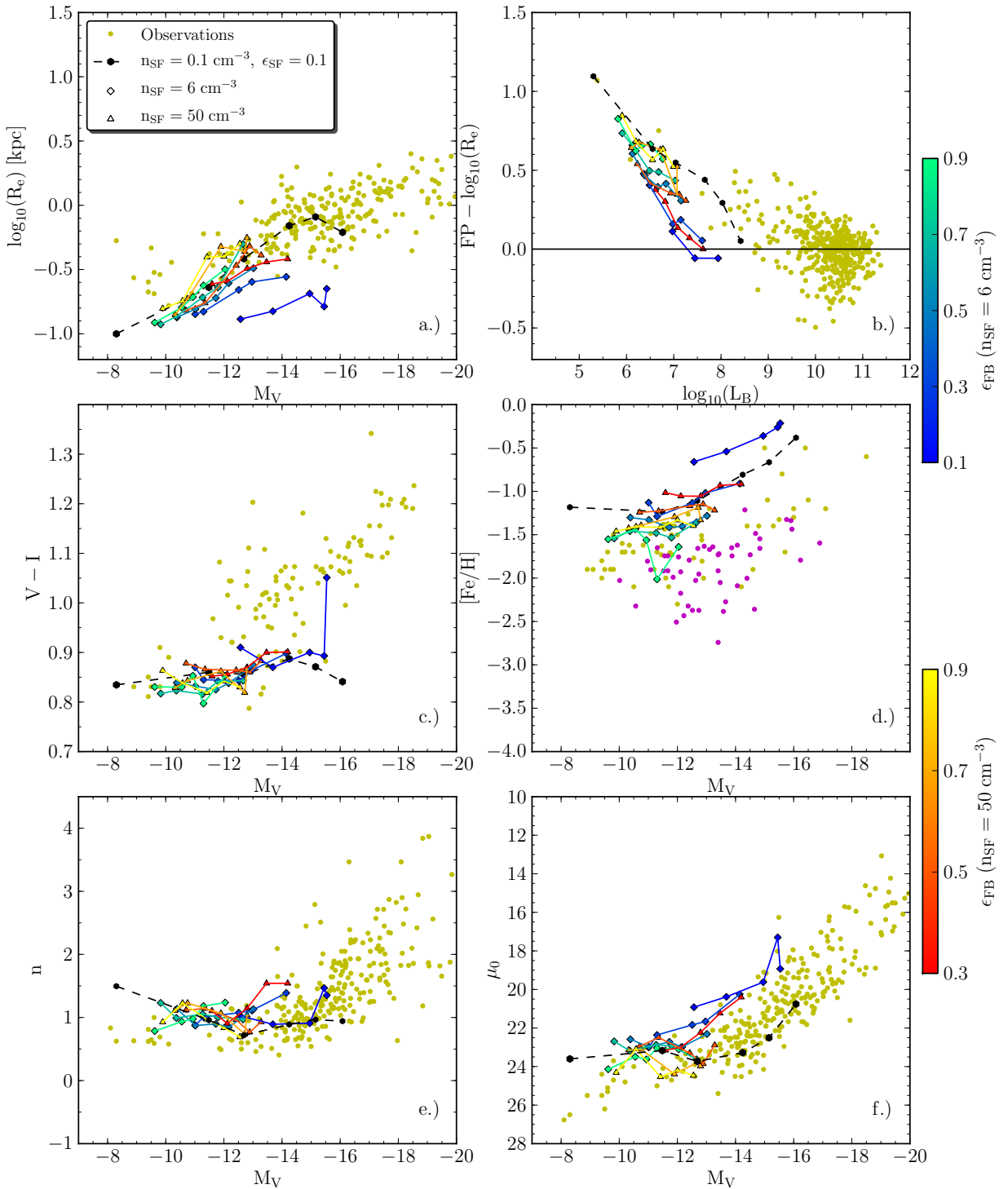
Figure 3.6: Some scaling relations and the surface brightness parameters as a function of the magnitude. In a.), the half-light radius R_e is plotted, b.) shows the vertical deviation of the simulated dwarf galaxies from the giant galaxies' FP, in c.) the $V - I$ color is plotted, d.) shows the iron content [Fe/H]. In panel e.) and f.), the Sérsic index n and central surface brightness μ_0 are plotted. All these quantities are plotted against the V-band magnitude, except the FP which are plotted as a function of the B-band luminosity. (Continued on the next page.)

Figure 3.6: (Previous page.) The models with a density threshold of 6 cm^{-3} and 50 cm^{-3} are represented by blue-green diamonds and yellow-red triangles, respectively, where the color scales represent a varying feedback efficiency. For each color, the datapoints are connected by a line showing the mass evolution of the models. In the case of $n_{SF} = 0.1$ cm^{-3}, represented by the black line, the models from N03 until N09 are plotted. In the cases of higher densities, represented by the colored lines, the datapoints are from models N05-N09. Our models are compared with observational data obtained from De Rijcke et al. (2005), Graham and Guzmán (2003) , LG data come from Peletier and Christodoulou (1993), Peletier and Christodoulou (1993), Irwin and Hatzidimitriou (1995), Saviane et al. (1996), Grebel et al. (2003), McConnachie and Irwin (2006), McConnachie et al. (2007), Zucker et al. (2007), Perseus data from De Rijcke et al. (2009), Antlia data from Smith Castelli et al. (2008). For the [Fe/H]-M$_V$ plot, data from Grebel et al. (2003), Sharina et al. (2008) and Lianou et al. (2010) was used, the yellow and magenta dots represent data from dSph and dIrr galaxies, respectively.

3.3.4.4 Metallicity

In panel d.) of Fig. 3.6 a plot of iron content [Fe/H] as a function of the V-band magnitude is shown. The mass-weighted value of [Fe/H] is a measure of the metallicity of a galaxy. The yellow and magenta dots represent observational data from dwarf spheroidal and dwarf elliptical galaxies and irregular dwarf galaxies, respectively. Some general conclusions we can take away from this figure are:

- Low-mass models with low density threshold, $n_{SF} \approx 0.1$ cm^{-3}, and low feedback, $\epsilon_{FB} \approx 0.1$, keep forming stars throughout cosmic history and do not expel enriched gas. As a consequence, they turn out to be too metal rich, compared with observed dwarf galaxies. Models with higher n_{SF} compare much more favorably with the data in this respect.

- For a fixed n_{SF}, increasing ϵ_{FB} produces more metal poor galaxies. This is likely due to the fact that the increased feedback extinguishes star formation more rapidly and disperses the metal enriched gas more widely.

- Increasing n_{SF} at fixed ϵ_{FB} and fixed mass, results in an increase of the metallicity and of the stellar mass when going from $n_{SF} = 0.1$ cm^{-3} to $n_{SF} = 6$ cm^{-3}. A further increase of n_{SF} at fixed ϵ_{FB}, up to $n_{SF} = 50$ cm^{-3}, has a much smaller impact on metallicity and stellar mass. The former is likely due to more vigorous star formation in less easily dispersable high density regions.

3.3.4.5 Surface brightness profiles

We fitted a Sérsic profile, of the form

$$I(R) = I_0 e^{-\left(\frac{R}{R_0}\right)^{1/n}},$$ (3.2)

to the surface brightness profiles of the simulated galaxies. The Sérsic parameter n and the central surface brightness μ_0 are plotted respectively in the panels e.) and f.) of Fig. 3.6 as a function of the V-band magnitude.

- For a fixed n_{SF}, when increasing the ϵ_{FB}, there is a weak trend for the Sérsic parameter

n and the central surface brightness to decrease. More vigorous feedback appears to result in more diffuse dwarf galaxies, as one would expect.

- As an echo of the R_e-M_V relation, simulations with high density threshold, $n_{SF} > 0.1$ cm^{-3}, and low feedback efficiency, $\epsilon_{FB} = 0.1-0.3$, are systematically too compact, with $\mu_0 \sim 20$ mag arcsec^{-2}, compared with the observations.

- The models with high density thresholds and strong feedback are in general agreement with the observations.

3.3.4.6   The Tully-Fisher relation

Panel a.) of Fig. 3.7 shows the B-band Tully-Fisher relation (TFR) between the circular velocity, denoted by V_c, and the luminosity in the B-band, L_B. The simulations are compared with observational data and with the Tully-Fisher relation for early-type (full gray line) and for spiral galaxies (dotted gray line) that was determined by De Rijcke et al. (2007). Additionally, four faint dwarfs were added to the plot: Leo P (Rhode et al., 2013; Bernstein-Cooper et al., 2014), Pisces A and B (Tollerud et al., 2015), with the conversion from g and g-r to B magnitudes as described by Jester et al. (2005), DDO210 (Cole et al., 2014). These dwarf galaxies show the same deviation from the observationally determined TFR for early-type and spiral galaxies as our simulations: all simulations predict that the TFR becomes substantially shallower in the dwarf regime, below luminosities of the order of $L_B \sim 10^7 L_{\odot,B}$. This can be seen as a consequence of the very steep M_{star}-M_{halo} relation in the dwarf galaxy regime (see paragraph 3.3.4.8). For a fixed n_{SF}, an increase in feedback efficiency does not influence V_c very much since there are so few stars that V_c is set by the dark-matter halo. The effect on the stellar mass, and consequently on L_B, is, however, quite large. Therefore, increasing ϵ_{FB} at fixed n_{SF} and dark-matter mass causes galaxies to shift leftwards in panel a.) of Fig. 3.7. Except for this effect, once n_{SF} and ϵ_{FB} are raised above their minimum values of 0.1 cm^{-3} and 0.1, respectively, there is no significant differences between the TFRs traced by the different series of models.

3.3.4.7   The Faber-Jackson relation

The Faber-Jackson (FJR) relation, plotted in panel b.) of Fig. 3.7 is the relation between the stellar central velocity dispersion and the luminosity in the *B*-band. The stellar central velocity dispersion is a projection of the velocity dispersion along the line of sight. This is measured by fitting an exponential function to the dispersion profile and retaining the maximum of the function as the central value.

From this figure we see:

- For a fixed n_{SF}, when increasing the ϵ_{FB}, the velocity dispersion decreases first after which it settles around a value which depends on the dark-matter mass of the model.

- For a fixed ϵ_{FB}, when increasing n_{SF}, only a minor influence on the velocity dispersion is observed.
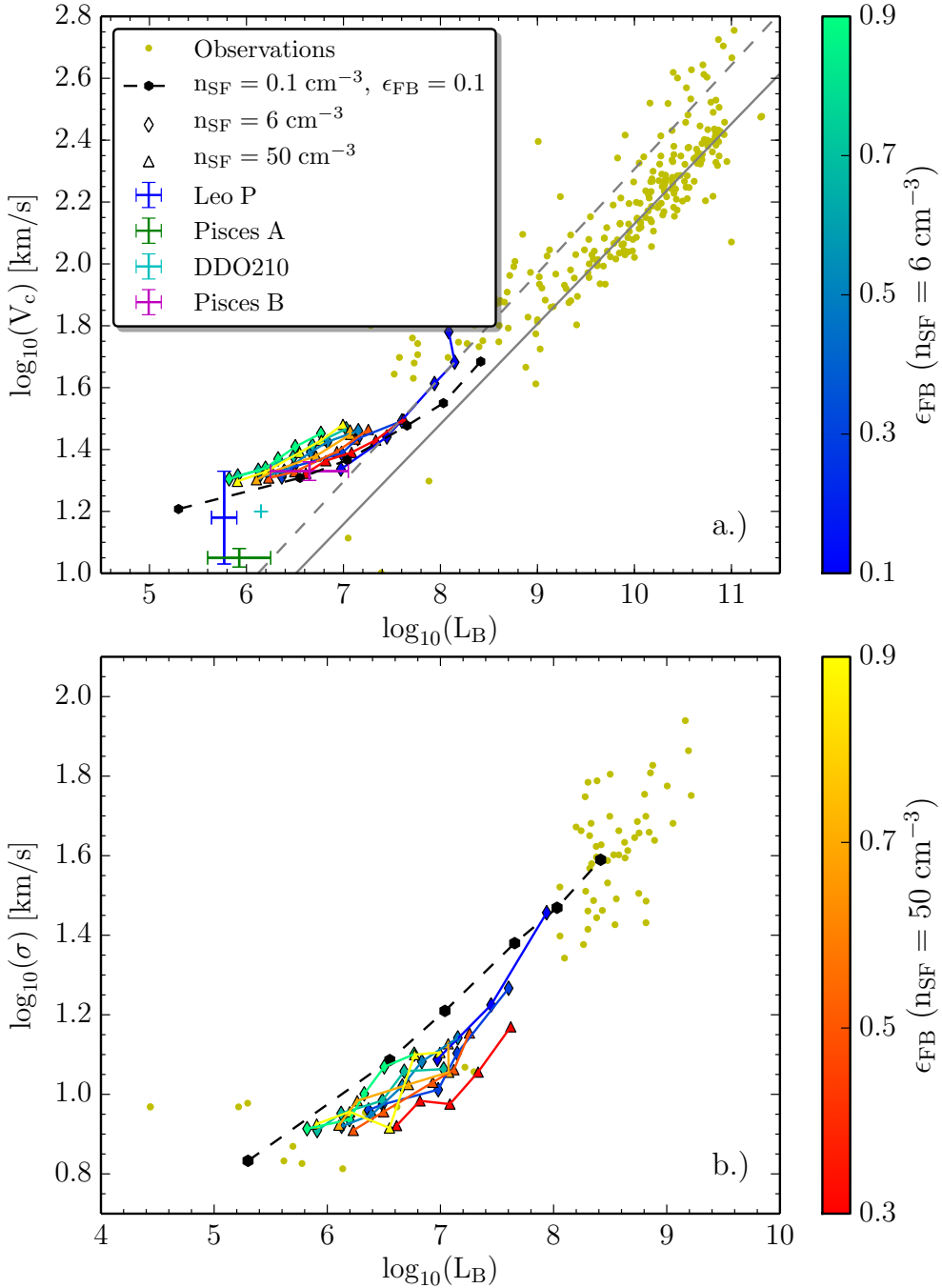
Figure 3.7: The top panel shows the Tully-Fisher relation between the circular velocity and the luminosity in the B-band. The full gray line shows the TF relation for early type galaxies, the dashed gray line is the TF relation of spiral galaxies as determined by De Rijcke et al. (2007). The lower panel shows the Faber-Jackson relation between the velocity dispersion and the luminosity in the B-band.

3.3.4.8   The M_{star}-M_{halo} relation

In Fig. 3.8, the M_{star}-M_{halo} relation of the simulations at $z = 0$ is plotted. We can make similar conclusions here as were made in the SFH section:

- If n_{SF} is fixed, the stellar mass will decrease if the ϵ_{FB} is increased. This is what was expected because with more feedback the gas is distributed over a larger area and the infall of the gas to the appropriate density threshold will take longer.

- If ϵ_{FB} is fixed, for increasing n_{SF}, the stellar mass increases too. When feedback is very small, the gas density will stay high and the star formation will not be interrupted, resulting in a high stellar mass. The effect is smaller for higher feedback.

In Fig. 3.8, our different sets of models are found to be in agreement with the results from the Aquila simulation where a density threshold of 10 cm^{-3} and a feedback efficiency of 0.7 was used. While the initial conditions of our dwarf galaxy simulations are admittedly quite simplified, they do have high spatial resolution and realistic implemented physics. It is therefore encouraging that they compare favorably with cosmological simulations like the Aquila simulation, which have cosmologically well motivated initial conditions but in which dwarf galaxies are very close to the resolution limit (Sawala et al., 2012). However it is impossible by further tuning of the feedback efficiency and/or the density threshold to reproduce the trend that was derived by Guo et al. (2010).

By increasing the density threshold and feedback efficiency, the stellar mass is reduced by almost two orders of magnitude, but there still remains a difference of many orders of magnitude between our simulations and the M_{star}-M_{halo} relation from Guo et al. (2010). It is also interesting to notice that although our models do not reproduce the relation, they do have a very similar slope.

3.4   Discussion and conclusions

3.4.1   Cusp to core

Whether the halo density profile is cusped or cored has been a point of discussion for quite some time. Observationally, evidence for cored DM profiles is found (Gentile et al., 2004), but from cosmological DM simulations a cusped density profile is deduced (Navarro et al., 1996b; Moore et al., 1996). The inherent limitation due to the angular resolution of the observations is ruled as a cause of the observed flat density profiles by de Blok and Bosma (2002). Gentile et al. (2005) also excluded the possibility of non-circular gas motions which might result in a rotation curve that is best fitted by a cored halo, while the dark matter halo actually has a cuspy profile. However, from the simulation point of view, Mashchenko et al. (2006) mentioned a natural transition of a cusp to a flattened core when the dark matter halo is gravitationally heated by bulk gas motions.

Our simulations are set up with a cusped NFW halo in agreement with cosmological simulations. The infall of gas causes an adiabatic compression of the dark halo. When gas is evacuated from the central regions, be it by a fast re-expansion as the gas pressure builds up or by supernova feedback, the dark-matter halo reacts non-adiabatically and kinetic energy
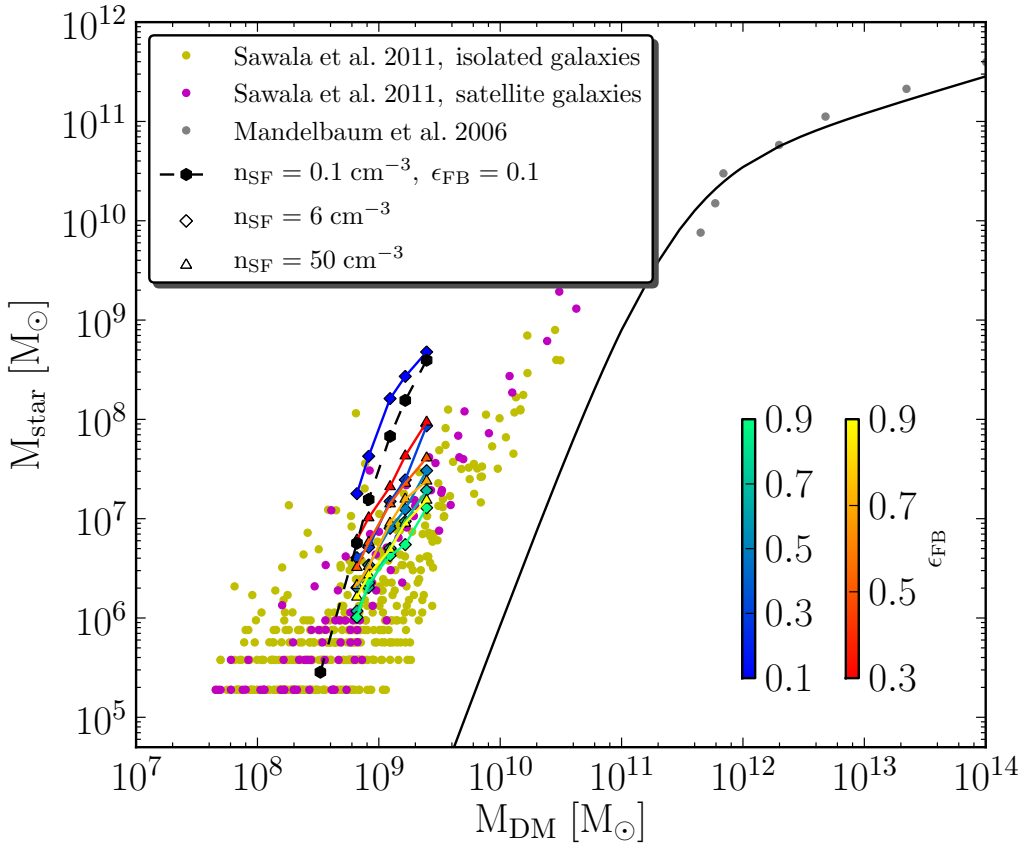
Figure 3.8: The stellar mass versus the DM halo mass, plotted in comparison with the models by Sawala et al. (2012). The gray dots show data from gravitational lensing from Mandelbaum et al. (2006). The black line is the trend for this relation that was determined by Guo et al. (2010).

of the gas is transferred to the dark matter. This results in a flattening of the central density and so the cusp is converted into a core. We can conclude that the conversion of the cusped halo density profile to a cored profile is realized by the removal of baryons from the galaxy center (Read and Gilmore, 2005), whether this is due to a re-expansion of the gas or by feedback effects or by another process.

3.4.2 Degeneracy

By increasing both the density threshold and the feedback efficiency, the simulated galaxies move along the observed kinematic and photometric scaling relations. These two parameters, the feedback efficiency ϵ_{FB} and the density threshold n_{SF}, correlate with each other and an increase of the one can be counteracted by an increase of the other, resulting in galaxies with similar properties. To be more specific: the individual galaxies are drastically different for different parameter values but they all line up along the same scaling relations and can therefore be seen as good analogs of observed dwarf galaxies.

The feedback efficiency quantifies the fraction of the 10^{51} ergs of energy that are released during a supernova explosion and thermally injected into the ISM. For each value of the density threshold we can determine the feedback efficiency range for which the models are in agreement with the observations, although we are not able to deduce a unique n_{SF}/ϵ_{FB}-combination which would be the "correct" representation of the physical processes that happen in galaxies.

For a certain density threshold, a lower limit of the corresponding ϵ_{FB}-parameter can be determined from the effective radius: the galaxies become too centrally concentrated when the feedback is too low. From the scaling relations we cannot deduce an upper limit for the ϵ_{FB}-parameter, but one could argue that the ISM cannot receive more energy than there is released by the supernova explosion, resulting in a maximal value for the feedback efficiency of 1.

In the case of a density threshold of $n_{SF} = 0.1$ cm^{-3}, the models are generally in good agreement with the observations besides the somewhat high metallicities. This is also the reason why the feedback efficiency was not varied in this case. If we compare the high density threshold models, $n_{SF} > 0.1$ cm^{-3}, with the observations we can conclude that the feedback efficiency should be larger then ~ 0.3. For a density threshold of $n_{SF} = 6$ cm^{-3}, we prefer a value of 0.7 for the feedback. Similarly we prefer a feedback efficiency of 0.9 in the case of a density threshold of $n_{SF} = 50$ cm^{-3}

The fact that different n_{SF}/ϵ_{FB}-combinations result in simulated galaxies with properties that are in agreement with the observations invokes a warning for future simulations and indicates that there is still some work left to determine the density of the star forming regions and the fraction of supernova energy that is absorbed by the ISM, quantities which are hard to determine observationally.

There are however other parameters that might influence the star-formation rate and our degeneracy, which are not investigated here:

- Given the fact that, as we discussed in subsection 2.3.1, the star-formation efficiency $c_\star$ was found by other authors not to have a significant impact on stellar mass, we did not investigate it in detail in this paper.

- The choice of the IMF, for which in our simulations a Salpeter IMF is used, determines the mass distribution of stars. The fraction of high-mass stars influences the number of SNIa and SNII explosions and as a consequence it will influence the amount of feedback and the chemical evolution. However, given the large number of IMF parameterizations available in the literature, testing them is a very daunting task which falls outside the scope of this paper. Moreover, part of the IMF-variation is quantified approximately by the variation in ϵ_{FB} which we do investigate.

- There are other possible feedback implementations, next to the release of feedback energy as thermal energy to the gas. It also could be released as kinetic energy by kicking the gas particles or by blast-wave feedback (Mayer et al., 2008).

- Other implementations of star formation, e.g. based on a subgrid model of H_2-formation (Pelupessy et al., 2004), are possible.

3.4.3   The dwarf galaxy dark-matter halo occupancy

To conclude, Fig. 3.9 shows the models which best agree with the observations for each
density threshold that was used in our analysis. Increasing n_{SF} together with ϵ_{FB} leads to a
strong reduction, of almost two orders of magnitude, of the stellar mass, especially in the
most massive models. However, with the physics included in our simulations, we are unable
to reproduce the M_{star}-M_{halo} relation of Guo et al. (2010). Surprisingly, the best models
trace a M_{star}-M_{halo} relation with a slope that is similar to that of the relation of Guo et al.
(2010). Our simulations are in agreement with results from cosmological simulations, which
have, however, much lower spatial resolution in the dwarf regime Sawala et al. (2012). We
did not explore yet higher values for n_{SF} and ϵ_{FB} because it is clear from Fig. 3.9 that
the reduction of M_{star} stagnates for high n_{SF}-values. Moreover, to compensate for the high
density threshold, an unphysical large value for ϵ_{FB}, higher than 1, would be required. Thus,
we arrive at ($n_{SF} = 6\,\mathrm{cm}^{-3}$, $\epsilon_{FB} \sim 0.7$) and ($n_{SF} = 50\,\mathrm{cm}^{-3}$, $\epsilon_{FB} \sim 0.9$) as the models which
are in best agreement with the observed photometric and kinematical scaling relations and
with the M_{star}-M_{halo} relation derived directly from cosmological simulations.
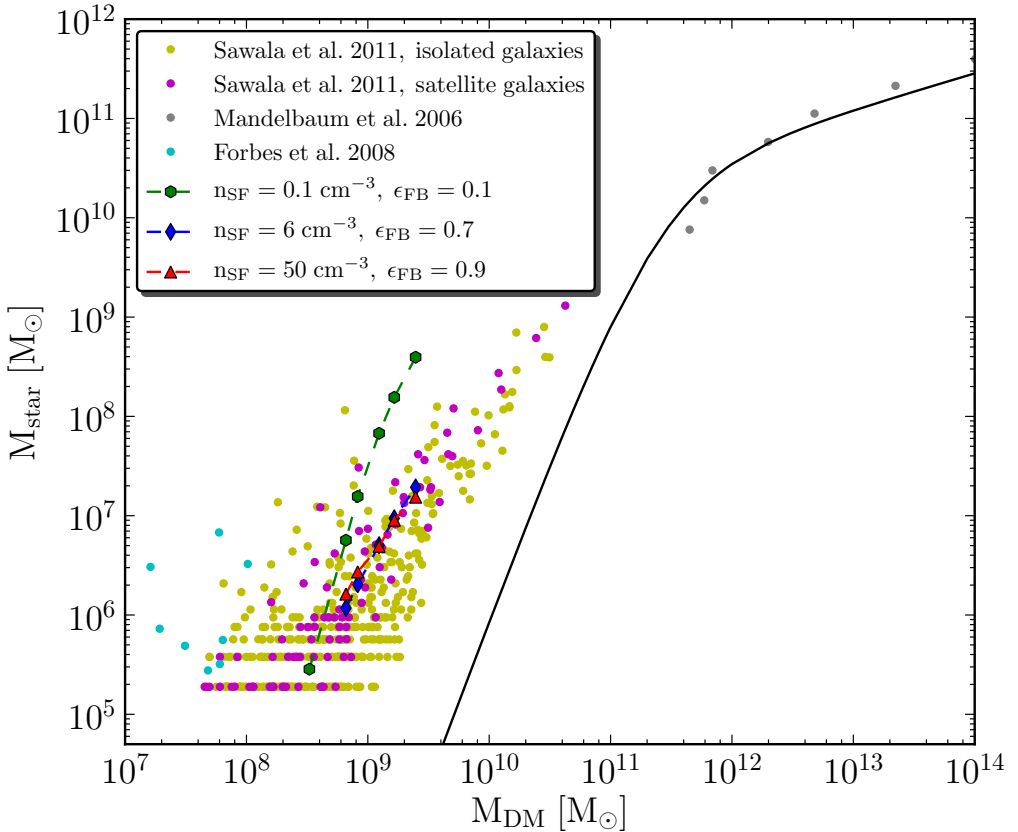
Figure 3.9: The M_{star}-M_{halo} of our best models for different density threshold compared to the
relation of Guo et al. 2010, other simulations from Sawala et al. 2012 and observations
from Mandelbaum et al. 2006.

While it appears impossible to place isolated dwarf galaxies on the M_{star}-M_{halo} relation of Guo et al. (2010), it is possible to envisage external influences that may further reduce M_{star}, as already mentioned in the Introduction:

- Not properly taking into account the effects of reionization may lead to an overestimation of the gas content of dwarfs and an underestimation of the gas cooling time. However, even taking into account reionization, the dwarf galaxies simulated by Sawala et al. (2011) had much too high stellar masses.

- At a given gas density, the star-formation efficiency of dwarf galaxies could be lower than that of more massive stellar systems because of their lower metallicity and hence lower dust content. This could be mimicked by reducing the star-formation efficiency parameter $c_\star$ (see eq. (2.13)) in the dwarf regime. However, Stinson et al. (2006) have shown that, because of self-regulation, the star-formation rate is very insensitive to this parameter: varying $c_\star$ between 0.05 and 1 left the mean star-formation rate virtually unchanged.

- External processes such as ram-pressure stripping and tidal stirring may lead to a premature cessation of star formation and hence lower M_{star} (Mayer et al., 2006). However, these processes are only effective if the gravitational potential wells of dwarf galaxies are sufficiently shallow and if they are stripped early enough in cosmic history, before they converted their gas into stars. It is unclear whether these constraints are met. In De Rijcke et al. (2010), and references therein, it was argued that the number of red-sequence, quenched dwarf galaxies increased significantly over the last half of the Hubble time and that the dwarf galaxies now residing in the Fornax cluster were accreted less than a few crossing times age (i.e. less than a few Gyr). This timescale would have left dwarf galaxies ample time to form stars before entering the cluster.

4

Dwarf galaxy merger trees

"Numerical simulations of dwarf galaxy merger trees"

4.1   Introduction

Numerical simulations of individual dwarf galaxies, as described it the previous chapter, have several advantages over full-fledged cosmological simulations: one can achieve very high spatial resolution and one has full control over the initial conditions, provided the latter are sufficiently realistic and cosmologically motivated. Thus, it can be easier to study the impact of certain physical parameters, such as mass or angular momentum, on the evolution of a galaxy. However, real galaxies obviously do not evolve in isolation from the rest of the Universe. For one, according to current cosmological theory, even dwarf galaxies have formed through a series of mergers in a bottom-up fashion.

Isolated dwarf galaxy simulations are not computationally demanding, have a well determined initial set-up, and can achieve high spatial resolution. They can be extended to also include ram-pressure stripping or interactions with a massive neighbor (Mayer et al., 2001b). Such simulations have shown that the total galaxy mass is the main parameter determining the appearance and evolution of dwarf galaxies (Valcke et al., 2008; Revaz et al., 2009; Sawala et al., 2010). Schroyen et al. (2011) suggest angular momentum as a crucial second parameter that determines individual star formation modes and offers an explanation for the

observed metallicity gradients (Tolstoy et al., 2004; Koleva et al., 2009; Tolstoy et al., 2009; Kirby et al., 2011; Battaglia et al., 2011).

Supposedly more realistic simulations of dwarf galaxies can be obtained from large ab initio cosmological simulations. However, due to their low mass, the dwarf galaxies in such simulations are often seriously undersampled making it difficult to produce robust predictions for their observational properties (Sawala et al., 2011). For example, the dark matter particle mass in the Millennium simulation (Springel et al., 2005) and the Millennium-II simulations (Boylan-Kolchin et al., 2009) is, respectively, 8.6×10^8 h^{-1} $M_\odot$ and 6.88×10^6 h^{-1} $M_\odot$. Similarly the Bolshoi simulations (Klypin et al., 2011) have a mass resolution of 1.35×10^8 h^{-1} $M_\odot$. A significant improvement to increase the mass resolution is to re-simulate a small part of a cosmological simulation box to follow the formation and evolution of a dwarf galaxy of interest in full detail (Governato et al., 2010; González-Samaniego et al., 2013). Although we are not interested in running cosmological simulations, we could use their merger histories for the halos from which dwarf galaxies can be formed. However, Srisawat et al. (2013) discussed that the identification of haloes in large cosmological simulations is not straightforward and the resulting merger trees can be different depending on which halo finder method is used. Moreover, one has no handle on the number or the properties (e.g. final mass) of the formed dwarfs.

In this chapter, we present a third way of producing more cosmologically sound dwarf galaxy simulations. The Press-Schechter (PS) formalism (Press and Schechter, 1974) uses the spherical collapse model, which is a simple model for the nonlinear structure formation in the Universe, to derive the conditional mass function. The extended Press-Schechter (EPS) theory (Bond et al., 1991; Lacey and Cole, 1993) or excursion set approach uses this conditional mass function to estimate the rate at which smaller objects merge into larger objects or the halo formation distribution. With the help of Monte Carlo algorithms a merger tree can be constructed in a top-down fashion starting from its final mass. There are many algorithms available to investigate structure formation based on this method. A detailed comparison of existing Monte Carlo algorithms and a general overview of the EPS theory can be found in Zhang et al. (2008), along with a comparison of the algorithms of Kauffmann and White (1993); Lacey and Cole (1993); Somerville and Kolatt (1999); Cole et al. (2000) and three new algorithms. However, the results of the algorithms that use EPS overpredict the abundance of small haloes and underpredict the abundance of larger haloes with increasing redshift compared to the result of the cosmological N-body simulations (Lacey and Cole, 1994; Tormen, 1998; Sheth and Tormen, 1999; Zhang et al., 2008). This is likely due to the "spherical" approximation which is used in EPS while real haloes are rather triaxial (Bardeen et al., 1986). But, as the results from the spherical collapse model produce merger trees with statistical properties which have the same trends with mass and redshift as merger trees from the Millennium simulation, Parkinson et al. (2008) adapted the GALFORM algorithm of Cole et al. (2000) to fit the conditional mass function of the Millennium simulation.

We will use the EPS theory to produce a merger tree that fixes the timing of the mergers leading up to a galaxy of a given mass at $z = 0$. The orbital parameters of the individual mergers are sampled from probability distribution functions derived from cosmological simulations. We then use our N-body/SPH code to simulate in full detail the merger sequence and the build-up and evolution of the galaxy. Using this approach, one is able to build simulated galaxies in a more cosmologically realistic way while retaining some of the benefits

of the isolated-galaxy simulations, such as high resolution and control over the final galaxy mass. Additionally, this analytical approach enables us to investigate the full range of possible merger histories where in the case of a large cosmological simulation the number of merger trees is rather limited. We benefit from a strict handle on the properties of our merger trees, for example: final halo mass, halo mass build-up in time, etc.

4.2   Simulations

We build on our experience with isolated models (see Valcke et al. (2008); Schroyen et al. (2011, 2013) and chapter 3) in order to construct a dwarf galaxy with a hierarchical structure formation history. First, we construct a merger tree (see subsection 4.2.2) whose leaves are populated with isolated dwarf galaxy models with cosmologically motivated initial conditions (ICs) (see subsection 4.2.1). These protogalaxies are then evolved and merged according to a cosmological motivated merger tree. The simulations start at a redshift of $z = 13.5$ and run for 13.5 Gyr until $z = 0$, this will have an influence on the construction of the gas halo as this depends on the critical density of the universe (see subsection 2.2.2).

4.2.1   Initial conditions isolated galaxies and recipes

In this chapter, we will simulate models with dark matter haloes with an NFW density profile as described by equations 2.8. For the gas cloud, we use a pseudo-isothermal density profile (see subsection 2.2.2). The initial gas metallicity is set to 10^{-4} $Z_\odot$, the initial temperature is 10^4 K. We use a gravitational softening length of 0.03 kpc for all particles.

We use a flat Λ-dominated cold dark matter cosmology with $h = 0.71, \Omega_{tot} = 1, \Omega_m = 0.2383, \Omega_{DM} = 0.1967$. The gas mass is set to be 0.2115 times that of the dark-matter, in accordance to the employed cosmology.

We use the subgrid physics as described in section 2.3 and choose the density threshold for star formation to have a value of 10 amu cm^{-3} due to the trend to use a high density threshold in simulations (Governato et al., 2010; Guedes et al., 2011; Cloet-Osselaer et al., 2012; Schroyen et al., 2013) which map the regions of active star formation more accurate. By using a high density threshold, star formation occurs more in small gas clumps and is less centrally concentrated, in agreement with observed galaxies (Schroyen et al., 2013).

Based on the results of chapter 3, where we showed that there is a degeneracy between the density threshold for star formation and the feedback efficiency factor the value of ϵ_{SF} is set to 0.7, which was shown to result in dwarf galaxies with properties comparable to real dwarf galaxies. In addition, a high density threshold for star formation in combination with a suitable feedback efficiency partially reduces the final stellar mass of the galaxy which is generally overpredicted in simulations (Scannapieco et al., 2012; Sawala et al., 2011).

4.2.2   Merger trees

We have used the GALFORM algorithm (Cole et al., 2000), as modified by Parkinson et al. (2008), to construct merger trees. This algorithm is based on the EPS theory which starts

from an initial Gaussian random density fluctuation field and uses the analytical model of cosmological spherical collapse to construct a density threshold above which a halo becomes virialized. For a halo of a given mass at a certain redshift, it predicts the conditional mass function of its progenitors at a higher redshift. With Monte Carlo techniques a path can be constructed from the final mass of the galaxy, the root of the tree, to the leaves, which are the smallest galaxies considered in the calculation, at some high redshift. Parkinson et al. (2008) adjusted the algorithm to fit the conditional mass function of the Millennium simulation (Springel, 2005). The construction of the merger tree proceeds from its root at $z = 0$ to its leaves, which we place at a lookback time of approximately 13.5 Gyr, corresponding to a redshift of $z = 13.5$. This redshift interval is divided into 20 bins of equal size. A few examples of the merger trees that are used can be found in Fig. 4.1. There, the sizes of the circles give an indication of the mass of the haloes.

As we do not run cosmological simulations, our haloes do not grow in time due to accretion. As visible in the merger trees in Fig. 4.1, the only way to gain mass is by merging. However, the output of the merger tree algorithm takes mass accretion into account. When the mass growth in a timestep is smaller than some resolution mass it will be considered accreted mass and it will be added to the main halo mass. As we want our final mass to be well determined we distribute the accreted mass of a parent halo over its progenitors in proportion to their masses. This way, the entire final mass is already present in the simulations from a redshift of $z = 13.5$, but it is distributed over all the haloes. An overview of our different merger tree simulations can be found in Table 4.1. This table shows the final masses of the haloes, their resolution mass which is used in the merger tree algorithm, the number of DM particles which is used to simulate the dark matter halo and the mass resolution of the dark matter in the simulation. Thus, the tree construction process provides us with the masses of the leaves of the merger tree in combination with their future merger history. We now have to place these leaf galaxies on suitable orbits in order to merge at the appropriate time.

For the determination of these orbits, we approximate every merger as a 2-body problem. As each progenitor is simulated as an isolated simulation, we need to add the simulations together at a certain time, position and with a certain velocity in order to make them merge at the desired moment. The methods used to determine these positions and velocities are described in the Appendix B.

In Fig. 4.2, a few snapshots of the evolution of a typical merger simulation are shown. The gas density is rendered in color, the young stars ($\leq$0.1 Gyr) are plotted as magenta dots, the other star particles as black dots. The most lightweight galaxies cannot compress the gas

M_{halo}	M_{res}	#DM particles	m_p
10×10^9 M$_\odot$	0.75×10^8 M$_\odot$	800 000	12 500 M$_\odot$
7.5×10^9 M$_\odot$	0.50×10^8 M$_\odot$	400 000	18 750 M$_\odot$
5.0×10^9 M$_\odot$	0.25×10^8 M$_\odot$	400 000	12 500 M$_\odot$
2.5×10^9 M$_\odot$	0.25×10^8 M$_\odot$	400 000	6 250 M$_\odot$
1.0×10^9 M$_\odot$	0.1×10^8 M$_\odot$	400 000	2 500 M$_\odot$

Table 4.1: Details of the input parameters for the merger trees. In the first column the halo mass is shown, the second column shows the mass resolution which is the smallest possible halo mass. The third column shows the amount of dark matter particles in the simulation and the last column shows the mass of one dark matter particle.
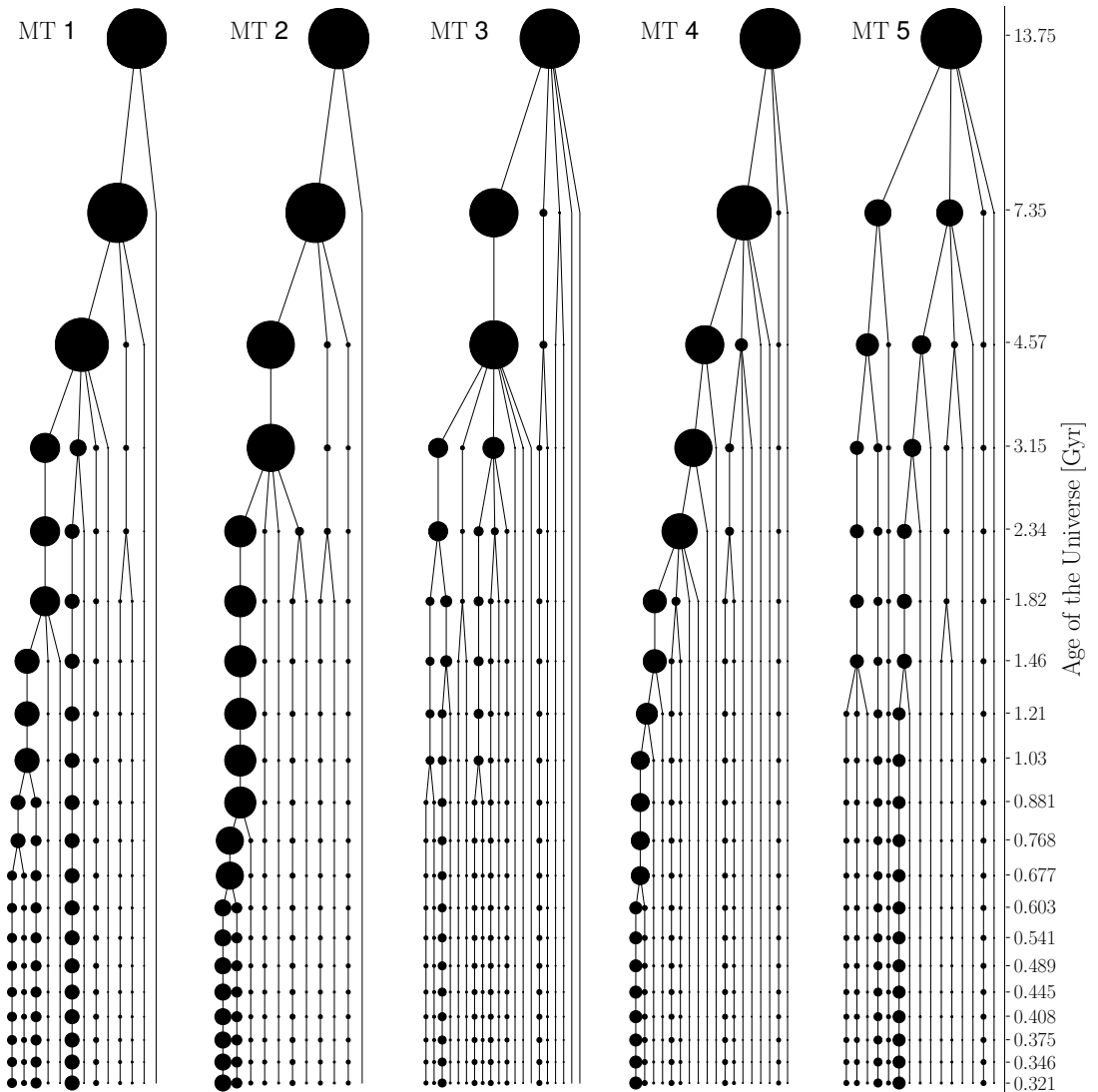
Figure 4.1: The 5 merger trees of the haloes with a final mass of $M_h=2.5\times10^9$ $M_\odot$. The size of the circles gives an indication of the mass of the halo. The evolution is shown as a function of the age of the universe which corresponds with the redshift range from 13.5, when the Universe is 0.32 Gyr old to $z = 0$.

to densities above the star-formation threshold and remain starless. In fact, initially only the most massive halo is able to ignite star formation (see first panel). The addition of smaller galaxies with gas can trigger bursts of enhanced star formation. With time, the merger activity subsides (see last panel).
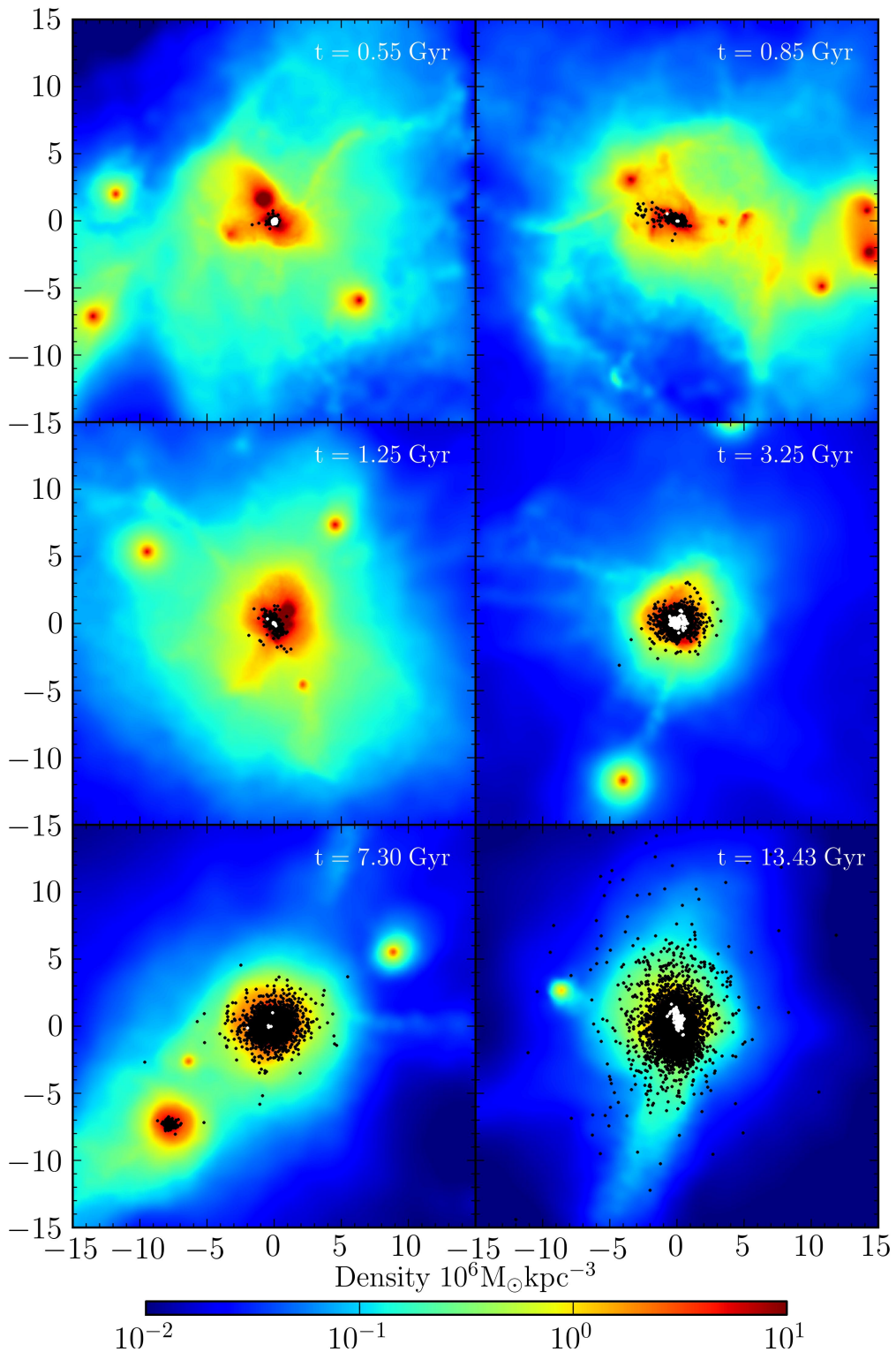
Figure 4.2: Snapshots of the merger simulation corresponding with tree MT4 from Fig. 4.1. The colorscale represents the gas density, the magenta dots show the young stars which are younger then 0.1 Gyr and the black dots show all the stars in the galaxy. In each panel the snapshot time is indicated, the x and y-labels are in kpc.

4.3   Analysis

4.3.1   Star formation histories

In Fig. 4.3 and Fig. 4.4 the star-formation histories (SFHs) of different merger trees are shown, all with the same final halo mass of respectively 2.5×10^9 M$_\odot$ (Fig. 4.3) and 7.5×10^9 M$_\odot$ (Fig. 4.4). For comparison, the SFH of an isolated model with the same final halo mass is plotted in these figures.

4.3.1.1   Isolated galaxies

The isolated models form most of their stellar mass during the first 2 Gyr of the simulation after which star formation shuts down for approximately 2 Gyr due to the depletion of gas by SN feedback which prevents the gas density to reach the threshold for star formation. The star formation restarts around 4 Gyr when part of the gas has been able to return. After that, star formation can proceed in an episodic fashion, such as in the isolated model presented in Fig. 4.3, or as low-level residual star formation, as in the isolated model presented in Fig. 4.4. The major difference between the different mass models in isolation is the amplitude of
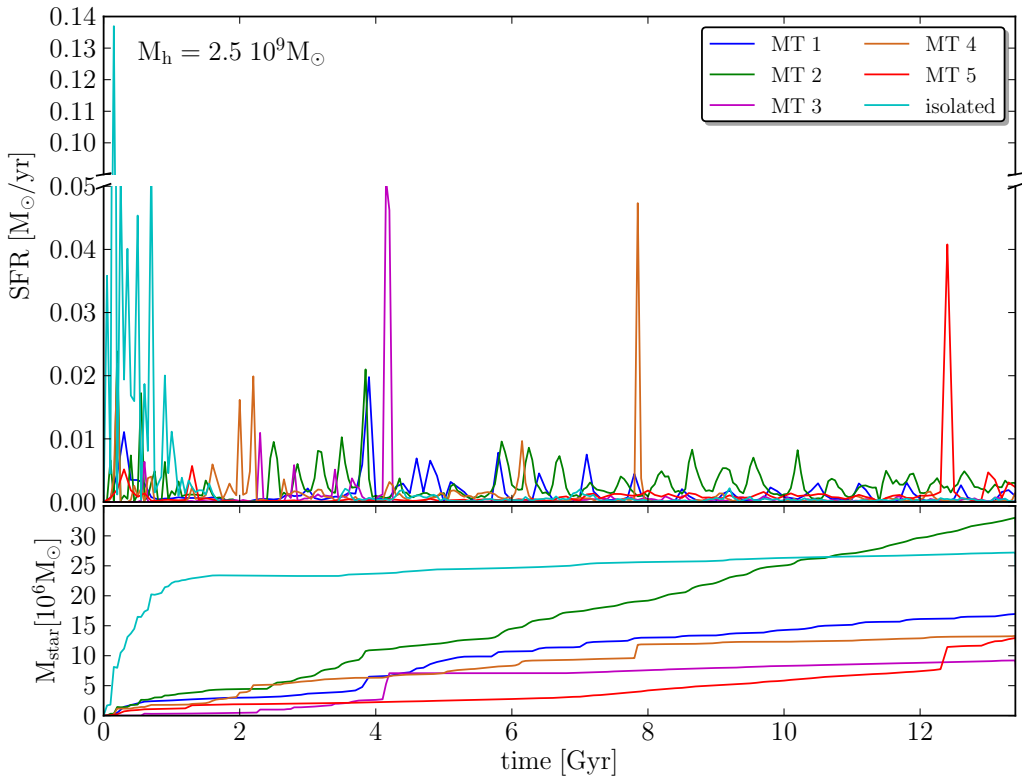
Figure 4.3: Top panel: the total SFR of several merger trees and a reference isolated simulation with the same final halo mass of 2.5×10^9 M$_\odot$ as a function of time. Bottom panel: the stellar mass as a function of time.
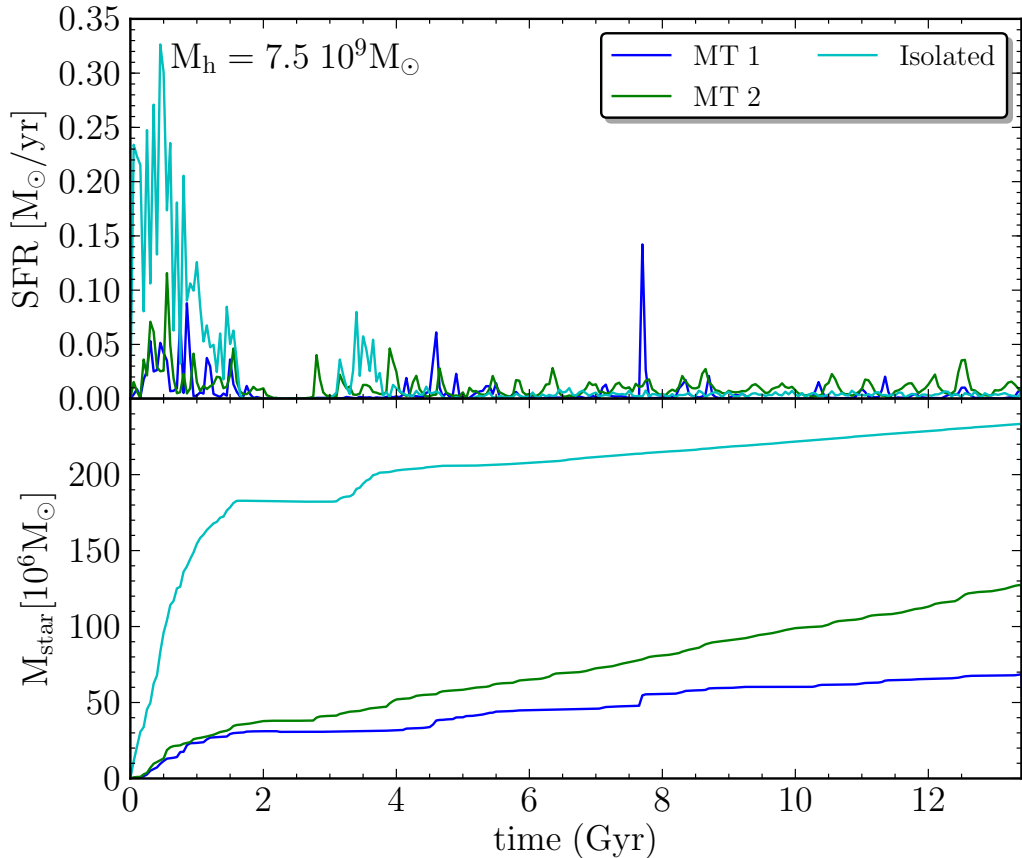
Figure 4.4: Identical as Fig. 4.3 but for a final halo mass of 7.5×10^9 M$_\odot$.

the star formation, which increases with increasing mass.

4.3.1.2 Merged galaxies

In Figs. 4.3 and 4.4, the sum of the SFR of all the members of a merger tree is plotted. In the first two Gyrs of the simulation, it is difficult to disentangle the difference between star formation occurring naturally inside any given halo and star formation prompted by mergers. After this period, the peaks in the SFH can be shown to correspond to the major merger events in the merger trees. For example, in Fig. 4.3, we see a peak for MT3 around 4.25 Gyr in the simulations which corresponds with the major merger in MT3 around 4.57 Gyr in Fig. 4.1. Similarly, a peak in the SFH of MT4 is seen around 7.8 Gyr and in MT5 around 12.5 Gyr, these correspond respectively with a major merger around 7.35 Gyr for MT4 and around 13.75 Gyr for MT5. We see that these SF peaks are in close agreement with the desired merger history we wanted to generate. However, small deviations are possible and they are due to:

1. The 2-body approximation that is used to determine the orbital parameters. In the simulation multiple mergers will be possible.

2. The calculated merging time is the time to pericenter but the large peaks in the star formation will occur only when they actually merge.

As in binary merger studies (Di Matteo et al., 2007; Cox et al., 2006; Torrey et al., 2012; Scudder et al., 2012), we see that the peaks in the SFR occur at the end of the merging process of two galaxies. At the first pericenter passage their is a modest increase of the SFR due to tidal squeezing of the gas while a larger increase is noticeable when the galaxies really collide. For example in Fig. 4.3, showing the results for models with a final halo mass of M_h=2.5 10^9 $M_\odot$, the small SF peaks at 3.65 Gyr of MT3 and at 6.2 Gyr at MT4 are created by the first pericenter passage of the halo before the large peak in SFR. There is no such first small peak for MT5 since the merger proceeds very rapidly. However, now the main star-formation peak is somewhat broadened. MT2, and to a lesser extent also MT1, lacks strong starbursts that would otherwise suppress subsequent star formation. Its minor mergers keep stirring up the gas and cause many small star-formation events. Its mass therefore gradually builds up and, in the case of MT2, eventually exceeds that of the isolated model.

We also see a double peak in the SFH for the more massive merger tree MT1 with final halo mass of M_h=7.5 10^9 $M_\odot$ in Fig. 4.4 at 7.2 Gyr and 7.7 Gyr and a triple peak due to a merger with three components at 4.15 Gyr, 4.6 Gyr and 4.8 Gyr. MT2 in Fig. 4.4 has some major mergers very early on in the simulation but for the main part of its evolution it is has a continuously supply of gas by minor mergers.

Di Matteo et al. (2007) did a statistical study of binary interactions and mergers of galaxies of all morphologies from ellipticals to late type spirals. However, our sample is less numerous and contains less massive and less disky systems but we can check if we observe similar trends. To start with, a negative correlation was found for the peak star-formation rate and the strength of the tidal interaction between a galaxy pair at first pericenter passage. The latter can be quantified by the pericenter distance, r_p, the pericenter velocity, v_p, or the tidal parameter, T_p, defined as the sum of the tidal forces of each component each described by:

$$T_{p,i} = \log_{10}\left[\frac{M_{comp}}{M_i}\left(\frac{D_i}{r_p}\right)^3\right] \quad i = 1, 2 \tag{4.1}$$

with M_i the mass of the galaxy, M_{comp} the mass of the companion, r_p the pericenter distance and D_i the scalelength of the galaxy, calculated as the radius containing 75% of the dark matter mass. Although we of course have much less data to rely on, Table 4.2 shows a similar trend for the most massive major mergers of MT3, MT4 and MT5 of the models with final halo mass of M_h=2.5 10^9 $M_\odot$, where we see that a decrease in pericenter distance corresponds to an increase in the amplitude of the SF peak. Similarly, an increase in the velocity at the pericenter, v_p, corresponds in the models with a decrease in SFR_{peak} in our data, although Di Matteo et al. (2007) found no correlation between these two parameters. However, our models have a similar trend as the models of Di Matteo et al. (2007) where an increase of SFR_{peak} occurs when the characteristic encounter time, $t_{enc} = \frac{r_p}{v_p}$ increases. The explanation for these trends provided by Di Matteo et al. (2007) is that a gentler first pericenter passage allows the orbiting galaxies to retain more of their gas for future consumption during the final merger phase.

Di Matteo et al. (2007) found a clear trend for galaxy pairs to have lower peak star formation rates when they merge if they experienced intense tidal forces at first pericenter passage. This is due to two effects. On the one hand, stronger tidal squeezing on the way to pericenter leads

to a slightly enhanced gas consumption by star formation around pericenter passage while, on the other hand, stronger expansion of the outer parts of the system after pericenter passage induces a more significant loss of gas in tidal tails. We find a similar trend that galaxies which endure a strong tidal force during their first pericenter passage have lower SF peaks when they merge.

Table 4.3 shows the final stellar mass of the different simulations. For the same halo mass, the merger simulations produce less stars than the isolated simulations. So, while mass is the main parameter determining the properties of isolated simulated galaxies, this is no longer true for the merger simulations. Mergers are able to fling large amounts of gas to large radii, where it is inaccessible for star formation and the merger history will determine when gas will be delivered to the center of a galaxy.

In addition, we can distinguish two extreme types of merger trees which reflect most clearly how the merger history influences a galaxy's star formation history and final stellar mass. On the one hand, merger trees can have a massive progenitor present early on in the simulation which subsequently grows through minor mergers, such as MT1, MT2, and, to a lesser extent, MT4 (see Fig. 4.1). At the other extreme, there are merger trees with many low-mass progenitors that merge only late in cosmic history, such as MT3 and MT5. In the former, the massive progenitor is already relatively efficient at forming stars from the start of the simulation while subsequent minor mergers will fuel further star formation. This leads to a continuously increasing stellar mass. In the latter, the many low-mass progenitors are inefficient star formers and the stellar mass increases mostly during merger-induced bursts. The former type of merger tree also leads to galaxies with higher stellar masses at a given halo mass than the latter type. Of course, merger trees fill in the continuum between these two extreme types. For instance, MT4 has a merger tree that is intermediate between the two extreme cases.

Recently, observed SFHs, derived from colour-magnitude diagrams, have become available for sizable samples of dwarf galaxies (Monelli et al., 2010b,a; Cole et al., 2007; Weisz et al., 2011; Hidalgo et al., 2011; McQuinn et al., 2010a,b). The time resolution of these SFHs can be as good as 10 Myr for the most recent epochs, deteriorating to over 500 Myr for stellar populations older than 1 Gyr. The SFHs derived by e.g. McQuinn et al. (2010a) for the last 1.5 Gyr are well resolved and show that the SFRs of dwarf galaxies can fluctuate strongly and erratically, with no discernible periodicity. These authors find that a burst produces between 3 and 26 % of the final stellar mass in the observed dwarfs. In our simulations, a starburst produces between 7 % and 29 % of the final stellar mass. A notable exception is the extreme,

MT	r_p [kpc]	v_p [km/sec]	t_{enc} [Myr]	SFR_{peak} [$M_\odot$/yr]	T_p
MT3	2.36 kpc	40.5	56.9	0.051	5.40
MT4	0.91 kpc	141.3	6.3	0.049	6.71
MT5	0.12 kpc	398.9	0.29	0.040	9.53

Table 4.2: The properties of the most massive major mergers of MT3, MT4 and MT5 of the models with M_h=2.5 10^9 $M_\odot$. The columns show (1) the pericenter distance, (2) the velocity at the pericenter, (3) the duration of the encounter, (4) the peak in the SF due to the merger, and (5) the tidal parameter.

6-fold merger in simulation MT3 with halo mass 2.5×10^9 M$_\odot$ at 4 Gyr, which produces 47 % of the stellar mass. The observed bursty dwarfs have SFRs that vary from 0.0003 M$_\odot$/year (Antlia) over 0.05 M$_\odot$/year (IC4682) up to 0.4 M$_\odot$/year (NGC5253). Our simulated dwarfs have mean SFRs of the order 0.005-0.01 M$_\odot$/year, comparable to e.g. UGC4483, NGC4163, UGC6458, and NGC6822. The observed ratio of the burst peak SFR to the mean SFR falls in the range $b \sim 3 - 14$. The simulated galaxies see peak increases of the order of $b \sim 10$ in the strongest starbursts and $b \sim 2$ in the weakest bursts.

In section 4.3.1.1 we already pointed out that the isolated non-rotating galaxy simulations often have episodic SFHs. The merger tree SFHs, on the other hand, are much more erratic and variable, without fixed periodicity, much like the SFHs of real dwarfs.

4.3.2   Scaling relations

Here we compare the gross properties of the simulated dwarfs, both with and without merger trees, with observed kinematic and photometric scaling relations at $z = 0$. For the observational data: the data from De Rijcke et al. (2005) are converted from B-band to V-band using the relation: (B-V)=0.7. From the Graham and Guzmán (2003) paper we converted their B-band magnitudes into V-band magnitudes as described in De Rijcke et al. (2009) (using a B-V colour-magnitude relation constructed from the M_V-(V-I)-[Fe/H] relation in combination with SSP models for 10-Gyr-old stellar populations (from Vazdekis et al. (1996))). The LG data and the data from De Rijcke et al. (2009), Grebel et al. (2003), Hunter and Elmegreen (2006), Dunn (2010) and Kirby et al. (2013) are presented in the V-band, so no transformation was needed. The V-band magnitudes of van Zee (2000) and van Zee et al. (2004) are deduced from their B-band magnitude and their B-V colour. For the Antlia data from Smith Castelli et al. (2008), the C-T_1 colours were (as in De Rijcke et al. (2009)) converted into V-I colours using empirical (C-T_1)-[Fe/H] and [Fe/H]-(V-I)-relations, the V-band colours were obtained using the conversion factors of Buzzoni (2005) provided in Smith Castelli et al. (2008). For the σ-L$_B$ plot we need the data in B-band, which was available for all the observations with the exception of Geha et al. (2003) where we transform the V-band magnitude to the B-band magnitude using $M_V = M_B$-0.7. We present the dIrr, dSph and dE data in Fig. 4.5 using respectively magenta, yellow and green dots.

4.3.2.1   Half-light radius R$_e$

In panel a.) of Fig. 4.5 the effective radius, R_e is shown as a function of the V-band magnitude. The black hexagons represent the isolated simulations, where the increase in V-band magnitude follows the increase in final halo mass (from respectively 10^9 M$_\odot$ to 10^{10} M$_\odot$). The merger simulations are indicated by different colours corresponding to different final halo masses. In Table 4.3, the value of the effective radius is given for each of the simulated models.

In the observational data, the effective radius increases with increasing V-band luminosity. The simulations have the same trend, but the slope of the merger simulations is steeper compared with the observational data with which the slope of the isolated models shows a better agreement. However, our isolated simulations are too compact while the merged galaxies are larger and more in agreement with observed dwarf galaxies.
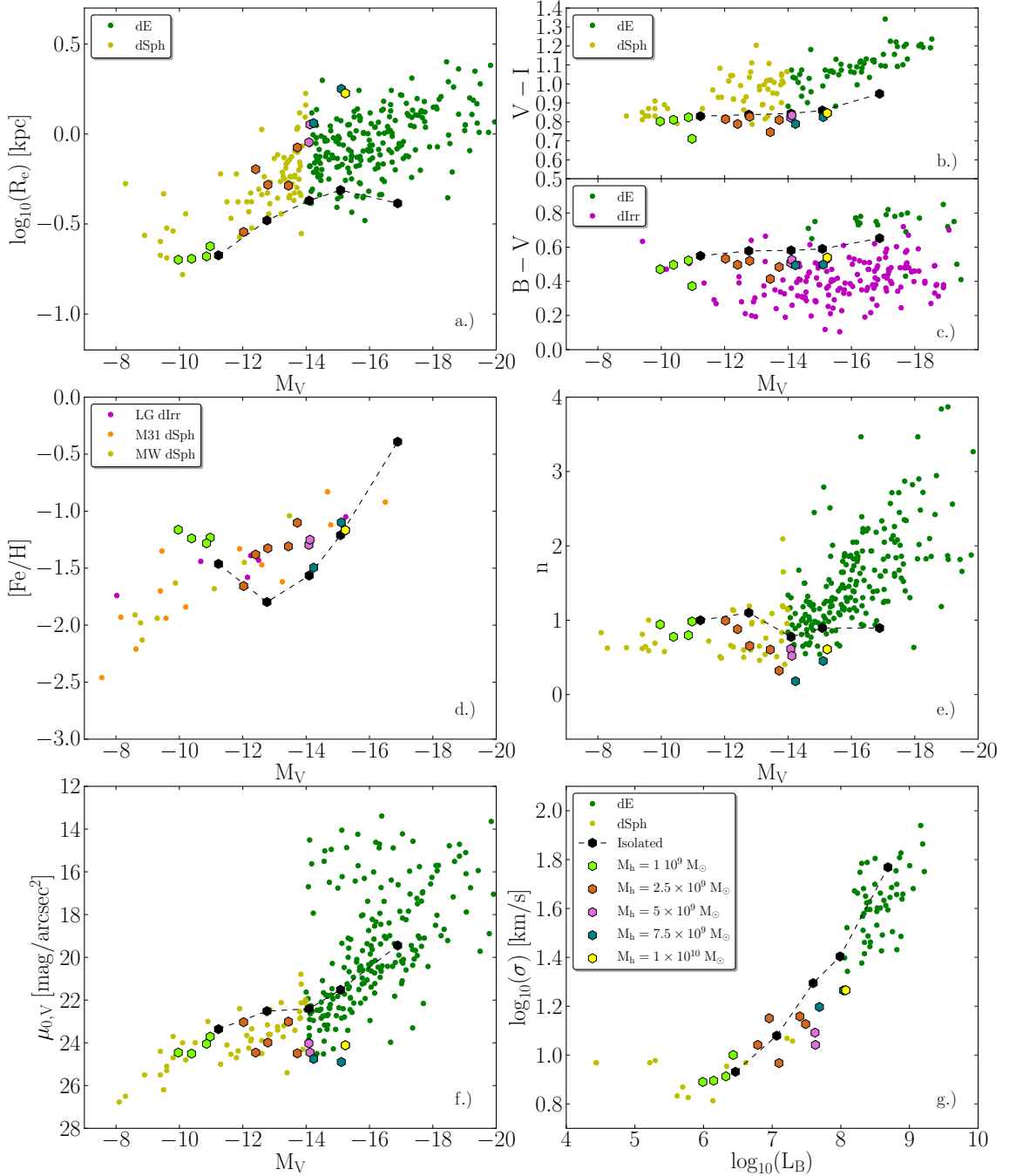
Figure 4.5: Some scaling relations and the surface brightness parameters as a function of the magnitude. In a.), the half-light radius R_e is plotted, in b.) and c.) the $V − I$ colour and $B − V$ colour is plotted, d.) shows the iron content [Fe/H]. In panel e.) and f.), the Sérsic index n and central surface brightness μ_0 are plotted and in g.) the Faber-Jackson (FJ) relation is plotted. All these quantities are plotted against the V-band magnitude, except the FJ relation which are plotted as a function of the B-band luminosity. (Continued on the next page.)

Figure 4.5: (Previous page.) The isolated models are plotted by connected black diamonds with increasing final halo mass. For the merger trees the models are represented by different symbols depending on the final dark matter mass as indicated by the legend. Our models are compared with observational data obtained from De Rijcke et al. (2005) (DR05, dEs), Graham and Guzmán (2003) (GG03, dEs), van Zee et al. (2004) (dEs), van Zee (2000) (dIrr), Hunter and Elmegreen (2006) (dIrr), LG data (dSphs) come from Peletier and Christodoulou (1993), Irwin and Hatzidimitriou (1995), Saviane et al. (1996), Grebel et al. (2003), McConnachie and Irwin (2006), McConnachie et al. (2007), Zucker et al. (2007), Perseus data from De Rijcke et al. (2009) (dSphs/dEs), Antlia data from Smith Castelli et al. (2008) (dEs). For the [Fe/H]$-M_V$ plot, data from Kirby et al. (2013) was used for MW dSphs, M31 dSphs and Local Group dIrr. For the Faber-Jackson relation data from Geha et al. (2003) (dEs), Kleyna et al. (2005) (dSphs), Mateo (1998) (dEs/dSphs), Peterson and Caldwell (1993) (dEs), van Zee et al. (2004) (dEs) and De Rijcke et al. (2005) (dEs) is used. The dIrr, dSph and dE are shown by dots in different colours, respectively magenta, yellow and green.

The larger effective radius of dwarf galaxies with merger histories indicates that star formation is more widespread in these galaxies. One important factor in determining the size of a galaxy's stellar body is the depth of its DM potential, as this influences the gravitational force on the gas. In the isolated models we already notice a conversion of the cusped NFW profile to a cored density profile due to baryonic processes (Cloet-Osselaer et al., 2012). In subsection 4.4.1, we show that the flattening of the cusp is more pronounced in galaxies with a merger history. This may explain the difference in R_e between simulated galaxies with and without merger histories in panel a.) of Fig. 4.5. Moreover, the difference between the isolated models and the merger models increases with halo mass. This may be due to the fact that the dark matter density distribution flattens more in more massive merger models.

4.3.2.2   The V−I and B−V colour.

The V−I and B−V colour as a function of the V-band magnitude is shown in respectively panel b) and c) of Fig. 4.5. The V−I colour has a value significantly below V−I∼ 0.7 mag only in stellar populations with ages below a few 100 Myr. We see that the V−I colour is constant around a value of ∼ 0.8 mag for the entire magnitude range with a scatter of 0.05 mag. There are some galaxies which, due to a late star formation burst, have smaller values for V−I. For example, MT5 from Fig. 4.3 has the lowest V−I value in its mass range (see Table 4.3), due to a recent peak in star formation at 12.4 Gyr. The other MTs have similar values for their V−I colour which is due either to a similar late SF peak or by continuous star formation at a small rate. Likewise, the B−V colour scatters within 0.1 mag around a value of ∼ 0.5 mag for the entire luminosity range.

In terms of the V−I colour, the simulations are significantly bluer than dSphs and dEs, with the merger simulations slightly bluer than the isolated simulations. In terms of the B−V colour, the simulations are comparable to observed dIrrs, although on the red side of the dIrr colour distribution.

This is caused by the larger gas fraction of the simulated dwarfs since there are no environmental effects present that could remove gas. As a result, low level star formation occurs

during the last 6 Gyr of the simulations generating young, blue stars. The isolated galaxies are generally redder as most of their stars have been formed early on in the simulation. Overall, very different SFHs due to different merger histories all result in approximately the same V−I and B−V colour.

Our rather blue models, which are more in agreement with observed dIrr due to their large gas content and ongoing star formation, could be transformed into red and dead dSph by external interventions which remove the gas and shut down star formation for the last Gyr of the simulation. Examples of such external processes are: ram-pressure stripping (Mayer et al., 2006; Boselli et al., 2008), tidal interactions (Mayer et al., 2001b,a), and the UV background (Shaviv and Dekel, 2003). However, for the simulations presented here we did not implement such external processes, so star formation continues till $z = 0$ and the simulated galaxies are bluer than the observed dSph/dE galaxies. and more in agreement with the observed dIrrs which are characterized by ongoing star formation.

Incorporating gas depleting processes, as for example the cosmic UV background, in the simulation code will be discussed in section 5.1.

4.3.2.3   The metallicity

Panel d) in Fig 4.5 shows the luminosity weighted Iron abundance, [Fe/H], a tracer of the metallicity of the stars, as a function of the V-band magnitude. The simulations are compared with observational data from Kirby et al. (2013) for Local Group dIrrs, M31 dSphs, and Milky Way dSphs represented by respectively magenta, orange and yellow dots.

With increasing mass, the isolated simulations tend to become too compact leading to fast and self-enriching star formation. This causes the bright side of their M_V-[Fe/H] relation to be too steep. For the least massive merger models, with halo masses around 10^9 M$_\odot$, the metallicity is too high by about 0.4 dex compared with the observational data. This is because only near the galaxy center does the gas density exceed the density threshold for star formation. This centrally concentrated star formation then self-enriches too much. Star formation is centrally concentrated in the least massive isolated model as well but in this case a significant fraction of the stars form early on from almost unenriched gas, causing the mean metallicity to be lower than in the merger models.

The metallicities of the more massive merger models are in better agreement with the observations. In the latter, star formation occurs spatially more widespread and self-enriches less. Except for the least massive ones, the metallicities of the merger simulations compare well with those of the observed Local Group dwarfs.

In Fig. 4.6, the metallicity distribution function (MDF) of the different merger trees and the isolated simulations at $z = 0$ is plotted in a histogram. As explained in paragraph 4.2.1, the gas already has a very small metallicity ($Z = 10^{-4}$ $Z_\odot$) from the start of the simulation. All stars formed from this gas will have exactly the same Iron abundance of [Fe/H]$= -4.45$, causing a spike in the MDF at this metallicity. This is an artifact of our idealized initial conditions.

The isolated simulated galaxies generally have a larger fraction of metal-poor stars than galaxies with a merger history. This is due to the first, large star formation peak consuming the metal-poor gas reservoir in isolated simulated galaxies. In merger simulations, the inter-

Table 4.3: Final properties of our simulations. The different blocks represent different final halo. Columns: (1) model type, (2) the final stellar mass in units of 10^6 M$_\odot$, (3) V-I colour, (4) mass-weighted metallicity, (5) the Sérsic index. (6) the mean surface brightness within the half-light radius, (7) the central one dimensional velocity dispersion, (8) the logarithm of the final specific stellar angular momentum, (9) the ellipticity, (10) the ratio of the maximal stellar velocity divided by the central one dimensional velocity of the galaxy and of a isotropic rotator, (11) and (12) respectively the amount of major and minor mergers in the formation histories, where we consider minor mergers to have mass ratios greater than 1:3.

model	$M_{\star,f}$ [10^6 M$_\odot$]	R_e [kpc]	$V-I$	[Fe/H]	n	$\mu_{0,V}$ [mag]	$\sigma_{1D,c}$ [km/s]	$\log j_{\star,f}$ [km sec^{-1} kpc]	e	$(V/\sigma)^\star$	# MM	# mM
$M_h = 1 \times 10^9$ M$_\odot$												
Isol	5.61	0.21	0.83	-1.46	1.00	22.81	8.54	-0.29	0.26	0.57	0	0
MT 1	1.36	0.24	0.71	-1.23	0.98	23.71	10.01	0.25	0.42	1.12	4	5
MT 2	2.71	0.21	0.82	-1.28	0.80	24.05	8.18	-0.74	0.11	0.36	3	8
MT 3	1.25	0.20	0.81	-1.24	0.78	24.51	7.85	-0.35	0.32	0.59	6	9
MT 4	0.79	0.20	0.80	-1.16	0.94	24.46	7.76	-0.39	0.34	0.53	4	12
$M_h = 2.5 \times 10^9$ M$_\odot$												
Isol	27.22	0.33	0.84	-1.80	1.10	21.94	11.99	0.57	0.12	2.05	0	0
MT 1	16.97	0.52	0.83	-1.33	0.66	23.99	9.27	0.64	0.20	1.46	4	8
MT 2	33.13	0.84	0.81	-1.10	0.32	24.49	13.39	1.03	0.22	1.89	3	7
MT 3	9.22	0.29	0.81	-1.66	0.99	23.04	11.00	0.24	0.16	0.56	11	8
MT 4	13.40	0.64	0.79	-1.38	0.88	24.46	14.14	0.39	0.43	0.26	4	13
MT 5	12.97	0.52	0.75	-1.31	0.60	23.01	14.39	0.42	0.11	0.52	6	8
$M_h = 5 \times 10^9$ M$_\odot$												
Isol	94.86	0.43	0.84	-1.56	0.77	21.82	19.69	0.69	0.22	1.14	0	0
MT 1	55.50	0.90	0.82	-1.30	0.61	24.03	12.35	0.49	0.06	0.50	7	12
MT 2	65.50	1.13	0.83	-1.25	0.52	24.45	11.00	0.11	0.31	0.19	5	17
$M_h = 7.5 \times 10^9$ M$_\odot$												
Isol	233.56	0.49	0.86	-1.21	0.90	20.93	25.33	0.71	0.10	1.23	0	0
MT 1	68.70	1.15	0.79	-1.50	0.18	24.75	15.73	1.02	0.26	0.40	12	8
MT 2	127.58	1.78	0.82	-1.10	0.45	24.90	18.38	1.42	0.21	0.86	5	15
$M_h = 1 \times 10^{10}$ M$_\odot$												
Isol	1288.10	0.41	0.95	-0.39	0.89	18.79	58.69	0.40	0.16	0.17	0	0
MT 1	178.56	1.68	0.85	-1.17	0.61	24.12	18.42	1.31	0.47	0.45	5	7
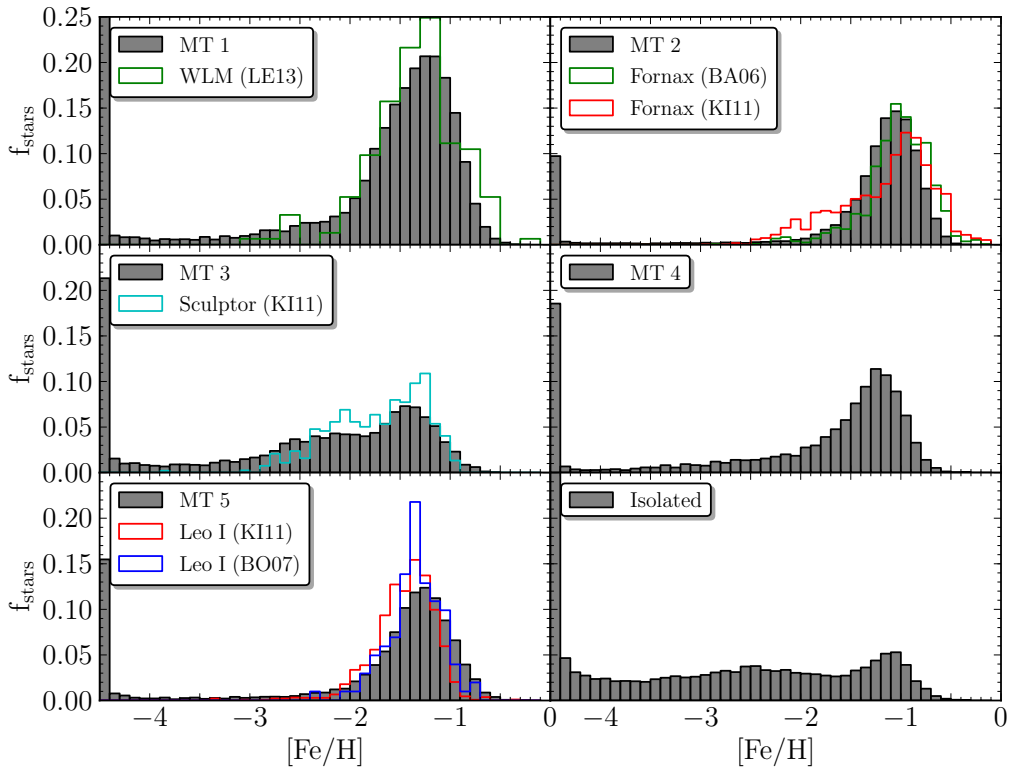
Figure 4.6: A histogram of the metallicity distribution of the stars. The simulations all produce dwarf galaxies with final halo mass of 2.5×10^9 M$_\odot$. The simulations are compared with observational data from Battaglia et al. (2006) (BA06), Kirby et al. (2011) (KI11) and Bosler et al. (2007) (BO07).

action induced star formation rapidly boosts the metallicity to [Fe/H]~ -1, thus suppressing the low-metallicity tail. One notable exception is MT3 whose merger tree contains relatively few mergers during the first 3 Gyr. Star formation in its isolated progenitor galaxies produces a population of low-metallicity stars, peaking in the metallicity range [Fe/H]~ -3 to -2.

As an illustration, we compare the MDFs of some of the merger tree simulations with those of observed Local Group dwarf galaxies: Fornax, Sculptor, Leo I and WLM. With absolute magnitudes of, respectively, $M_V = -13.3$ mag, -11.1 mag, -11.8 mag and -14.92 mag (Irwin and Hatzidimitriou, 1995; Mateo, 1998; Łokas, 2009; de Vaucouleurs et al., 1991) these galaxies fall in the luminosity interval covered by the simulations. Each galaxy is compared with a merger tree simulation that closely matches its mean metallicity: [Fe/H]=-0.99, -1.68, and -1.43 for Fornax, Sculptor, and Leo I (Kirby et al., 2011) and WLM with [Fe/H]=-1.28 (Leaman et al., 2013), respectively, and [Fe/H]=-1.1, -1.66, -1.31, and -1.33 for MT2, MT3, MT5, and MT1 respectively. All MDFs, simulated and observed, are normalized to unity over the metallicity interval from [Fe/H]=-4 to [Fe/H]=0. The Fornax MDFs are taken from Battaglia et al. (2006) (BA06) and Kirby et al. (2011) (KI11), those of Sculptor from KI11, those of Leo I from KI11 and from Bosler et al. (2007) (BO07) and the WLM MDF is taken from Leaman et al. (2013). Clearly, there can be a significant author-to-

author difference between observed MDFs of the same galaxy. This could be caused by the different number of stars included in the samples and by the different spatial extents covered by the observations, if the stellar populations are spatially segregated.

The low-metallicity tail of the Fornax data of BA06 was explained to originate from the infall of a metal poor component based on its non-equilibrium kinematics and radial metallicity gradient. The analysis of KI11 suggested Fornax to have an extended SFH due to the metal-rich peak in the MDF which is caused by star formation from previously enriched gas. As MT2 already has a massive component containing roughly half of its final mass at one Gyr in the simulation after which it receives metal-poor gas from multiple minor mergers triggering SF, this explains why the simulation is most in line with the results of KI11. The same is true for the MDFs of MT1 and MT4.

Like MT3, Sculptor has a bimodal MDF with a high-metallicity peak around $[Fe/H] \sim -1.3$ and a low-metallicity peak below $[Fe/H] \sim -2$. We merely wish to illustrate that such bimodal MDFs are also found among real dwarfs in this luminosity range. Moreover, the agreement is not perfect: MT3 contains more low-metallicity stars than Sculptor and the high-metallicity peak is less strong.

We can conclude from Fig. 4.6 that the peaked MDFs of the merger-tree simulations are much more in agreement with the observations than the flat MDFs of the isolated models.

4.3.2.4   The Sérsic parameters

Panels e) and f) show in Fig. 4.5 show respectively the Sérsic index n and the central surface brightness in the V-band, $\mu_{0,V}$. In both cases the simulations are compared to observational data of dE/dSph galaxies. Generally, for all mass models and different merger trees, the models overlap with the Sérsic parameter data in the regime of the dwarf spheroidals. The scatter in the simulations is mainly due to the different merger histories.

Sérsic index, n   The merger simulations have similar n-values as the observational data and are smaller or equal compared to the Sérsic indices of isolated simulations. We see that neither the merger tree, nor the flattening of the central core has a significant influence on the Sérsic index of the simulations.

Central surface brightness in the V-band, $\mu_{0,V}$ The isolated models follow the trend of increasing central surface brightness with increasing V-band magnitude. The most massive merger simulations have lower central surface brightnesses compared to the isolated models but are still in agreement with the observations. This low $\mu_{0,V}$-value is due to the flatter DM core which causes star formation to occur less centrally and results in a more extended, less dense stellar body.

4.3.2.5   The Faber-Jackson relation

After the photometric relations, we now turn to the kinematic relations, where panel g.) of Fig. 4.5 shows the velocity dispersion of the stars as a function of the B-band luminosity. Our simulations follow the same trend as the observational data. The isolated simulations have velocity dispersions which are somewhat large compared to the observations. The merger

simulations are better in agreement with the observations but they show some spread which is due to the different merger histories which result in different flattenings of the dark matter core.

For more massive haloes, the velocity dispersion of the merged galaxies deviates markedly from that of the isolated galaxies. Again, this is most likely due to the stronger flattening of the dark matter halo in more massive galaxies, see subsection 4.4.1. Due to the lower central density and the shallower potential, stellar velocities will be lower, resulting in a lower velocity dispersion.

4.4 Discussion

4.4.1 The dark matter halo

In order to create dark-matter density profiles, the isolated simulations are centered on the center of mass of the dark matter haloes. For the merger simulations, this approach is less obvious since the merging process of the dark matter haloes produces tidal tails which extend to large radii. As a result, the center of mass of a halo can deviate significantly from what one would consider "by eye" to be the location of the center of the main halo. Moreover, as can be seen in Fig. 4.7 and Fig. 4.8, the dark-matter haloes of galaxies with a merger history contain substantial substructure until the end of the simulation. To find the center of the main halo, we use a side program of the SHADOWFAX code (Vandenbroucke, in prep.). In this program, a 3D Voronoi tessellation (Schaap and van de Weygaert, 2000) is used to determine the density at the position of each dark matter particle, where the densities are determined as the inverse of the volume of the corresponding Voronoi cell. The 15 particles with the highest densities and hence the smallest Voronoi cell, are then selected. Finally, the center of the halo is equated to that particle out of those 15 which has the largest mass within a 2 kpc sphere in order to avoid local density peaks. A visual check proved that this procedure yields a meaningful estimate for the halo center. The dark-matter density profile is derived from the mass enclosed inside increasingly large spherical shells centered on the halo center identified as explained above.

In Figs. 4.9 and 4.10, the density profiles of the merged haloes with halo mass of respectively 2.5×10^9 M$_\odot$ and 7.5×10^9 M$_\odot$ are plotted at $z = 0$ together with the density profiles of an equally massive isolated galaxy at $z = 0$ and $z = 13.5$. Very often, we see a conversion from the initially cusped NFW-profile (black dots) to a cored, or at least less steep, density profile (cyan dots) in the isolated galaxy simulations due to the effects of stellar feedback (Cloet-Osselaer et al., 2012). Each individual subhalo of the mergers initially start with an NFW profile but the most massive halo of each model with a merger history appears to become even shallower at $z = 0$ than the isolated ones. Comparing the dark-matter density profiles in Figs. 4.9 and 4.10 with the merger trees that produced them (see e.g. Fig. 4.1) and the corresponding star-formation histories (see e.g. Figs 4.3 and 4.4) shows that the former is a non-trivial function of the merger history and the baryonic processes. The absorption of the orbital energy involved in a major merger will tend to inflate the dark-matter halo, causing the cusp to weaken. If a merger causes a rapid inflow of gas, it may compress the cusp whereas gas expulsion by supernovae may weaken the cusp.
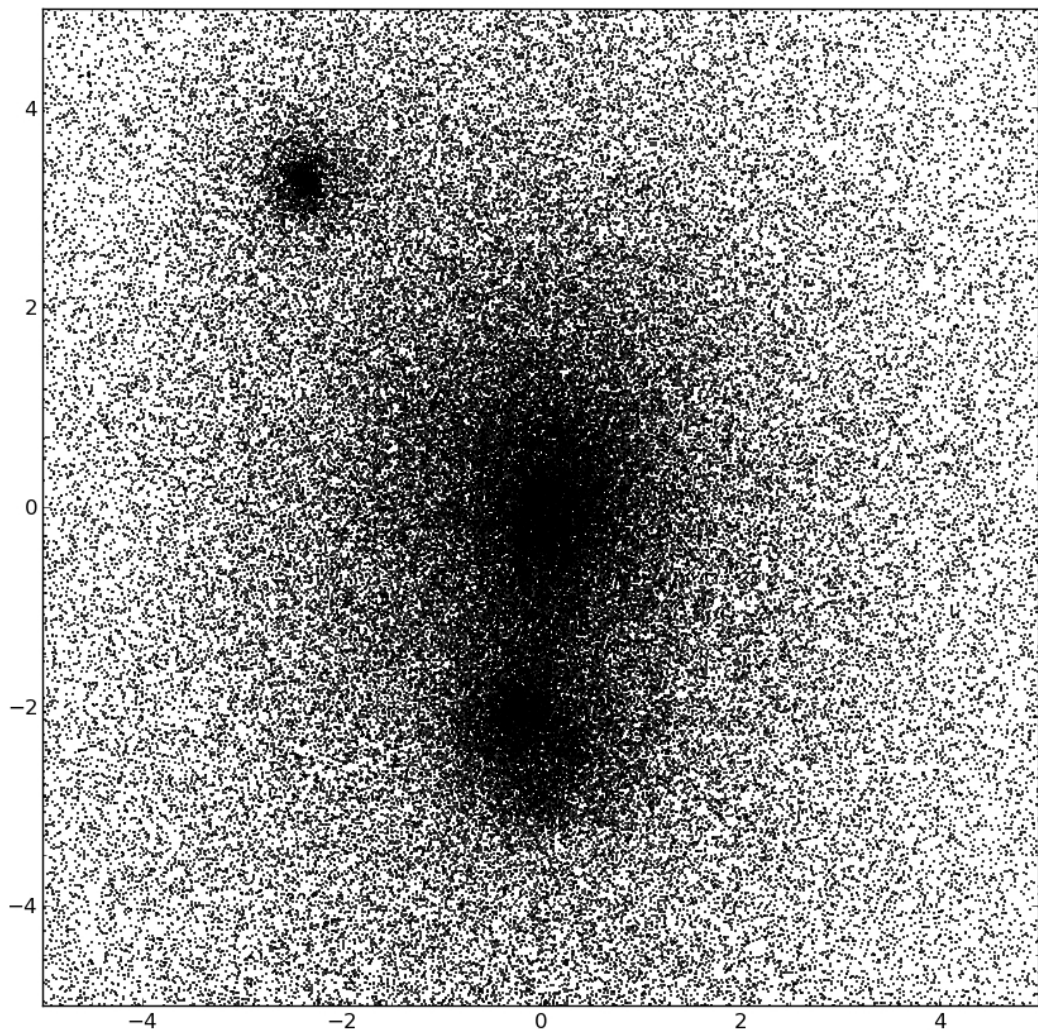
Figure 4.7: The dark matter distribution of a halo with mass 2.5×10^9 $M_\odot$ at z=0. The units on the the box are in kpc.

In Fig. 4.11 and Fig. 4.12 the evolution of the inner slope of the dark-matter density profile, denoted by γ, is plotted for respectively MT2 and MT3 of the merger models with final halo mass of $M_{h,f}$=2.5×10^{9}M$_\odot$. γ is determined by a least-square fit of a Nuker law (Lauer et al., 1995)

$$\rho(r) = \frac{\rho_s}{r^\gamma (r^\beta + r_s^\beta)^\alpha},$$ (4.2)

to the density profile This function corresponds with a broken power-law function, where the break radius is described by r_s and the sharpness of the transition is set by β. γ represents the slope in the inner part, e.g. for $r \ll r_s$, $\rho(r) \sim r^{-\gamma}$, and α determines the outer power law as for $r \gg r_s$ $\rho(r) \sim r^{-\alpha\beta-\gamma}$. The NFW profile corresponds to $\gamma = 1$, $\beta = 1$, and $\alpha = 2$. We omit the inner 60 pc from the fit; this corresponds to twice the gravitational softening length. The scatter on the value of γ is caused by the combined effect of inaccuracies on the determination of the real center of the dark matter halo and the fitting procedure.
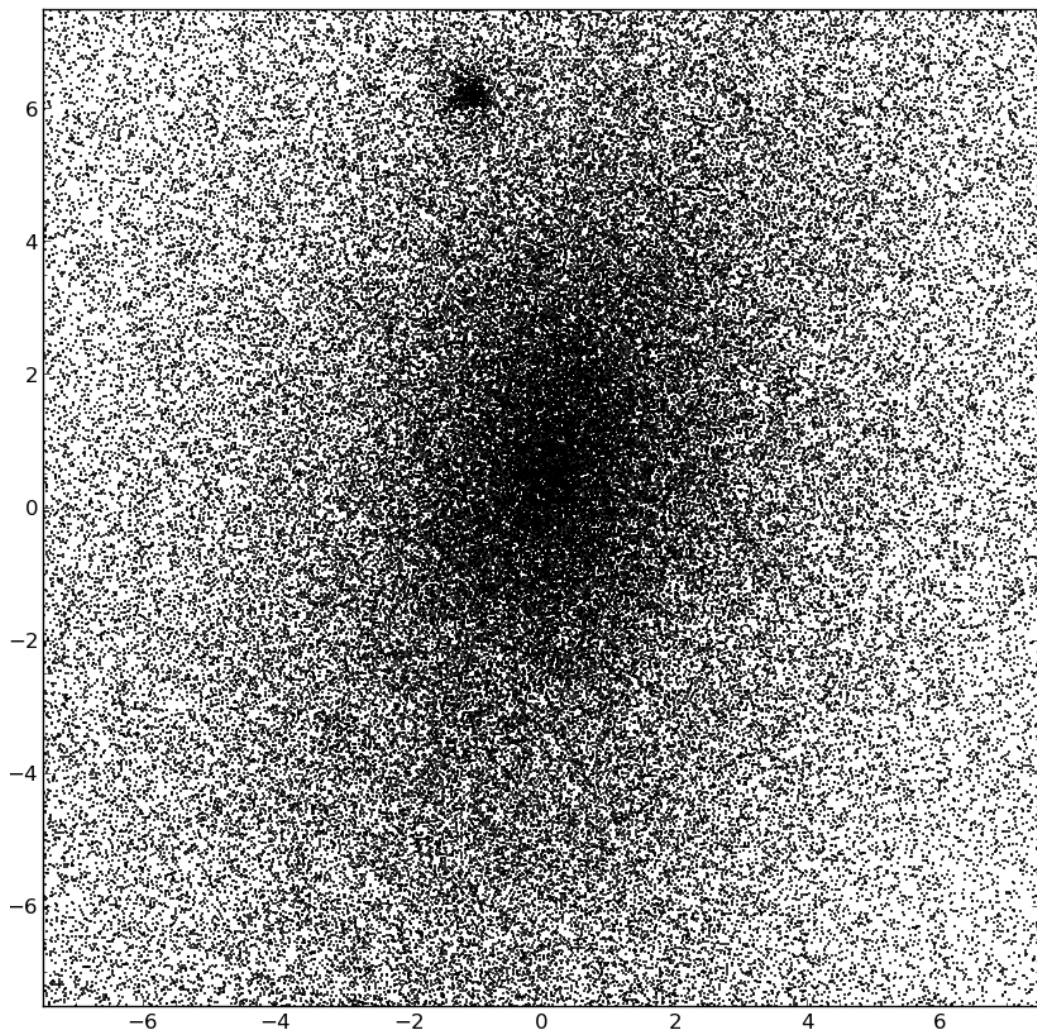
Figure 4.8: The dark matter distribution of a halo with mass 7.5×10^9 M$_\odot$ at z=0. The units of the box are in kpc.

MT2 is a merger tree which already starts with a quite massive halo at early times, e.g. ~53% of the final halo mass is present in the main halo after one Gyr in the simulation and the halo grows by the subsequent addition of minor mergers, each containing ~1%-10% of the final halo mass. In Fig. 4.11, one first notices the adiabatic contraction of the halo, signaled by an increase of γ to values above 1, due to the initial collapse of gas in the dark-matter potential well. Afterwards, the slope gradually decreases again due to the rapid removal of gas from the inner regions during repeated small starbursts triggered by the many minor merger events. MT1 and MT4 show a similar behavior as MT2 in this regard.

MT3, on the other hand, is a merger tree where the mass builds up slowly over time, e.g. only ~33% of the final halo mass is present in the main halo after one Gyr. Here, we trace the evolution of the slope γ in the most massive halo present at each point of time in the tree MT3. A major merger occurs at 4 Gyr resulting in a large star formation peak and a subsequent shutdown of star formation. As shown in Fig. 4.12, the slope initially rapidly
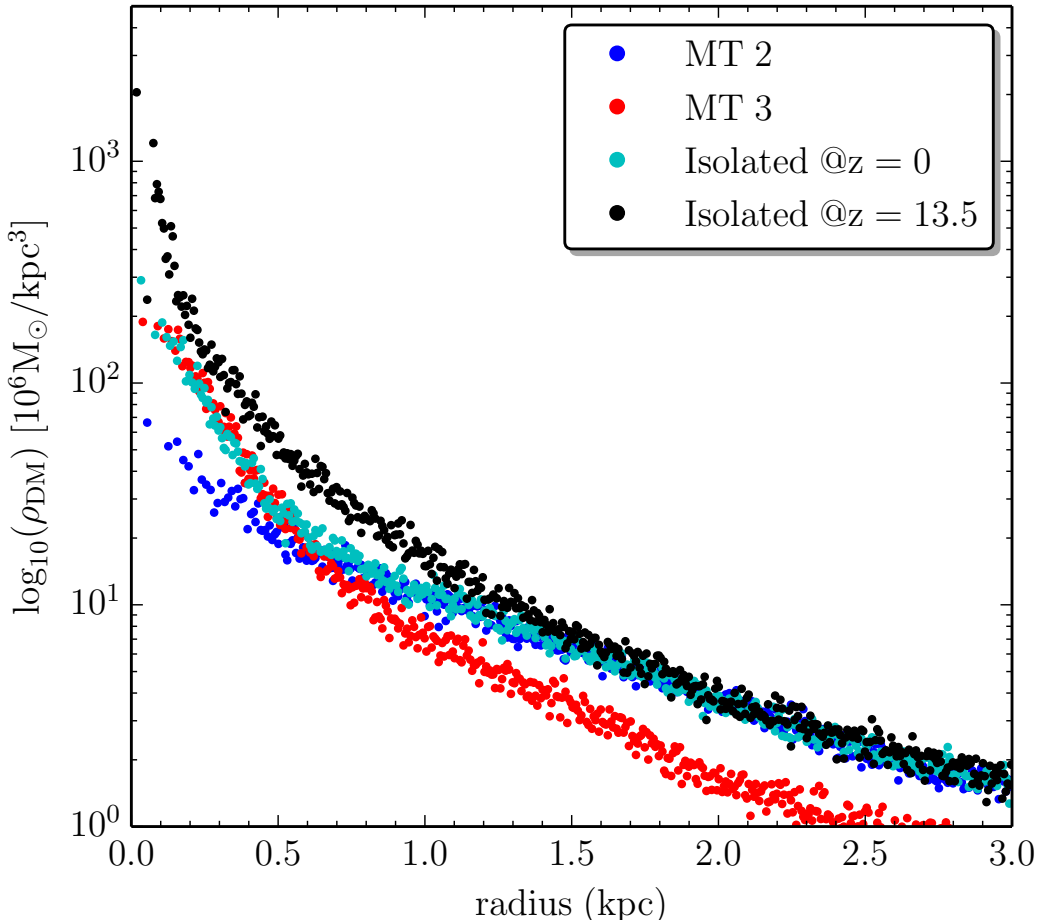
Figure 4.9: The dark matter density profile of the merger simulations MT2 and MT3 at $z = 0$ and one isolated galaxy with a final halo mass of 2.5×10^9 M$_\odot$ at $z = 0$ and $z = 13.5$.

increases above 1, as in MT2. In this case, however, star formation is very low powered and the dark-matter cusp appears quite resilient against any small-scale gas motions. Only after the steep increase of the star-formation rate and the feedback activity connected with the major merger around 4 Gyr does the slope drop below $\gamma = 1$. The starburst is actually so strong that star formation is halted for the next 1.5 Gyr and, when restarted, remains very weak and unable to further affect the dark-matter profile. In this case, the inner dark-matter slope remains stable. The dark-matter density profile of MT5 behaves similarly to that of MT3.

As shown in the literature, baryonic processes can explain the discrepancy between the cored dark matter density profiles of observed galaxies and the cusped dark matter density profiles deduced from cosmological simulations. First, the rapid removal of gas due to stellar feedback results in a non-adiabatically response of the dark matter halo and introduces a flattening of the cusped dark matter halo (Navarro et al., 1996a; Read and Gilmore, 2005; Mashchenko et al., 2006; Governato et al., 2010; Pontzen and Governato, 2012; Governato et al., 2012; Cloet-Osselaer et al., 2012; Brooks and Zolotov, 2014). Secondly, the transfer of energy
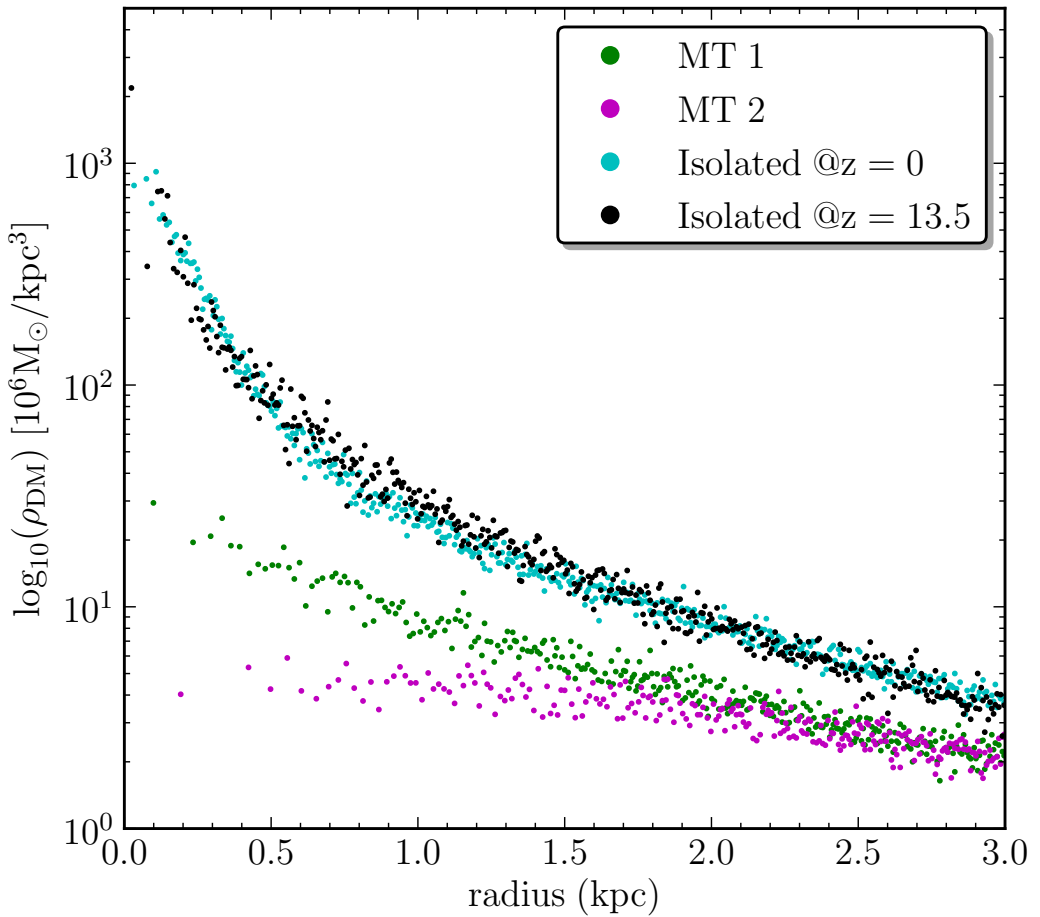
Figure 4.10: The dark matter density profile of the merger simulations at $z = 0$ and one isolated galaxy with a final halo mass of 7.5×10^9 $M_\odot$ at $z = 0$ and $z = 13.5$.

and/or angular momentum to the dark matter by infalling objects can transfer the cusped inner dark matter density profile into a more cored profile (Goerdt et al., 2006, 2010; Cole et al., 2011). Repeated minor mergers can trigger small starbursts that rapidly evacuate gas from the galaxy center, with each burst slightly lowering the slope of the dark-matter density profile. Strong starbursts caused by major mergers have the same effect but, during star-formation lulls, the dark-matter density profile remains stable.

Recently, Laporte and Peñarrubia (2015) discussed the regrowth of an initially DM core into a cusp in a cosmological simulation by the merging with cusped DM substructures which are dense enough to reach the central regions without being tidally disrupted. Oñorbe et al. (2015) found consistent results in the FIRE simulation where hydrodynamics and star formation were included by comparing two mergers with similar final stellar masses but with an early and late epoch of star formation. They found DM cores to be largest in systems that formed their stars quite late ($z < 2$), after the early epoch of cusp building mergers has ended. For our simulations, MT4 and MT5 also have comparable stellar masses and MT4 could be seen as the merger where most of its mass is generated in an early epoch
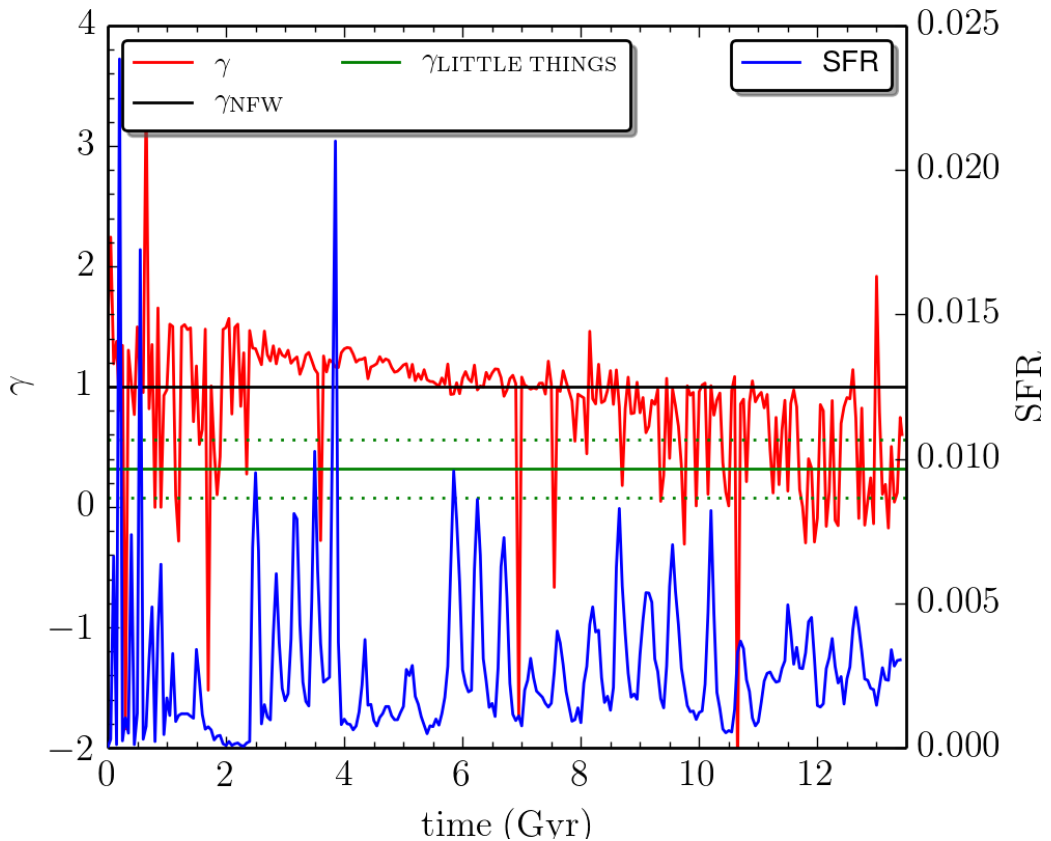
Figure 4.11: The evolution of the slope of the most massive component of MT2 in red. The SFR is plotted by the blue line. The slope of an NFW profile with $\gamma=1$ is plotted as a reference by the black line. The green line shows the mean value of the slopes of the 26 LITTLE THINGS analyzed by Oh et al. (2015), who found $\gamma = 0.32 \pm 0.24$.

of star formation and MT5 with a late epoch of star formation. However, the difference between their flattenings is rather limited to $\gamma=0.25$ for MT4 and $\gamma=0.22$ for MT5. Based on these results we cannot claim to see this effect of regrowth of the dark matter cusp. A more extended sample of merger trees composed of more models with comparable masses and different merger histories might give us more insight into this effect.

Merger trees with more massive final haloes show the same behavior, although Fig. 4.10, which shows the density profiles of haloes with final mass $M_h=7.5\times10^9$ $M_\odot$, suggests that the flattening effect is much more pronounced for higher masses. This is likely caused by the stronger fluctuations in the star-formation rate (see Fig. 4.4) and by the fact that more massive merging galaxies need to absorb more orbital kinetic energy. Tree MT2 in this mass series of simulations contains a massive progenitor already early on which grows mainly through minor mergers. Star formation continues throughout the simulation, constantly reducing the inner dark-matter slope. MT1 contains major mergers that stop star formation for considerable timespans, limiting the flattening of the dark-matter cusp.

We conclude that the dark matter haloes are strongly influenced by the merger history and the resulting baryonic processes. Oh et al. (2011b) determined the inner density slopes within
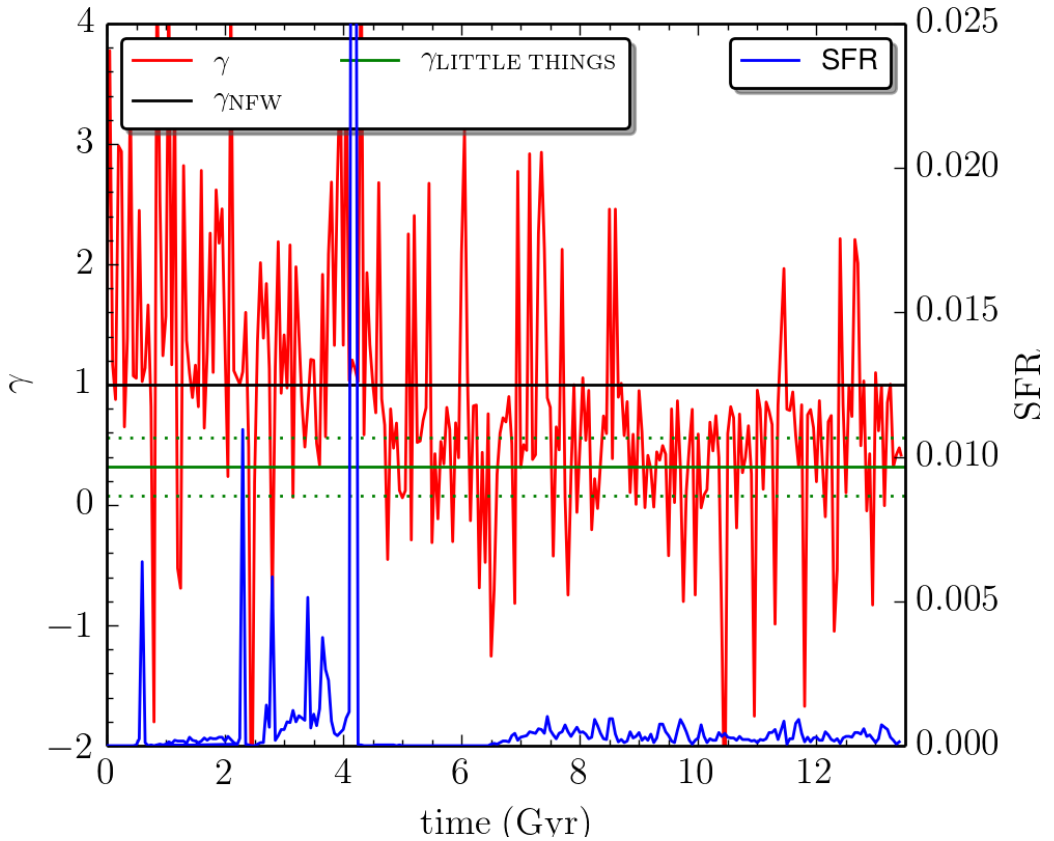
Figure 4.12: Analogous to Fig. 4.11 but for the case of MT3.

the central kiloparsec of the seven THINGS dwarf galaxies. They define the inner density slope γ from a fit to the density profile and concluded a value of $\gamma = 0.29 \pm 0.07$ for the THINGS dwarf galaxies sample. In Oh et al. (2011a), the inner density profiles of simulated dwarf galaxies in a cosmological N-body/SPH simulation were reported to have a slope of $\gamma = 0.4 \pm 0.1$. More recently, Oh et al. (2015) determined the mean slope of the 26 dwarfs in the LITTLE THINGS to be $\gamma = 0.32 \pm 0.24$. Here, we find, for instance, that for the inner dark-matter density slope of the haloes with final mass M=2.5×10^9 M$_\odot$ $\gamma = 0.56 \pm 0.27$. In order to explain the different slopes of the equally massive dark matter haloes, we have shown that small star formation peaks, due to repeated minor mergers, are efficient at lowering the slope. Major mergers cause a spike in the star-formation rate but feedback rapidly shuts down star formation, thus limiting the effect on the inner dark-matter density profile slope. This effect happens over all the full mass range but is more pronounced in the more massive models. The resulting shallow gravitational potential probably explains the large effective radii (see subsection 4.3.2.1) and low central velocity dispersions (see subsection 4.3.2.5) observed in some of the simulated galaxies.
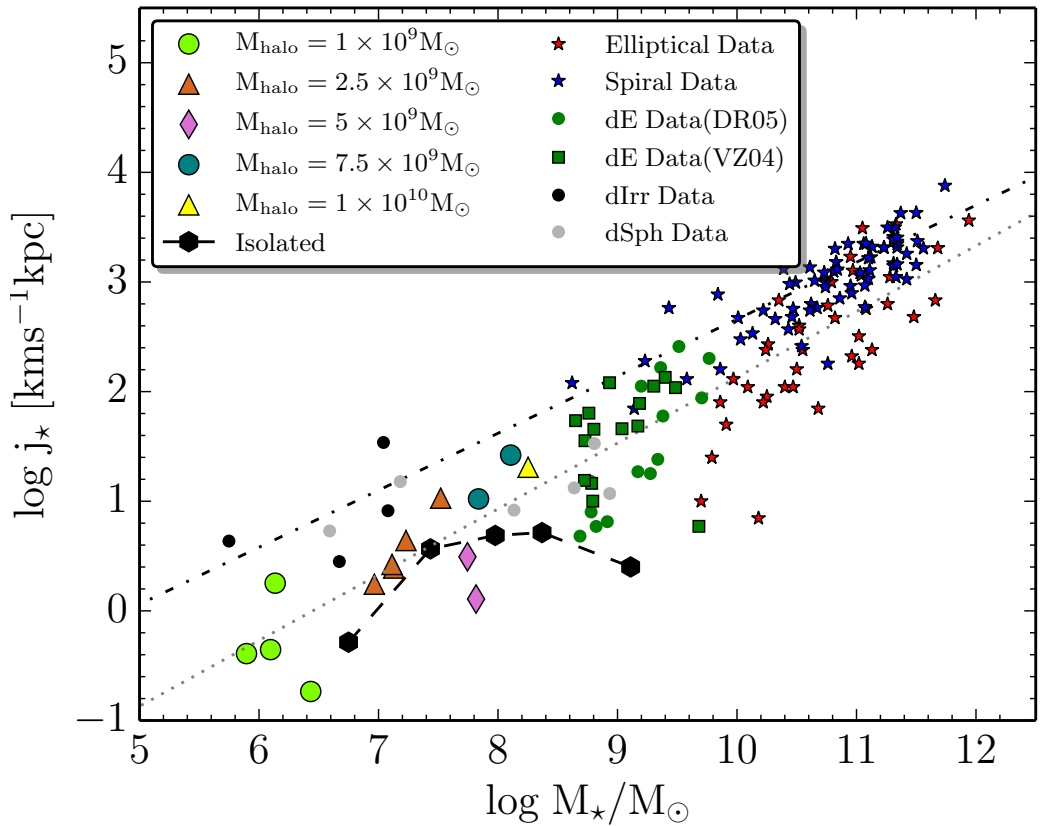
Figure 4.13: The stellar specific angular momentum at the end of the simulations ($z = 0$) as a function of the stellar mass. Observational data of elliptical galaxies and spiral galaxies are taken from Romanowsky and Fall (2012) and a fit to the datapoints is plotted by a respectively the dotted and dash-dotted line. dE data of De Rijcke et al. (2005)(DR05) and van Zee et al. (2004)(VZ04) are plotted next to dIrr data and dSph data from Leaman et al. (2012), Kirby et al. (2012), Kirby et al. (2014), McConnachie (2012), De Rijcke et al. (2006), McConnachie and Irwin (2006), Worthey et al. (2004), and Hidalgo et al. (2013).

4.4.2 Stellar specific angular momentum

Fig. 4.13 shows the specific angular momentum of the stars, $j_\star$, calculated as the length of the vector sum of the angular momenta of all the stars, using the center of mass of the most massive stellar body as a reference point, divided by the total stellar mass, as a function of the stellar mass, $M_\star$, at $z = 0$. The isolated simulations are represented by connected black hexagons, with increasing stellar mass corresponding to increasing halo mass. The merger simulations, shown as indicated by the legend, represent different final masses of the dark matter halo. For comparison, observational data are also plotted. The data of the spiral and elliptical galaxies are taken from Romanowsky and Fall (2012), the observational data of dE from De Rijcke et al. (2005)(DR05) and van Zee et al. (2004)(VZ04) and data for dIrr and dSph are taken from Worthey et al. (2004), De Rijcke et al. (2006), McConnachie and Irwin (2006), Leaman et al. (2012), Kirby et al. (2012), McConnachie (2012), Hidalgo et al. (2013), and Kirby et al. (2014). The simulations have similar specific angular momentum as
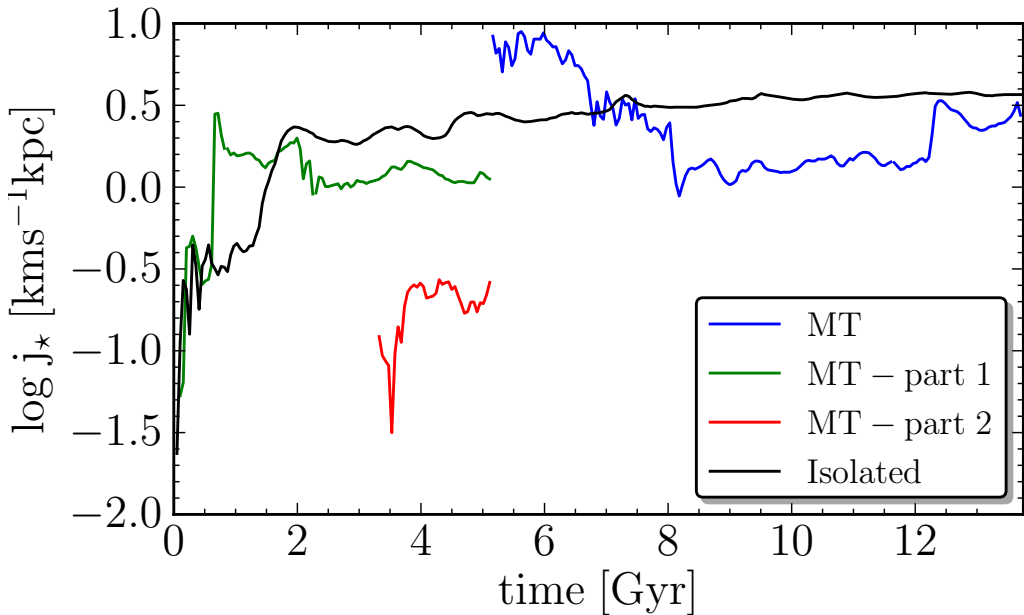
Figure 4.14: The evolution of the stellar specific angular momentum in time for an isolated simulation (dotted line) and for the merger simulation MT4, both with $M_{h,f}=2.5\times10^9 M_\odot$ (black, dark-gray and light-gray line).

the observed dwarf galaxies.

Like the observed galaxies, the simulated galaxies follow a trend of increasing stellar specific angular momentum with increasing stellar mass. At a given halo mass, the scatter on $j_\star$, caused by the different merger histories and star-formation histories, can be as large as an order of magnitude. In particular, merger histories that involve many mergers tend to produce galaxies with small $j_\star$ since the angular momenta of these mergers can cancel each other. Merger trees that involve few mergers have less opportunities for canceling orbital angular momenta and can produce galaxies with high $j_\star$.

In Fig. 4.14 the evolution of the stellar specific angular momentum is shown for an isolated simulation (dotted line) and a merger simulation (black, dark-gray and light-gray line), both with a final halo mass of 2.5×10^9 $M_\odot$.

Isolated galaxies The stochastic nature of star formation is responsible for most of the stellar angular momentum that is created during the first Gyr of the simulation as stars are not created in a perfectly spherically symmetric way. In Fig. 4.14, the black line shows the evolution of the stellar specific angular momentum of an isolated galaxy. During the first Gyr, a large increase in stellar specific angular momentum occurs due to a large star formation peak. In the next Gyr, stars are mainly born out of the turbulent ISM. As the stars inherit the kinematics of the gas particles they are born from, the specific stellar angular momentum will increase. In addition, SNIa feedback asymmetrically accelerates the gas and, as a reaction, affects the stellar motions, increasing the specific stellar angular momentum.

Merged galaxies The evolution of the stellar specific angular momentum for a merger

simulation is plotted in Fig. 4.14. Around 5 Gyr into the simulation, two branches of the merger tree, represented by the green and red line, are put together. The joint system continues as indicated by the blue line. The large increase of $j_\star$ is the result of the vector sum of both the initial $j_\star$s of the branches, together with their orbital angular momentum. The incoming galaxy passes by the main galaxy at ~6.4 Gyrs and starts to return to the main galaxy at ~6.8 Gyr. At 7.8 Gyr it actually merges with the main galaxy, causing a large peak in the star formation rate (see Fig. 4.3). As the SF is centrally concentrated, it will not change the angular momentum much but the stellar mass will increase, resulting in a net decrease of the specific angular momentum. The same happens during the first two SF peaks of MT4 (see Fig. 4.3) at 2 and 2.2 Gyr which correspond to two decreases in $j_\star$ in the dark-gray curve in Fig. 4.14. For this specific merger, the net increase of the angular momentum is matched by the increase in stellar mass, producing only a small change of $j_\star$.

Around 12.3 Gyr there is another flyby of a galaxy which was thus far unable to form stars. When this galaxy enters the dense environment of the main galaxy it starts to form stars. After passing by the main galaxy, it keeps forming stars resulting in an increase of $j_\star$, due to more off-center star formation.

Mergers involving small haloes incapable of forming stars or of triggering a star-formation event when captured influence the stellar specific angular momentum in a more indirect way: their angular momentum is absorbed by the main halo and can later be transferred to newborn stars.

From Fig. 4.13 we conclude that the merger simulations follow the observational trend, e.g. it is in line with the dotted trendline of the elliptical galaxies, which tend to have a lower specific angular momentum than spiral galaxies at a given stellar mass. This is a consequence of the fact that, depending on the orbits of the mergers, their mass ratio, their number, etc., the specific angular momentum *can* be higher in more massive galaxies. In other words: a galaxy that formed through a high orbital angular momentum, late, almost equal-mass merger will end up with a high stellar specific angular momentum.

4.4.3   Kinematics

4.4.3.1   Anisotropy diagram

The ratio of the maximum rotational velocity of the stars, V_{max}, and the central velocity dispersion of the stars, σ_c, is plotted in Fig. 4.15 as a function of the ellipticity $\varepsilon = 1 - \frac{b}{a}$, with b and a the isophotal minor and major axis, respectively. To determine the flattening, the simulated galaxy is first rotated to align the z-axis with its rotation axis. Next, the density is evaluated at the effective radius in the equatorial plane, this isophote's major axis a. Subsequently, the location along the z-axis is determined where the same density is reached, this isophote's minor axis b. From this, the ellipticity of this isophote immediately follows. The maximum velocity is determined as the maximum of the least-square fitted function of the following form to the rotation velocity curve Giovanelli and Haynes (2002):

$$V(r) = a \left(1 - e^{-r/b}\right) \left(1 + c\frac{r}{b}\right). \tag{4.3}$$
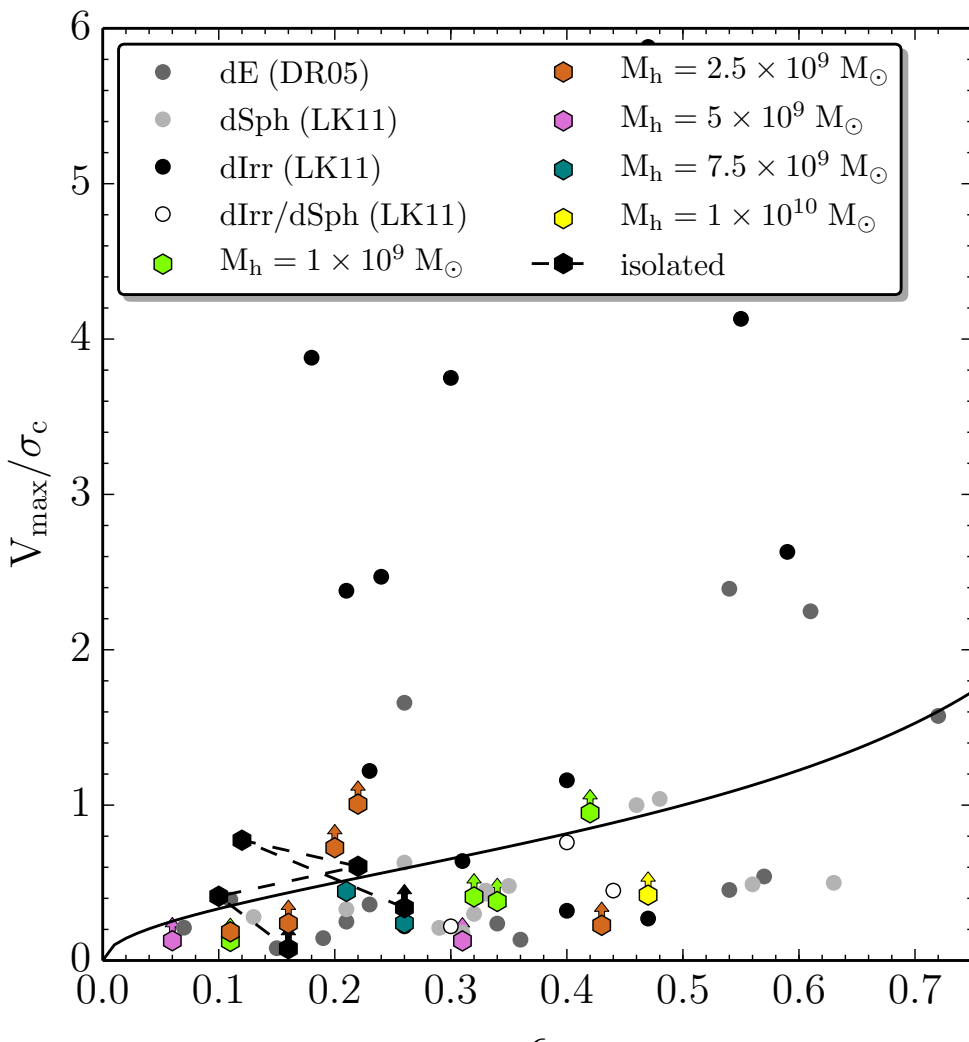
Figure 4.15: (V_{max}/σ_c), the ratio of the maximal rotation velocity of the stars and the central velocity dispersion of the stars as a function of the ellipticity. The simulations at $z = 0$ are plotted together with dE data from De Rijcke et al. (2005), and dSph and dIrr data from Łokas et al. (2011). The black solid line shows the (V/σ) relation for an oblate isotropic rotator. The arrows indicate that the estimation of V_{max} should be considered as a lower limit.

In some cases the rotation curve keeps increasing up to the last data point and the V_{max}-value should be considered as a lower limit. The fitted range that was used depends on the size of the galaxy and was chosen to be around 5 times the effective radius which is in agreement with the 'best range' suggested by Romanowsky and Fall (2012), between 3 and 6 R_e, to calculate the rotation velocity for $j_\star$-estimates.

Fig. 4.16 shows an example of the determination of V_{max}: the rotational velocity profile of an isolated simulation and of a merger simulation, respectively in black and gray. To each profile a fit is made and for the isolated simulation this reaches a maximum while for the merger simulations the fit keep increasing so V_{max} is taken to be the value at $5R_e$. The
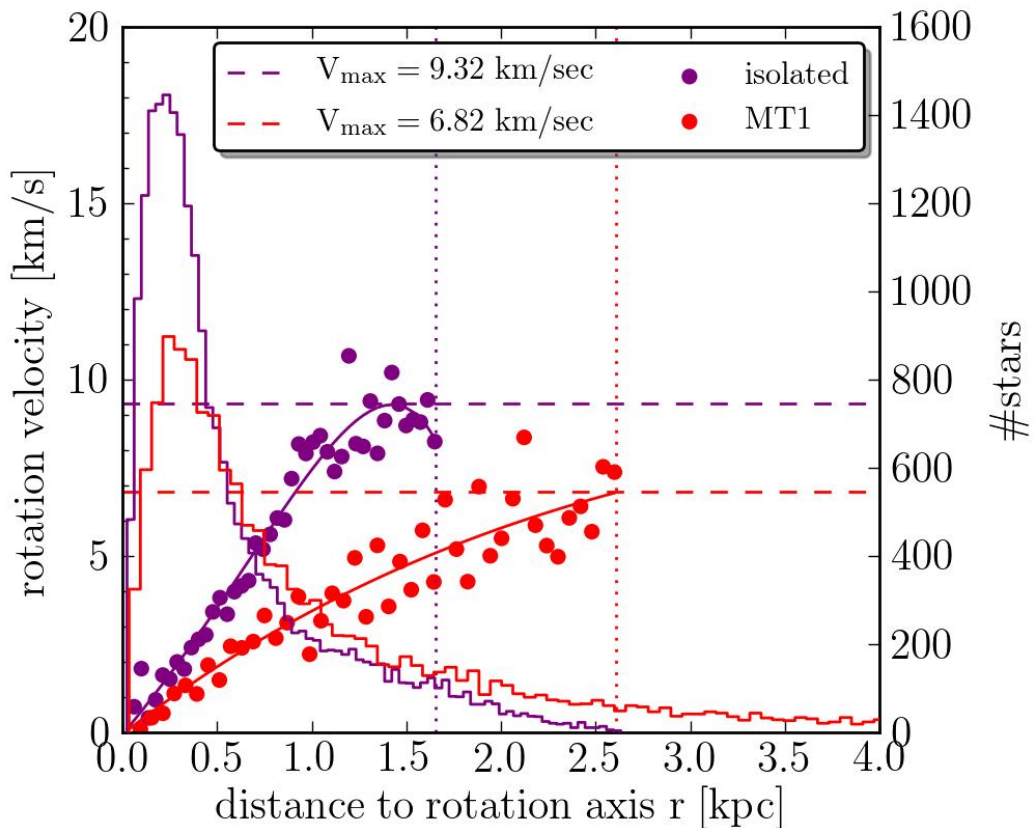
Figure 4.16: The rotation velocity profile and a histogram of the distribution of stars as a function of radius. The dots represent the data of respectively the isolated model in black and of MT1 in gray and the line is the fit to the data. The dotted line indicates the location of $5R_e$ and the dashed line shows the location of V_{max}.

location of $5R_e$ is indicated by the dotted line while the value of V_{max} is shown by the dashed line. The histogram shows the distribution of the stars. In the isolated simulation the stars are more centrally concentrated and most of the angular momenta is located at large radii. In the merger simulations, the stellar body extends much further compared to the isolated simulation.

Most of the simulations are located below the relation for oblate isotropic rotators defined as $(V/\sigma)_{theo} = \sqrt{\varepsilon/(1-\varepsilon)}$ and indicated by the black line in Fig. 4.15. This shows that velocity anisotropy plays a substantial role in stabilizing them. In Table 4.3, the value $(V/\sigma)^\star$ is shown for the simulations, this is the ratio of V_{max}/σ_c and the theoretical value for an isotropic oblate rotator. Hence, a $(V/\sigma)^\star$-value of one corresponds to an isotropic oblate rotator. Most merger simulations have $(V/\sigma)^\star$ values lower then 1. Some of the isolated simulations have $(V/\sigma)^\star$-values much larger than one. However, their maximum rotation velocity is reached by stars at the outskirts of the stellar body, beyond ~ 5 half-light radii. Therefore, for these galaxies, no relation between V_{max}/σ_c and the stellar body's ellipticity is expected.

Cox et al. (2006) found that dissipationless and dissipational (with a gas fraction of 0.4)

binary mergers remnants are located in different locations in the anisotropy diagram, with the former having much lower $(V/\sigma)^*$-values than the latter. The location of the merger simulations agrees with the dissipational binary merger remnants of Cox et al. (2006), which could be expected as our simulations are all gas rich mergers. The merger simulations cover a wider range in ellipticities, between 0.06 and 0.47, compared to the isolated models which have ellipticities between 0.10 and 0.26 indicating that the merger events are efficient in creating flattened galaxies. However, there is no clear connection between the characteristics of the merger tree and the final ellipticity. For example, the merger simulations with a final halo mass of 7.5×10^9 M$_\odot$ have very different merger histories but have almost identical final ellipticities.

4.4.3.2   Shapes - Triaxiality

In Fig. 4.17, the shape diagram of the simulated galaxies is plotted. Each galaxy has first been aligned with the principal axes of its inertia tensor (Franx et al., 1991; González-García and van Albada, 2005; Cox et al., 2006). The order of the three axes is determined from the density profile along each axis, with $c < b < a$. Then, the two axis ratios c/a and b/a are measured similarly to the flattening ε in the previous paragraph: the density is evaluated at the effective radius along the longest axis and those positions along the shortest and intermediate axes are determined where the same density is reached. Oblate spheroids have $b/a = 1$, which puts them on the right vertical axis of Fig. 4.17. Prolate spheroids have $b/a = c/a$ and fall on the diagonal, marked by a black line, in Fig. 4.17.

The isolated models are all quite round, with axes ratio above ~ 0.8. The models with a merger history, on the other hand, can be much more flattened, with axis ratios down to 0.4. Moreover, their shapes can be significantly triaxial. The dashed line in Fig. 4.17 traces the locus of maximum triaxiality, given by

$$\frac{c}{a} = 2\frac{b}{a} - 1,$$ (4.4)

and many merger models indeed end up close to this line. This is at least in qualitative agreement with the flattening distribution analysis of Virgo dwarfs by Binggeli and Popescu (1995). These authors find that the apparent ellipticity distribution of dwarf ellipticals can only be reproduced by adopting a modest degree of triaxiality, corresponding to $b/a \sim 0.8 - 0.9$ (and even smaller b/a-values for later type dwarfs).

4.5   Conclusion

We performed a set of simulations of dwarf galaxies with final masses in the range of 10^9 M$_\odot$ to 10^{10} M$_\odot$. We have shown that simulations based on merger trees constructed by the Parkinson et al. (2008) algorithm and using orbital parameters drawn from the Benson (2005) velocity distributions are a viable and time-saving alternative to full-fledged cosmological simulations. While the simulations presented in this chapter do not take into account all possible effects playing a role in dwarf galaxy evolution, e.g. they lack a cosmological UV background and external gas removing processes, they do allow to investigate the effects of
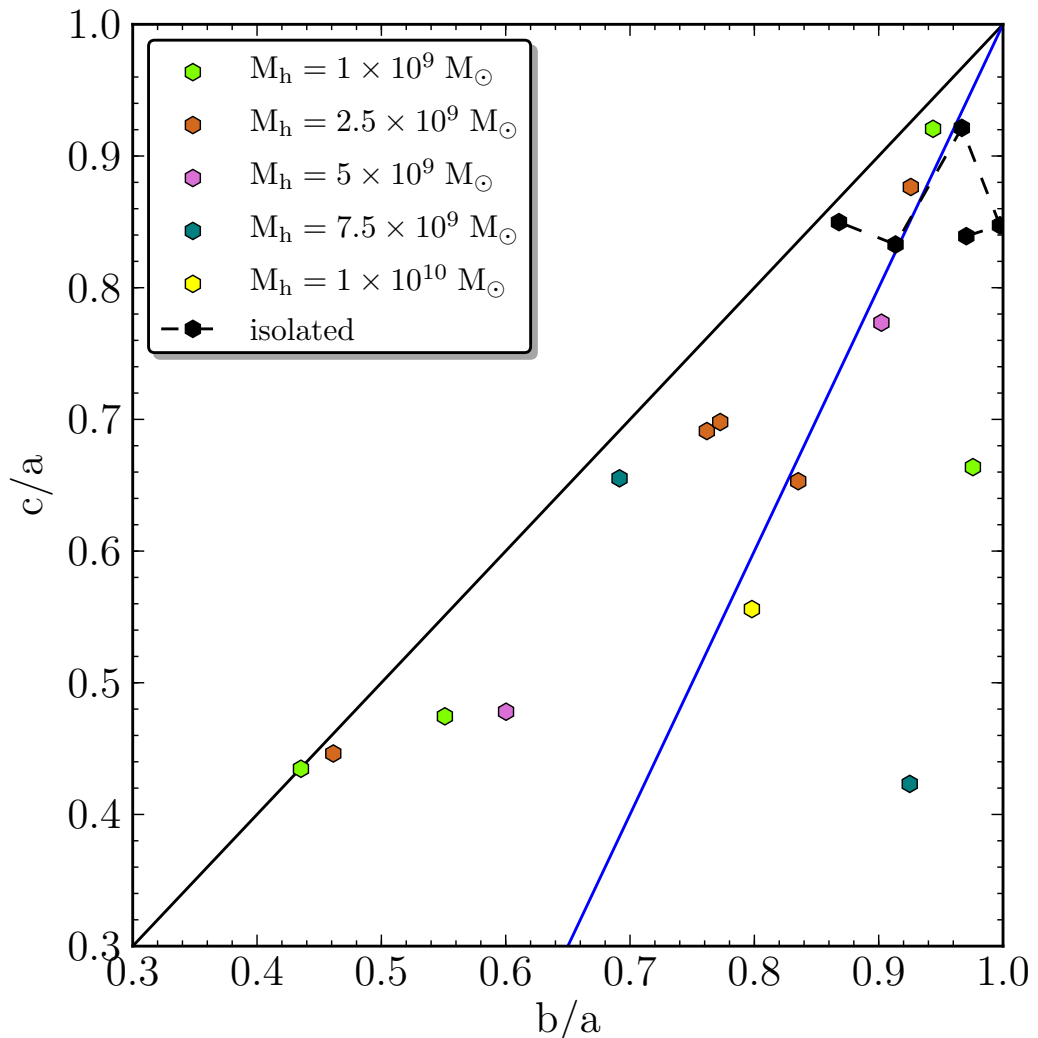
Figure 4.17: The shape diagram where the axis ratio b/a is plotted as a function of c/a with $c < b < a$. The black line corresponds with prolate spheroids which for which $b = c$ while oblate spheroids are located near the $b/a = 1$ line. The dashed line corresponds to the models with maximum triaxiality.

the galaxies' past merger histories on its star-formation history, internal kinematics, and its dark matter density profile.

The implementation of a hierarchical merger history in the simulations introduces more variability into the typically periodic SFR of the isolated simulations. The merger simulations can have short bursts in their SFH which is likely to be unresolved in the observed SFHs of dwarfs. The variability of the SFHs of the simulated dwarfs is in agreement with the complex SFHs that are observed (Skillman et al., 2003; Monelli et al., 2010b,a; Weisz et al., 2011). The star formation histories of the galaxies with a merger history show that their stellar mass is built up more slowly in time compared to the isolated systems.

Mergers can trigger strong star-formation episodes that, through the concerted feedback of

many supernova explosions, can shut down star formation for up to several gigayears. This impulsive removal of gas also contributes to the destruction of the central density cusp of the initial NFW dark matter haloes. Especially in galaxies that grow through a sequence of minor mergers, each one leading to a short burst of star formation, the central dark-matter density cusp significantly flattens over time. The cusp also flattens in isolated galaxies (Cloet-Osselaer et al., 2012) but the effect is much more pronounced when taking mergers into consideration.

Within our merger trees, we consider two main types which have very different influences on their final properties: (i) merger trees with an early massive progenitor that experiences subsequent minor mergers and (ii) merger trees with many small progenitors that merge only quite late. The former generally have shallower dark-matter potentials due to the minor mergers which are more efficient in flattening the cusp in combination with the larger amount of feedback they experience as they have larger stellar mass compared to the other type (at a fixed halo mass). Since there is already a quite massive progenitor present early on, fewer subsequent mergers are required to build up the mass of the final galaxy. This gives less opportunity for the orbital angular momentum of the mergers to cancel, leading to a galaxy with a higher specific angular momentum.

The latter accumulate their mass more slowly, with generally a major merger quite late in the simulation. The dark matter density profile stays more peaked which produces galaxies with smaller half-light radii and higher stellar surface densities. More mergers are required to build up the mass of the final galaxy, giving more opportunity to cancel the orbital angular momentum of the mergers, leading to a galaxy with a lower specific angular momentum.

All merger-tree simulations have shallower dark-matter potentials than isolated models of equal mass and in turn lead to galaxies that have larger effective radii, lower central velocity dispersions, and lower central surface brightness. They generally overlap with the observed dwarfs in diagrams where these properties are presented as a function of luminosity although the trend to become more diffuse with increasing stellar mass is perhaps stronger than in the observational data. The $V - I$ and $B - V$ colours are insensitive to the details of the merger tree. Due to the ongoing star formation, the colours of the simulated dwarfs are bluer than those of dSphs and are more in agreement with those of dIrrs.

Except for the least massive merger models, which tend to be too metal-rich, the merger simulations overlap with the locus of the dSphs and dIrrs in a metallicity versus luminosity diagram. We show that the features in the metallicity distribution functions of merger simulations can also be found in observed dwarfs with similar mean metallicities, like Fornax, LeoI, Sculptor, and WLM.

We compare the final specific stellar angular momentum of our simulations with observational data and conclude that they follow the trend of the observations. Fiacconi et al. (2015) found the same result for the more massive galaxies in the ARGO simulation. The final $j_\star$-value of the merger simulations depends on many variables, such as the orbit of a merger, its mass ratio, the number of mergers etc. For example, a late major merger with high orbital angular momentum will result in a galaxy with a high stellar specific angular momentum. Because of the randomizing effect of the merger history, $j_\star$ can vary by over an order of magnitude at a given mass.

Most models fall below the locus of the isotropic oblate rotators in the $v_{\mathrm{max}}/\sigma_c$ versus

ellipticity diagram. This indicates that they have significantly anisotropic orbital distributions. This is corroborated by their place in the shape diagram of c/a versus b/a, with many merger models being strongly triaxial. This is at least qualitatively in agreement with the observed shapes of dwarf galaxies.

5

Recent work

5.1 New cooling and heating curves

In the previous chapters we showed the results of simulations that did not include the effects of reionization. Recently, our simulation code was extended with new cooling and heating curves that include the effects of an ultra-violet background.

De Rijcke et al. (2013) calculated new tables of radiative cooling and heating rates depending on the following five parameters: gas temperature (T), density (ρ_{gas}), composition (Fe and Mg content) and redshift (z). For the cooling they take into account the following processes: the inverse Compton cooling off the cosmic microwave background and cooling by radiative free-free, free-bound, and bound-bound reactions between electrons and ions. In addition, they included ionization and heating by the cosmic UV background from Faucher-Giguère et al. (2009) and by the interstellar radiation field of Mathis et al. (1983) in a modified version of ChiantiPy. ChiantiPy is a python interface to the CHIANTI atomic database for astronomical spectroscopy (Dere et al., 1997; Landi et al., 2013) and provides electron collision ionization and recombination rates. The modified version is equipped with hydrogen and proton collision ionization rates, photo-ionization rates, charge-exchange reactions, and a new solver for the ionization equilibrium. In addition, a form of self-shielding is implemented to account for the neutral hydrogen that absorbs the UV radiation and prevent the gas from heating. This self-shielding is approximated by exponentially suppressing the H-ionizing part of the cosmic UV background for HI densities above a density threshold for self-shielding,

which is set to 0.007 cm^{-3}.

These new cooling and heating curves to which we will refer in the following as 'new' cooling, are implemented in our adapted version of the Gadget-2 code and they are an improvement compared to the previously used cooling curves (see subsection 2.3.3), to which we will refer in the following as 'old' cooling. The new cooling takes into account the UV background (UVB). Wiersma et al. (2009) argued that the collisional ionization approximation might not be valid anymore when the UVB is taken into account. Therefore, the ionization equilibrium is now calculated within the modified version of ChiantiPy.

In addition, De Rijcke et al. (2013) discussed the iron abundance ratios alone to be a poor quantifier for the metal content of dwarf galaxies. The cooling curves from Sutherland and Dopita (1993) assume the solar neighborhood's chemical enrichment history, which is different from the chemical enrichment history of dwarf galaxies, which have low metallicities and low [α/Fe]. In De Rijcke et al. (2013) a simplified chemical-evolution model is proposed with a 'fast' contribution to the elemental yields due to SNII and massive intermediate-mass stars (IMS) and a 'slow' one due to contribution from SNIa and less massive IMS. Hence, we follow the iron abundance [Fe/H] to trace the overall metallicity and [Mg/Fe] to quantify the α-enhancement which is mainly produced by SNII explosions compared to SNIa explosions. De Rijcke et al. (2013) showed that this simple model is able to adequately predict the abundances of the other elements based on these two parameters.

Additionally, Vandenbroucke et al. (2013) showed that with this improved treatment of ionization, the partially ionized gas will have an internal potential energy reservoir caused by the small amounts of potential energy from ion-electron pairs. In the multicomponent, optically thin ISM this breaks the linear dependence of the internal energy on temperature and as a consequence, the 'entropy formulation' that was originally used in Gadget-2 no longer holds and was replaced by the 'energy equation'. Fig. 5.2 shows in the left panel the dependence of the specific internal energy on the temperature when taking the potential energy reservoir into account (black line) and when not taking it into account (gray line). This shows that there is no longer a linear relation between temperature and the internal energy. The right panel shows the adiabatic index as a function of temperature which can be determined from the temperature derivative of the internal energy and is shown not to be constant as a function of time. Whereas in the previously used version of Gadget-2 with the entropy equation, the adiabatic index was fixed to 5/3.

A 5D interpolation routine depending on temperature, density, redshift, [Fe/H] and [Mg/Fe] is implemented in our simulation code to retrieve the cooling and heating rates and the ionization equilibrium. We expect this to better represent the behavior of the interstellar gas. Additionally, the entropy formulation was replaced by the energy formulation and the gas temperature is linked to the internal energy using the obtained ionization equilibrium.

In the following, we will discuss the effect of these new cooling curves on our models. Figure 5.3 shows in the upper panel the SFH and in the lower panel the cumulative stellar mass of a model with M_h=2.5 10^9 $M_\odot$ with the 'old' cooling curves represented by the green line. The blue line shows the SFH/cumulative stellar mass of a similar model with the 'new' cooling. Additionally, the total SFH and cumulative stellar mass of a branch of MT3 (originally with $M_{h,f}$= 2.5 10^9 $M_\odot$, but the branch has a final mass of $M_{h,f}$=8.19 10^8 $M_\odot$) is shown by the cyan line for the old cooling and by the magenta line for the new cooling in respectively the upper and lower panel. The simulation of the merger tree branch did not run until $z = 0$, but
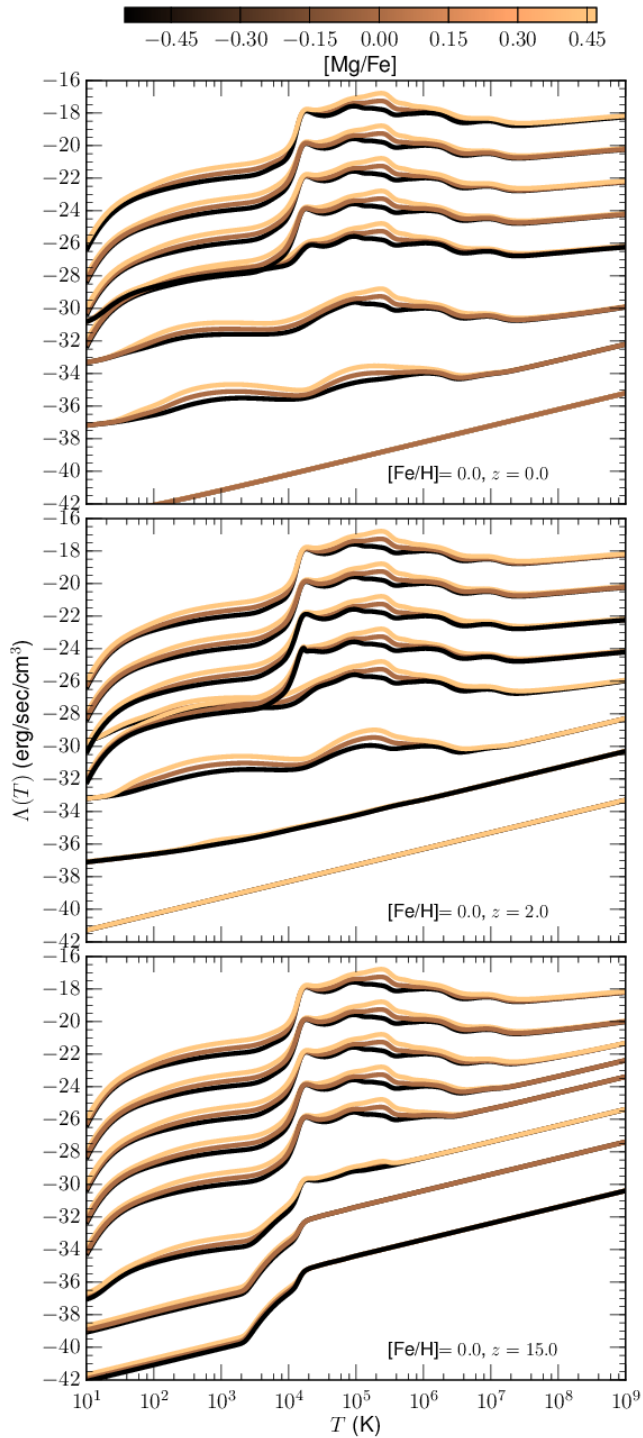
Figure 5.1: The logarithm of the cooling rate as a function of temperature for fixed [Fe/H]=0, and for $z = 0$ (top panel), $z = 2$ (middle panel) and $z = 15$ (bottom panel), plotted for different densities (from the top curve downwards: $n_H = 100, 10, 1, 10^1$, 10^2 , 10^4 , 10^6 , 10^9 cm^3) and [Mg/Fe]-values (color code). Figure from De Rijcke et al. (2013).
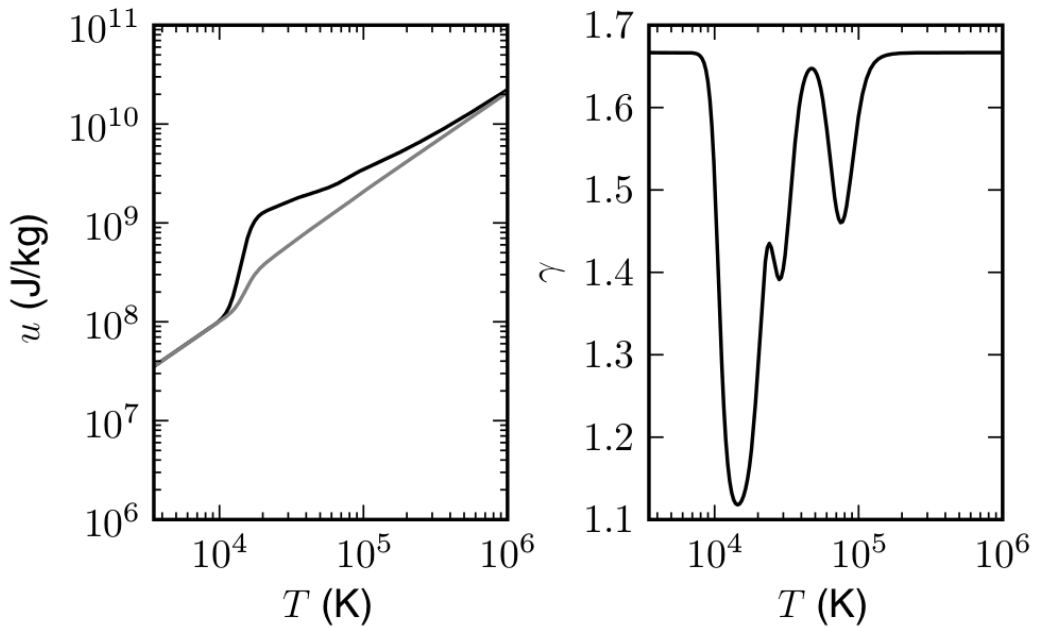
Figure 5.2: The left panel shows the specific internal energy as a function of the temperature for a gas consisting of 92% H and 8% He. The gray line shows the internal energy when not taking into account the internal potential energy reservoir. The right panel shows the adiabatic index as a function of temperature. Figure from Vandenbroucke et al. (2013).

the 7 Gyrs that are shown are sufficient to compare the general trends of the simulations. The simulations of the isolated model with the new cooling is still running, however, the last 0.6 Gyr, no new stars have been formed.

The implementation of the UVB did introduce major changes to our simulations: while the simulations with the 'old' cooling show some moderate star formation from 4 Gyr up to the end of the simulation after the initial peak in the first 1.5 Gyr, the simulations with the 'new' cooling form most of their stellar mass in the first 1.5 Gyr after which the lack of cold and dense gas prevents further star formation. In the less massive merger tree branch, star formation is completely shut down after 1.5 Gyr, whereas in the more massive model, very little star formation can occur in the first 3 Gyr. As there were quite some new elements in the new cooling and heating curves it was not clear what was causing the shutdown of star formation. SNIa feedback was considered as a possible mechanism as the feedback energy of the first SF episode, which is larger due to more efficient cooling at high z, is released explosively (i.e. during a period of 0.33 Gyr) with a delay time of 1.5 Gyr after they are born, in agreement with the timescale of the shutdown of star formation. We tested if this feedback could be able to expel all the gas of the main galaxy. However, as our low mass models also experienced the same effect and after we updated our release of SNIa energy Strolger et al. (2010), where SNIa is not "prompt" released, it became clear that this was not the main cause. The time at which the gas removal happens corresponds to time the UVB gets a quite large influence on the heating and dispersing of the gas content of the galaxy. As a consequence of this, the models with the 'new' cooling have a lower final stellar mass compared to the corresponding models with the 'old' cooling.
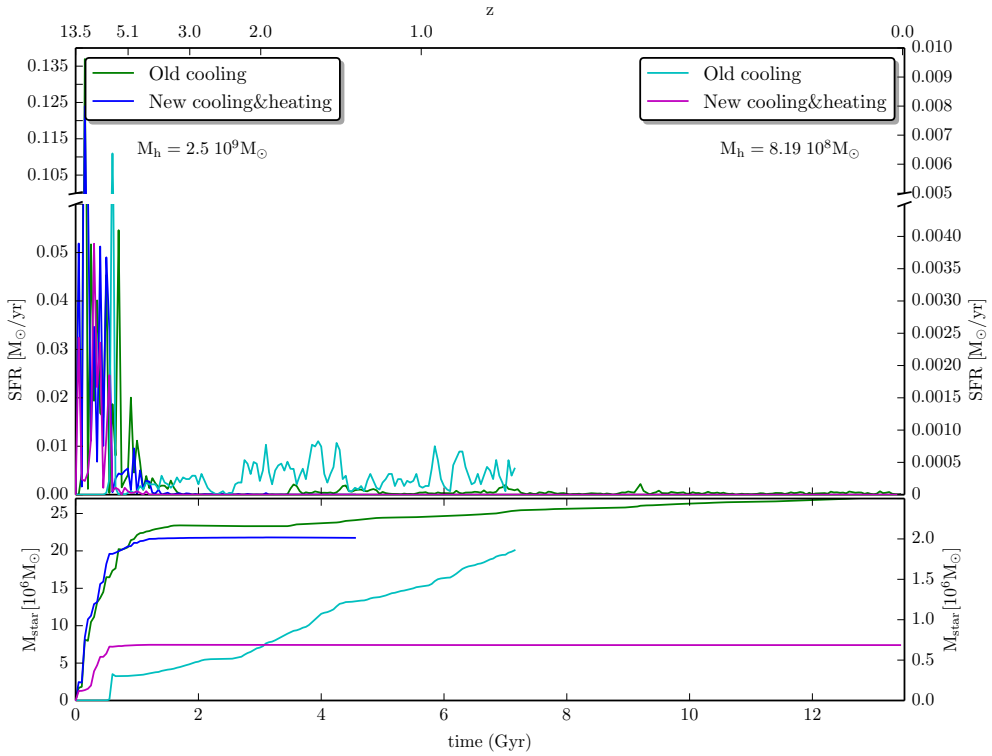
Figure 5.3: The SFH of an isolated model with $M_h = 2.5\ 10^9\ M_\odot$ and a branch of a merger tree with final mass of $M_h = 8.19\ 10^8\ M_\odot$ with the old cooling curves (respectively green and cyan line) compared to the new cooling and heating curves of De Rijcke et al. (2013) (respectively blue and magenta line).

Fig. 5.1 shows a set of cooling curves for a fixed [Fe/H]=0, decreasing gas densities, with more efficiently cooling when the gas is denser, different [Mg/Fe]-values indicated by the color scale and for different redshift in the different panels. They illustrate that for the 'new' cooling curves the contribution of the UVB is very small at high redshifts (i.e. the bottom panel of Fig. 5.1 for $z = 15$) and as a consequence, the cooling is mainly determined by the inverse Compton scattering which has a $(1 + z)^4$-dependence, but only starts modestly from $\sim 2\ 10^3$ K due to some ionization electrons from ions with small ionizing potentials and starts fully from 10^4 K when H is not fully recombined anymore. Hence, the gas cools more efficient at high redshifts and the gas halo will collapse earlier and star formation will start earlier. This is less clear in the case of the halo with M_h=2.5 10^9 $M_\odot$, but in the case of the branch of MT3, the four subhaloes with halo masses of respectively 1.49 10^8 $M_\odot$, 1.95 10^8 $M_\odot$, 3.54 10^8 $M_\odot$, 8.19 10^8 $M_\odot$ are all unable to cool enough and collapse to ignite star formation until they merge around 0.5 Gyr. Whereas the two most massive subhaloes are able to ignite star formation at 0.05 Gyr in the simulations with the 'new' cooling and the two less massive subhaloes start forming stars around 0.15 Gyr, far before they are really merge.

The lower panel of Fig. 5.3 shows that the build-up of stellar mass is quite similar in both models with M_h=2.5 10^9 $M_\odot$ in the first 1.25 Gyr as the UVB increases with time (and

peaks around $z = 2$) and the galaxy is still protected by self-shielding. During this time, star formation is self-regulated by the interplay of the star formation criteria and dilution of the ISM by stellar feedback. After 1.25 Gyr the UVB is able to heat and disperse the gas halo making star formation impossible.

Fig. 5.4 and Fig. 5.5 shows the total SFH of mergers with a final halo mass of M_h=2.5 10^9 $M_\odot$ and with a merger history according to respectively MT2 and MT3. In green/black the results are shown for the merger run with the new cooling, a high density threshold for star formation is used, n_{SF}=1000 cm^{-3}. The blue/magenta line show the corresponding simulation with the old cooling and with a lower density threshold of n_{SF}=10 cm^{-3}. We see that the models with the new cooling curves form more stars during the first Gyr compared to the models with the old cooling. Due to more efficient cooling at high z, there are progenitors that did not form stars in the simulation with the old cooling curves, that now do form stars. But due to their low masses, they will be faster influenced by the UVB and will not have the gas supplying role they had in the simulations with the old cooling. This partially destroys the wide range of different SFH we saw in chapter 4 and which we discussed to be present in the observations of dwarf galaxies. In the outlook in chapter 8 I will propose some processes that
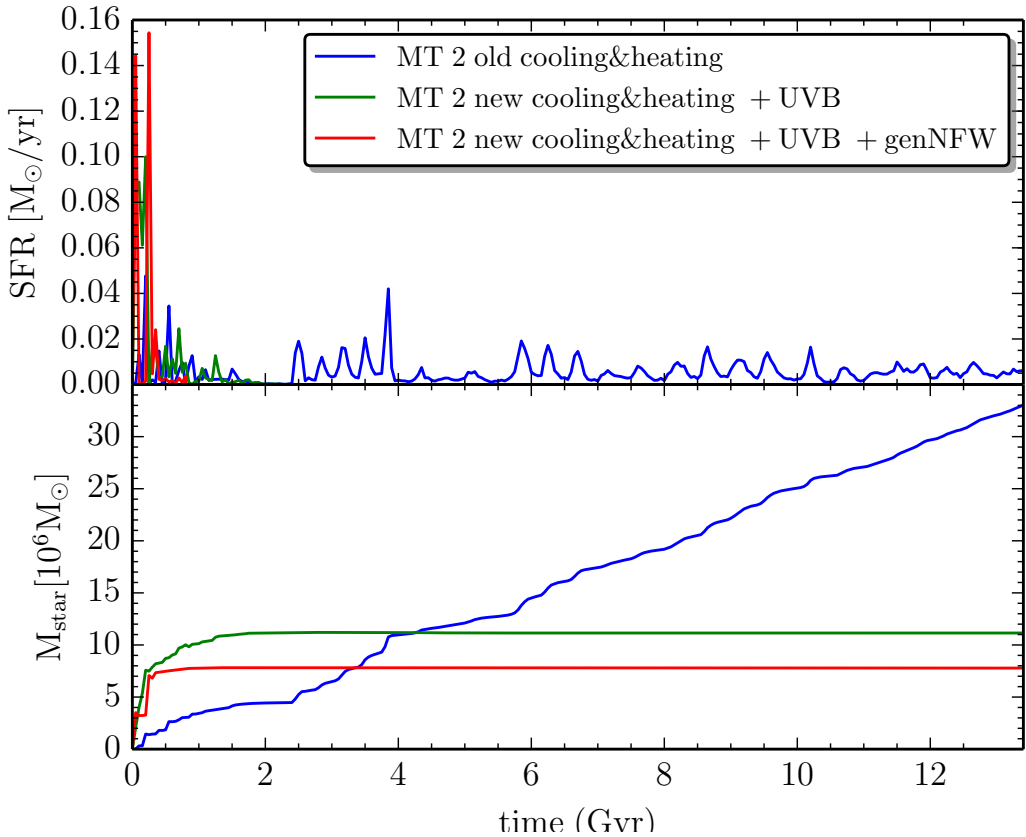
Figure 5.4: The total SFH of MT2 with a final halo mass of 2.5 10^9 $M_\odot$ and a high density threshold for star formation, n_{SF}=1000 cm^{-3}. The green line shows the SFH of the re-simulated MT2 with the new cooling and heating curves. In the case of the red line, the GenNFW DM density profiles (see section 5.2) are used for the progenitors with masses lower then 10^9 $M_\odot$.
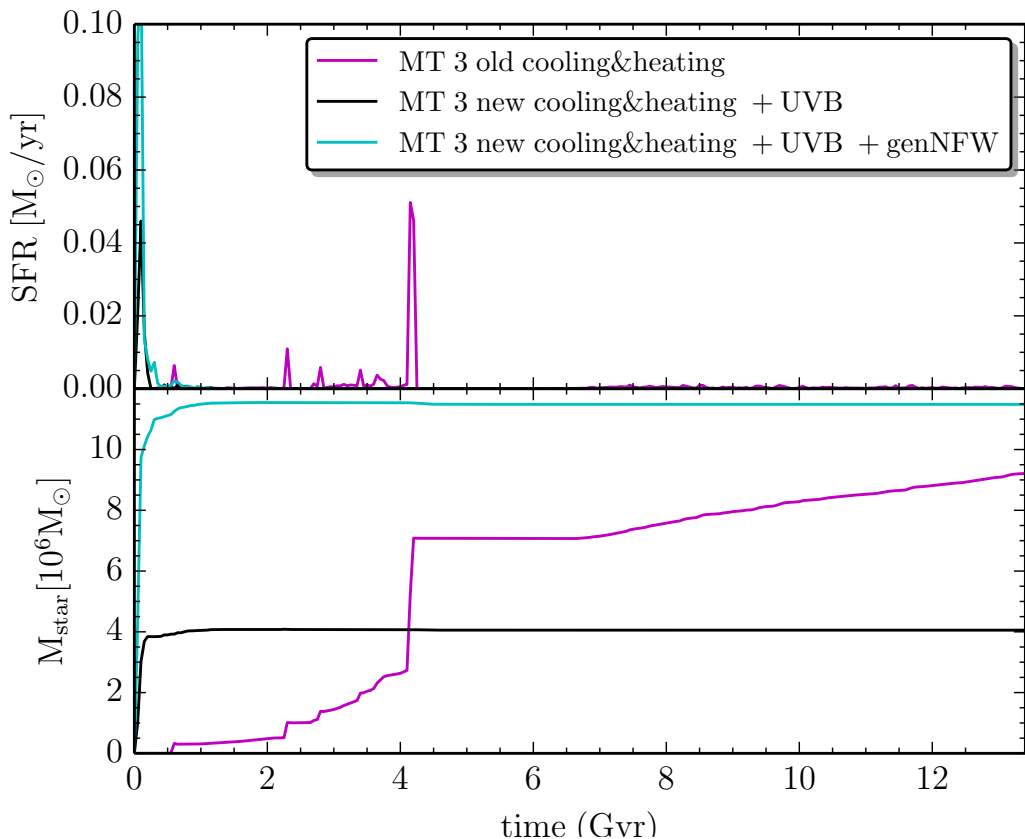
Figure 5.5: Similar to Fig. 5.5 but for a merger history according to MT3.

are currently under investigation in our dwarf galaxy group to obtain again a more variable SFH, which comes down to lowering the initial peak of star formation in the first Gyr of the simulation and of enabling star formation later on in the simulation.

We can conclude that the new cooling curves have an influence on the start of the star formation as the cooling is more efficient and the UVB is negligible at high z. Additionally, the UVB has a large impact on the simulations as the models are almost completely deprived of their gas content in time as they are heated by the UVB. Generally, this implies that the final stellar mass is reduced.

5.2 General NFW haloes (GenNFW)

Cosmological simulations produce dark matter haloes with NFW profiles at $z = 0$. Hence, using a NFW profile as an initial condition for our individual models is legitimate when starting from not too high redshifts as we might assume the haloes to have a NFW profile by that time. Gao et al. (2008) looked at the dependence on redshift and halo mass of the density profiles of massive relaxed dark matter haloes ($M_h \geq 3 \ 10^{11} \ h^{-1} \ M_\odot$) in large cosmological simulations. They showed halo concentrations to depend only weakly on halo mass where this dependence decreases with increasing redshift, in agreement with Zhao et al. (2003a) for

masses in the range of 10^{10} up to 10^{15} h^{-1} $M_\odot$. This suggests that halo densities reflect the density of the universe at the their formation time. Extending this relation to lower massive haloes should be done with care as Zhao et al. (2003b) showed that the concentration is not only a function of a (=$1/(1+z)$), the scale factor of the universe, but also connected to the mass growth rate, i.e. the faster the mass grow, the slower c increases.

However, Cen et al. (2004) found in very high resolution tree particle-mesh N-body simulations (Bode and Ostriker, 2003) that dark matter haloes in the mass range $10^{6.5}$-$10^9 M_\odot$ might not have a universal dark matter profile at redshifts in the range of $z = 6 - 11$.

They propose a variant of the NFW profile which depends on mass and redshift:

$$\rho(r) = \frac{\rho_0}{(r/r_{-2})^\alpha (1 + r/r_{-2})^{4-2\alpha}} \tag{5.1}$$

which reduces itself to a NFW profile for $\alpha = 1$. The r_{-2} radius is defined as the radius where the logarithmic slope of the density profile is -2 and is different from the scale radius r_s we defined for the NFW. The value of α and r_{-2} is drawn from respectively the Gaussian distribution function and a log-normal function:

$$P(\alpha) = \frac{1}{\sqrt{2\pi}\sigma_\alpha} \exp\left(-\frac{(\alpha - \alpha_0)^2}{2\sigma_\alpha^2}\right) \tag{5.2}$$

$$P(r_{-2}) = \frac{1}{r_{-2}\sqrt{2\pi}\sigma_{r_{-2}}} \exp\left(-\frac{(\ln r_{-2} - \ln r_{-2}^0)^2}{2\sigma_{r_{-2}}}\right) \tag{5.3}$$

where r_{-2} is given in units of r_{vir}, the virial radius, defined as the radius at which the average density equals 200 times the critical density of the universe at a certain redshift. Cen et al. (2004) provided us with values for $\alpha_0(M_h,z)$, $\sigma_\alpha(M_h,z)$, $r_{-2}^0(M_h,z)$ and $\sigma_{r_{-2}}(M_h,z)$ for three mass bins and four redshift bins. For each parameter, we fitted the following function through these datapoints depending on the mass and the redshift:

$$f(M,z) = a(1+z)^b \left[\frac{M}{10^7 M_\odot}\right]^{(1+z)c} \tag{5.4}$$

With this fitting function we can easily get the values of these parameters for different masses and redshifts and use them to randomly sample the values of α and r_{-2} from the distribution functions 5.2 and 5.3.

Fig. 5.6 compares the dark matter density profile of two haloes with identical mass, i.e. 0.9 10^9 $M_\odot$. The red and blue dots show respectively the more centrally concentrated NFW halo and the GenNFW halo which has a more shallow inner slope. The GenNFW halo has a value of 0.85 for the inner slope α and 0.54 kpc for r_{-2}, which are extracted from the distribution functions 5.2 and 5.3. The theoretical density profiles are overplotted as solid lines in the corresponding colour. The cyan dots represent the density profile of the gas which is sampled according to a pseudo-isothermal profile for the corresponding NFW dark matter halo. The green dots show the density profile of the gas which is distributed according to a scaled version of the GenNFW profile. It is sampled with similar techniques as the dark matter halo (see Appendix A.2) but with the following density profile:

$$\rho_{gas}(r) = 0.2115\rho_{DM}(r) \tag{5.5}$$

with $\rho_{DM}(r)$ see Eq. A.19
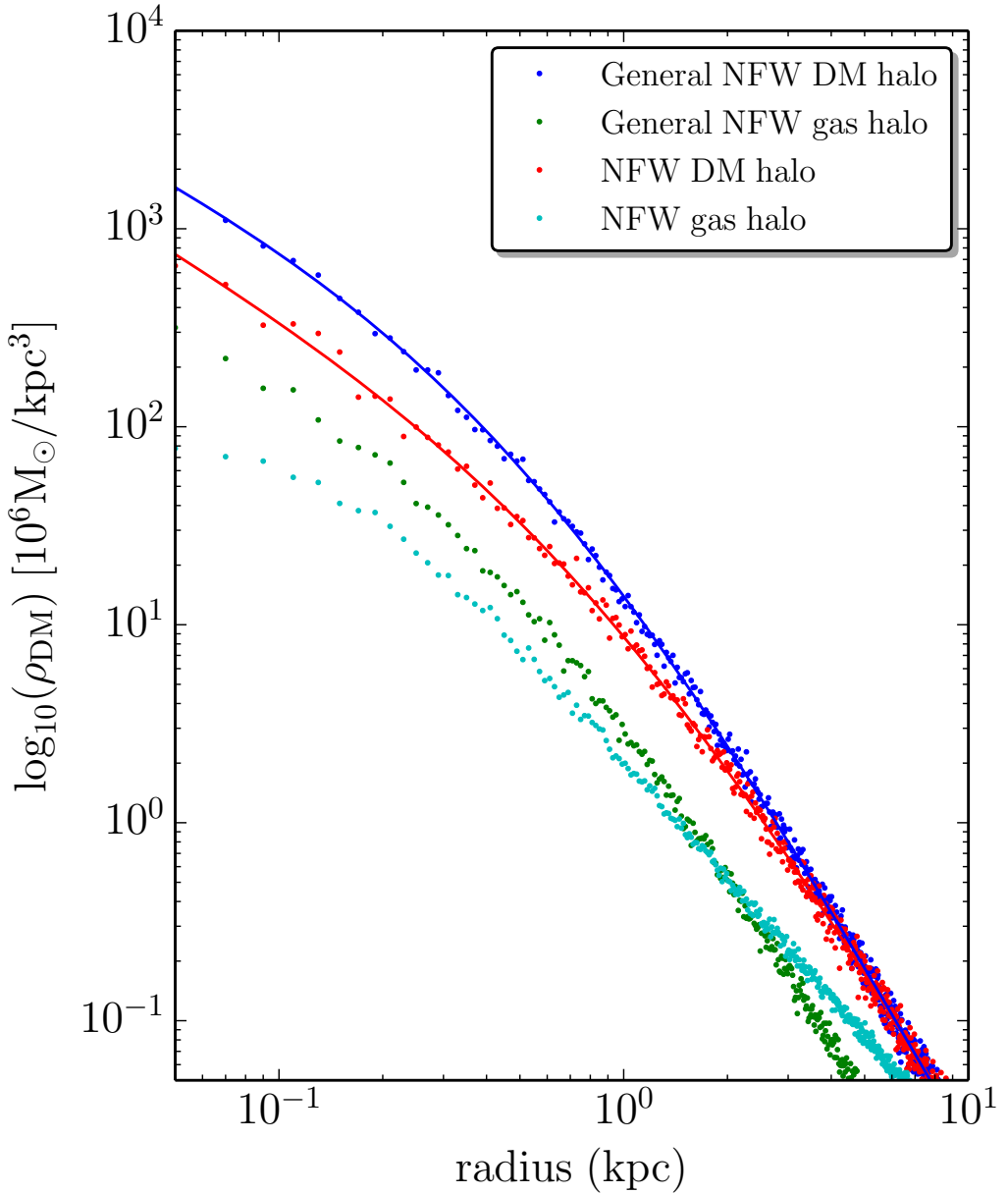
Figure 5.6: Comparison of the dark matter halo profiles of a NFW halo (red solid line, see Eq. 2.8) and of a general NFW halo (blue solid line). The corresponding coloured dots show the density profile deduced from the sampled halo and the solid line. Both haloes with a halo mass of $0.90 \, 10^9 \, M_\odot$. The cyan and green dots show respectively the pseudo-isothermal gas sphere (see Eq. 2.9) of the NFW halo and the scaled gas sphere of the general NFW halo.

Fig. 5.7 shows the star formation history of two simulations with the same halo mass, $M_h = 0.9 \, 10^9 \, M_\odot$, and density threshold for star formation, $n_{SF} = 1000 \, \mathrm{cm}^{-3}$, but with different density profile for the dark matter and the gas. As a result of the higher inner density of the gas
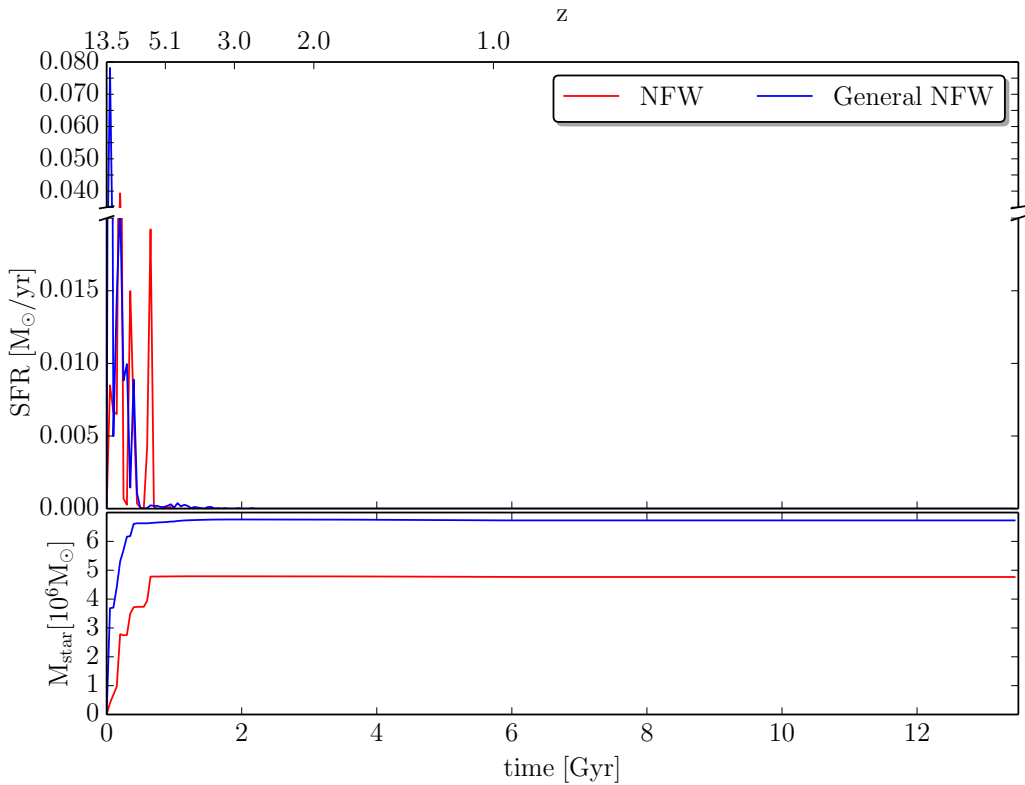
Figure 5.7: The SFH of the simulations with NFW halo and pseudo-isothermal gas sphere (red line) compared to the GenNFW halo with scaled gas halo (blue line).

halo of the GenNFW (see Fig. 5.6), the density criterium for star formation will be reached sooner compared to the NFW where the pseudo-isothermal gas halo needs more time to collapse to reach such densities, e.g. in the simulation with the NFW density profile, the first star is born at 0.022 Gyr in the simulation where for the GenNFW density profile, the first star is already born at 0.009 Gyr. As a consequence, the GenNFW generates more stars in the first epochs compared to the NFW and has a larger final stellar mass. In addition, due to the higher inner densities of the gas, the ISM of the GenNFW is more protected against the UVB by self-shielding. Hence, star formation is shutted down earlier in the case of the NFW compared to the GenNFW where there is some small amount of star formation up until 1.75 Gyr.

Fig. 5.4 and Fig. 5.5 shows the total SFH of mergers with a final halo mass of $M_h=2.5$ 10^9 $M_\odot$ and with a merger history according to respectively MT2 and MT3. In green/black and red/cyan, the results are shown for the merger run with the new cooling and heating curves discussed in section 5.1, a high density threshold for star formation is used, $n_{SF}=1000$ cm^{-3}, and where the subhaloes are constructed respectively with a NFW and a GenNFW profile and the gas is respectively distributed according to a pseudo-isothermal density profile and a density profile scaled to the GenNFW density distribution. The simulation of MT3 with GenNFWs produces much more stars compared to the simulation with NFWs. We see the similar trend as seen in the isolated case: the simulations with a less cuspy dark matter density profile will produce more final stellar mass. The opposite is true for the simulation

of MT2: the final stellar mass of the simulation with GenNFW is lower then for the original NFW. In the SFH, we see that the initial peak of the simulations with GenNFW is larger in accordance with our hypothesis for the isolated case, this initial peak probably introduces more feedback which shuts down the star formation for a short time after which we see again a peak in the star formation. This effect is not seen in MT3 as the stars are formed in the more, smaller haloes.

We can conclude that the use of the GenNFW density profiles in isolated simulations results in models that have generally higher stellar masses at the end of the simulation. This is mainly caused by the less cuspy density profile of the dark matter halo and the accordingly scaled gas. As a consequence, the inner density of the gas sphere is higher in the case of the GenNFW compared to the pseudo-isothermal gas sphere and the density threshold is reached faster in the case of the GenNFW. In the case of simulations with a merger history, the total star formation is driven by self-regulation before the UVB depletes the gas content and shuts down the star formation and the final stellar mass depends on the amount of stars that have been formed by that time.

5.3 Color Magnitude Diagram (CMD) and star formation histories

Because we like to validate our simulations with observations, we will now focus on the star formation histories (SFHs) which describe the number of stars formed as a function of time. It is straightforward to generate these from our models, as we know the mass of a stellar particle and when it was created. The observationally deduced SFHs are generally constructed from the synthetic CMD that most closely reproduces the observations. This synthetic CMD is created through Monte Carlo simulations that use theoretical stellar evolution tracks to select different sets of initial conditions. More information about the creation of synthetic CMDs can be found in a review paper of Cignoni and Tosi (2010). More particularly, we would like to compare our simulations with the results from the LCID ACS team who obtained very deep CMD data for a small set of dwarf galaxies.

With our code, we can construct color magnitude diagrams in the opposite manner as done for the observations: we have a set of SSP's (single age, single metallicity) particles and for each SSP we retrieve the corresponding isochrone from a bilinear interpolation between the age and metallicity of a set of isochrones. We use the BaSTI isochrones (Pietrinferni et al., 2004) which cover a range of $0.0001 \leq Z \leq 0.04$ for metallicity (i.e. the mass fraction of the initial heavy elements abundance), a range of $0.245 \leq Y \leq 0.303$ for the yields (i.e. the mass fraction of the initial helium abundance) and a range of ages with increasing timebins starting from 0.03 Gyr up to 13.5 Gyr. Then, we add this isochrone to the CMD grid, by adding the contribution of the number of stars of each mass bin to the corresponding CMD gridpoint. The number of stars in a certain mass bin, N_i, limited by the lower mass limit $m_{l,i}$ and the upper mass limit $m_{u,i}$, is calculated from the SSP's mass according to a Salpeter IMF:

$$N_i = \int_{m_{l,i}}^{m_{u,i}} \Phi(m) dm \frac{M_{SSP}}{\int_{m_l}^{m_u} m\Phi(m) dm} \tag{5.6}$$

Finally, we convolve the CMD grid to mimic the observed CMDs from the LCID papers.

We use the observational errors for the Cetus CMD that are presented in Monelli et al. (2010b) and scale them to correct for the distance between us and IC1613. We convolve each gridpoint with a 2D Gaussian function with variable sigmas σ_x and σ_y, respectively the observational errors $\sigma_{F475W-F814W}$ and σ_{F814W}:

$$f(x,y) = \frac{1}{2\pi\sigma_x\sigma_y} e^{-((x-\mu_x)^2/(2\sigma_x^2)+(y-\mu_y)^2/(2\sigma^2))}$$

(5.7)

μ_x and μ_y are the grid points around which the convolution takes place.

We obtained detailed observational CMDs from the LCID consortium for IC1613 (Skillman et al., 2014). Table 5.3 shows the observational properties of IC1613 and the best resembling merger tree. This merger tree corresponds to MT2 of the models with a final halo mass of 7.5 10^9 $M_\odot$ from chapter 4 for which more properties are shown in Table 4.3.

	IC1613	Merger
D (kpc)	770[a]	n/a
(m-M)$_0$	24.40±0.014[a]	n/a
M_v(mag)	-15.2±0.2[b]	-15.11
$\mu_{0,V}$(mag)	22.7±0.6[c]	24.22±0.40
Stellar mass ($M_\odot$)	10^{8}[d]	1.27×10^8
[Fe/H]	-1.38±0.31[b]	-1.10
R_e (kpc)	~1.4[d]	1.60

[a](Bernard et al., 2010)
[b](Cole et al., 1999)
[c](Bernard et al., 2007)
[d](Skillman et al., 2014)

The observational data and model have comparable stellar mass, V-band magnitude and effective radius. The blue line in the upper panel of Fig. 5.8 shows the evolution of the cumulative stellar mass fraction of the merger simulation. The green and red lines are the results from the analysis of the observed CMD by Skillman et al. (2014), from which they conclude that IC1613 has a continuous star formation rate. They used respectively the IAC method, which is explained in great detail in Hidalgo et al. (2011) in combination with the BaSTI stellar evolution library (Pietrinferni et al., 2004) and the MATCH method (Dolphin, 2012) in combination with the PADUA stellar evolution library (Girardi et al., 2010) to obtain a synthetic CMD that is most closely related to the observed CMD. The SSPs in the synthetic CMD have a Kroupa IMF (Monelli et al., 2010a). The different stellar mass histories obtained by the different methods are partially due to the different stellar evolution libraries that are used and partially due to the different binning and weighting that is used by the different methods. Our model shows a continuous star formation in agreement with the observed star formation history in IC1613 (Skillman et al., 2014). The lower panel of Fig. 5.8 shows the age-metallicity relation of our model (blue line) compared to the observations of (Skillman et al., 2014) (green line).

In Figure 5.9, we compare the metallicity distribution function of our model with the one from Kirby et al. (2013) based on spectroscopically determined metallicities of 125 RGB stars in IC1613 selected from the photometric catalog of Bernard et al. (2007). Compared to the observations, the model has more metal rich stars and a low metallicity tail. The large bin with stars with [Fe/H] = -4.5 is due to the initial metallicity of 10^4 $Z_\odot$ of the gas particles from which star particles are born. These stars enrich the gas resulting in a long low
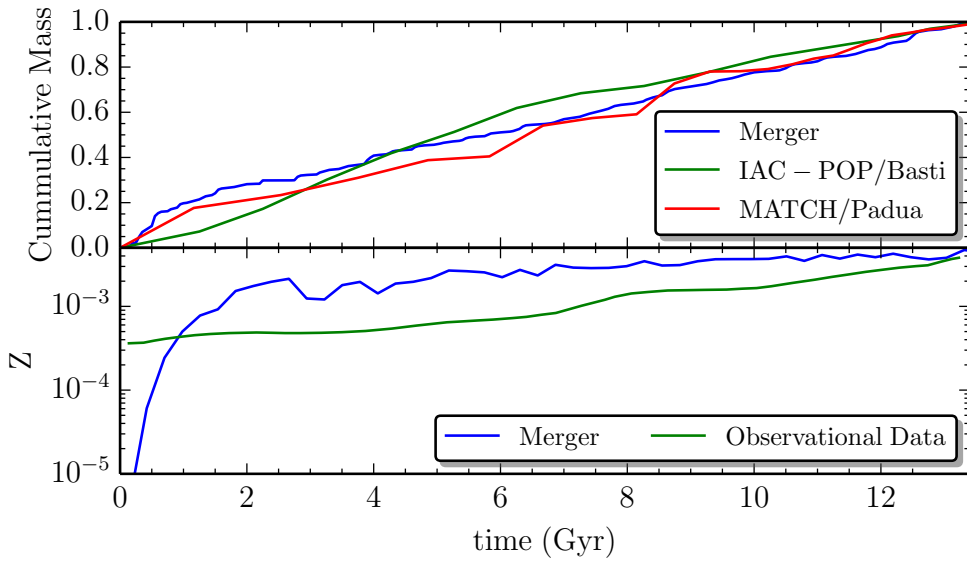
Figure 5.8: Upper panel: The cumulative stellar mass fraction of the model (see Table 5.3) and the observational data from Skillman et al. (2014). The observational data is analyzed with different methods indicated by different colors. The green line shows the solution obtained with IAC-pop using the BaSTI stellar evolution library. The red line shows the MATCH method (Dolphin, 2012) that used the PADUA stellar evolution library from Girardi et al. (2010). Lower panel: the age-metallicity relation of our merger compared to the results of Skillman et al. (2014).

metallicity tail from stars born out of this gas. The model has a mean [Fe/H] that is a little higher than the observations as a result of some more SF in the early evolution (0-2Gyr) that starts the chemical enrichment early on.

Figure 5.10 compares the CMD of our model (left panel) with the observed CMD of IC1613 (middle panel), where the color scale shows the logarithm of the number of stars in the gridded CMDs. The model was normalized to the number of stars in the observational data of IC1613, e.g. 165,573 stars. In the right panel the residuals are shown in units of Poisson errors calculated as $(n_o - n_m)/\sqrt{n_m}$, with n_o and n_m respectively the observed and modeled number of stars in a certain grid point. The residuals are overplotted with two isochrones: (i) the dotted line shows the isochrone of a young star with a metallicity of 20% of the solar metallicity, for which our model is oversampled. Fig. 5.8 shows that there is more star formation within the last Gyr in the simulation compared to the observations. Hence, when refraining the youngest stars (e.g. younger then ∼0.3 Gyr), the residual improves. (ii) The dashed line represents the track of an old very metal-poor star, the RGB is oversampled on the left side and undersampled on the right side. The lowest metallicity isochrone that is used in Skillman et al. (2014) corresponds to 0.00036, when limiting the isochrones down to this metallicity, the contributions shown by the dashed line disappear. The width and location of the RGB is known to be an indication of the metal content as it is more sensitive to metallicity than age (VandenBerg et al., 2006). The mean metallicity of our simulation is higher than the observed mean metallicity, which is visible in the residuals: the right side of the RGB is oversampled (blue) compared to the left side which is undersampled (red) in our model. On the other side, the red clump is undersampled in our model.
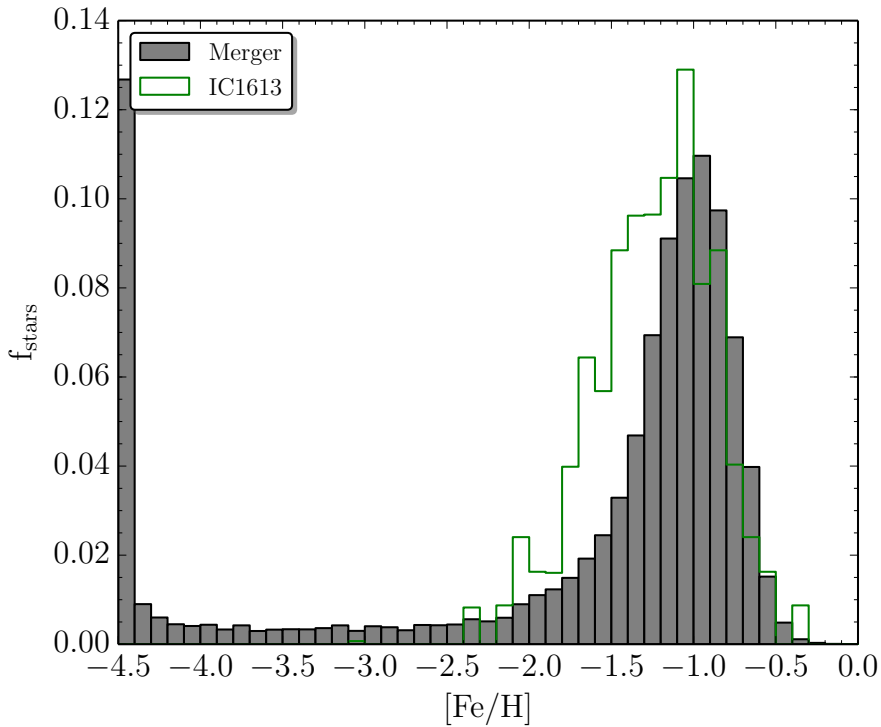
Figure 5.9: The metallicity distribution function of our merger of which the properties are shown in
Table 5.3 compared to the observed metallicity distribution function from IC1613 from
Kirby et al. (2013).

Fig. 5.11 shows the effect of selecting different regions of the galaxy to construct the CMD
by comparing them with the total CMD shown in Fig. 5.10. The CMDs in the upper row
of Fig. 5.11 are constructed with star particles that fulfill the following distance criterion:
(i) left panel: within one effective radius, (ii) middle panel: between one and two effective
radii and (iii) right panel: between two effective radii and 15 kpc. In each panel the fraction
of the 35 628 star particles that is used to construct the CMD is shown. In the lower row
we compare each CMD with the total CMD of our model from Fig. 5.10: the residuals
are shown in units of Poisson error determined as $(n_{tot} - n_{part})/\sqrt{n_{part}}$ with n_{tot} the counts
of the total CMD in a certain gridpoint and n_{part} the counts in the partial CMD in the
corresponding gridpoint. The middle panel is constructed using the largest number of star
particles and is most in agreement with the total CMD. The left panel, shows the CMD
constructed from the innermost stars and the residuals indicate that the model contains
more young stars and fewer old stars compared to the total CMD. From the right panel,
we can conclude that there are more old stars in the outer regions as the residuals show
that their contribution is larger compared to the total CMD. This suggests that there exists
a stellar population gradient in our merger simulation and we assume that it is caused by
the interactions between the protogalaxies that make stars drift away. This effect is similar
as observed in real dwarf galaxies: the gradients are such that the mean age of the stellar
population is younger toward the center of the galaxy. Similar metallicity gradients are also
observed in some real dwarf galaxies (de Boer et al., 2012; Hidalgo et al., 2013).
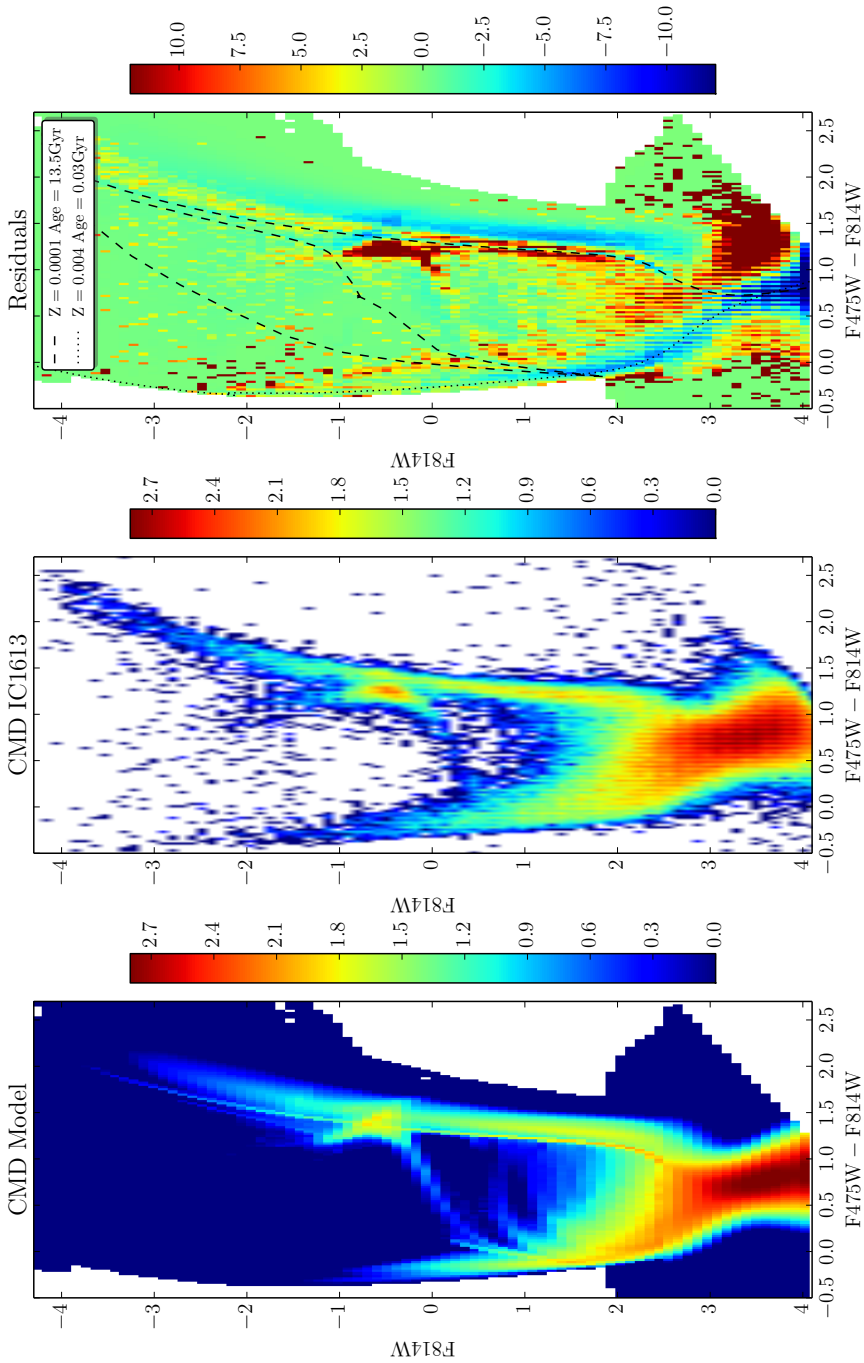
Figure 5.10: The CMD of IC1613 (middle panel) compared to the merger simulation (left panel), see Table 5.3 for its properties. The residuals of these CMDs in Poisson errors are shown in the right panel. In the residual panel two isochrones are overplotted, the dotted line represent a theoretical isochrone from the BaSTI library for a young star with a metallicity of 20% of the solar metallicity. While the dashed line represents the track of an old very metal poor star.
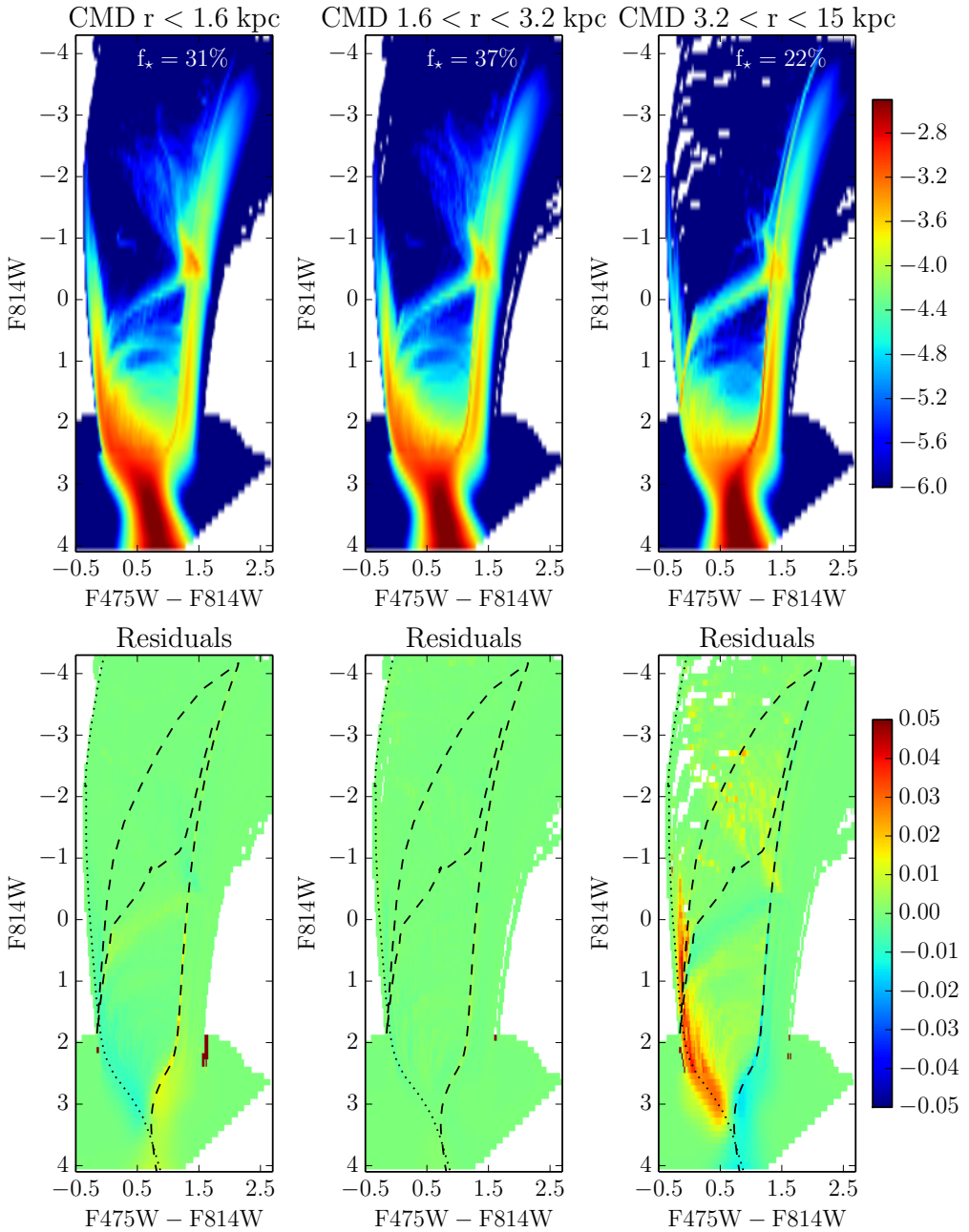
Figure 5.11: The CMDs of our merger model (see Table 5.3) with a cut on the radius. From left to right: (i) stars within the half light radius, r_e=1.6 kpc, (ii) stars outside the half light radius and inside two times the half light radius and (iii) stars outside two time the half light radius. The total simulation contains 35 268 star particles, the fraction of star particles in each interval is plotted in the corresponding panel.
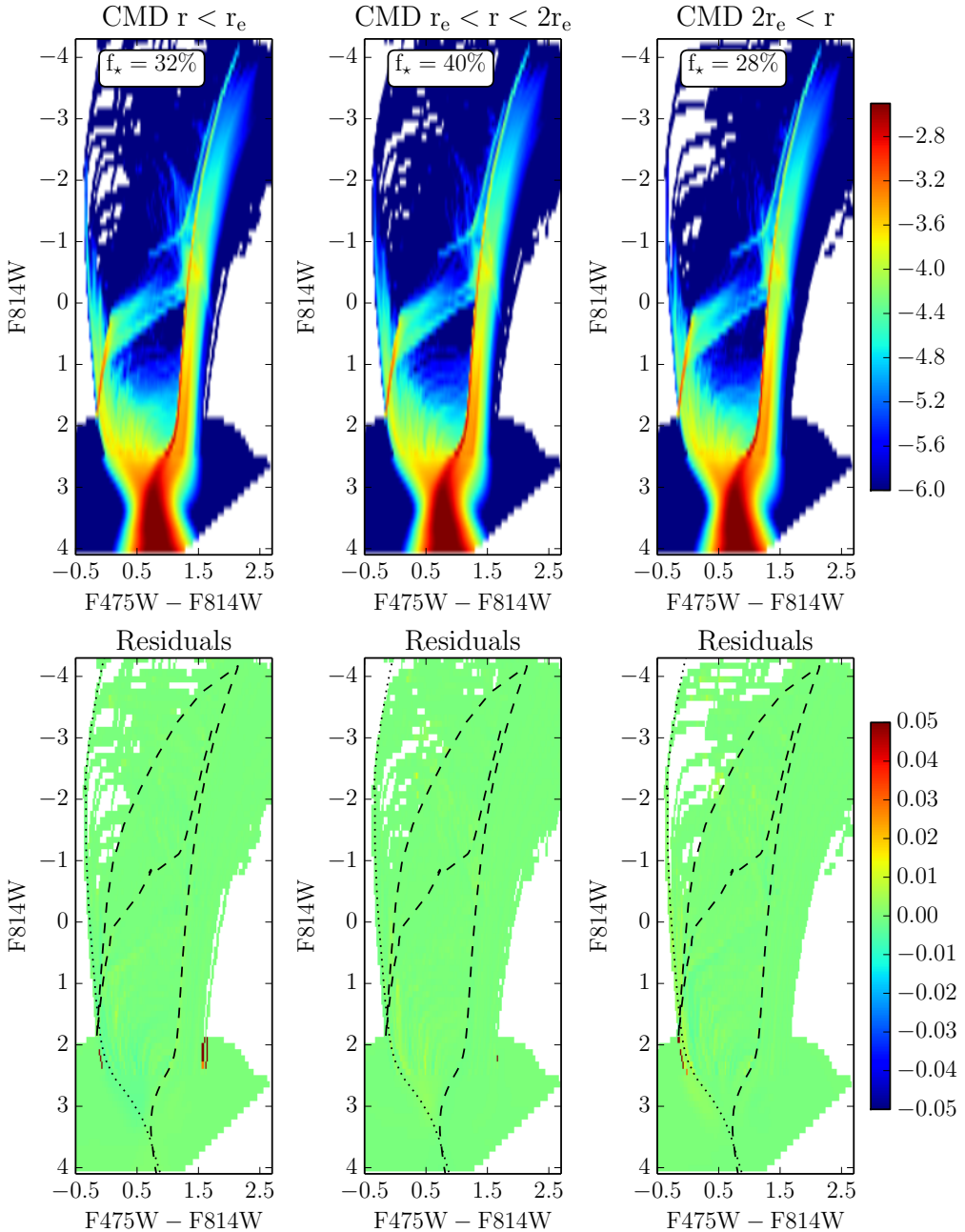
Figure 5.12: The CMDs of an isolated model with final halo mass of $M_{f,h}=5\ 10^9\ M_\odot$ constructed with a cut on the radius. From left to right: (i) stars within the half light radius, $r_e=0.39$ kpc, (ii) stars outside the half light radius and inside two times the half light radius and (iii) stars outside two time the half light radius. The total simulation contains 40 064 star particles, the fraction of star particles in each interval is plotted in the corresponding panel.

Fig. 5.12 shows the equivalent of Fig. 5.11 but for the isolated simulation from chapter 4 with final halo mass of $M_{f,h} = 5\ 10^9\ M_\odot$: again the total CMD is compared with the CMDs constructed with only part of the star particles, where they are selected on radius. The effective radius is only 0.39 kpc and from the residuals of the inner CMD (lower left plot in Fig. 5.12) we see that there are some indications that there are more young stars in the center compared to the total CMD. From the effective radius on, the contribution of the young stars seems to be little undersampled. This again suggest the existence of a stellar metallicity gradient that is less large compared to the merger simulations. However, we need to interpret this with care because there are only few stars formed in the last Gyr in the isolated simulation but these new stars will preferentially form within the effective radius.

From our modeled CMDs we can validate the assumptions that are made when analyzing observational CMD which are generally constructed from observations of only parts of the galaxies. For example, for the observational CMD of IC1613, only ∼9% was observed. Of course it would be better to obtain data from the entire galaxy but a balance has to be found between expensive observation time. Additionally, the central regions are difficult for the data-reduction as they are generally too crowded to individually resolve the faintest stars. In the particular case of IC1613, Skillman et al. (2014) argued that the 9% observed region within the core radius and the effective radius gives a representative view of the stellar populations present in the galaxy. In our merger simulation we also observe that the bin from one to two effective radii most closely resembles the total CMD.

Carraro et al. (2001) compared the CMDs of isolated simulated galaxies with those observed in the local Universe to check the implementation of star formation and chemical enrichment in their code. They found their models and in particularly their CMDs to be in agreement with the observations. They concluded that the implementation of star formation, i.e. the virialization of the dark matter halo and the collapse of baryons in the DM potential wells, may lead to the very different SFH as observed in the Universe, depending on the time of collapse and hence linked to the initial density of the system. We use the same mechanism to implement star formation in our code, but because star formation is self-regulated in our simulations, it is mainly driven by the supply of gas by the mergers and hence different merger trees introduce a wide range of different SFH.

We can conclude that the CMDs are a powerful tool to compare our simulations with the observations. We selected a merger simulation and showed that its properties show similarities to those of IC1613 in matter of star formation history and metallicity. We also found evidence for a stellar metallicity gradient in our merger simulation. Finally, we can use the comparison of the observed with the simulated CMDs to validate our implementation of star formation in the simulations.

5.4   Baryonic Tully Fisher relation (BTFR)

The Tully-Fisher relation (TFR) is the observed relation between luminosity and rotation velocities originally determined for spiral galaxies and is used as a powerful tool to determine distances to galaxies (Tully and Fisher, 1977). Additionally, it has been used to test the correctness of physical principles of galaxy formation given by the ΛCDM cosmology and

alternative theories like MOND (Steinmetz and Navarro, 1999; McGaugh, 2012). However, galaxies with rotation velocities lower than 90 km/s deviate from this relation. As these fainter galaxies generally are more gas-rich, replacing the luminosity by the baryonic mass, i.e. $M_{baryon} = M_{star} + M_{gas}$, results in a power-law relation between the rotation velocity and the baryonic mass over several orders of rotation velocities referred to as the baryonic Tully-Fisher relation (BTFR) (McGaugh et al., 2000). The TFR relation connects two different tracers of the mass and hence a correlation could be expected. At one side the optical luminosity traces the stellar mass which is connected to the total mass of a galaxy. On the other side, the rotation velocity which is deduced from the width of the 21 cm line, traces the dark matter. However, as the mass-to-light ratios differ for different types of galaxies, and luminosity is color dependent, it is not the ideal tracer of the total mass, resulting in TFRs with different slopes for the different bandpasses and for different galaxy types (Tully et al., 1998; Verheijen, 2001; De Rijcke et al., 2007).
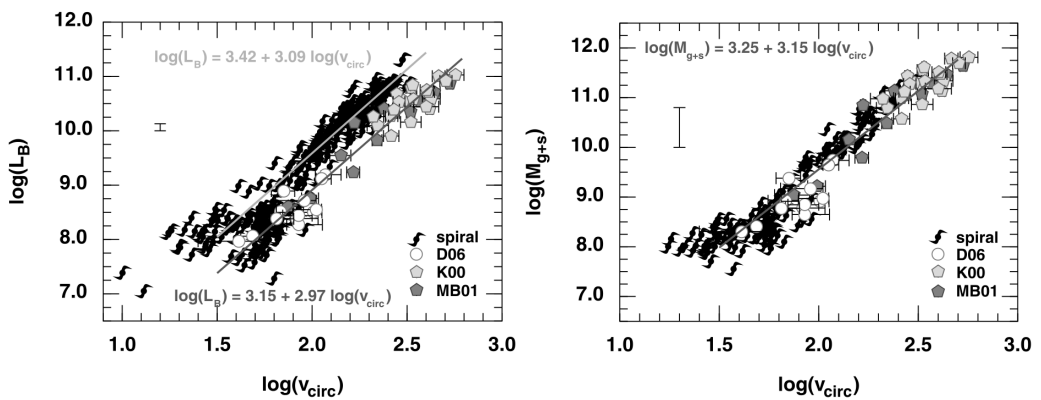
Figure 5.13: Left panel: The B-band TFR of early-type and late-type galaxies. The late-type galax-ies are represented by spirals with the data taken from Tully and Pierce (2000); Côté et al. (2000); McGaugh (2005); Geha et al. (2006). Early-type data for dEs originates from De Rijcke et al. (2006) (D06) shown by circles and for Es from Kronawitter et al. (2000) (K00) and Magorrian and Ballantyne (2001) (MB01) indicated by pentagons. Right panel: The BTFR of the same galaxies as in the left panel. Both figures are taken from De Rijcke et al. (2007).

Fig. 5.13 shows in the left panel the B-band TFR with parallel fitted TFRs for early-type and late-type galaxies as deduced by De Rijcke et al. (2007). In the right panel the BTFR is shown for the early and late-type galaxies: there is only a single BTFR over many decades of mass (Verheijen, 2001; De Rijcke et al., 2007; Begum et al., 2008a; Stark et al., 2009; Gurovich et al., 2010).

We will compare our simulations with the BTFR determined by McGaugh (2012) (see Fig. 1.3) which calibrated the BTFR with gas-rich galaxies as their stellar masses can be more accurately measured than the star-dominated galaxies as they are less affected by the sys-tematic errors introduced by the adopted mass-to-light ratio or by the initial mass function that is used (McGaugh, 2011).

To realistically compare our models with the observations, we determine the baryonic mass as the sum of the HI gas mass and the stellar mass in the snapshots. With the new cooling and heating curves (see section 5.1), the neutral fraction of the gas can be determined from
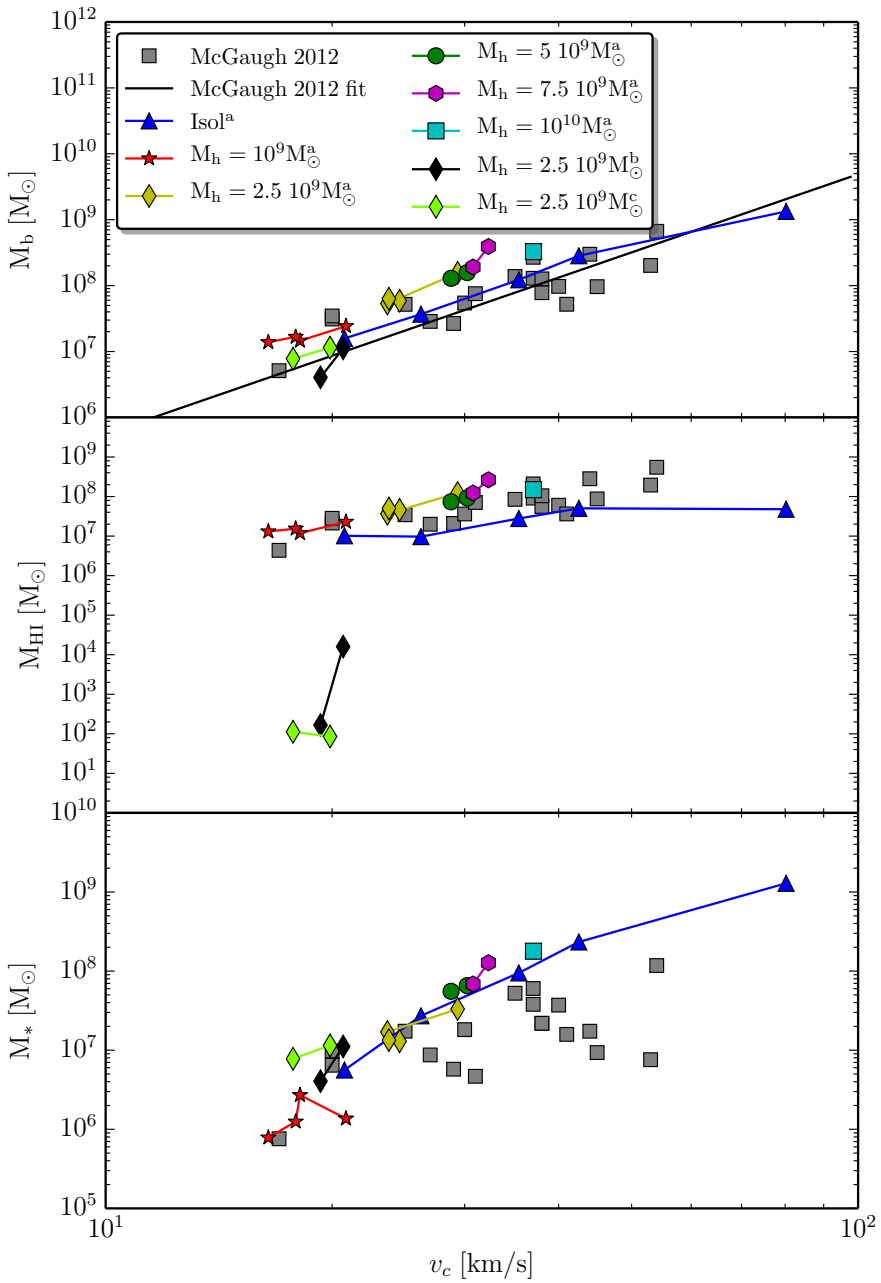
Figure 5.14: Upper panel: the BTFR for the merger trees of chapter 4 and the re-simulated MT2
and MT3 with M_h=2.5 10^9 $M_\odot$ with the cooling and heating curves of De Rijcke et al.
(2007). The gray dots and the black line represent respectively the observational data
and the fit to the data of McGaugh (2012).
(^{a}) Old cooling, n_{SF}=10 cm^{-3}, ϵ_{FB}=0.7, and NFW profiles
(^{b}) New cooling, n_{SF}=1000 cm^{-3}, ϵ_{FB}=0.7, and NFW profiles
(^{c}) New cooling, n_{SF}=1000 cm^{-3}, ϵ_{FB}=0.7, and GenNFW profiles profiles.

a 5D interpolation over the temperature, Fe and Mg abundance, the redshift and the density. We reran MT2 and MT3 with $M_{h,final}=2.5 \cdot 10^9 M_\odot$ with these new cooling and heating curves and hence can self-consistently deduce the neutral fraction of the gas. We can also post-process the simulations run with the old cooling curves. The circular velocity is determined as the maximum rotation velocity generated by the potential of the mass within a certain radius $(\sqrt{GM(<r)/r})_{max}$, where we assume our system to be spherical symmetric.

Fig. 5.14 shows in the upper panel the BTFR relation. In the middle and lower panel, respectively the HI gas mass and the stellar mass is shown as a function of the maximal circular velocity. The observational data of McGaugh (2012) are shown by gray squares and their fitted relation is plotted by the gray line. The isolated simulations of chapter 4 are shown by blue triangles with increasing masses corresponding to increasing maximal circular velocities. The merger simulations of chapter 4 are plotted by different symbols and colors as indicated in the legend. For the mergers with $M_h=2.5 \cdot 10^9 M_\odot$, indicated by the diamond symbols, we indicate three different setups of the simulations by different colors:

yellow: Simulations with the old cooling (see subsection 2.3.3), a density threshold for star formation of $n_{SF} = 10$ cm^{-3} (see subsection 2.3.1) and a feedback efficiency of $\epsilon_{FB}=$ 0.7 (see subsection 2.3.2). Their initial dark matter haloes have NFW profiles (see subsection 2.2.1).

black: Simulations with the new cooling (see section 5.1), $n_{SF} = 1000$ cm^{-3} and $\epsilon_{FB}= 0.7$. Their initial dark matter haloes have NFW profiles.

light green: Simulations with the new cooling, $n_{SF} = 1000$ cm^{-3} and $\epsilon_{FB}= 0.7$. Their initial dark matter haloes have GenNFW profiles (see section 5.2).

The isolated models nicely follow the BTFR over the entire mass range. The mergers with the old cooling are somewhat above the BTFR, but as can be seen from the middle and lower panel, this is mostly due to a larger HI gas mass as their stellar masses are comparable. The simulations with the new cooling are more in agreement with the BTFR-fit from McGaugh (2012), however, we already argued in section 5.1 that, for the moment, they are not a good representation of the 'general' dwarf. Their location in the second panel clearly shows that they only retain little amounts of neutral gas due to the UVB. We already discussed in section 5.2 that the use of dark matter haloes with a GenNFW profile has a limited effect on the final stellar mass. The final HI mass of the models with the new cooling does show some influence of the chosen dark matter profile: the models with GenNFW are less efficient in keeping their gas content. Although, with only two simulations of each kind it is difficult to make strong predictions.

This relation is more closely related to observational quantities than the M_{star}-M_{halo} relation from subsection 3.4.3 as the halo mass is difficult to determine from observations and even for simulations it is not always straightforward: an often used approximation is to use M_{200}, the mass within the radius where the density drops below 200 times the critical density of the universe at that time. We noticed in our merger simulations that the dark matter mass is widely spread out due to interactions resulting in a M_{200} that is between 60-80% of the final dark matter mass M_f we generally state. Hence, using v_{circ} gives a better representation of the actual potential well of the galaxy and is closely related to what we can observe.

We can conclude that the BTFR is a very powerful relation to compare our models with observations and to test our knowledge of galaxy formation and evolution models. From the

results shown in this subsection, it is clear that the models with UVB contain too little gas, while the models without UVB contain too much stars. Observational evidence of low-mass gas-rich galaxies contradicts the upper mass limit of 'dark' haloes (i.e. haloes that are unable to form stars) set by simulations. This is one of the problems that will be addressed by the next generation of astronomers.

6

English summary

Today, dwarf galaxies are the most numerous type of galaxy in the Universe and they probably were even more numerous in the past. In the picture of the hierarchical bottom-up structure formation of the ΛCDM cosmology, large structures are created by the subsequent merging of smaller structures. Hence, the dwarfs we observe today are the survivors of these protogalaxies that originate from the clumping of dark matter in the primordial density perturbations.

We present simulations run with our adapted version of the N-body/SPH code Gadget-2 (Springel, 2005). Gravity and hydrodynamics are implemented using a particle representation for the dark matter and the gas. The initial conditions of our simulations are cosmologically motivated: using dark matter density profiles and mass assembly histories that are appropriate for dwarf galaxies.

In the first part of this work, we focused on simulating isolated dwarf galaxies. Because we simulate isolated galaxies, we can reach very high mass resolutions. However, we are still unable to resolve single stars, and processes like star formation, stellar feedback, and the heating and cooling of the gas are implemented as sub-grid physics. We performed a parameter analysis of two important star formation parameters: the density threshold for star formation, n_{SF}, which tracks the dense clumps of gas where star formation happens, and the feedback efficiency ϵ_{FB}, the fraction of the 10^{51} ergs of energy that is released by SN explosions that is absorbed by the ISM. A degeneracy is found between these two parameters: for increasing density thresholds for star formation, an increase of the feedback efficiency is needed in order to maintain a breathing star formation (Cloet-Osselaer et al., 2012). We determined the n_{SF}-ϵ_{FB} combinations for which the models agree best with the observed photometric and kinematical scaling relations. In essence, for a certain density threshold n_{SF}, a minimal feedback efficiency is needed to disrupt star formation locally after which the gas has to recollapse. This minimal feedback increases for increasing n_{SF} as the gas has to

fall into higher densities.

We found the 'cusp-to-core' problem, i.e. the contradiction between the inner density slope of dark matter haloes which are observed to be cuspy in cosmological simulations, but are deduced to be cored from observations, to be solved naturally by the inclusion of baryonic physics (Cloet-Osselaer et al., 2012). When excluding baryons from the simulation, the initial NFW profile remains stable, while with the inclusion of baryons, the feedback originating from star formation is able to flatten the inner density of the dark matter halo.

We showed that our models deviate from the relation between the stellar and halo mass that was determined by Guo et al. (2010) using abundance matching techniques. This relation was determined from comparing the number of observed galaxies with the number of simulated galaxies in cosmological simulations down to halo masses of $8 \ 10^{10}$ $M_\odot$ after which this relation is linearly extended to lower masses. Although we are unable to align our models with the M_{star}-M_{halo} relation, our results do reproduce its slope and they are in agreement with the analysis from Sawala et al. (2012) of the 'Aquila simulation'.

In the second part of this work, we wanted to provide our models with a more realistic formation history. To mimic the hierarchical structure formation, we constructed merger trees with the Parkinson et al. (2008) algorithm that uses the extended Press-Schechter theory which analytically describes the structure formation of the Universe. We then start each progenitor as an isolated dwarf galaxy and merge them together at times indicated by the merger tree and we use orbital parameters drawn from the velocity distribution functions of Benson (2005). We show our procedure to be a worthy alternative for the computationally demanding cosmological simulations that include baryonic physics and star formation.

We show that this method enables us to produce dwarf galaxies that are in agreement with the photometric and kinematic scaling relations (Cloet-Osselaer et al., 2014). With a small set of merger tree simulations with final halo masses in the range of 10^9-10^{10} $M_\odot$ we are able to obtain a variability in the star formation histories which is also seen in the observed dwarfs. Our simulations clearly show that the mergers provide the fuel (i.e. gas) to ignite strong star-formation episodes and subsequent feedback is shown to be very efficient in lowering the inner density cusp of the dark matter.

The influence of the merger history on the final properties of our models can be characterized with two extreme cases. On one hand, a merger tree can start with an early massive progenitor and only experience subsequent minor mergers while on the other hand, a merger tree can consist of many small progenitors which only merge quite late. Models with the same final halo mass generally have higher stellar masses in the first case and as a consequence they experience more stellar feedback and hence have shallower dark matter potentials. We also noticed that many small star-formation episodes introduced by many small mergers are more efficient in lowering the inner core than a single large star-formation episode. The number of mergers is also correlated with the specific angular momentum: the more mergers there occur, the more chance they cancel out, resulting in higher specific angular momenta for the models with an early massive progenitor.

Compared to our isolated models, the mergers all have less shallow dark matter potentials resulting in galaxies with larger effective radii, lower central velocity dispersions and lower central surface brightnesses but they are in agreement with the photometric and kinematic scaling relations. We also found evidence for the merger simulations to be strongly triaxial

and to have significant anisotropic orbital distributions, similar to real dwarfs.

In the final chapter of this work we present the recent developments of our Dwarf Galaxy Group, to which I contributed. In the first section we discuss the influence of the new cooling and heating curves of De Rijcke et al. (2013) in which the ultra-violet background radiation was taken into account. The UVB is very effective in heating and dispersing the gas content of our models, limiting star formation to the first Gyrs of the simulations. In the second section we take into account that at high z, it is possible that the progenitors did not yet have an NFW profile. We provided our progenitors with masses below 10^9 M$_\odot$ with a variant of the NFW profile of which the parameters were selected from the distribution functions provided by Cen et al. (2004) which depend on the redshift and their mass. We distributed the gas according to a scaled version of the dark matter distribution which results in star formation igniting earlier as the density for star formation is reached sooner.

In the third section we compare a color-magnitude diagram of one of our simulations with CMD data of IC1613 from the LCID group: although it was not constructed to really be a model of IC1613 we do see quite some similarities and are able to explain their differences. We show that, when applying a radial cut when constructing the color magnitude diagrams, our merger simulations show a stellar metallicity gradient which we explain to originate from the interactions between the protogalaxies. To conclude this chapter, we look into the baryonic Tully-Fisher relation and show that this is a very powerful relation in aligning simulations with observations.

7

Nederlandse samenvatting
–Summary in Dutch–

Dwerggalaxiëen zijn de meest voorkomende soort sterrenstelsels in ons heelal en ze kwamen waarschijnlijk in het verleden nog frequenter voor. Volgens de ΛCDM kosmologie werden de structuren op hiërarchische wijze gevormd. Dit wil zeggen dat grotere structuren gevormd werden door het opeenvolgend versmelten van kleinere structuren. Bijgevolg zijn de dwergen die we vandaag waarnemen ontstaan uit deze proto-sterrenstelsels die ontstaan zijn uit het samenklonteren van donkere materie in de primordiale dichtheidsfluctuaties.

In dit werk stellen we simulaties voor die gecreëerd zijn met onze aangepaste versie van de N-body/SPH-code Gadget-2 (Springel, 2005). We stellen de donkere materie en gas voor als deeltjes en implementeren de zwaartekracht en hydrodynamica als krachten die werken tussen de verschillende deeltjes. Onze simulaties starten met kosmologisch gemotiveerde eigenschappen: voor de donkere materie gebruiken we dichtheidsprofielen en massaverzamel-geschiedenissen die geschikt zijn voor dwergsterrenstelsels.

In het eerste deel van dit werk hebben we ons gefocust op het simuleren van dwergsterren-stelsels in isolatie. Aangezien we ze geïsoleerd simuleren kunnen we een grote massaresolutie bereiken. Desondanks is het nog steeds onmogelijk om individuele sterren te resolveren en moeten we processen zoals stervorming, stellaire feedback en het verhitten en koelen van het gas implementeren als sub-gridfysica. Dit wil zeggen dat we enkel criteria kunnen op-leggen voor de 'gemiddelde' stervorming en feedback van de verzameling van sterren die een sterdeeltje voorstelt in onze simulatie. We hebben een parameteranalyse gedaan van twee be-langrijke stervormingsparameters: ten eerste het dichtheidscriterium voor stervorming, n_{SF}, wat er op neer komt dat de dichtste concentraties in het gas selecteert waar stervorming gebeurt, en ten tweede de feedbackefficiëntie, ϵ_{FB}, dit is de fractie van de energie die vrij-komt bij supernova-explosies (een parameter die vaststaat op een waarde van 10^{51} ergs)

die opgenomen wordt door het interstellair medium. We hebben een ontaarding gevonden tussen deze twee stervormingsparameters: wanneer we het dichtheidscriterium verhogen zien we dat we de feedbackefficiëntie ook moeten verhogen om een 'ademende' stervorming te behouden (Cloet-Osselaer et al., 2012). Op basis van de overeenkomst van onze modellen met de waargenomen fotometrische en kinematische schalingsrelaties hebben we enkele optimale n_{SF}-ϵ_{FB} combinaties bepaald voor onze simulaties. Finaal komt het erop neer dat voor een zeker dichtheidscriterium, een minimale feedback nodig is om de stervorming lokaal te onderbreken waarna het gas opnieuw de kans krijgt om in te vallen en terug sterren te vormen. Deze minimale feedback stijgt wanneer het dichtheidscriterium stijgt.

Het 'cusp-to-core' probleem is de tegenstelling tussen de binnenste helling van een donkere-materiehalo waarvan men waargenomen heeft dat die een kern vertoont ('core') terwijl er uit kosmologische simulaties blijkt dat deze gepiekt is in het centrum ('cusp'). In onze simulaties zien we dat ons initieel gepiekte centrum van de donkere-materiehalo's ten gevolge van de interacties van de baryonische materie (i.e. gas en sterren) gereduceerd wordt tot een kern (Cloet-Osselaer et al., 2012). Wanneer we ter controle geen baryonen in onze simulatie steken, blijft het initiële gepiekte donkere-materiecentrum behouden.

We tonen aan dat onze modellen afwijken van de door Guo et al. (2010) bepaalde relatie tussen de stellaire massa en donkere-materiemassa. Deze relatie werd bepaald door het linken van de meest massieve donkere-materiehalo's uit kosmologische simulaties aan de meest heldere sterrenstelsels. Dit proces werd uitgevoerd tot donkere-materiehalo's met een massa van $8 \cdot 10^{10}$ $M_{\odot}$ waarna het lineair geëxtrapoleerd werd naar lagere massa's. Hoewel onze modellen niet op deze relatie liggen reproduceren ze wel de helling van de relatie en zijn ze wel in overeenkomst met de resultaten van de 'Aquila simulatie' die geanalyseerd werden door Sawala et al. (2012).

In het tweede deel van dit werk hebben we geprobeerd onze modellen een realistischere vormingsgeschiedenis te geven. Om de hiërarchische structuurvorming na te bootsen hebben we versmeltingsbomen opgesteld met het algoritme van Parkinson et al. (2008). Dit algoritme maakt gebruik van de uitgebreide Press-Schechter theorie die de structuurvorming van het heelal op een analytische manier beschrijft. Vervolgens starten we elke 'voorouder' als een geïsoleerd dwergsterrenstelsel en laten hen versmelten op de tijdstippen die bepaald zijn door de versmeltingsboom en we gebruiken de baanparameters die uit de snelheidsdistributiefuncties van Benson (2005) getrokken worden. We tonen aan dat onze methode een waardevol alternatief is voor computationeel veeleisende kosmologische simulaties waarin stervorming en gasfysica inbegrepen zijn.

We hebben aangetoond dat we met deze methode in staat zijn om dwergsterrenstelsels te produceren die in overeenkomst zijn met de fotometrische en kinematische schalingsrelaties. Met een klein aantal van deze simulaties met een finale donkere-materiemassa tussen 10^9-10^{10} $M_{\odot}$ zijn we in staat een variabiliteit in stervormingsgeschiedenissen te verkrijgen die ook te zien is bij waargenomen dwergen. Onze simulaties tonen dat de versmeltingsprocessen de nodige brandstof leveren, in dit geval gas, om sterke stervormingspieken te starten en dat de daaropvolgende feedback heel efficiënt is in het afplatten van de donkere-materiehalo.

De invloed van de versmeltingsboom op de finale eigenschappen van onze modellen kan worden gekarakteriseerd door twee extreme gevallen. Aan de ene kant hebben we een versmeltingsboom die al vroeg start met een relatief zware voorouder en die vervolgens enkel kleine mergers ondergaat. Aan de andere kant kan een versmeltingsboom ook opgebouwd zijn uit

vele kleine voorouders die pas laat effectief versmelten. Modellen met dezelfde finale donkere materie massa zullen in het eerste geval meer sterren vormen en bijgevolg ook meer feedback genereren waardoor hun donkere materie minder gepiekt zal zijn. We merkten ook op dat vele kleine stervormingspiekjes efficiënter zijn in het afplatten van de donkere-materiehalo dan een singuliere grote stervormingspiek. Daarnaast is het aantal versmeltingen ook gecorreleerd met het finale specifieke impulsmoment: hoe meer versmeltingen er gebeuren, hoe groter de kans is dat ze elkaar zullen teniet doen. Dit resulteert in hogere specifieke impulsmomenten voor de modellen met een vroege massieve vforouder aangezien deze meestal het minste versmeltingen kennen.

In vergelijking met onze geïsoleerde modellen hebben de mergers meer afgeplatte donkere-materiepotentialen wat resulteert in sterrenstelsel met grotere effectieve stralen, lagere centrale snelheidsdispersies en lagere centrale oppervlaktehelderheden maar die wel nog steeds in overeenstemming zijn met de fotometrische en kinematische schalingsrelaties. We hebben ook kunnen aantonen dat de finale modellen sterk triaxiaal zijn en duidelijke anisotrope orbitale distributies vertonen, in overeenstemming met echte dwergen.

In het finale hoofdstuk presenteren we de recente ontwikkelingen van onze Dwarf Galaxy Group, waarvan ik deel uitmaak. In de eerste sectie bespreken we de invloed van de nieuwe koelings- en verhittingscurves van De Rijcke et al. (2013) waarbij rekening gehouden werd met de ultra-violette achtergrondstraling. Deze achtergrondstraling is heel efficiënt in het verhitten en uiteendrijven van het gas in onze modellen waardoor er enkel sterren gevormd worden in de eerste miljarden jaren van de simulaties. In de tweede sectie houden we er rekening mee dat het op hoge roodverschuiving mogelijk is dat de voorouders nog geen NFW-dichtheidsprofiel hebben voor de donkere materie. We voorzien onze voorouders met massa's lager dan 10^9 $M_\odot$ met een dichtheidsprofiel dat een variant is van het NFW-profiel en met parameters die bepaald zijn uit de distributiefuncties van Cen et al. (2004) die zowel afhankelijk zijn van de roodverschuiving als van de massa. Het gas wordt verdeeld volgens een geschaalde versie van de dichtheidsverdeling van de donkere materie wat resulteert in een vroegere start van de stervorming aangezien het dichtheidscriterium vroeger bereikt wordt.

In de derde sectie vergelijken we het kleur-magnitudediagram van één van onze simulaties met de observationele kleur-magnitudediagram van IC1613 van de LCID groep. Ondanks het feit dat dit model niet gemaakt was om echt een model te zijn voor IC1613 zien we redelijk veel gelijkenissen en zijn we in staat de verschillen te verklaren. We tonen aan dat, wanneer we de sterren binnen verschillende stralen selecteren om deze kleur-magnitudediagrammen te maken, onze versmeltingssimulaties een stellaire metalliciteitsgradiënt vertonen die afkomstig is van de interacties tussen de proto-sterrenstelsels. We sluiten dit hoofdstuk af met de baryonische Tully-Fisherrelatie en tonen aan dat dit een heel krachtige relatie is om onze simulaties in overeenkomst te brengen met onze observaties.

8

Outlook

It was an illusion to think this PhD would have a strict and clear ending. Now I will summarize the future steps that might be done and the things that would benefit of some improvements. More work for the dwarf galaxy group who have been working on this (amongst other things) while I was writing...

- The color magnitude diagrams have always been some kind of side-project. Although during the last weeks, they have shown the variety of things they can be used for. However, we need more merger simulations to have more material to compare the observed CMDs with.

- The new cooling and heating curves and more particularly the UVB have introduced some challenging consequences which need to be understood and some concepts will have to be adapted in order to keep our simulations in line with the observations. As we showed in section 5.1, the new cooling and heating curves result in models which deviate from the wide variety observed dwarfs in terms of SFH, metallicity, ... Our dwarf galaxy group has been busy improving the implemented physics in order to simulate more realistic dwarfs. It has been a key property to lower the initial star formation peak because the resulting feedback disrupts the gas content and made it more vulnerable to be heated by the UVB. We tried various mechanisms to do this: from adapting the implementation of SNIa to the introduction of POP-III stars. Our efforts will soon be summarized in an upcoming paper (Verbeke et al. 2015, in prep.)

- The merger simulations are an improvement to our previously isolated models. However, we still lack the continuously growth of the dark matter halo by accretion. Although it could be argued that this accretion is mimicked in the merger simulations through gravitational interaction between the main dark matter halo and the surrounded dark matter that is widely distributed over ranges of ∼300 kpc due to the interactions.

- The GALFORM algorithm uses a lower mass limit for the subhaloes which is in the range of 0.005-0.01 of the final halo mass (see Table 4.1). The merger tree could be sampled in greater detail when going to lower resolution masses but then more attention should be payed to the approximated Keplerian trajectories that are used to determine the orbital parameters of the mergers.

- The orbital parameters from Benson (2005) could be updated to more recent determinations of the orbital parameters based on the latest simulations. In (Jiang et al., 2014) the orbital parameters of the infalling haloes are determined from the DOVE simulation. Although they report their results are similar to the results of Benson (2005) which are based on simulations with satellite-to-host halo masses in the range of 0.05 to 0.5. They determined distribution functions for satellite galaxies with lower mass ratios compare to host galaxy, which could be an improvement when decreasing the resolution mass in the GALFORM algorithm.

References

Aarseth, S. J. (2003). *Gravitational N-Body Simulations*.

Amorisco, N. C., Zavala, J., and de Boer, T. J. L. (2014). Dark Matter Cores in the Fornax and Sculptor Dwarf Galaxies: Joining Halo Assembly and Detailed Star Formation Histories. *ApJL*, 782:L39.

Annibali, F., Grützbauch, R., Rampazzo, R., Bressan, A., and Zeilinger, W. W. (2011). Nature vs. nurture in the low-density environment: structure and evolution of early-type dwarf galaxies in poor groups. *A&A*, 528:A19.

Bardeen, J. M., Bond, J. R., Kaiser, N., and Szalay, A. S. (1986). The statistics of peaks of Gaussian random fields. *ApJ*, 304:15–61.

Barnabè, M., Czoske, O., Koopmans, L. V. E., Treu, T., Bolton, A. S., and Gavazzi, R. (2009). Two-dimensional kinematics of SLACS lenses - II. Combined lensing and dynamics analysis of early-type galaxies at z = 0.08-0.33. *MNRAS*, 399:21–36.

Barnes, J. and Hut, P. (1986). A hierarchical O(N log N) force-calculation algorithm. *Nature*, 324:446–449.

Bastidas Fry, A., Governato, F., Pontzen, A., Quinn, T., Tremmel, M., Anderson, L., Menon, H., Brooks, A. M., and Wadsley, J. (2015). All about baryons: revisiting SIDM predictions at small halo masses. *ArXiv e-prints*.

Bate, M. R. and Burkert, A. (1997). Resolution requirements for smoothed particle hydrodynamics calculations with self-gravity. *MNRAS*, 288:1060–1072.

Battaglia, G., Helmi, A., and Breddels, M. (2013). Internal kinematics and dynamical models of dwarf spheroidal galaxies around the Milky Way. , 57:52–79.

Battaglia, G., Tolstoy, E., Helmi, A., Irwin, M., Parisi, P., Hill, V., and Jablonka, P. (2011). Study of the Sextans dwarf spheroidal galaxy from the DART Ca II triplet survey. *MNRAS*, 411:1013–1034.

Battaglia, G., Tolstoy, E., Helmi, A., Irwin, M. J., Letarte, B., Jablonka, P., Hill, V., Venn, K. A., Shetrone, M. D., Arimoto, N., Primas, F., Kaufer, A., Francois, P., Szeifert, T., Abel, T., and Sadakane, K. (2006). The DART imaging and CaT survey of the Fornax dwarf spheroidal galaxy. *A&A*, 459:423–440.

Begum, A., Chengalur, J. N., Karachentsev, I. D., and Sharina, M. E. (2008a). Baryonic Tully-Fisher relation for extremely low mass Galaxies. *MNRAS*, 386:138–144.

Begum, A., Chengalur, J. N., Karachentsev, I. D., Sharina, M. E., and Kaisin, S. S. (2008b). FIGGS: Faint Irregular Galaxies GMRT Survey - overview, observations and first results. *MNRAS*, 386:1667–1682.

Behroozi, P. S., Conroy, C., and Wechsler, R. H. (2010). A Comprehensive Analysis of Uncertainties Affecting the Stellar Mass-Halo Mass Relation for 0 z 4. *ApJ*, 717:379– 403.

Bennett, C. L., Larson, D., Weiland, J. L., Jarosik, N., Hinshaw, G., Odegard, N., Smith, K. M., Hill, R. S., Gold, B., Halpern, M., Komatsu, E., Nolta, M. R., Page, L., Spergel, D. N., Wollack, E., Dunkley, J., Kogut, A., Limon, M., Meyer, S. S., Tucker, G. S., and Wright, E. L. (2013). Nine-year Wilkinson Microwave Anisotropy Probe (WMAP) Observations: Final Maps and Results. *ApJS*, 208:20.

Benson, A. J. (2005). Orbital parameters of infalling dark matter substructures. *MNRAS*, 358:551–562.

Bernard, E. J., Aparicio, A., Gallart, C., Padilla-Torres, C. P., and Panniello, M. (2007). Stellar Content and Recent Star Formation History of the Local Group Dwarf Irregular Galaxy IC 1613. *AJ*, 134:1124–1132.

Bernard, E. J., Monelli, M., Gallart, C., Aparicio, A., Cassisi, S., Drozdovsky, I., Hidalgo, S. L., Skillman, E. D., and Stetson, P. B. (2010). The ACS LCID Project. II. Faint Variable Stars in the Isolated Dwarf Irregular Galaxy IC 1613. *ApJ*, 712:1259–1276.

Bernstein-Cooper, E. Z., Cannon, J. M., Elson, E. C., Warren, S. R., Chengular, J., Skillman, E. D., Adams, E. A. K., Bolatto, A. D., Giovanelli, R., Haynes, M. P., McQuinn, K. B. W., Pardy, S. A., Rhode, K. L., and Salzer, J. J. (2014). ALFALFA Discovery of the Nearby Gas-rich Dwarf Galaxy Leo P. V. Neutral Gas Dynamics and Kinematics. *AJ*, 148:35.

Binggeli, B. and Popescu, C. C. (1995). Dwarf galaxies in the Virgo cluster. III. Flattening distributions. *A&A*, 298:63.

Bode, P. and Ostriker, J. P. (2003). Tree Particle-Mesh: An Adaptive, Efficient, and Parallel Code for Collisionless Cosmological Simulation. *ApJS*, 145:1–13.

Bond, J. R., Cole, S., Efstathiou, G., and Kaiser, N. (1991). Excursion set mass functions for hierarchical Gaussian fluctuations. *ApJ*, 379:440–460.

Boselli, A., Boissier, S., Cortese, L., and Gavazzi, G. (2008). The Origin of Dwarf Ellipticals in the Virgo Cluster. *ApJ*, 674:742–767.

Bosler, T. L., Smecker-Hane, T. A., and Stetson, P. B. (2007). The chemical abundances of the stellar populations in the Leo I and II dSph galaxies. *MNRAS*, 378:318–338.

Boylan-Kolchin, M., Springel, V., White, S. D. M., Jenkins, A., and Lemson, G. (2009). Resolving cosmic structure formation with the Millennium-II Simulation. *MNRAS*, 398:1150– 1164.

Bromm, V. and Yoshida, N. (2011). The First Galaxies. *ARA&A*, 49:373–407.

Brook, C. B., Stinson, G., Gibson, B. K., Roškar, R., Wadsley, J., and Quinn, T. (2012). Hierarchical formation of bulgeless galaxies - II. Redistribution of angular momentum via galactic fountains. *MNRAS*, 419:771–779.

Brooks, A. M. and Zolotov, A. (2014). Why Baryons Matter: The Kinematics of Dwarf Spheroidal Satellites. *ApJ*, 786:87.

Brown, T. M., Tumlinson, J., Geha, M., Simon, J. D., Vargas, L. C., VandenBerg, D. A., Kirby, E. N., Kalirai, J. S., Avila, R. J., Gennaro, M., Ferguson, H. C., Muñoz, R. R., Guhathakurta, P., and Renzini, A. (2014). The Quenching of the Ultra-faint Dwarf Galaxies in the Reionization Era. *ApJ*, 796:91.

Burstein, D., Bender, R., Faber, S., and Nolthenius, R. (1997). Global Relationships Among the Physical Properties of Stellar Systems. *AJ*, 114:1365–+.

Buyle, P., Michielsen, D., de Rijcke, S., Ott, J., and Dejonghe, H. (2006). The CO content of the Local Group dwarf irregular galaxies IC5152, UGCA438 and the Phoenix dwarf. *MNRAS*, 373:793–798.

Buyle, P., van Hese, E., de Rijcke, S., and Dejonghe, H. (2007). Radial-orbit instability of a family of anisotropic Hernquist models with and without a supermassive black hole. *MNRAS*, 375:1157–1170.

Buzzoni, A. (2005). Broad-band colours and overall photometric properties of template galaxy models from stellar population synthesis. *MNRAS*, 361:725–742.

Cannon, J. M., Giovanelli, R., Haynes, M. P., Janowiecki, S., Parker, A., Salzer, J. J., Adams, E. A. K., Engstrom, E., Huang, S., McQuinn, K. B. W., Ott, J., Saintonge, A., Skillman, E. D., Allan, J., Erny, G., Fliss, P., and Smith, A. (2011). The Survey of H I in Extremely Low-mass Dwarfs (SHIELD). *ApJL*, 739:L22.

Carraro, G., Chiosi, C., Girardi, L., and Lia, C. (2001). Dwarf elliptical galaxies: structure, star formation and colour-magnitude diagrams. *MNRAS*, 327:69–79.

Cen, R., Dong, F., Bode, P., and Ostriker, J. P. (2004). Properties of Cold Dark Matter Halos at z6. *ArXiv Astrophysics e-prints*.

Cignoni, M. and Tosi, M. (2010). Star Formation Histories of Dwarf Galaxies from the Colour-Magnitude Diagrams of Their Resolved Stellar Populations. *Advances in Astronomy*, 2010:3.

Cloet-Osselaer, A., De Rijcke, S., Schroyen, J., and Dury, V. (2012). The degeneracy between star formation parameters in dwarf galaxy simulations and the M_{star}-M_{halo} relation. *MNRAS*, 423:735–745.

Cloet-Osselaer, A., De Rijcke, S., Vandenbroucke, B., Schroyen, J., Koleva, M., and Verbeke, R. (2014). Numerical simulations of dwarf galaxy merger trees. *MNRAS*, 442:2909–2925.

Cole, A. A., Skillman, E. D., Tolstoy, E., Gallagher, III, J. S., Aparicio, A., Dolphin, A. E., Gallart, C., Hidalgo, S. L., Saha, A., Stetson, P. B., and Weisz, D. R. (2007). Leo A: A Late-blooming Survivor of the Epoch of Reionization in the Local Group. *ApJL*, 659:L17–L20.

Cole, A. A., Tolstoy, E., Gallagher, III, J. S., Hoessel, J. G., Mould, J. R., Holtzman, J. A., Saha, A., Ballester, G. E., Burrows, C. J., Clarke, J. T., Crisp, D., Griffiths, R. E., Grillmair, C. J., Hester, J. J., Krist, J. E., Meadows, V., Scowen, P. A., Stapelfeldt, K. R., Trauger, J. T., Watson, A. M., and Westphal, J. R. (1999). Stellar Populations at the Center of IC 1613. *AJ*, 118:1657–1670.

Cole, A. A., Weisz, D. R., Dolphin, A. E., Skillman, E. D., McConnachie, A. W., Brooks, A. M., and Leaman, R. (2014). Delayed Star Formation in Isolated Dwarf galaxies: Hubble Space Telescope Star Formation History of the Aquarius Dwarf Irregular. *ApJ*, 795:54.

Cole, D. R., Dehnen, W., and Wilkinson, M. I. (2011). Weakening dark matter cusps by clumpy baryonic infall. *MNRAS*, 416:1118–1134.

Cole, S., Lacey, C. G., Baugh, C. M., and Frenk, C. S. (2000). Hierarchical galaxy formation. *MNRAS*, 319:168–204.

Collins, M. L. M., Chapman, S. C., Rich, R. M., Ibata, R. A., Martin, N. F., Irwin, M. J., Bate, N. F., Lewis, G. F., Peñarrubia, J., Arimoto, N., Casey, C. M., Ferguson, A. M. N., Koch, A., McConnachie, A. W., and Tanvir, N. (2013). A Kinematic Study of the Andromeda Dwarf Spheroidal System. *ApJ*, 768:172.

Côté, S., Carignan, C., and Freeman, K. C. (2000). The Various Kinematics of Dwarf Irregular Galaxies in Nearby Groups and Their Dark Matter Distributions. *AJ*, 120:3027–3059.

Cox, T. J., Dutta, S. N., Di Matteo, T., Hernquist, L., Hopkins, P. F., Robertson, B., and Springel, V. (2006). The Kinematic Structure of Merger Remnants. *ApJ*, 650:791–811.

Curtis, H. D. (2010a). Chapter 2 - the two-body problem. In Curtis, H. D., editor, *Orbital Mechanics for Engineering Students (Second Edition)*, Aerospace Engineering, pages 61 – 153. Butterworth-Heinemann, Boston, second edition edition.

Curtis, H. D. (2010b). Chapter 3 - orbital position as a function of time. In Curtis, H. D., editor, *Orbital Mechanics for Engineering Students (Second Edition)*, Aerospace Engineering, pages 155 – 197. Butterworth-Heinemann, Boston, second edition edition.

Da Costa, G. S., Jerjen, H., and Bouchard, A. (2007). ESO540-032: a Transition-Type Dwarf in the Sculptor Group. *ArXiv e-prints*.

Dalcanton, J. J., Williams, B. F., Seth, A. C., Dolphin, A., Holtzman, J., Rosema, K., Skillman, E. D., Cole, A., Girardi, L., Gogarten, S. M., Karachentsev, I. D., Olsen, K., Weisz, D., Christensen, C., Freeman, K., Gilbert, K., Gallart, C., Harris, J., Hodge, P., de Jong, R. S., Karachentseva, V., Mateo, M., Stetson, P. B., Tavarez, M., Zaritsky, D., Governato, F., and Quinn, T. (2009). The ACS Nearby Galaxy Survey Treasury. *ApJS*, 183:67–108.

David, L. P., Forman, W., and Jones, C. (1990). The evolution of the interstellar medium in elliptical galaxies. I - The early wind phase. *ApJ*, 359:29–41.

de Blok, W. J. G. (2010). The Core-Cusp Problem. *Advances in Astronomy*, 2010:5.

de Blok, W. J. G. and Bosma, A. (2002). High-resolution rotation curves of low surface brightness galaxies. *A&A*, 385:816–846.

de Boer, T. J. L., Tolstoy, E., Hill, V., Saha, A., Olsen, K., Starkenburg, E., Lemasle, B., Irwin, M. J., and Battaglia, G. (2012). The star formation and chemical evolution history of the sculptor dwarf spheroidal galaxyâ. *A&A*, 539:A103.

De Looze, I., Baes, M., Boselli, A., Cortese, L., Fritz, J., Auld, R., Bendo, G. J., Bianchi, S., Boquien, M., Clemens, M., Ciesla, L., Davies, J., di Serego Alighieri, S., Grossi, M., Jones, A., Madden, S. C., Pappalardo, C., Pierini, D., Smith, M. W. L., Verstappen, J., Vlahakis, C., and Zibetti, S. (2013). The Herschel Virgo Cluster Survey - XIV. Transition-type dwarf galaxies in the Virgo cluster. *MNRAS*, 436:1057–1073.

De Rijcke, S., Michielsen, D., Dejonghe, H., Zeilinger, W. W., and Hau, G. K. T. (2005). Formation and evolution of dwarf elliptical galaxies. I. Structural and kinematical properties. *A&A*, 438:491–505.

De Rijcke, S., Penny, S. J., Conselice, C. J., Valcke, S., and Held, E. V. (2009). Hubble Space Telescope survey of the Perseus cluster - II. Photometric scaling relations in different environments. *MNRAS*, 393:798–807.

De Rijcke, S., Prugniel, P., Simien, F., and Dejonghe, H. (2006). The internal dynamics of the Local Group dwarf elliptical galaxies NGC 147, 185 and 205. *MNRAS*, 369:1321–1333.

De Rijcke, S., Schroyen, J., Vandenbroucke, B., Jachowicz, N., Decroos, J., Cloet-Osselaer, A., and Koleva, M. (2013). New composition-dependent cooling and heating curves for galaxy evolution simulations. *MNRAS*, 433:3005–3016.

De Rijcke, S., Van Hese, E., and Buyle, P. (2010). The Conversion of Late-type Into Early-type Dwarf Galaxies by Ram-pressure Stripping in the Fornax Cluster. *ApJL*, 724:L171–L175.

De Rijcke, S., Zeilinger, W. W., Hau, G. K. T., Prugniel, P., and Dejonghe, H. (2007). Generalizations of the Tully-Fisher Relation for Early- and Late-Type Galaxies. *ApJ*, 659:1172–1175.

de Vaucouleurs, G., de Vaucouleurs, A., Corwin, Jr., H. G., Buta, R. J., Paturel, G., and Fouqué, P. (1991). *Third Reference Catalogue of Bright Galaxies. Volume I: Explanations and references. Volume II: Data for galaxies between 0^h and 12^h. Volume III: Data for galaxies between 12^h and 24^h*.

Dere, K. P., Landi, E., Mason, H. E., Monsignori Fossi, B. C., and Young, P. R. (1997). CHIANTI - an atomic database for emission lines. *A&AS*, 125:149–173.

Di Matteo, P., Combes, F., Melchior, A.-L., and Semelin, B. (2007). Star formation efficiency in galaxy interactions and mergers: a statistical study. *A&A*, 468:61–81.

Dolphin, A. E. (2012). On the Estimation of Systematic Uncertainties of Star Formation Histories. *ApJ*, 751:60.

Duc, P.-A., Brinks, E., Springel, V., Pichardo, B., Weilbacher, P., and Mirabel, I. F. (2000). Formation of a Tidal Dwarf Galaxy in the Interacting System Arp 245 (NGC 2992/93). *AJ*, 120:1238–1264.

Dunn, J. M. (2010). The evolution of dwarf galaxies: a comparison of UBVR photometry. *MNRAS*, 408:392–399.

Elbert, O. D., Bullock, J. S., Garrison-Kimmel, S., Rocha, M., Oñorbe, J., and Peter, A. H. G. (2014). Core Formation in Dwarf Halos with Self Interacting Dark Matter: No Fine-Tuning Necessary. *ArXiv e-prints*.

Faucher-Giguère, C.-A., Lidz, A., Zaldarriaga, M., and Hernquist, L. (2009). A New Calculation of the Ionizing Background Spectrum and the Effects of He II Reionization. *ApJ*, 703:1416–1443.

Feldmann, R. and Mayer, L. (2015). The Argo simulation - I. Quenching of massive galaxies at high redshift as a result of cosmological starvation. *MNRAS*, 446:1939–1956.

Fiacconi, D., Feldmann, R., and Mayer, L. (2015). The Argo simulation - II. The early build-up of the Hubble sequence. *MNRAS*, 446:1957–1972.

Franx, M., Illingworth, G., and de Zeeuw, T. (1991). The ordered nature of elliptical galaxies - Implications for their intrinsic angular momenta and shapes. *ApJ*, 383:112–134.

Frebel, A. and Bromm, V. (2012). Chemical Signatures of the First Galaxies: Criteria for One-shot Enrichment. *ApJ*, 759:115.

Gallart, C. (2012). *Constraints on the Effects of Reionization in the Star Formation History of Dwarf Galaxies: Some Conclusions from the LCID Project*, page 103.

Gallart, C. and Lcid Team (2007). The ACS LCID project: overview and first results. In Vazdekis, A. and Peletier, R., editors, *IAU Symposium*, volume 241 of *IAU Symposium*, pages 290–294.

Gao, L., Navarro, J. F., Cole, S., Frenk, C. S., White, S. D. M., Springel, V., Jenkins, A., and Neto, A. F. (2008). The redshift dependence of the structure of massive Λ cold dark matter haloes. *MNRAS*, 387:536–544.

Garrison-Kimmel, S., Boylan-Kolchin, M., Bullock, J. S., and Lee, K. (2014). ELVIS: Exploring the Local Volume in Simulations. *MNRAS*, 438:2578–2596.

Garrison-Kimmel, S., Rocha, M., Boylan-Kolchin, M., Bullock, J. S., and Lally, J. (2013). Can feedback solve the too-big-to-fail problem? *MNRAS*, 433:3539–3546.

Gatto, A., Fraternali, F., Read, J. I., Marinacci, F., Lux, H., and Walch, S. (2013). Unveiling the corona of the Milky Way via ram-pressure stripping of dwarf satellites. *MNRAS*, 433:2749–2763.

Geha, M., Blanton, M. R., Masjedi, M., and West, A. A. (2006). The Baryon Content of Extremely Low Mass Dwarf Galaxies. *ApJ*, 653:240–254.

Geha, M., Guhathakurta, P., and van der Marel, R. P. (2003). Internal Dynamics, Structure, and Formation of Dwarf Elliptical Galaxies. II. Rotating versus Nonrotating Dwarfs. *AJ*, 126:1794–1810.

Gentile, G., Burkert, A., Salucci, P., Klein, U., and Walter, F. (2005). The Dwarf Galaxy DDO 47 as a Dark Matter Laboratory: Testing Cusps Hiding in Triaxial Halos. *ApJL*, 634:L145–L148.

Gentile, G., Salucci, P., Klein, U., Vergani, D., and Kalberla, P. (2004). The cored distribution of dark matter in spiral galaxies. *MNRAS*, 351:903–922.

Gingold, R. A. and Monaghan, J. J. (1977). Smoothed particle hydrodynamics - Theory and application to non-spherical stars. *MNRAS*, 181:375–389.

Giovanelli, R. and Haynes, M. P. (2002). The Inner Scale Length of Spiral Galaxy Rotation Curves. *ApJL*, 571:L107–L111.

Girardi, L., Williams, B. F., Gilbert, K. M., Rosenfield, P., Dalcanton, J. J., Marigo, P., Boyer, M. L., Dolphin, A., Weisz, D. R., Melbourne, J., Olsen, K. A. G., Seth, A. C., and Skillman, E. (2010). The ACS Nearby Galaxy Survey Treasury. IX. Constraining Asymptotic Giant Branch Evolution with Old Metal-poor Galaxies. *ApJ*, 724:1030–1043.

Gnedin, N. Y., Tassis, K., and Kravtsov, A. V. (2009). Modeling Molecular Hydrogen and Star Formation in Cosmological Simulations. *ApJ*, 697:55–67.

Goerdt, T., Moore, B., Read, J. I., and Stadel, J. (2010). Core Creation in Galaxies and Halos Via Sinking Massive Objects. *ApJ*, 725:1707–1716.

Goerdt, T., Moore, B., Read, J. I., Stadel, J., and Zemp, M. (2006). Does the Fornax dwarf spheroidal have a central cusp or core? *MNRAS*, 368:1073–1077.

González-García, A. C. and van Albada, T. S. (2005). Encounters between spherical galaxies - II. Systems with a dark halo. *MNRAS*, 361:1043–1054.

González-Samaniego, A., Colín, P., Avila-Reese, V., Rodríguez-Puebla, A., and Valenzuela, O. (2013). Simulations of isolated dwarf galaxies formed in dark matter halos with different mass assembly histories. *ArXiv:1308.4753*.

Governato, F., Brook, C., Mayer, L., Brooks, A., Rhee, G., Wadsley, J., Jonsson, P., Willman, B., Stinson, G., Quinn, T., and Madau, P. (2010). Bulgeless dwarf galaxies and dark matter cores from supernova-driven outflows. *Nature*, 463:203–206.

Governato, F., Zolotov, A., Pontzen, A., Christensen, C., Oh, S. H., Brooks, A. M., Quinn, T., Shen, S., and Wadsley, J. (2012). Cuspy no more: how outflows affect the central dark matter and baryon distribution in Λ cold dark matter galaxies. *MNRAS*, 422:1231–1240.

Graham, A. W. and Guzmán, R. (2003). HST Photometry of Dwarf Elliptical Galaxies in Coma, and an Explanation for the Alleged Structural Dichotomy between Dwarf and Bright Elliptical Galaxies. *AJ*, 125:2936–2950.

Grebel, E. K., Gallagher, I. J. S., and Harbeck, D. (2003). The Progenitors of Dwarf Spheroidal Galaxies. *AJ*, 125:1926–1939.

Guedes, J., Callegari, S., Madau, P., and Mayer, L. (2011). Forming Realistic Late-type Spirals in a ΛCDM Universe: The Eris Simulation. *ApJ*, 742:76.

Guo, Q., White, S., Li, C., and Boylan-Kolchin, M. (2010). How do galaxies populate dark matter haloes? *MNRAS*, 404:1111–1120.

Gurovich, S., Freeman, K., Jerjen, H., Staveley-Smith, L., and Puerari, I. (2010). The Slope of the Baryonic Tully-Fisher Relation. *AJ*, 140:663–676.

Hidalgo, S. L., Aparicio, A., Skillman, E., Monelli, M., Gallart, C., Cole, A., Dolphin, A., Weisz, D., Bernard, E. J., Cassisi, S., Mayer, L., Stetson, P., Tolstoy, E., and Ferguson, H. (2011). The ACS LCID Project. V. The Star Formation History of the Dwarf Galaxy LGS-3: Clues to Cosmic Reionization and Feedback. *ApJ*, 730:14.

Hidalgo, S. L., Monelli, M., Aparicio, A., Gallart, C., Skillman, E. D., Cassisi, S., Bernard, E. J., Mayer, L., Stetson, P., Cole, A., and Dolphin, A. (2013). The ACS LCID project. IX. Imprints of the early Universe in the radial variation of the star formation history of dwarf galaxies. *ArXiv e-prints*.

Hinshaw, G., Larson, D., Komatsu, E., Spergel, D. N., Bennett, C. L., Dunkley, J., Nolta, M. R., Halpern, M., Hill, R. S., Odegard, N., Page, L., Smith, K. M., Weiland, J. L., Gold, B., Jarosik, N., Kogut, A., Limon, M., Meyer, S. S., Tucker, G. S., Wollack, E., and Wright, E. L. (2013). Nine-year Wilkinson Microwave Anisotropy Probe (WMAP) Observations: Cosmological Parameter Results. *ApJS*, 208:19.

Hopkins, P. F., Narayanan, D., and Murray, N. (2013). The meaning and consequences of star formation criteria in galaxy models with resolved stellar feedback. *MNRAS*, 432:2647–2653.

Hunter, D. A. and Elmegreen, B. G. (2006). Broadband Imaging of a Large Sample of Irregular Galaxies. *ApJS*, 162:49–79.

Hunter, D. A., Ficut-Vicas, D., Ashley, T., Brinks, E., Cigan, P., Elmegreen, B. G., Heesen, V., Herrmann, K. A., Johnson, M., Oh, S.-H., Rupen, M. P., Schruba, A., Simpson, C. E., Walter, F., Westpfahl, D. J., Young, L. M., and Zhang, H.-X. (2012). Little Things. *AJ*, 144:134.

Irwin, M. and Hatzidimitriou, D. (1995). Structural parameters for the Galactic dwarf spheroidals. *MNRAS*, 277:1354–1378.

Jester, S., Schneider, D. P., Richards, G. T., Green, R. F., Schmidt, M., Hall, P. B., Strauss, M. A., Vanden Berk, D. E., Stoughton, C., Gunn, J. E., Brinkmann, J., Kent, S. M., Smith, J. A., Tucker, D. L., and Yanny, B. (2005). The Sloan Digital Sky Survey View of the Palomar-Green Bright Quasar Survey. *AJ*, 130:873–895.

Jiang, L., Cole, S., Sawala, T., and Frenk, C. S. (2014). Orbital parameters of infalling satellite haloes in the hierarchical ΛCDM model. *ArXiv e-prints*.

Katz, N., Weinberg, D. H., and Hernquist, L. (1996). Cosmological Simulations with TreeSPH. *ApJS*, 105:19–+.

Kauffmann, G. and White, S. D. M. (1993). The merging history of dark matter haloes in a hierarchical universe. *MNRAS*, 261:921–928.

Kirby, E. N., Bullock, J. S., Boylan-Kolchin, M., Kaplinghat, M., and Cohen, J. G. (2014). The dynamics of isolated Local Group galaxies. *MNRAS*, 439:1015–1027.

Kirby, E. N., Cohen, J. G., and Bellazzini, M. (2012). The Dynamics and Metallicity Distribution of the Distant Dwarf Galaxy VV124. *ApJ*, 751:46.

Kirby, E. N., Cohen, J. G., Guhathakurta, P., Cheng, L., Bullock, J. S., and Gallazzi, A. (2013). The Universal Stellar Mass-Stellar Metallicity Relation for Dwarf Galaxies. *ApJ*, 779:102.

Kirby, E. N., Lanfranchi, G. A., Simon, J. D., Cohen, J. G., and Guhathakurta, P. (2011). Multi-element Abundance Measurements from Medium-resolution Spectra. III. Metallicity Distributions of Milky Way Dwarf Satellite Galaxies. *ApJ*, 727:78.

Kirby, E. N., Simon, J. D., Geha, M., Guhathakurta, P., and Frebel, A. (2008). Uncovering Extremely Metal-Poor Stars in the Milky Way's Ultrafaint Dwarf Spheroidal Satellite Galaxies. *ApJL*, 685:L43–L46.

Kleyna, J. T., Wilkinson, M. I., Evans, N. W., and Gilmore, G. (2005). Ursa Major: A Missing Low-Mass CDM Halo? *ApJL*, 630:L141–L144.

Klimentowski, J., Łokas, E. L., Kazantzidis, S., Mayer, L., and Mamon, G. A. (2009). Tidal evolution of discy dwarf galaxies in the Milky Way potential: the formation of dwarf spheroidals. *MNRAS*, 397:2015–2029.

Klypin, A., Kravtsov, A. V., Valenzuela, O., and Prada, F. (1999). Where Are the Missing Galactic Satellites? *ApJ*, 522:82–92.

Klypin, A. A., Trujillo-Gomez, S., and Primack, J. (2011). Dark Matter Halos in the Standard Cosmological Model: Results from the Bolshoi Simulation. *ApJ*, 740:102.

Koleva, M., Bouchard, A., Prugniel, P., De Rijcke, S., and Vauglin, I. (2013). The transmutation of dwarf galaxies: stellar populations. *MNRAS*, 428:2949–2965.

Koleva, M., de Rijcke, S., Prugniel, P., Zeilinger, W. W., and Michielsen, D. (2009). Formation and evolution of dwarf elliptical galaxies - II. Spatially resolved star formation histories. *MNRAS*, 396:2133–2151.

Kronawitter, A., Saglia, R. P., Gerhard, O., and Bender, R. (2000). Orbital structure and mass distribution in elliptical galaxies. *A&AS*, 144:53–84.

Lacey, C. and Cole, S. (1993). Merger rates in hierarchical models of galaxy formation. *MNRAS*, 262:627–649.

Lacey, C. and Cole, S. (1994). Merger Rates in Hierarchical Models of Galaxy Formation - Part Two - Comparison with N-Body Simulations. *MNRAS*, 271:676.

Landi, E., Young, P. R., Dere, K. P., Del Zanna, G., and Mason, H. E. (2013). CHIANTIAn Atomic Database for Emission Lines. XIII. Soft X-Ray Improvements and Other Changes. *ApJ*, 763:86.

Laporte, C. F. P. and Peñarrubia, J. (2015). Under the sword of Damocles: plausible regeneration of dark matter cusps at the smallest galactic scales. *MNRAS*, 449:L90–L94.

Lauer, T. R., Ajhar, E. A., Byun, Y.-I., Dressler, A., Faber, S. M., Grillmair, C., Kormendy, J., Richstone, D., and Tremaine, S. (1995). The Centers of Early-Type Galaxies with HST.I.An Observational Survey. *AJ*, 110:2622.

Leaman, R., Venn, K. A., Brooks, A. M., Battaglia, G., Cole, A. A., Ibata, R. A., Irwin, M. J., McConnachie, A. W., Mendel, J. T., Starkenburg, E., and Tolstoy, E. (2013). The Comparative Chemical Evolution of an Isolated Dwarf Galaxy: A VLT and Keck Spectroscopic Survey of WLM. *ApJ*, 767:131.

Leaman, R., Venn, K. A., Brooks, A. M., Battaglia, G., Cole, A. A., Ibata, R. A., Irwin, M. J., McConnachie, A. W., Mendel, J. T., and Tolstoy, E. (2012). The Resolved Structure and Dynamics of an Isolated Dwarf Galaxy: A VLT and Keck Spectroscopic Survey of WLM. *ApJ*, 750:33.

Lianou, S., Grebel, E. K., and Koch, A. (2010). Dwarf spheroidals in the M 81 group - Metallicity distribution functions and population gradients. *A&A*, 521:A43.

Liesenborgs, J., de Rijcke, S., Dejonghe, H., and Bekaert, P. (2009). Non-parametric strong lens inversion of SDSS J1004+4112. *MNRAS*, 397:341–349.

Łokas, E. L. (2009). The mass and velocity anisotropy of the Carina, Fornax, Sculptor and Sextans dwarf spheroidal galaxies. *MNRAS*, 394:L102–L106.

Łokas, E. L., Kazantzidis, S., and Mayer, L. (2011). Evolutionary Tracks of Tidally Stirred Disky Dwarf Galaxies. *ApJ*, 739:46.

Łokas, E. L. and Mamon, G. A. (2001). Properties of spherical galaxies and clusters with an NFW density profile. *MNRAS*, 321:155–166.

Lucy, L. B. (1977). A numerical approach to the testing of the fission hypothesis. *AJ*, 82:1013–1024.

Magorrian, J. and Ballantyne, D. (2001). Mass profiles and anisotropies of early-type galaxies. *MNRAS*, 322:702–714.

Maio, U., Dolag, K., Ciardi, B., and Tornatore, L. (2007). Metal and molecule cooling in simulations of structure formation. *MNRAS*, 379:963–973.

Mandelbaum, R., Seljak, U., Kauffmann, G., Hirata, C. M., and Brinkmann, J. (2006). Galaxy halo masses and satellite fractions from galaxy-galaxy lensing in the Sloan Digital Sky Survey: stellar mass, luminosity, morphology and environment dependencies. *MNRAS*, 368:715–731.

Mashchenko, S., Couchman, H. M. P., and Wadsley, J. (2006). The removal of cusps from galaxy centres by stellar feedback in the early Universe. *Nature*, 442:539–542.

Mateo, M. L. (1998). Dwarf Galaxies of the Local Group. *ARA&A*, 36:435–506.

Mathis, J. S., Mezger, P. G., and Panagia, N. (1983). Interstellar radiation field and dust temperatures in the diffuse interstellar matter and in giant molecular clouds. *A&A*, 128:212–229.

Mayer, L., Governato, F., Colpi, M., Moore, B., Quinn, T., Wadsley, J., Stadel, J., and Lake, G. (2001a). The Metamorphosis of Tidally Stirred Dwarf Galaxies. *ApJ*, 559:754–784.

Mayer, L., Governato, F., Colpi, M., Moore, B., Quinn, T., Wadsley, J., Stadel, J., and Lake, G. (2001b). Tidal Stirring and the Origin of Dwarf Spheroidals in the Local Group. *ApJL*, 547:L123–L127.

Mayer, L., Governato, F., and Kaufmann, T. (2008). The formation of disk galaxies in computer simulations. *Advanced Science Letters*, 1:7–27.

Mayer, L., Mastropietro, C., Wadsley, J., Stadel, J., and Moore, B. (2006). Simultaneous ram pressure and tidal stripping; how dwarf spheroidals lost their gas. *MNRAS*, 369:1021–1038.

McConnachie, A. W. (2012). The Observed Properties of Dwarf Galaxies in and around the Local Group. *AJ*, 144:4.

McConnachie, A. W., Arimoto, N., and Irwin, M. (2007). Deconstructing dwarf galaxies: a Suprime-Cam survey of Andromeda II. *MNRAS*, 379:379–392.

McConnachie, A. W. and Irwin, M. J. (2006). Structural properties of the M31 dwarf spheroidal galaxies. *MNRAS*, 365:1263–1276.

McGaugh, S. S. (2005). The Baryonic Tully-Fisher Relation of Galaxies with Extended Rotation Curves and the Stellar Mass of Rotating Galaxies. *ApJ*, 632:859–871.

McGaugh, S. S. (2011). Novel Test of Modified Newtonian Dynamics with Gas Rich Galaxies. *Physical Review Letters*, 106(12):121303.

McGaugh, S. S. (2012). The Baryonic Tully-Fisher Relation of Gas-rich Galaxies as a Test of ΛCDM and MOND. *AJ*, 143:40.

McGaugh, S. S., Schombert, J. M., Bothun, G. D., and de Blok, W. J. G. (2000). The Baryonic Tully-Fisher Relation. *ApJL*, 533:L99–L102.

McQuinn, K. B. W., Skillman, E. D., Cannon, J. M., Dalcanton, J., Dolphin, A., Hidalgo-Rodríguez, S., Holtzman, J., Stark, D., Weisz, D., and Williams, B. (2010a). The Nature of Starbursts. I. The Star Formation Histories of Eighteen Nearby Starburst Dwarf Galaxies. *ApJ*, 721:297–317.

McQuinn, K. B. W., Skillman, E. D., Cannon, J. M., Dalcanton, J., Dolphin, A., Hidalgo-Rodríguez, S., Holtzman, J., Stark, D., Weisz, D., and Williams, B. (2010b). The Nature of Starbursts. II. The Duration of Starbursts in Dwarf Galaxies. *ApJ*, 724:49–58.

Monelli, M., Gallart, C., Hidalgo, S. L., Aparicio, A., Skillman, E. D., Cole, A. A., Weisz, D. R., Mayer, L., Bernard, E. J., Cassisi, S., Dolphin, A. E., Drozdovsky, I., and Stetson, P. B. (2010a). The ACS LCID Project. VI. The Star Formation History of The Tucana dSph and The Relative Ages of the Isolated dSph Galaxies. *ApJ*, 722:1864–1878.

Monelli, M., Hidalgo, S. L., Stetson, P. B., Aparicio, A., Gallart, C., Dolphin, A. E., Cole, A. A., Weisz, D. R., Skillman, E. D., Bernard, E. J., Mayer, L., Navarro, J. F., Cassisi, S., Drozdovsky, I., and Tolstoy, E. (2010b). The ACS LCID Project. III. The Star Formation History of the Cetus dSph Galaxy: A Post-reionization Fossil. *ApJ*, 720:1225–1245.

Moore, B., Ghigna, S., Governato, F., Lake, G., Quinn, T., Stadel, J., and Tozzi, P. (1999). Dark Matter Substructure within Galactic Halos. *ApJL*, 524:L19–L22.

Moore, B., Katz, N., and Lake, G. (1996). On the Destruction and Overmerging of Dark Halos in Dissipationless N-Body Simulations. *ApJ*, 457:455–+.

Napolitano, N. R., Romanowsky, A. J., Capaccioli, M., Douglas, N. G., Arnaboldi, M., Coccato, L., Gerhard, O., Kuijken, K., Merrifield, M. R., Bamford, S. P., Cortesi, A., Das, P., and Freeman, K. C. (2011). The PN.S Elliptical Galaxy Survey: a standard ΛCDM halo around NGC 4374? *MNRAS*, 411:2035–2053.

Navarro, J. F., Eke, V. R., and Frenk, C. S. (1996a). The cores of dwarf galaxy haloes. *MNRAS*, 283:L72–L78.

Navarro, J. F., Frenk, C. S., and White, S. D. M. (1996b). The Structure of Cold Dark Matter Halos. *apj*, 462:563–+.

Nickerson, S., Stinson, G., Couchman, H. M. P., Bailin, J., and Wadsley, J. (2011). Mechanisms of baryon loss for dark satellites in cosmological smoothed particle hydrodynamics simulations. *MNRAS*, 415:257–270.

Oñorbe, J., Boylan-Kolchin, M., Bullock, J. S., Hopkins, P. F., Kereš, D., Faucher-Giguère, C.-A., Quataert, E., and Murray, N. (2015). Forged in FIRE: cusps, cores, and baryons in low-mass dwarf galaxies. *ArXiv e-prints*.

Oh, S.-H., Brook, C., Governato, F., Brinks, E., Mayer, L., de Blok, W. J. G., Brooks, A., and Walter, F. (2011a). The Central Slope of Dark Matter Cores in Dwarf Galaxies: Simulations versus THINGS. *AJ*, 142:24.

Oh, S.-H., de Blok, W. J. G., Brinks, E., Walter, F., and Kennicutt, Jr., R. C. (2011b). Dark and Luminous Matter in THINGS Dwarf Galaxies. *AJ*, 141:193.

Oh, S.-H., Hunter, D. A., Brinks, E., Elmegreen, B. G., Schruba, A., Walter, F., Rupen, M. P., Young, L. M., Simpson, C. E., Johnson, M., Herrmann, K. A., Ficut-Vicas, D., Cigan, P., Heesen, V., Ashley, T., and Zhang, H.-X. (2015). High-resolution mass models of dwarf galaxies from LITTLE THINGS. *ArXiv e-prints*.

Okamoto, T., Gao, L., and Theuns, T. (2008). Mass loss of galaxies due to an ultraviolet background. *MNRAS*, 390:920–928.

Ott, J., Stilp, A. M., Warren, S. R., Skillman, E. D., Dalcanton, J. J., Walter, F., de Blok, W. J. G., Koribalski, B., and West, A. A. (2012). VLA-ANGST: A High-resolution H I Survey of Nearby Dwarf Galaxies. *AJ*, 144:123.

Papaderos, P., Loose, H.-H., Fricke, K. J., and Thuan, T. X. (1996). Optical structure and star formation in blue compact dwarf galaxies. II. Relations between photometric components and evolutionary implications. *A&A*, 314:59–72.

Papastergis, E., Giovanelli, R., Haynes, M. P., and Shankar, F. (2014). Is there a "too big to fail" problem in the field? *ArXiv e-prints*.

Parkinson, H., Cole, S., and Helly, J. (2008). Generating dark matter halo merger trees. *MNRAS*, 383:557–564.

Peñarrubia, J., Pontzen, A., Walker, M. G., and Koposov, S. E. (2012). The Coupling between the Core/Cusp and Missing Satellite Problems. *ApJL*, 759:L42.

Peletier, R. F. and Christodoulou, D. M. (1993). A photometric and dynamical study of the Helix galaxy NGC 2685. *AJ*, 105:1378–1391.

Pelupessy, F. I., van der Werf, P. P., and Icke, V. (2004). Periodic bursts of star formation in irregular galaxies. *A&A*, 422:55–64.

Penny, S. J., Forbes, D. A., Strader, J., Usher, C., Brodie, J. P., and Romanowsky, A. J. (2014). Ultracompact dwarfs in the Perseus Cluster: UCD formation via tidal stripping. *MNRAS*, 439:3808–3816.

Peterson, R. C. and Caldwell, N. (1993). Stellar velocity dispersions of dwarf elliptical galaxies. *AJ*, 105:1411–1419.

Pietrinferni, A., Cassisi, S., Salaris, M., and Castelli, F. (2004). A Large Stellar Evolution Database for Population Synthesis Studies. I. Scaled Solar Models and Isochrones. *ApJ*, 612:168–190.

Planck Collaboration, Ade, P. A. R., Aghanim, N., Armitage-Caplan, C., Arnaud, M., Ashdown, M., Atrio-Barandela, F., Aumont, J., Baccigalupi, C., Banday, A. J., and et al. (2014). Planck 2013 results. XVI. Cosmological parameters. *A&A*, 571:A16.

Pontzen, A. and Governato, F. (2012). How supernova feedback turns dark matter cusps into cores. *MNRAS*, 421:3464–3471.

Press, W. H. and Schechter, P. (1974). Remark on the Statistical Significance of Flares in Poisson Count Data. *ApJ*, 193:437–442.

Read, J. I. and Gilmore, G. (2005). Mass loss from dwarf spheroidal galaxies: the origins of shallow dark matter cores and exponential surface brightness profiles. *MNRAS*, 356:107–124.

Revaz, Y., Jablonka, P., Sawala, T., Hill, V., Letarte, B., Irwin, M., Battaglia, G., Helmi, A., Shetrone, M. D., Tolstoy, E., and Venn, K. A. (2009). The dynamical and chemical evolution of dwarf spheroidal galaxies. *A&A*, 501:189–206.

Rhode, K. L., Salzer, J. J., Haurberg, N. C., Van Sistine, A., Young, M. D., Haynes, M. P., Giovanelli, R., Cannon, J. M., Skillman, E. D., McQuinn, K. B. W., and Adams, E. A. K. (2013). ALFALFA Discovery of the Nearby Gas-rich Dwarf Galaxy Leo P. II. Optical Imaging Observations. *AJ*, 145:149.

Romanowsky, A. J. and Fall, S. M. (2012). Angular Momentum and Galaxy Formation Revisited. *ApJS*, 203:17.

Roychowdhury, S., Chengalur, J. N., Begum, A., and Karachentsev, I. D. (2009). Star formation in extremely faint dwarf galaxies. *MNRAS*, 397:1435–1453.

Saitoh, T. R., Daisaka, H., Kokubo, E., Makino, J., Okamoto, T., Tomisaka, K., Wada, K., and Yoshida, N. (2008). Toward First-Principle Simulations of Galaxy Formation: I. How Should We Choose Star-Formation Criteria in High-Resolution Simulations of Disk Galaxies? *PASJ*, 60:667–.

Salpeter, E. E. (1955). The Luminosity Function and Stellar Evolution. *ApJ*, 121:161.

Salvadori, S. and Ferrara, A. (2009). Ultra faint dwarfs: probing early cosmic star formation. *MNRAS*, 395:L6–L10.

Salzer, J. J. and Norton, S. A. (1999). Gas rich Low Surface Brightness galaxies - progenitors of blue compact dwarfs? In Davies, J. I., Impey, C., and Phillips, S., editors, *The Low Surface Brightness Universe*, volume 170 of *Astronomical Society of the Pacific Conference Series*, page 253.

Saviane, I., Held, E. V., and Piotto, G. (1996). CCD photometry of the Tucana dwarf galaxy. *A&A*, 315:40–51.

Sawala, T., Frenk, C. S., Fattahi, A., Navarro, J. F., Theuns, T., Bower, R. G., Crain, R. A., Furlong, M., Jenkins, A., Schaller, M., and Schaye, J. (2014). The chosen few: the low mass halos that host faint galaxies. *ArXiv e-prints*.

Sawala, T., Guo, Q., Scannapieco, C., Jenkins, A., and White, S. (2011). What is the (dark) matter with dwarf galaxies? *MNRAS*, 413:659–668.

Sawala, T., Scannapieco, C., Maio, U., and White, S. (2010). Formation of isolated dwarf galaxies with feedback. *MNRAS*, 402:1599–1613.

Sawala, T., Scannapieco, C., and White, S. (2012). Local Group dwarf galaxies: nature and nurture. *MNRAS*, 420:1714–1730.

Scannapieco, C., Wadepuhl, M., Parry, O. H., Navarro, J. F., Jenkins, A., , V., Teyssier, R., Carlson, E., Couchman, H. M. P., Crain, R. A., Dalla Vecchia, C., Frenk, C. S., Kobayashi, C., Monaco, P., Murante, G., Okamoto, T., Quinn, T., Schaye, J., Stinson, G. S., Theuns, T., Wadsley, J., White, S. D. M., and Woods, R. (2012). The Aquila comparison project: the effects of feedback and numerical methods on simulations of galaxy formation. *MNRAS*, 423:1726–1749.

Scannapieco, C., White, S. D. M., Springel, V., and Tissera, P. B. (2009). The formation and survival of discs in a ΛCDM universe. *MNRAS*, 396:696–708.

Schaap, W. E. and van de Weygaert, R. (2000). Continuous fields and discrete samples: reconstruction through Delaunay tessellations. *A&A*, 363:L29–L32.

Schaye, J., Crain, R. A., Bower, R. G., Furlong, M., Schaller, M., Theuns, T., Dalla Vecchia, C., Frenk, C. S., McCarthy, I. G., Helly, J. C., Jenkins, A., Rosas-Guevara, Y. M., White, S. D. M., Baes, M., Booth, C. M., Camps, P., Navarro, J. F., Qu, Y., Rahmati, A., Sawala, T., Thomas, P. A., and Trayford, J. (2015). The EAGLE project: simulating the evolution and assembly of galaxies and their environments. *MNRAS*, 446:521–554.

Schmidt, M. (1959). The Rate of Star Formation. *apj*, 129:243–+.

Schroyen, J., De Rijcke, S., Koleva, M., Cloet-Osselaer, A., and Vandenbroucke, B. (2013). Stellar orbits and the survival of metallicity gradients in simulated dwarf galaxies. *MNRAS*, 434:888–905.

Schroyen, J., de Rijcke, S., Valcke, S., Cloet-Osselaer, A., and Dejonghe, H. (2011). Simulations of the formation and evolution of isolated dwarf galaxies - II. Angular momentum as a second parameter. *MNRAS*, 416:601–617.

Scudder, J. M., Ellison, S. L., Torrey, P., Patton, D. R., and Mendel, J. T. (2012). Galaxy pairs in the Sloan Digital Sky Survey - V. Tracing changes in star formation rate and metallicity out to separations of 80 kpc. *MNRAS*, 426:549–565.

Sellwood, J. A. and Athanassoula, E. (1986). Unstable modes from galaxy simulations. *MNRAS*, 221:195–212.

Sharina, M. E., Karachentsev, I. D., Dolphin, A. E., Karachentseva, V. E., Tully, R. B., Karataeva, G. M., Makarov, D. I., Makarova, L. N., Sakai, S., Shaya, E. J., Nikolaev, E. Y., and Kuznetsov, A. N. (2008). Photometric properties of the Local Volume dwarf galaxies. *MNRAS*, 384:1544–1562.

Shaviv, N. J. and Dekel, A. (2003). Photo-evaporation by thermal winds in dwarf galaxies. *ArXiv:astro-ph/0305527*.

Shen, S., Madau, P., Conroy, C., Governato, F., and Mayer, L. (2014). The Baryon Cycle of Dwarf Galaxies: Dark, Bursty, Gas-rich Polluters. *ApJ*, 792:99.

Sheth, R. K. and Tormen, G. (1999). Large-scale bias and the peak background split. *MNRAS*, 308:119–126.

Skillman, E. D., Hidalgo, S. L., Weisz, D. R., Monelli, M., Gallart, C., Aparicio, A., Bernard, E. J., Boylan-Kolchin, M., Cassisi, S., Cole, A. A., Dolphin, A. E., Ferguson, H. C., Mayer, L., Navarro, J. F., Stetson, P. B., and Tolstoy, E. (2014). The ACS LCID Project. X. The Star Formation History of IC 1613: Revisiting the Over-cooling Problem. *ApJ*, 786:44.

Skillman, E. D., Tolstoy, E., Cole, A. A., Dolphin, A. E., Saha, A., Gallagher, J. S., Dohm-Palmer, R. C., and Mateo, M. (2003). Deep Hubble Space Telescope Imaging of IC 1613. II. The Star Formation History. *ApJ*, 596:253–272.

Smith Castelli, A. V., Bassino, L. P., Richtler, T., Cellone, S. A., Aruta, C., and Infante, L. (2008). Galaxy populations in the Antlia cluster - I. Photometric properties of early-type galaxies. *MNRAS*, 386:2311–2322.

Somerville, R. S. and Kolatt, T. S. (1999). How to plant a merger tree. *MNRAS*, 305:1–14.

Spergel, D. N., Bean, R., and Nolta, M. R. (2007). Three-Year Wilkinson Microwave Anisotropy Probe (WMAP) Observations: Implications for Cosmology. *ApJS*, 170:377–408.

Springel, V. (2005). The cosmological simulation code GADGET-2. *MNRAS*, 364:1105–1134.

Springel, V., Wang, J., Vogelsberger, M., Ludlow, A., Jenkins, A., Helmi, A., Navarro, J. F., Frenk, C. S., and White, S. D. M. (2008). The Aquarius Project: the subhaloes of galactic haloes. *MNRAS*, 391:1685–1711.

Springel, V., White, S. D. M., Jenkins, A., Frenk, C. S., Yoshida, N., Gao, L., Navarro, J., Thacker, R., Croton, D., Helly, J., Peacock, J. A., Cole, S., Thomas, P., Couchman, H., Evrard, A., Colberg, J., and Pearce, F. (2005). Simulating the joint evolution of quasars, galaxies and their large-scale distribution. *Nature 435:629-636,2005*.

Srisawat, C., Knebe, A., Pearce, F. R., Schneider, A., Thomas, P. A., Behroozi, P., Dolag, K., Elahi, P. J., Han, J., Helly, J., Jing, Y., Jung, I., Lee, J., Mao, Y.-Y., Onions, J., Rodriguez-Gomez, V., Tweed, D., and Yi, S. K. (2013). Sussing Merger Trees: The Merger Trees Comparison Project. *MNRAS*, 436:150–162.

Stark, D. V., McGaugh, S. S., and Swaters, R. A. (2009). A First Attempt to Calibrate the Baryonic Tully-Fisher Relation with Gas-Dominated Galaxies. *AJ*, 138:392–401.

Steinmetz, M. and Navarro, J. F. (1999). The Cosmological Origin of the Tully-Fisher Relation. *ApJ*, 513:555–560.

Stinson, G., Seth, A., Katz, N., Wadsley, J., Governato, F., and Quinn, T. (2006). Star formation and feedback in smoothed particle hydrodynamic simulations - I. Isolated galaxies. *MNRAS*, 373:1074–1090.

Stinson, G. S., Brook, C., Prochaska, J. X., Hennawi, J., Shen, S., Wadsley, J., Pontzen, A., Couchman, H. M. P., Quinn, T., Macciò, A. V., and Gibson, B. K. (2012). MAGICC haloes: confronting simulations with observations of the circumgalactic medium at z=0. *MNRAS*, 425:1270–1277.

Stinson, G. S., Dalcanton, J. J., Quinn, T., Gogarten, S. M., Kaufmann, T., and Wadsley, J. (2009). Feedback and the formation of dwarf galaxy stellar haloes. *MNRAS*, 395:1455–1466.

Stinson, G. S., Dalcanton, J. J., Quinn, T., Kaufmann, T., and Wadsley, J. (2007a). Breathing in Low-Mass Galaxies: A Study of Episodic Star Formation. *ApJ*, 667:170–175.

Stinson, G. S., Quinn, T., Dalcanton, J., Wadsley, J., and Gogarten, S. (2007b). Supernova Feedback in Smoothed Particle Hydrodynamics Simulations of Dwarf Galaxy Formation. In *American Astronomical Society Meeting Abstracts*, volume 39 of *Bulletin of the American Astronomical Society*, page 766.

Strigari, L. E., Koushiappas, S. M., Bullock, J. S., and Kaplinghat, M. (2007). Precise constraints on the dark matter content of MilkyWay dwarf galaxies for gamma-ray experiments. *Phys.Rev. D*, 75(8):083526.

Strolger, L.-G., Dahlen, T., and Riess, A. G. (2010). Empirical Delay-time Distributions of Type Ia Supernovae from the Extended Goods/Hubble Space Telescope Supernova Survey. *ApJ*, 713:32–40.

Sutherland, R. S. and Dopita, M. A. (1993). Cooling functions for low-density astrophysical plasmas. *ApJS*, 88:253–327.

Sweet, S. M., Drinkwater, M. J., Meurer, G., Bekki, K., Dopita, M. A., Kilborn, V., and Nicholls, D. C. (2014). Choirs H I Galaxy Groups: The Metallicity of Dwarf Galaxies. *ApJ*, 782:35.

Tammann, G. A. (1994). Dwarf Galaxies in the Past. In Meylan, G. and Prugniel, P., editors, *European Southern Observatory Conference and Workshop Proceedings*, volume 49 of *European Southern Observatory Conference and Workshop Proceedings*, page 3.

Teyssier, R., Pontzen, A., Dubois, Y., and Read, J. I. (2013). Cusp-core transformations in dwarf galaxies: observational predictions. *MNRAS*, 429:3068–3078.

Thornton, K., Gaudlitz, M., Janka, H.-T., and Steinmetz, M. (1998). Energy Input and Mass Redistribution by Supernovae in the Interstellar Medium. *apj*, 500:95–+.

Tollerud, E. J., Boylan-Kolchin, M., and Bullock, J. S. (2014). M31 satellite masses compared to ΛCDM subhaloes. *MNRAS*, 440:3511–3519.

Tollerud, E. J., Geha, M. C., Grcevich, J., Putman, M. E., and Stern, D. (2015). Two Local Volume Dwarf Galaxies Discovered in 21cm Emission: Pisces A and B. *ApJL*, 798:L21.

Tolstoy, E., Hill, V., and Tosi, M. (2009). Star-Formation Histories, Abundances, and Kinematics of Dwarf Galaxies in the Local Group. *ARA&A*, 47:371–425.

Tolstoy, E., Irwin, M. J., Helmi, A., Battaglia, G., Jablonka, P., Hill, V., Venn, K. A., Shetrone, M. D., Letarte, B., Cole, A. A., Primas, F., Francois, P., Arimoto, N., Sadakane, K., Kaufer, A., Szeifert, T., and Abel, T. (2004). Two Distinct Ancient Components in the Sculptor Dwarf Spheroidal Galaxy: First Results from the Dwarf Abundances and Radial Velocities Team. *ApJL*, 617:L119–L122.

Tormen, G. (1998). The assembly of matter in galaxy clusters. *MNRAS*, 297:648–656.

Torrey, P., Cox, T. J., Kewley, L., and Hernquist, L. (2012). The Metallicity Evolution of Interacting Galaxies. *ApJ*, 746:108.

Travaglio, C., Hillebrandt, W., Reinecke, M., and Thielemann, F.-K. (2004). Nucleosynthesis in multi-dimensional SN Ia explosions. *A&A*, 425:1029–1040.

Trujillo-Gomez, S., Klypin, A., Primack, J., and Romanowsky, A. J. (2011). Galaxies in ΛCDM with Halo Abundance Matching: Luminosity-Velocity Relation, Baryonic Mass-Velocity Relation, Velocity Function, and Clustering. *ApJ*, 742:16.

Tsujimoto, T., Nomoto, K., Yoshii, Y., Hashimoto, M., Yanagida, S., and Thielemann, F.-K. (1995). Relative frequencies of Type Ia and Type II supernovae in the chemical evolution of the Galaxy, LMC and SMC. *MNRAS*, 277:945–958.

Tully, R. B. and Fisher, J. R. (1977). A new method of determining distances to galaxies. *A&A*, 54:661–673.

Tully, R. B. and Pierce, M. J. (2000). Distances to Galaxies from the Correlation between Luminosities and Line Widths. III. Cluster Template and Global Measurement of H_0. *ApJ*, $533 : 744 - -780$.

Tully, R. B., Pierce, M. J., Huang, J.-S., Saunders, W., Verheijen, M. A. W., and Witchalls, P. L. (1998). Global Extinction in Spiral Galaxies. *AJ*, 115:2264–2272.

Valcke, S., De Rijcke, S., and Dejonghe, H. (2008). Simulations of the formation and evolution of isolated dwarf galaxies. *MNRAS*, 389:1111–1126.

Valcke, S., De Rijcke, S., Rödiger, E., and Dejonghe, H. (2010). Kelvin-Helmholtz instabilities in smoothed particle hydrodynamics. *MNRAS*, 408:71–86.

van den Bosch, F. C. and Swaters, R. A. (2001). Dwarf galaxy rotation curves and the core problem of dark matter haloes. *MNRAS*, 325:1017–1038.

van Zee, L. (2000). The Evolutionary Status of Isolated Dwarf Irregular Galaxies. I. UBV and Hα Imaging Observations. *AJ*, 119:2757–2779.

van Zee, L., Barton, E. J., and Skillman, E. D. (2004). Stellar Populations of Dwarf Elliptical Galaxies: UBVRI Photometry of Dwarf Elliptical Galaxies in the Virgo Cluster. *AJ*, 128:2797–2814.

VandenBerg, D. A., Bergbusch, P. A., and Dowler, P. D. (2006). The Victoria-Regina Stellar Models: Evolutionary Tracks and Isochrones for a Wide Range in Mass and Metallicity that Allow for Empirically Constrained Amounts of Convective Core Overshooting. *ApJS*, 162:375–387.

Vandenbroucke, B., De Rijcke, S., Schroyen, J., and Jachowicz, N. (2013). Physics of a Partially Ionized Gas Relevant to Galaxy Formation SimulationsThe Ionization Potential Energy Reservoir. *ApJ*, 771:36.

Vazdekis, A., Casuso, E., Peletier, R. F., and Beckman, J. E. (1996). A New Chemo-evolutionary Population Synthesis Model for Early-Type Galaxies. I. Theoretical Basis. *ApJS*, 106:307.

Verheijen, M. A. W. (2001). The Ursa Major Cluster of Galaxies. V. H I Rotation Curve Shapes and the Tully-Fisher Relations. *ApJ*, 563:694–715.

Vogelsberger, M., Genel, S., Springel, V., Torrey, P., Sijacki, D., Xu, D., Snyder, G., Nelson, D., and Hernquist, L. (2014). Introducing the Illustris Project: simulating the coevolution of dark and visible matter in the Universe. *MNRAS*, 444:1518–1547.

Walter, F., Brinks, E., de Blok, W. J. G., Bigiel, F., Kennicutt, Jr., R. C., Thornley, M. D., and Leroy, A. (2008). THINGS: The H I Nearby Galaxy Survey. *AJ*, 136:2563–2647.

Wechsler, R. H., Bullock, J. S., Primack, J. R., Kravtsov, A. V., and Dekel, A. (2002). Concentrations of Dark Halos from Their Assembly Histories. *ApJ*, 568:52–70.

Weilbacher, P. M., Duc, P.-A., and Fritze-v. Alvensleben, U. (2003). Tidal dwarf candidates in a sample of interacting galaxies. II. Properties and kinematics of the ionized gas. *A&A*, 397:545–555.

Weisz, D. R., Dalcanton, J. J., Williams, B. F., Gilbert, K. M., Skillman, E. D., Seth, A. C., Dolphin, A. E., McQuinn, K. B. W., Gogarten, S. M., Holtzman, J., Rosema, K., Cole, A., Karachentsev, I. D., and Zaritsky, D. (2011). The ACS Nearby Galaxy Survey Treasury. VIII. The Global Star Formation Histories of 60 Dwarf Galaxies in the Local Volume. *ApJ*, 739:5.

Wiersma, R. P. C., Schaye, J., and Smith, B. D. (2009). The effect of photoionization on the cooling rates of enriched, astrophysical plasmas. *MNRAS*, 393:99–107.

Worthey, G., Mateo, M., Alonso-García, J., and España, A. L. (2004). Stellar Populations in the Outer Reaches of M31 and M32 from WFPC2 Photometry. *PASP*, 116:295–299.

Yoshii, Y., Tsujimoto, T., and Nomoto, K. (1996). The Lifetime of Type Ia Supernova Progenitors Deduced from the Chemical Evolution in the Solar Neighborhood. *ApJ*, 462:266.

Zhang, J., Fakhouri, O., and Ma, C.-P. (2008). How to grow a healthy merger tree. *MNRAS*, 389:1521–1538.

Zhao, D. H., Jing, Y. P., Mo, H. J., and Börner, G. (2003a). Mass and Redshift Dependence of Dark Halo Structure. *ApJL*, 597:L9–L12.

Zhao, D. H., Mo, H. J., Jing, Y. P., and Börner, G. (2003b). The growth and structure of dark matter haloes. *MNRAS*, 339:12–24.

Zolotov, A., Brooks, A. M., Willman, B., Governato, F., Pontzen, A., Christensen, C., Dekel, A., Quinn, T., Shen, S., and Wadsley, J. (2012). Baryons Matter: Why Luminous Satellite Galaxies have Reduced Central Masses. *ApJ*, 761:71.

Zucker, D. B., Kniazev, A. Y., and Bell, E. F. (2007). Andromeda X, a New Dwarf Spheroidal Satellite of M31: Photometry. *ApJL*, 659:L21–L24.

A

Sampling a dark matter halo

Here, we describe how we sample a dark matter halo with a predefined density profile with a discrete set of particles. We generally know the total mass of the dark matter halo and its density profile. We determine the boundary radius, r_b, where we cut of the dark matter halo. As our dark matter density profiles are all isotropic we can use spherical symmetric coordinates and the probability density function of a particle n to reside at a radius r higher then r_{low} and lower then a radius r_{high} is described by:

$$P(r_{low} < r < r_{high}) = \int_{r_{low}}^{r_{high}} 4\pi\rho(r)r^2 dr \qquad (A.1)$$

Now we discritize our phase space in 500 cells and determine the normalized cumulative distribution function (CDF) in each cell by:

$$F(r) = P(R < r) = \frac{\int_0^R 4\pi\rho(r)r^2 dr}{\int_0^{r_b} 4\pi\rho(r)r^2 dr} \qquad (A.2)$$

In the algorithm itself, the integrals are approximated by finite sums. Then we select a random number between 0 and 1 and trace the corresponding cell in the CDF, which also supplies us with the corresponding r_{low} and r_{high}. Then a traditional acceptance-rejectance technique, see Fig. A.1 for a schematic view, is used where a random r_{rand} is chosen uniformly between r_{low} and r_{high} and this r_{rand} is accepted if the density at r_{rand} is lower then a random number drawn uniformly between 0 and the density in r_{low}, $\rho(r_{low})$ as the density is a decreasing function for increasing radii. Next, v_r, $v_\cdot$ and $v_\oplus$ are drawn from the isotropic distribution function for the NFW model, again with an acceptance-rejectance technique. This isotropic distribution function was constructed from the NFW density profile using the standard Eddington formula (Buyle et al., 2007; Łokas and Mamon, 2001). As the NFW is a spherical symmetric system with an isotropic velocity tensor, the distribution function
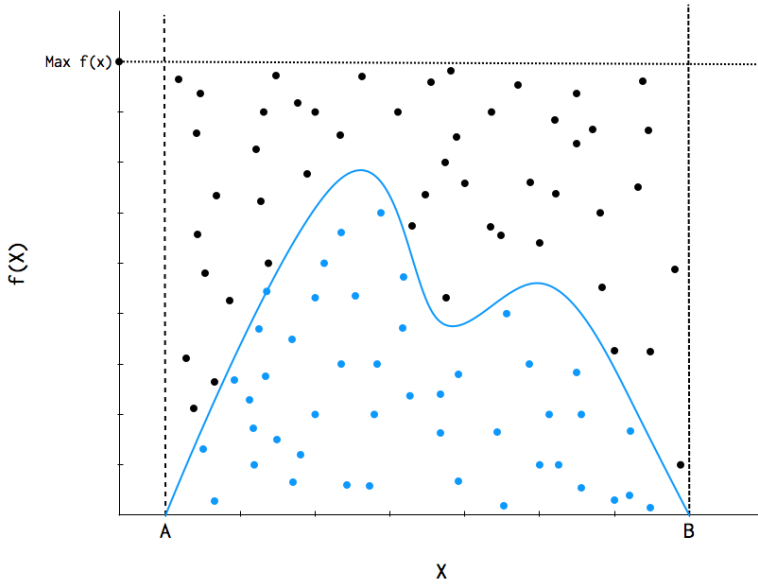
Figuur A.1: A visualisation of the acceptance-rejection technique. For a certain X value, a random number is chosen between 0 and max f(X), if this random number is located under the blue line, X is accepted.

depends on the phase-space coordinates only trough energy and is described by:

$$f(\mathcal{E}) = \frac{1}{\sqrt{8}\pi^2}\left[\int_0^{\mathcal{E}} \frac{d^2\rho}{d\Phi^2}\frac{d\Phi}{\sqrt{\mathcal{E}-\Phi}} + \frac{1}{\mathcal{E}^{1/2}}\left(\frac{d\rho}{d\Phi}\right)_{\Phi=0}\right] \tag{A.3}$$

with $\mathcal{E}$ the relative energy and Φ the potential. As indicated by Łokas and Mamon (2001), it can be shown that the second term in the brackets is zero. Next, we transform this equation to the integration variable r and the derivatives to r are indicated by ':

$$f(\mathcal{E}) = \frac{1}{\sqrt{8}\pi^2}\int_0^{r_{low}}\left(\frac{\rho'(r)\Phi''(r)}{\Phi'(r)} - \rho''(r)\right)\frac{1}{\Phi'(r)}\frac{1}{\sqrt{\mathcal{E}-\Phi(r)}}\frac{1}{(1+r)^2}dr \tag{A.4}$$

We already determined the radius r of the particle and from this we can calculate it maximal energy (if it would all be potential energy) to be $E_{max} = \Phi(r)$, with this E_{max} also the maximum value of our distribution function can be determined as $f(E_{max})$. The maximal velocity of the paricles (if all energy would be kinetic energy) would be $v_{max} = \sqrt{2\Phi(r)}$. Now we select v_r, v_ϕ and v_θ again by a acceptance-rejection technique:

1. for each of the velocities a random number is uniformly generated between $-v_{max}$ and v_{max}

2. there is checked if $v_r^2 + v_\phi^2 + v_\theta^2$ does not exceed v_{max}^2, and if so, there are new random numbers generated.

3. a random number is uniformly taken between 0 and $f(E_{max})$.

4. it is checked if $f(E = \phi(r) - (v_r^2 + v_\phi^2 + v_\theta^2)/2)$ is lower then this random number: if so, the velocities are excepted, if not we start again at 1.

This technique provides us with v_r, v_ϕ and v_θ for a particle at radius r. Subsequent, due to the spherical symmetry of our system ϕ and $\cos(\theta)$ can simply be drawn from uniform distributions over the intervals $[0, 2\pi]$ and $[-1, 1]$, respectively and there carthesian coordinates are calculated by:

$$
\begin{aligned}
x &= r\cos\phi\sin\theta & v_x &= v_r\cos\phi\sin\theta + v_\theta\cos\phi\cos\theta - v_\phi\sin\phi \\
y &= r\sin\phi\sin\theta & v_y &= v_r\sin\phi\sin\theta + v_\theta\sin\phi\cos\theta - v_\phi\cos\phi \\
z &= r\cos\theta & v_z &= v_r\cos\theta - v_\theta\sin\theta
\end{aligned}
\tag{A.5}
$$

A.1 The NFW halo.

Determination of the NFW parameters

For the NFW halo for which the density profile is described by:

$$
\rho_{\mathrm{NFW}}(r) = \frac{\rho_s}{(r/r_s)(1 + r/r_s)^2}
\tag{A.6}
$$

with r_s the scale parameter at which the density equals ρ_s. This density depends on the critical density and on the value of the concentration parameter, c. We define the boundary radius to be equal to $r_b = r_s \times c$. In practice, we have the concentration parameter c and r_s from the literature (cfr. equations 2.7 and 2.8). However, we only use these equations to determine the concentration parameter. ρ_s is determined witch the use of the critical density of the universe at z=0 and the concentration parameter, i.e. equation 2.6. Next, r_s is determined by assuming the total mass to rely within the radius r_b:

$$
M_{tot} = 4\pi \int_0^{r_b} r^2 \rho(r)\,dr
$$

$$
\Rightarrow = 4\pi\rho_s r_s^3 \int_0^{x_b} \frac{x^2}{x(1+x)^2}\,dx \qquad\qquad x = r/r_s \text{ and } x_b = r_b/r_s = c
$$

$$
\Rightarrow = 4\pi\rho_s r_s^3 \int_0^{x_b} \frac{x+1-1}{(1+x)^2}\,dx
$$

$$
\Rightarrow = 4\pi\rho_s r_s^3 \left[\int_0^{x_b} \frac{dx}{1+x} - \int_0^{x_b} \frac{dx}{(1+x)^2} \right]
$$

$$
\Rightarrow = 4\pi\rho_s r_s^3 \left[\ln(1+x_b) + \frac{1}{1+x_b} - 1 \right]
$$

$$
\Rightarrow M_{tot} = 4\pi\rho_s r_s^3 \left[\ln(1+x_b) - \frac{x_b}{1+x_b} \right].
\tag{A.7}
$$

$$
\Rightarrow r_s = \left[\frac{M_{tot}}{4\pi\rho_s[\ln(1+x_b) - x_b/(1+x_b)]} \right]^{1/3}.
\tag{A.8}
$$

For further calculations it might be usefull to express ρ_s as a function of the total mass and the scale radius:

$$\Rightarrow \rho_s = \frac{M_{tot}}{4\pi r_s^3 [\ln(1 + x_b) - x_b/(1 + x_b)]} \tag{A.9}$$

Determination of f(E)

We will now describe how the different components in f(E) are determined. For the density profile we replace the result of A.9 in A.6:

$$\rho(r) = \frac{M_{tot}}{4\pi r_s^3} \frac{1}{\ln(1 + x_b) - \frac{x_b}{1+x_b}} \frac{1}{(r/r_s)(1 + r/r_s)^2} \tag{A.10}$$

For the first derivative of the density to the radius:

$$\rho'(r) = \frac{d}{dr}\left(\frac{M_{tot}}{4\pi r_s^3} \frac{1}{\ln(1 + x_b) - \frac{x_b}{1+x_b}} \left(\frac{r}{r_s}\right)^{-1}\left(1 + \frac{r}{r_s}\right)^{-2}\right)$$

$$\Rightarrow = \frac{M_{tot}}{4\pi r_s^3} \frac{1}{\ln(1 + x_b) - \frac{x_b}{1+x_b}}\left[-\frac{1}{r_s}\left(\frac{r}{r_s}\right)^{-2}\left(1 + \frac{r}{r_s}\right)^{-2} - 2\left(\frac{r}{r_s}\right)^{-1}\left(1 + \frac{r}{r_s}\right)^{-3}\frac{1}{r_s}\right]$$

$$\Rightarrow = \frac{M_{tot}}{4\pi r_s^4} \frac{1}{\ln(1 + x_b) - \frac{x_b}{1+x_b}}\left[\frac{-1 - 3\frac{r}{r_s}}{(\frac{r}{r_s})^2(1 + \frac{r}{r_s})^3}\right]$$

$$\Rightarrow \rho'(r) = \frac{M_{tot}}{4\pi r_s^2} \frac{1}{\ln(1 + x_b) - \frac{x_b}{1+x_b}}\left[\frac{-1 - 3\frac{r}{r_s}}{r^2(1 + \frac{r}{r_s})^3}\right] \tag{A.11}$$

For the second derivative of the density to the radius:

$$\rho''(r) = \frac{d\rho'(r)}{dr} = \frac{M_{tot}}{4\pi r_s^2} \frac{1}{\ln(1 + x_b) - \frac{x_b}{1+x_b}}\left[\frac{-3/r_s}{r^2(1 + \frac{r}{r_s})^3} + \frac{2(1 + 3\frac{r}{r_s})}{r^3(1 + \frac{r}{r_s})^3} + \frac{3(1 + 3\frac{r}{r_s})/r_s}{r^2(1 + \frac{r}{r_s})^4}\right]$$

$$\Rightarrow = \frac{M_{tot}}{4\pi r_s^2} \frac{1}{\ln(1 + x_b) - \frac{x_b}{1+x_b}}\left[\frac{2 + 8r/r_s + 12(r/r_s)^2}{r^3(1 + \frac{r}{r_s})^4}\right]$$

$$\Rightarrow \rho''(r) = \frac{M_{tot}}{2\pi r_s^2} \frac{1}{\ln(1 + x_b) - \frac{x_b}{1+x_b}}\left[\frac{1 + 4r/r_s + 6(r/r_s)^2}{r^3(1 + \frac{r}{r_s})^4}\right] \tag{A.12}$$

The potential can be calculated from the density:

$$\Phi(r) = \underbrace{\frac{4\pi G}{r} \int_0^r \rho(r')r'^2 dr'}_{= \Phi_1} + \underbrace{4\pi G \int_r^\infty \rho(r')r'dr'}_{= \Phi_2} \tag{A.13}$$

$$\Phi_1(r) = \frac{4\pi G}{r} \int_0^r \frac{M_{tot}}{4\pi r_s^3} \frac{1}{ln(1+x_b) - \frac{x_b}{1+x_b}} \frac{1}{(r'/r_s)(1+r'/r_s)^2} r'^2 dr'$$

$$= \underbrace{\frac{GM_{tot}}{rr_s^3} \frac{1}{ln(1+x_b) - \frac{x_b}{1+x_b}}}_{= C_1/r} \int_0^r \frac{1}{(r'/r_s)(1+r'/r_s)^2} r'^2 dr'$$

$$= \frac{C_1}{r} r_s^3 \int_0^{r/r_s} \frac{x^2 dx}{x(1+x)^2} = \frac{C_1}{r} r_s^3 \int_0^{r/r_s} \frac{x+1-1}{(1+x)^2} dx \qquad \text{with } x = r'/r_s$$

$$= \frac{C_1}{r} r_s^3 \left[\int_0^{r/r_s} \frac{dx}{1+x} - \int_0^{r/r_s} \frac{dx}{(1+x)^2} \right]$$

$$= \frac{C_1}{r} r_s^3 \left[\int_1^{1+r/r_s} \frac{dy}{y} - \int_0^{r/r_s} \frac{dx}{(1+x)^2} \right] \qquad \text{with } y = 1+x$$

$$\Rightarrow \Phi_1(r) = C_1 r_s^3 \left[\frac{ln(1+r/r_s)}{r} - \frac{1}{r} \int_0^{r/r_s} \frac{dx}{(1+x)^2} \right] \qquad (A.14)$$

$$\Phi_2(r) = 4\pi G \int_r^\infty \frac{M_{tot}}{4\pi r_s^3} \frac{1}{ln(1+x_b) - \frac{x_b}{1+x_b}} \frac{1}{(r'/r_s)(1+r'/r_s)^2} r' dr'$$

$$= \underbrace{\frac{GM_{tot}}{r_s^3} \frac{1}{ln(1+x_b) - \frac{x_b}{1+x_b}}}_{= C_1} \int_r^\infty \frac{1}{(r'/r_s)(1+r'/r_s)^2} r' dr'$$

$$\Rightarrow \Phi_2(r) = C_1 r_s^2 \int_{r/r_s}^\infty \frac{dx}{(1+x)^2} \qquad \text{with } x = r'/r_s \qquad (A.15)$$

Introducing equations A.14 and A.15 in A.13, where the upper limit of Φ_2 can be limited to r_b/r_s as the density drops there to 0:

$$\Phi(r) = C_1 r_s^3 \left[\frac{ln(1+r/r_s)}{r} - \frac{1}{r} \int_0^{r/r_s} \frac{dx}{(1+x)^2} + \frac{1}{r_s} \int_{r/r_s}^{r_b/r_s} \frac{dx}{(1+x)^2} \right]$$

$$= C_1 r_s^3 \left[\frac{ln(1+r/r_s)}{r} - \frac{1}{r} \left(-\frac{1}{1+r/r_s} + 1 \right) + \frac{1}{r_s} \left(-\frac{1}{1+x_b} + \frac{1}{1+r/r_s} \right) \right]$$

$$= C_1 r_s^3 \left[\frac{ln(1+r/r_s)}{r} - \frac{1}{r} \left(\frac{-1+1+r/r_s}{1+r/r_s} \right) + \frac{1}{r_s} \left(-\frac{1}{1+x_b} + \frac{1}{1+r/r_s} \right) \right]$$

$$\Rightarrow \Phi(r) = \frac{GM_{tot}}{ln(1+x_b) - \frac{x_b}{1+x_b}} \left[\frac{ln(1+r/r_s)}{r} - \frac{1/r_s}{1+x_b} \right] \qquad (A.16)$$

The first derivative of the potential:

$$\Phi'(r) = \frac{d\Phi(r)}{dr} = \frac{GM_{tot}}{ln(1+x_b) - \frac{x_b}{1+x_b}} \left[-\frac{ln(1+r/r_s)}{r^2} + \frac{1}{rr_s(1+r/r_s)} \right] \qquad (A.17)$$

The second derivativ of the potential:

$$\Phi''(r) = \frac{d\Phi'(r)}{dr}$$

$$= \frac{GM_{tot}}{\ln(1+x_b) - \frac{x_b}{1+x_b}} \left[2\frac{ln(1+r/r_s)}{r^3} - \frac{2}{r^2 r_s(1+r/r_s)} + \frac{1}{rr_s^2(1+r/r_s)^2} \right]$$

$$= \frac{GM_{tot}}{\ln(1+x_b) - \frac{x_b}{1+x_b}} \left[\frac{2\ln(1+r/r_s)}{r^3} + \frac{-2r_s - 3r}{r^2 r_s^2(1+r/r_s)^2} \right]$$

$$\Phi''(r) = \frac{2GM_{tot}}{r^3} \frac{1}{\ln(1+x_b) - \frac{x_b}{1+x_b}} \left[\ln(1+r/r_s) - \frac{r(3r+2r_s)}{2r_s^2(1+r/r_s)^2} \right] \tag{A.18}$$

A.2   The general NFW halo.

Determination of the boundary radius, r_b

For the more general formula for dark matter haloes proposed by Cen et al. (2004) with the following density profile:

$$\rho(r) = \frac{\rho_0}{(r/r_{-2})^\alpha (1+r/r_{-2})^{4-2\alpha}} \tag{A.19}$$

with r_{-2} the radius where the logarithmic slope of the density profile is -2. From Cen et al. (2004) we are provided with distribution functions from which we can obtain values for α and r_{-2}.

We determine the boundary radius as the radius where the density is 10^4 lower then the density at r_{-2}. Hence, the following equation should be satisfied:

$$\rho(r_b) = 10^{-4}\rho(r_{-2}) \tag{A.20}$$

$$\Rightarrow \frac{\rho_0}{2^{4-2\alpha}} = 10^{-4} \times \frac{\rho_0}{\frac{r_b}{r_{-2}}(1+\frac{r_b}{r_{-2}})^{4-2\alpha}} \tag{A.21}$$

ρ_0 cancels out in this equation and finally we have to solve the following equation (for which we use fsolve from the SciPy library):

$$r_b^\alpha(r_{-2}+r_b)^{4-2\alpha} = \frac{2^{4-2\alpha}}{10^{-4}} r_{-2}^{4-\alpha} \tag{A.22}$$

ρ_0 is determined from assuming that the total mass of the halo has to reside in the boundary

radius:

$$M_{tot} = 4\pi \int_0^{r_b} r^2 \rho(r) dr$$

$$= 4\pi \int_0^{r_b} r^2 \frac{\rho_0}{(r/r_{-2})^\alpha (1 + r/r_{-2})^{4-2\alpha}} dr$$

$$= 4\pi \rho_0 r_{-2}^3 \int_0^{r_b/r_{-2}} \frac{x^2 dx}{x^\alpha (1+x)^{4-2\alpha}} \qquad \text{with } x = r/r_{-2}$$

$$= 4\pi \rho_0 r_{-2}^3 \int_0^{r_b/r_{-2}} x^{2-\alpha}(1+x)^{2\alpha-4} dx$$

$$= 4\pi \rho_0 r_{-2}^3 \left(\frac{r_b}{r_{-2}}\right)^{3-\alpha} \int_0^1 y^{2-\alpha} \left(1 - \left(-\frac{r_b}{r_{-2}}\right) y\right)^{2\alpha-4} dy \qquad \text{with } y = \frac{r_{-2}}{r_b} x$$

$$= 4\pi \rho_0 r_{-2}^\alpha r_b^{3-\alpha} B(3-\alpha, 1) {}_2F_1(4-2\alpha, 3-\alpha; 4-\alpha; -r_b/r_{-2})$$

Where wed use the following hypergeometric function, with B a beta function:

$$B(b, c-b) {}_2F_1(a, b; c; z) = \int_0^1 x^{b-1}(1-x)^{c-b-1}(1-zx)^{-a} dx \qquad (A.23)$$

with $\qquad \begin{cases} b - 1 = 2 - \alpha \\ c - b - 1 = 0 \\ a = 2\alpha - 4 \end{cases} \Rightarrow \begin{cases} b = 3 - \alpha \\ c = 4 - \alpha \\ a = 2\alpha - 4 \end{cases}$

$$\Rightarrow \rho_0 = \frac{M_{tot}}{4\pi r_{-2}^\alpha r_b^{3-\alpha} B(3-\alpha, 1) {}_2F_1(4-2\alpha, 3-\alpha; 4-\alpha; -r_b/r_{-2})} \qquad (A.24)$$

Determination of f(E)

We will now describe how the different components in f(E) are determined. For the density profile we use equation A.19 where we replace ρ_0 by equation A.24. For the first derivative of the density to the radius:

$$\rho'(r) = \frac{d\rho(r)}{dr} = \rho_0 \frac{d}{dr} \left[\left(\frac{r}{r_{-2}}\right)^{-\alpha} \left(1 + \frac{r}{r_{-2}}\right)^{2\alpha-4}\right]$$

$$= \rho_0 \left[-\alpha \left(\frac{r}{r_{-2}}\right)^{-\alpha-1} \frac{1}{r_{-2}} \left(1 + \frac{r}{r_{-2}}\right)^{2\alpha-4} + (2\alpha-4) \left(\frac{r}{r_{-2}}\right)^{-\alpha} \left(1 + \frac{r}{r_{-2}}\right)^{2\alpha-5} \frac{1}{r_{-2}}\right]$$

$$\Rightarrow \rho'(r) = \frac{\rho_0}{r_{-2}} \left[-\alpha \left(\frac{r}{r_{-2}}\right)^{-\alpha-1} \left(1 + \frac{r}{r_{-2}}\right)^{2\alpha-4} + (2\alpha-4) \left(\frac{r}{r_{-2}}\right)^{-\alpha} \left(1 + \frac{r}{r_{-2}}\right)^{2\alpha-5}\right]$$

$$(A.25)$$

The second derivative is:

$$\rho''(r) = \frac{d\rho'(r)}{dr}$$

$$\rho''(r) = \frac{\rho_0}{r_{-2}^2}\left[\alpha(\alpha+1)\left(\frac{r}{r_{-2}}\right)^{-\alpha-2}\left(1+\frac{r}{r_{-2}}\right)^{2\alpha-4}\right.$$
$$-2\alpha(2\alpha-4)\left(\frac{r}{r_{-2}}\right)^{-\alpha-1}\left(1+\frac{r}{r_{-2}}\right)^{2\alpha-5}$$
$$\left.+(2\alpha-4)(2\alpha-5)\left(\frac{r}{r_{-2}}\right)^{-\alpha}\left(1+\frac{r}{r_{-2}}\right)^{2\alpha-6}\right] \tag{A.26}$$

For the potential can be calculated from the density:

$$\Phi(r) = \underbrace{\frac{4\pi G}{r}\int_0^r \rho(r')r'^2\,dr'}_{=\Phi_1} + \underbrace{4\pi G\int_r^\infty \rho(r')r'\,dr'}_{=\Phi_2} \tag{A.27}$$

$$\Phi_1(r) = \frac{4\pi G}{r}\int_0^r \rho_0\left(\frac{r'}{r_{-2}}\right)^{-\alpha}\left(1+\frac{r'}{r_{-2}}\right)^{2\alpha-4}r'^2\,dr'$$
$$= \frac{4\pi G\rho_0 r_{-2}^3}{r}\int_0^{r/r_{-2}} x^{2-\alpha}\left(1+x\right)^{2\alpha-4}\,dx \qquad\qquad \text{with } x = r'/r_{-2}$$
$$= \frac{4\pi G\rho_0 r_{-2}^3}{r}\int_0^1 \left(\frac{r}{r_{-2}}\right)^{3-\alpha}y^{2-\alpha}\left(1-\left(-\frac{r}{r_{-2}}y\right)\right)^{2\alpha-4}\,dy \qquad \text{with } y = \frac{r_{-2}}{r}x$$

Here we can again use equation A.23:

$$\Phi_1(r) = 4\pi G\rho_0 r_{-2}^\alpha r^{2-\alpha}B(3-\alpha,1)_2F_1(4-2\alpha,3-\alpha;4-\alpha;-r/r_{-2}) \tag{A.28}$$

$$\Phi_2(r) = 4\pi G\int_r^\infty \rho_0\left(\frac{r'}{r_{-2}}\right)^{-\alpha}\left(1+\frac{r'}{r_{-2}}\right)^{2\alpha-4}r'\,dr'$$
$$= 4\pi G\rho_0 r_{-2}^2\int_{r/r_{-2}}^\infty x^{1-\alpha}\left(1+x\right)^{2\alpha-4}\,dx \qquad\qquad \text{with } x = r'/r_{-2}$$
$$= 4\pi G\rho_0 r_{-2}^2\int_0^{r/r_{-2}} y^{\alpha-1}\left(\frac{y+1}{y}\right)^{2\alpha-4}\frac{dy}{y^2} \qquad\qquad \text{with } y = \frac{r_{-2}}{r'} = \frac{1}{x}$$
$$= 4\pi G\rho_0 r_{-2}^2\int_0^{r/r_{-2}} y^{1-\alpha}\left(y+1\right)^{2\alpha-4}\,dy$$
$$= \frac{4\pi G\rho_0 r_{-2}^{4-\alpha}}{r^{2-\alpha}}\int_0^1 z^{1-\alpha}\left(1-\left(-\frac{r_{-2}}{r}\right)z\right)^{2\alpha-4}\,dz \qquad\qquad \text{with } z = \frac{r}{r_{-2}}y$$

Here we can again use equation A.23:

$$\Phi_2(r) = 4\pi G\rho_0 r_{-2}^{4-\alpha}r^{\alpha-2}B(2-\alpha,1)_2F_1(4-2\alpha,2-\alpha;3-\alpha;-r_{-2}/r) \tag{A.29}$$

When we combine the results of equation A.28 and equation A.29:

$$\Phi(r) = 4\pi G\rho_0\left[r_{-2}^\alpha r^{2-\alpha}B(3-\alpha,1)_2F_1(4-2\alpha,3-\alpha;4-\alpha;-r/r_{-2})\right.$$
$$\left.+r_{-2}^{4-\alpha}r^{\alpha-2}B(2-\alpha,1)_2F_1(4-2\alpha,2-\alpha;3-\alpha;-r_{-2}/r)\right] \tag{A.30}$$

For the derivatives of the potential we use the following definitions for the derivative of the hypergeometrical functions:

$$\frac{d\,_2F_1(a, b; c; z)}{dz} = \frac{ab}{c}\,_2F_1(a + 1, b + 1; c + 1; z) \tag{A.31}$$

For the first derivate of the potential:

$$\Phi'(r) = \Phi'_1(r) + \Phi'_2(r)$$

$$\rightarrow \Phi'_1(r) = 4\pi G\rho_0 r_{-2}^{\alpha}\Bigg[(2 - \alpha)r^{1-\alpha}B(3 - \alpha, 1)\,_2F_1(4 - 2\alpha, 3 - \alpha; 4 - \alpha; -r/r_{-2})$$

$$+ r^{2-\alpha}B(3 - \alpha, 1)\frac{(4 - 2\alpha)(3 - \alpha)}{4 - \alpha}\left(-\frac{1}{r_{-2}}\right)\,_2F_1(3 - 2\alpha, 2 - \alpha; 3 - \alpha; -r/r_{-2})\Bigg]$$

$$\rightarrow \Phi'_2(r) = 4\pi G\rho_0 r_{-2}^{4-\alpha}\Bigg[(\alpha - 2)r^{\alpha-3}B(2 - \alpha, 1)\,_2F_1(4 - 2\alpha, 2 - \alpha; 3 - \alpha; -r_{-2}/r)$$

$$+ r^{\alpha-2}B(2 - \alpha, 1)\frac{(4 - 2\alpha)(2 - \alpha)}{3 - \alpha}\left(\frac{r_{-2}}{r^2}\right)\,_2F_1(3 - 2\alpha, 1 - \alpha; 2 - \alpha; -r_{-2}/r)\Bigg]$$

And for the second derivative of the potential:

$$\Phi''(r) = \Phi''_1(r) + \Phi''_2(r)$$

$$\rightarrow \Phi''_1(r) = 4\pi G\rho_0 r_{-2}^{\alpha}\Bigg[(2 - \alpha)(1 - \alpha)r^{\alpha}B(3 - \alpha, 1)\,_2F_1(4 - 2\alpha, 3 - \alpha; 4 - \alpha; -r/r_{-2})$$

$$+ 2(2 - \alpha)r^{1-\alpha}B(3 - \alpha, 1)\frac{(4 - 2\alpha)(3 - \alpha)}{4 - \alpha}\left(-\frac{1}{r_{-2}}\right)$$

$$\,_2F_1(3 - 2\alpha, 2 - \alpha; 3 - \alpha; -r/r_{-2})$$

$$+ r^{2-\alpha}B(3 - \alpha, 1)\frac{(4 - 2\alpha)(3 - \alpha)}{4 - \alpha}\frac{(3 - 2\alpha)(2 - \alpha)}{3 - \alpha}\left(-\frac{1}{r_{-2}}\right)^2$$

$$\,_2F_1(2 - 2\alpha, 1 - \alpha; 2 - \alpha; -r/r_{-2})\Bigg]$$

$$\rightarrow \Phi''_2(r) = 4\pi G\rho_0 r_{-2}^{4-\alpha}\Bigg[(\alpha - 2)(\alpha - 3)r^{\alpha-2}B(2 - \alpha, 1)\,_2F_1(4 - 2\alpha, 2 - \alpha; 3 - \alpha; -r_{-2}/r)$$

$$+ (\alpha - 2)r^{\alpha-3}B(2 - \alpha, 1)\frac{(4 - 2\alpha)(2 - \alpha)}{3 - \alpha}\left(\frac{r_{-2}}{r^2}\right)$$

$$\,_2F_1(3 - 2\alpha, 1 - \alpha; 2 - \alpha; -r_{-2}/r)$$

$$+ (\alpha - 2)r^{\alpha-3}B(2 - \alpha, 1)\frac{(4 - 2\alpha)(2 - \alpha)}{3 - \alpha}\left(\frac{r_{-2}}{r^2}\right)$$

$$\,_2F_1(3 - 2\alpha, 1 - \alpha; 2 - \alpha; -r_{-2}/r)$$

$$+ r^{\alpha-2}B(2 - \alpha, 1)\frac{(4 - 2\alpha)(2 - \alpha)}{3 - \alpha}\frac{(3 - 2\alpha)(1 - \alpha)}{2 - \alpha}\left(\frac{r_{-2}}{r^2}\right)^2$$

$$\,_2F_1(1 - 2\alpha, -\alpha; 1 - \alpha; -r_{-2}/r)\Bigg]$$

B

Determination of the inital conditions of a merger simulation

As described in subsection 4.2.2, a merger tree provides us with the masses of the progenitors and their merging times. For each merger event, we select the most massive dark-matter halo among the haloes that need to be merged. This we call the "primary" halo. In case of a binary merger there is only one "secondary" halo; in case of a multiple merger, there can be several secondaries. Each primary/secondary merger is treated as a 2-body problem. We equate the time of the merger provided by the merger tree with the pericenter passage of the primary/secondary couple. First, we select the primary halo and calculate its corresponding virial radius, r_{vir}, by determining at which radius the density profile of the dark matter halo drops below ρ_{200}, 200 times the critical density ρ_{crit} of the universe at that redshift:

$$\rho_{200} = 200\rho_{crit} = 200\frac{3h^2 100^2}{8\pi G}[\Omega_m(1+z)^3 + 1 - \Omega_m] \tag{B.1}$$

Also the virial mass, M_{vir} is determined as the dark matter mass which is located within the virial radius. Then the virial velocity can be calculated as:

$$v_{vir} = \sqrt{GM_{vir}/r_{vir}} \tag{B.2}$$

Then, we use the 2D probability distribution function of Benson (2005) to randomly draw a value for the radial and tangential velocities of the incoming secondary halo as it crosses the primary's virial radius, denoted by v_r and $v_\perp$, expressed in units of the primary's virial velocity:

$$f(v_r, v_\perp) = a_1 v_\perp \exp\{-a_2(v_\perp - a_9)^2 - b_1(v_\perp)[v_r - b_2(v_\perp)^2]\} \tag{B.3}$$

with

$$b_1(v_\perp) = a_3 \exp\left[-a_4(v_\perp - a_5^2)\right] \tag{B.4}$$

$$b_2(v_\perp) = a_6 \exp\left[-a_7(v_\perp - a_8^2)\right] \tag{B.5}$$

and we used for the values a_{1-9} respectively

a_1	a_2	a_3	a_4	a_5	a_6	a_7	a_8	a_9
6.38	2.30	18.8	0.506	-0.0934	1.05	0.267	-0.154	0.157

In practice, almost all trajectories are nearly parabolic with an ellipticity close to 1. As Benson (2005) finds only a very weak correlation between the spatial distribution of subsequent mergers, we draw the orbital plane positions from an isotropic distribution. From this velocity information at the virial radius, we determine the orbital elements of the corresponding Kepler orbit, e.g. the semi-major axis, a, the ellipticity, e, the length of the specific relative angular momentum vector, $h = rv_\perp$ (Curtis, 2010a). They are determined as:

Elliptical trajectory

$$\frac{v^2}{2} - \frac{\mu}{r} = -\frac{\mu}{2a}$$

$$\Rightarrow a = \frac{\mu}{\frac{2\mu}{r} - v^2}$$

$$h^2 = \mu a(1 - e^2)$$

$$\Rightarrow e = \sqrt{\frac{1 - h^2}{\mu a}}$$

Hyperbolic trajectory

$$\frac{v^2}{2} - \frac{\mu}{r} = \frac{\mu}{2a}$$

$$\Rightarrow a = \frac{\mu}{v^2 - \frac{2\mu}{r}}$$

$$h^2 = \mu a(e^2 - 1)$$

$$\Rightarrow e = \sqrt{\frac{1 + h^2}{\mu a}} \tag{B.6}$$

To determine if we are dealing with an elliptical or hyperbolic trajectory we can use the formula for conservation of energy

$$\epsilon = \frac{v^2}{2} - \frac{\mu}{r} \tag{B.7}$$

If ϵ is positive we are dealing with a hyperbolic trajectory when it is negative we have an elliptical trajectory.

We want to follow each merger starting 2 Gyr before its pericenter passage. Therefore, we introduce the secondary halo into the simulation at a position and with a velocity that would bring it to the pericenter of its Kepler orbit 2 Gyr in the future. Obviously, since galaxies are deformable, they will not adhere to these Kepler orbits. This with the exception of the mergers occurring during the first 2 Gyr of a simulation. In that case, the time to reach pericenter is set to be the difference between the merging time and the start of the simulation. We note that it is perfectly possible for a merger to start when the previous merger that formed the primary is still ongoing, leading to complex multi-galaxy encounters.

To know where on the trajectory we have to start the second halo we need to distinguish between elliptical ($e < 1$) and hyperbolic ($e > 1$) trajectories. In both cases we need to find the true anomaly θ which is the angle between the line connecting the apse and the line connecting the focal point with a certain position on the ellipse/hyperbola.

B.1 Elliptical trajectory

In the case of an elliptical trajectory, we define an auxilary angle, the eccentric anomaly E, which is related to the mean anomaly by:

$$\cos E = \frac{e + \cos \theta}{1 + e \cos \theta} \tag{B.8}$$

and the physical relation is shown in Figure B.1. This eccentric anomaly is related to the mean anomaly M_e by the Kepler equation:

$$M_e = E - e \sin E \tag{B.9}$$

The angular velocity of the position vector of an elliptical orbit is not constant, but still during the period T 2π radians are covered and hence, the average angular velocity or mean motion n is $2\pi/T$. Now, the mean anomaly is defined as:

$$M_e = nt = \frac{2\pi}{T}t = \frac{\mu^2}{h^3}(1 + e^2)^{3/2}t \tag{B.10}$$

From the orbital elements and with the use of Kepler's third law stating that the period of a 'planet' is proportional to the semimajor axis to the three-halves power or

$$T = \frac{2\pi}{\sqrt{\mu}}a^{3/2} \tag{B.11}$$

equation B.10 reduces itself to:

$$M_e = nt = \sqrt{\frac{\mu}{a^3}}t \tag{B.12}$$
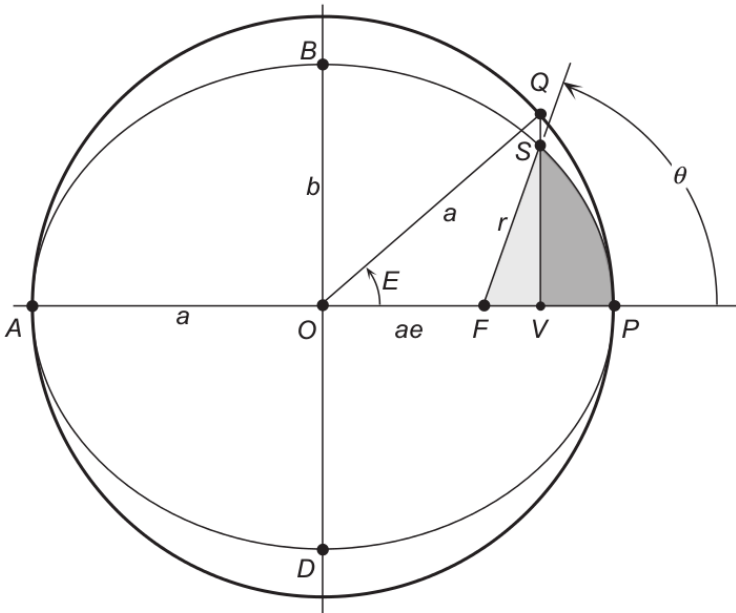
Figuur B.1: Visualisation of the relation between the true anomaly, θ, and the eccentric anomaly, . Figure from Curtis (2010b).

However, Kepler's equation has no analytical solutions and so we solve this numerically using Newton's method (Curtis, 2010b). This method is widely used for finding the root of a well-behaved function, for example $f(x) = 0$. The process is visualized in Figure B.2.We first take an initial guess x_i and determine the value of $f(x_i)$ and it's first derivative $f'(x_i)$. Then, the intercept x_{i+1} is determined by extending the tangent line equal to the slope of the curve at x_i:

$$f'(x_i) = \frac{0 - f(x_i)}{x_{i+1} - x_i} \tag{B.13}$$

$$\Rightarrow x_{i+1} = x_i - \frac{f(x_i)}{f'(x_i)} \tag{B.14}$$

We repeat this process untill the root x_i has been found, e.g. untill the ratio of $\frac{f(x_i)}{f'(x_i)}$ drops below a certain tolerance level.

If we apply this to our problem, we want to find the root of the function $f(E) = M_e - (E - e\sin E)$:

1. We initialize E_i to be equal to M_e

2. We determine the value of $f(E_i)$, and the value of $f'(E_i) = 1 - e\cos E_i$.

3. We check if $f(E_i)/f'(E_i)$ exceeds the tolerance.

4. If the tolerance is exceeded, the value of E is updated to $E_{i+1} = E_i - \frac{E_i - e\sin E_i - M_e}{1 - e\cos E_i}$ and the previous 2 steps are repeated.

5. If the tolerance is not exceeded, E_i is accepted as the root of $f(E)$ and we found our eccentric anomaly.

   Then we can use the following orbit equation for the ellipse in terms of the eccentric
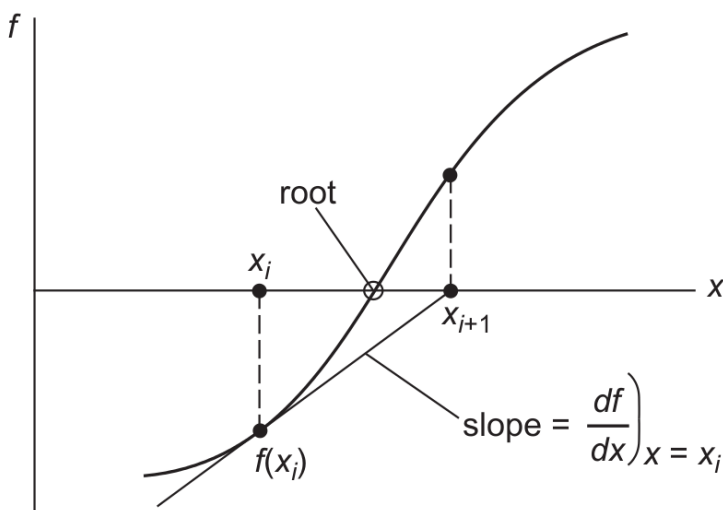
Figuur B.2: Visualisation of the Newton method to find the root of a well-behaved functionr. Figure from Curtis (2010b).

anomaly to deterime the starting radius:

$$r_{\text{start}} = a(1 + e \cos E) \tag{B.15}$$

Now we use equations B.6 to determine the corresponding velocities $v_{\text{r,start}}$ and $v_{\perp,\text{start}}$:

$$v_{\perp,\text{start}} = -\sqrt{\frac{\mu a(1 - e^2)}{r_{\text{start}}}} \tag{B.16}$$

$$v_{\text{r,start}} = \sqrt{\frac{2\mu}{r_{\text{start}}} - \frac{\mu}{a} - v_{\perp,\text{start}}^2} \tag{B.17}$$

B.2 Hyperbolic trajectory

In the case of a hyperbolic trajectory we again define an auxilary angle, the hyperbolic eccentric anomaly, F, which is related to the true anomaly, θ by:

$$\sinh F = \frac{y}{b} = \frac{\sqrt{e^2 - 1} \sin \theta}{1 + e \cos \theta} \tag{B.18}$$

Figure B.3 shows the hyperbolic parameters, for example y, the hight of the point above the apse line, and b, the semiminor axis of the hyperbola. In the same way as for the elliptical trajectory we define the hyperbolic mean anomaly, M_h as:

$$M_h = \frac{\mu^2}{h^3}(e^2 - 1)^{3/2} t \tag{B.19}$$
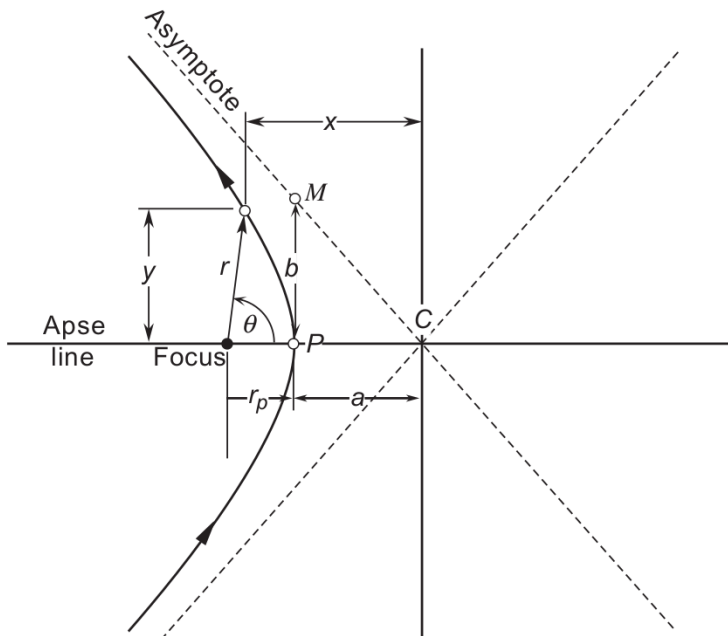
Figuur B.3: Visualisation of the hyperbolic parameters. Figure from Curtis (2010b).

The hyperbolic mean anomaly is related to the eccentric anomaly by Kepler's equation for the hyperbola:

$$M_h = e \sinh F - F \tag{B.20}$$

Again, we cannot solve this equation for F analytically and need to solve it numerically. We apply Newton's procedure to solve this equation as we want to find the root of:

$$f(F) = e \sinh F - F - M_h$$

(a) We start with an initial guess $F_0 = M_h$.

(b) Then we calculate $f(F_i)$, $f'(F_i)$ and the ratio$_i = f(F_i)/f'(F_i)$ with:

$$f'(F) = e \cosh F - 1$$

(c) We repeat the previous step when the ratio exceeds a certain tolerance (for example $10^{-}14$), with an updated value of

$$F_{i+1} = F_i - \frac{e \sinh F_i - F_i - M_h}{e \cosh F_i - 1}$$

(d) When the ratio is less then the tolerance, we accept the value F_i as the solution.

Now we can determine the starting radius, r_{start}, from the orbit equation in terms of the hyperbolic eccentric anomaly (Curtis, 2010b):

$$r = \frac{a(e^2 - 1)}{1 + e \cos \theta} = a(e \cosh F - 1) \tag{B.21}$$

Our system is spherical symmetric so ϕ can be randomly drawn from a uniform distribution between 0 and 2π and in the same manner, $\cos(\theta)$ can be drawn between $[-1, 1]$. Next, we can use the equations A.5 to get the relative location and velocity of the second halo compared to the main halo in a carthesian grid.